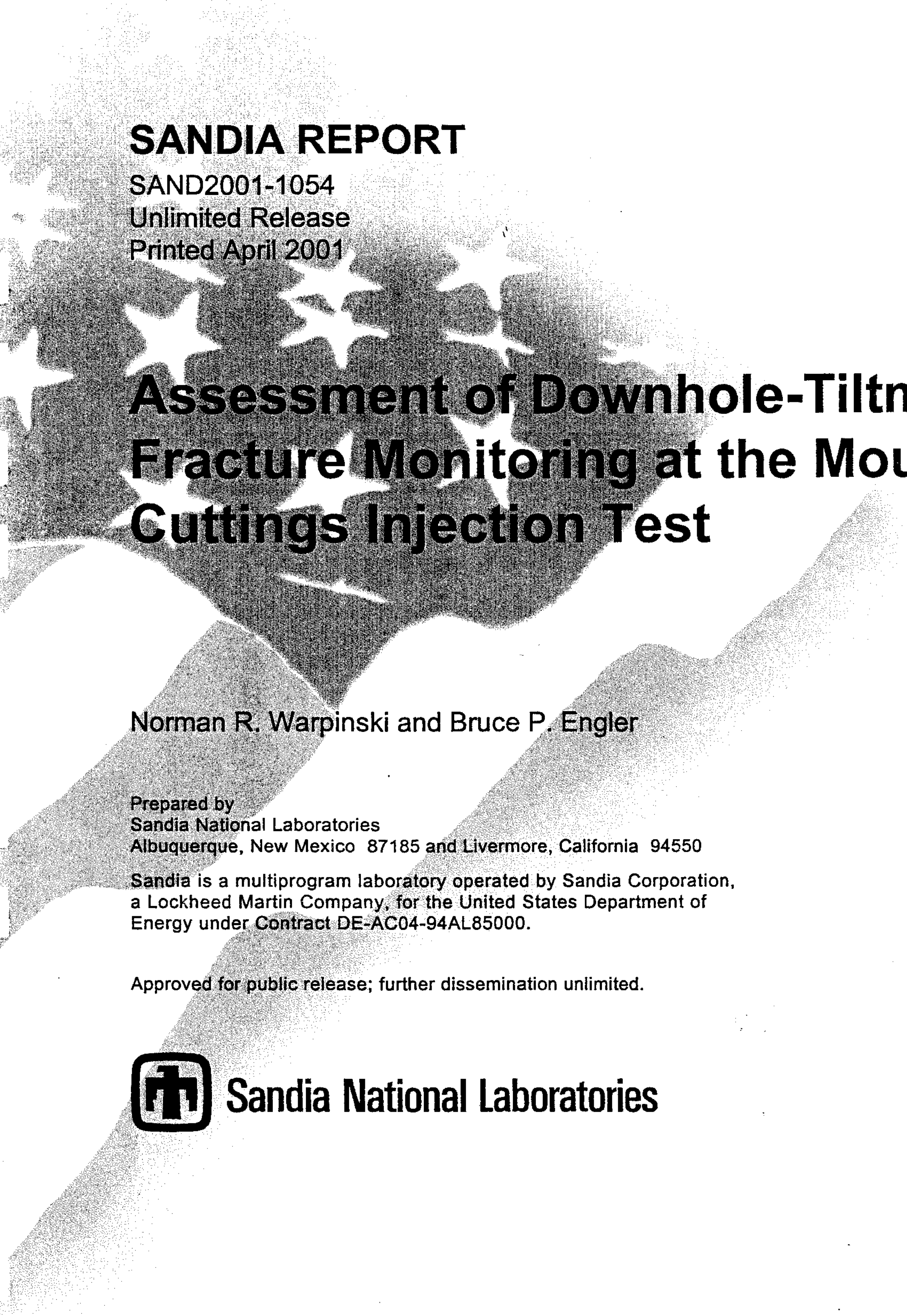

SANDIA REPORT

SAND2001-1054
Unlimited Release
Printed April 2001

Assessment of Downhole-Tiltmeter Fracture Monitoring at the Mounds Drill Cuttings Injection Test

Norman R. Warpinski and Bruce P. Engler

Prepared by
Sandia National Laboratories
Albuquerque, New Mexico 87185 and Livermore, California 94550

Sandia is a multiprogram laboratory operated by Sandia Corporation,
a Lockheed Martin Company, for the United States Department of
Energy under Contract DE-AC04-94AL85000.

Sandia National Laboratories

Issued by Sandia National Laboratories, operated for the United States Department of Energy by Sandia Corporation.

Available to DOE and DOE contractors from
U.S. Department of Energy
Office of Scientific and Technical Information
P.O. Box 62
Oak Ridge, TN 37831

Telephone: (865)576-8401
Facsimile: (865)576-5728
E-Mail: reports@adonis.osti.gov
Online ordering: http://www.doe.gov/bridge

Available to the public from
U.S. Department of Commerce
National Technical Information Service
5285 Port Royal Rd
Springfield, VA 22161

Telephone: (800)553-6847
Facsimile: (703)605-6900
E-Mail: orders@ntis.fedworld.gov
Online order: http://www.ntis.gov/ordering.htm

SAND 2001-1054
Unlimited Release
Printed April 2001

ASSESSMENT OF DOWNHOLE-TILTMETER FRACTURE MONITORING AT THE MOUNDS DRILL CUTTINGS INJECTION TEST

Norman R. Warpinski and Bruce P. Engler
Geophysical Technology Department
Sandia National Laboratories
P.O. Box 5800
Albuquerque, NM 87185-0750

ABSTRACT

A downhole-tiltmeter array was employed at the Mounds (OK) drill cuttings injection test to monitor the growth of the cuttings-induced fractures. Given the other diagnostics at this test, including microseismic monitoring, coreholes through the fractured zones, tracers, and bottom-hole pressure, this test provided an excellent test case to evaluate the capabilities of downhole-tiltmeter arrays for fracture imaging. This report documents the test data obtained during the injections, the crack model used for inverting the data, the inversion results, a comparison with other diagnostics, finite element studies, and conclusions derived from these studies.

Table of Contents

List of Figures

List of Tables

INTRODUCTION

The optimization of hydraulic fracturing has been a tedious process because of the complexities of reservoirs and an inability to directly observe the fracture. As a result, considerable effort is now being expended to "image" hydraulic fractures by measuring some earth response associated with the fracturing process. The most well-known of these imaging techniques is microseismic monitoring,[1-4] which has been employed since the 1970's (primarily in research projects). Although improvements in receivers, telemetry and computer processing have now made microseismic monitoring a feasible technology for routine industry use,[4] there are some reservoirs that may not emit sufficiently energetic microseisms, and there are some fracture attributes, such as the width, about which the microseismic method cannot provide any information.

Surface tiltmeters[5-8] also have a long history of use (since the 1970's), but their application has been limited because they are only able to resolve fracture azimuth and dip (e.g., fracture orientation), large scale fracture asymmetry, and the depth to the fracture center. In addition, they had primarily been limited to fracture depths of less than 5,000 ft. Recent improvements in tiltmeter designs[9] have helped to extend this application to greater depths, but have not been able to help resolve additional fracture attributes (e.g., length and height).

The recent applications of tiltmeters in downhole arrays, which was pioneered at the GRI/DOE funded M-Site experiment in the Piceance basin in Colorado,[10,11] has extended the ability of the tiltmeter to resolve additional features of the fracture. Although the M-Site tiltmeters were cemented in place, a wireline-run tiltmeter array[12,13] was introduced by a fracture service company in 1998, allowing tiltmeters to be used in routine industry fracture applications as well as advanced diagnostic research projects.

The advantage of the downhole-tiltmeter application is threefold. First, the dowhnole tiltmeter array is much closer to the hydraulic fracture than in the surface application. Second, the downhole-tiltmeter array is strategically located at a position where the earth deformation is largest (e.g., normal to the fracture opening). Third, it is not necessary to deal with all of the details of the surface layers to invert the data. These advantages make it possible to provide a measurement of the earth deformation caused by the hydraulic fracture and estimate some attributes of the fractures that were responsible for the induced response.

The downhole tiltmeter responds to the fracture-induced deformation in a relatively simple way, as shown in Figure 1. The fracture, assumed to have some generalized elliptic shape, deforms the earth a small amount for large distances. The maximum deformation is generally located normal to the center of the fracture and displacements above and below trend to zero at large vertical distances from the fracture.[14] The tilt, which is a vector quantity, is the derivative of the horizontal displacement with respect to the vertical direction (gravity). There is no vertical component of tilt. For a fracture, the tilt measured orthogonal to the fracture plane has a zero point at the center and oppositely signed responses above compared to below (the actual sign depends on the chosen convention). The peaks in the tilts are related to the height of the fracture relative to the distance away. Note also that the tilt can be decomposed into two orthogonal horizontal components.

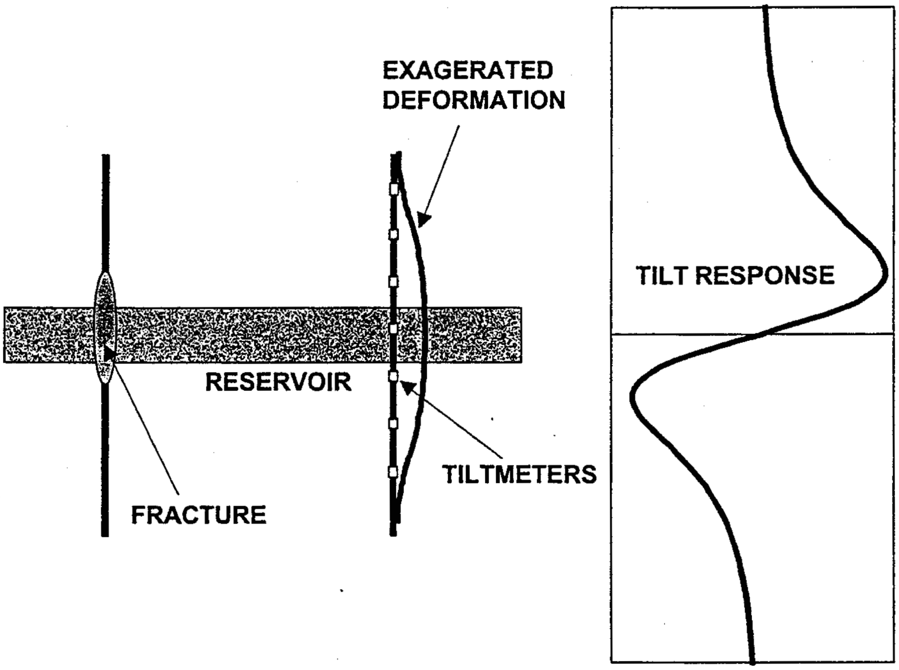

Figure 1. Schematic of fracture-induced deformation and the resultant tilt.

In practice, one would prefer to measure the strain or displacement at some remote distance, but both values would be extremely small and there is no clear reference point in a downhole well. The tiltmeter, with its resolution of a few nanoradians, is one of the few instruments that can detect the small deformation and it has a clear vertical (gravity) reference. Furthermore, since the tiltmeter gives the derivative of the displacement, an array of tiltmeters provides the same information that displacement measurements would provide.

Given that tiltmeters can detect the subtle deformations at large distances from hydraulic fractures, there still remain issues of how to deploy the tiltmeters so that they accurately measure the deformation and how to insure the accuracy and uniqueness of the inversion of the data in order to arrive at a reliable result. The wireline deployment of these tools will invariably be in a cased well and leads immediately to the issue of casing effects. One can perform structural calculations to show that the effect of the casing is negligible, but the physical example of a 90-ft stand of tubing or casing on the rig provides an easy example. When such a long stand is observed, it is often bowed by several degrees due to its own weight (a relatively small load). The hydraulic fracture induces downhole tilts that are typically 10^{-5} radians or 6×10^{-4} degrees. Clearly the casing offers insignificant resistance to such small bending moments and deforms easily with the earth. However, the casing may have an effect at interfaces or other locations where there are large gradients in the displacement (discontinuities in the tilt field). In such cases, the casing probably serves to dampen and smooth the response. The cement is probably insignificant as long as there is reasonable cement around the well (however, void regions could cause problems).

The second deployment issue is that of coupling. The tiltmeters at M-Site were cemented in place and their results agreed well with the microseismic imaging data.[10,11] However routine deployment of a downhole-tiltmeter array will require that the instruments be run on wireline. Two approaches are available: motor clamping and centralizer deployment. The motor clamping assures that the tiltmeters are well-coupled to the wellbore, but is a more complicated deployment and requires more electronics, controls and motors. The centralizer deployment is somewhat different than the usual deployment of tools on centralizers. Because the tools are light and are run on a wireline, they will not go down the casing unless the centralizer springs are very weak or the centralizer bow OD is slightly smaller than the casing ID. In such a case, the deployment the instruments are only coupled by virtue of laying against the wall (no spring load to maintain coupling). However, the centralizers prevent rocking by providing a two-point contact (centralizers are placed on the top and bottom of the instruments). While this approach seems reasonable for the extremely tiny deformations and the nearly quasi-static deformation process, there is little experience or confirmation with measurements of such small angular deformations under such conditions. This Mounds test actually gives us a chance to examine this issue by comparing the tiltmeter results with the microseismic and corehole measurements.

A third issue is borehole noise. Since the measured tilts are extremely small, there are borehole effects that could cause problems with the measurement. In a gas or oil well, bubbling gas offers the largest potential for inducing noise, but this test at Mounds was in a newly cased well with no open perforations. Other sources of noise could be curing cement (e.g., stress redistribution as the cement changes volume), thermal recovery after drilling, tidal effects, and instrument noise and drift. In any case, the cultural noise level should be determined in order to understand the accuracy and reliability of the results.

Since the tilt is a directed quantity, tiltmeters have two sensors (bi-axial) to measure the tilt in two orthogonal directions so that a magnitude and an angle can be determined. If the sensors are oriented, then the normal and parallel components of the tilt field (relative to the fracture) can be deduced and extra information can be extracted. However, in the wireline-run tiltmeters, there is not yet any means for orienting the tiltmeters and the data are generally used for their magnitudes only. Future instruments with orienting devices will provide additional usable data from the separate components.

Although the purpose of the Mounds experiment was to monitor and assess the details of cuttings injection, this test also allowed for some evaluation of the accuracy, reliability and capabilities of the wireline-run downhole tiltmeters. This report will describe the estimated fracture size and shape as well as accuracy and confidence issues.

MOUNDS TEST PLAN

Detailed descriptions of the Mounds testing and monitoring are given in three papers at the Rock Mechanics Symposium[15-17] and an overview SPE paper.[18] In brief, the Mounds Drill Cuttings Injection Experiment was an industry consortium project to evaluate our ability to model and monitor the disposal of contaminated drill cuttings in deep formations. The companies in the consortium included BP Exploration, Azerbaijan Oil Co., Schlumberger, Shell E&P Tech., Chevron, MSD, Halliburton Energy Services, Amoco, Mobil, Hughes-Christensen, Exxon Production Research, Arco, Gas Research Institute, Pinnacle Technologies and UPRC. The US Dept. of Energy provided additional support to Sandia National Laboratories through the Natural Gas and Oil Technology Partnership.

The Mounds location is in central Oklahoma just south of Tulsa. The facility is owned by Hughes-Christensen, who provided site use and some drilling support as part of their contribution. The formations used for injection operations were the Wilcox sandstone, a friable sandstone at a depth of approximately 2700 ft, and the Atoka shale, a laminated shale-siltstone sequence at a depth of approximately 1900 ft.

In a typical drill-cuttings injection operation,[19-26] cuttings may be injected continuously for 8-12 hours and then stopped for the night. Operations resume the next day and this "pulsed" injection schedule may continue for a few weeks. There may be intermittent shut down periods for several weeks while cuttings are accumulated or equipment is overhauled, and then injection may resume again in the same interval.

To simulate this type of process on a small scale, the project plan was to conduct multiple small volume injections that were followed by limited shut-in periods over a three day period. The overnight shut-ins would simulate the longer down times.

Monitoring of the cuttings injection included microseismic monitoring from one offset well, surface-tiltmeter monitoring, downhole-tiltmeter monitoring from a second offset well, tracer injections, bottom-hole pressure measurements, and the drilling of deviated coreholes through the disposal domain (based upon the diagnostic results). Figure 2 shows a plan view of the site layout with the tiltmeter monitoring well on the north and the microseismic monitoring well on the south. The expected fracture azimuth (from considerable previous stress and fracture diagnostic data at this site) was approximately east-west.[27] CICI is the cuttings injection well, CICA is the microseismic monitoring well, and CICB is the tiltmeter monitoring well. The names of the wells are given by their surface locations and the TD text indicates the location of the well at total depth.

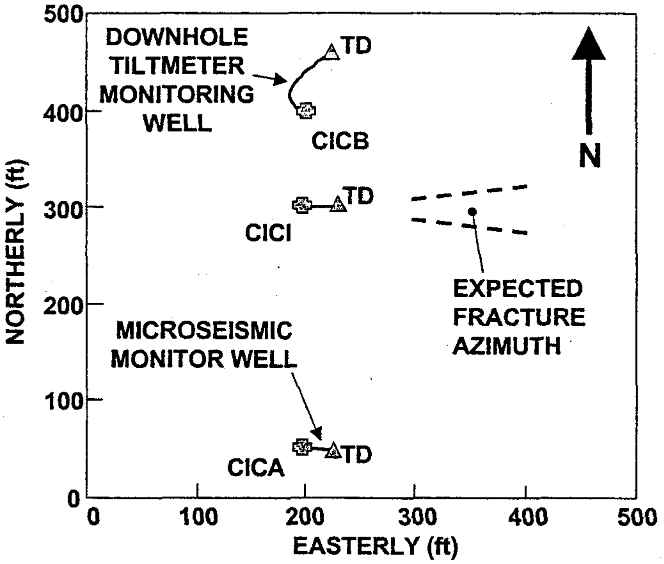

Figure 2. Mounds site layout during injection.

The downhole configuration for the Wilcox sandstone is shown in Figure 3. The Wilcox sandstone is approximately 70 ft thick with a 10-15 ft carbonate layer on top of it. The casing was set in the carbonate and an open-hole section was drilled through the Wilcox and down into the underlying shale/sandstone sequence. The bottom of the hole was backfilled with sand prior to the injection. Five microseismic receivers and eight downhole tiltmeters were situated in their monitoring wells such that the expected fracture was straddled by the arrays.

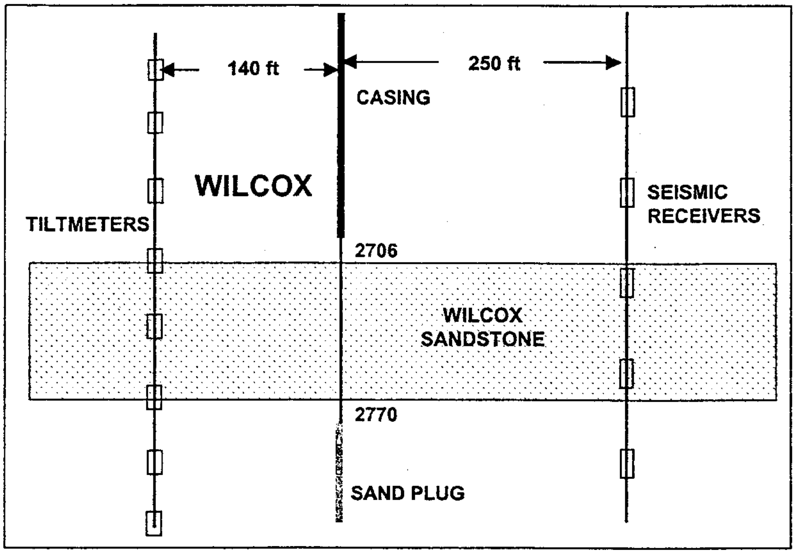

Figure 3. Experiment configuration for Wilcox testing.

The experiment configuration for the Atoka injections is shown in Figure 4. The major differences are (1) the Atoka shale is a very thick formation (covering the entire tiltmeter monitoring interval) and a 20 ft interval was used as the injection point and (2) the injection was performed through perforations rather than open hole.

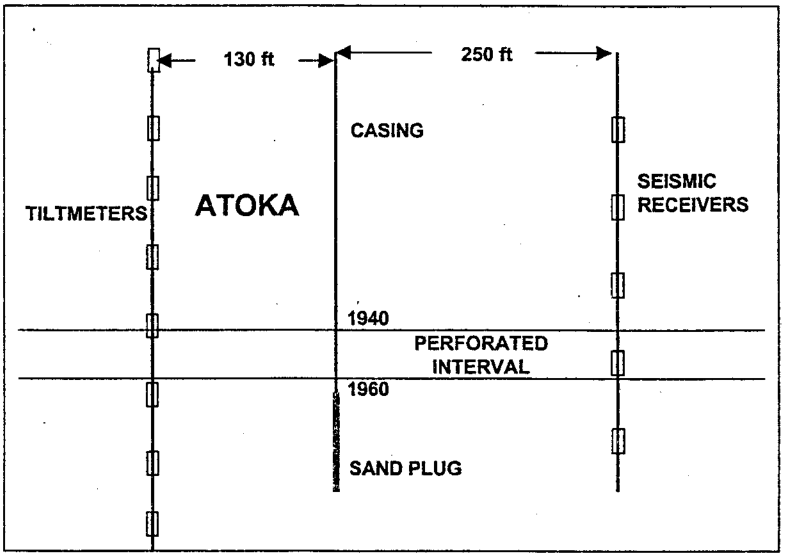

Figure 4. Experiment configuration for Atoka testing.

Details about the injections for the two sets of experiments are given in Tables 1 and 2 for the Wilcox and Atoka tests, respectively. These summaries are excerpted from detailed test results prepared by Pinnacle Technologies and compiled with all other data in a Mounds project CD.[28] In both sets of tests, there were several calibration tests using fresh water (FW) or drilling mud (mud) to measure stress or leakoff (labeled 0A, 0B, etc). These were followed by 17 slurry injections in the Wilcox sandstone and 20 injections in the Atoka shale. Each of the tests was displaced with drilling mud and tests at the end of each day also had a casing displacement of fresh water.

Table 1. Injection summary for Wilcox testing.

Injection	Fluid	Stage Vol. bbls.	Start Time min	Max Rate bpm	Max Press. psi	Instant. Shut In Press. psi	Net Press. psi
0A	FW	45.77	10:23	8.5	884	446	136
0B	FW	46.63	12:19	9.4	435	424	114
0C	FW	48.3	14:10	9.5	425	419	109
0D	Mud	68.9	14:44	5.5	457	451	141
0E	Mud	51.1	16:08	4.9	533	529	219
1 attempt	Slurry	11.3	17:35	2	498	488	178
1	Slurry	44	18:34	5.4	578		
	Mud	19.5	18:44	5.3	538	524	214
2	Slurry	45.2	20:08	5.5	553		
	Mud	20.8	20:17	5.2	548		
	FW	18.9	20:21	5.4	537	522	212
3	Slurry	60.66	9:50	5.9	554		
	Mud	17.89	10:03	5.9		518	514
4	Slurry	51.05	11:11	5.7			
	Mud	18.5	11:21	5.8	538	524	518
5	Slurry	49.4	12:33	5.2			
	Mud	20.6	12:43	5	548	532	528
6	Slurry	51.3	14:45	5.2			
	Mud	20.5	14:55	5.2	573	549	545
7	Slurry	52.9	15:59	5.4			
	Mud	17.4	16:09	5.5	586	566	563
8	Slurry	51.7	17:42	5.6			
	Mud	23.4	17:52	5.6	603	583	579
9	Slurry	51.4	19:10	5.3			
	Mud	18.2	19:20	5.7	629	610	608
10	Slurry	53.3	20:28	5.2			
	Mud	25.7	20:38	5.2	650	617	
	FW	12.4	20:42	5.7			612
11	Slurry	52.06	8:40	5.5			
	Mud	18.11	8:51	6	640	637	633
12	Slurry	51.5	10:39	5.4			
	Mud	22.6	10:49	5.7	687	639	633
13	Slurry	51.3	11:58	5.5			
	Mud	18.5	12:07	5.5	676	646	639
14	Slurry	52.4	13:10	4.7			
	Mud	17.5	13:22	4.6	673	661	656
15	Slurry	76.2	15:18	4.6			
	Mud	18.1	15:35	4.5	687	673	670
16	Slurry	77.8	17:03	5.4			
	Mud	17.2	17:18	5.3	692	676	673
17	Slurry	110.9	19:03	4.7			
	FW	18.1	19:26	4.6	636	619	615

Table 2. Injection summary for Atoka testing.

Injection	Fluid	Stage Vol. bbls.	Start Time min	Max Rate bpm	Max Press. psi	Istant. Shut In Press. psi	Net Press. psi
0A	FW	45.3	8:16	9.6	812	608	225
0B	FW	44.62	9:30	9.6	643	628	245
0C	Mud	65.28	10:35	5.2	745	724	341
1	Slurry	51.1	11:48	5			
	Mud	20.2	11:59	5	757	742	359
2	Slurry	46.3	13:38	5.5			
	Mud	13.5	13:49	5.6	777	70	387
3	Slurry	50	15:33	5.3			
	Mud	15	15:42	5.3	768	765	382
4	Slurry	51.4	17:06	5.1	795		
	Mud	13.8	17:16	5.2	784	779	396
5	Slurry	51.8	18:33	5.3	800		
	Mud	67.1	18:43	5.4	802		
	FW	28.4	18:46	5.4	812	807	424
6	Slurry	51.48	8:32	5.4			
	Mud	16.16	8:43	5.3	866	849	466
7	Slurry	52.26	9:53	5.4			
	Mud	15.3	10:02	5.6	852	848	465
8	Slurry	50.2	11:24	5.5			
	Mud	14.7	11:33	5.6	848	844	461
9	Slurry	51	12:53	5.4			
	Mud	14.1	13:03	5.6	849	844	461
10	Slurry	50.9	14:48	5.3			
	Mud	14.1	14:57	5.6	882	866	483
11	Slurry	50.3	16:27	5.2			
	Mud	14.7	16:37	5.4	863	853	470
12	Slurry	49.8	18:00	5			
	Mud	15.2	18:10	5	863	862	479
13	Slurry	50	19:28	5.4			
	Mud	16	19:38	5			
	FW	14.1	19:41	5	887	884	501
14	Slurry	50.95	8:01	5.3			
	Mud	14.3	8:11	5.4	864	856	473
15	Slurry	100.25	9:28	5.3			
	Mud	14.8	9:47	5.9	892	873	490
16	Slurry	100.4	11:25	5.3			
	Mud	14.6	11:44	5.7	885	863	480
17	Slurry	100.3	13:28	5.3			
	Mud	14.6	13:47	5.2	875	856	473
18	Slurry	100.2	14:58	5.8			
	Mud	15	15:16	6.1	869	841	458
19	Slurry	99.9	16:26	5.4			
	Mud	14.9	16:45	5.6	834	820	437
20	Slurry	100.4	18:00	5.2			
	FW	15.7	18:20	5.2	834	825	442

The bottom-hole pressures during these injection tests are shown in Figures 5 and 6 for the Wilcox and Atoka experiments, respectively. Maximum pressures for the slurry injections ranged from about 1700-1850 psi for the Wilcox tests and about 1600-1750 psi for the Atoka tests.

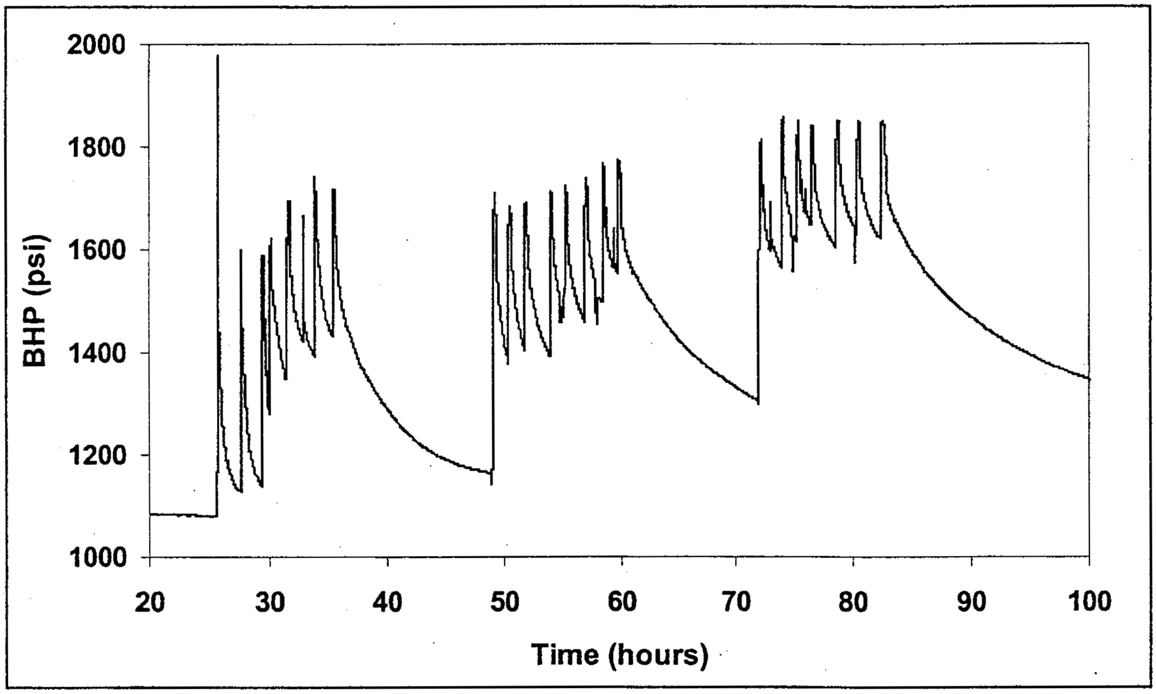

Figure 5. Wilcox bottom-hole pressure data.

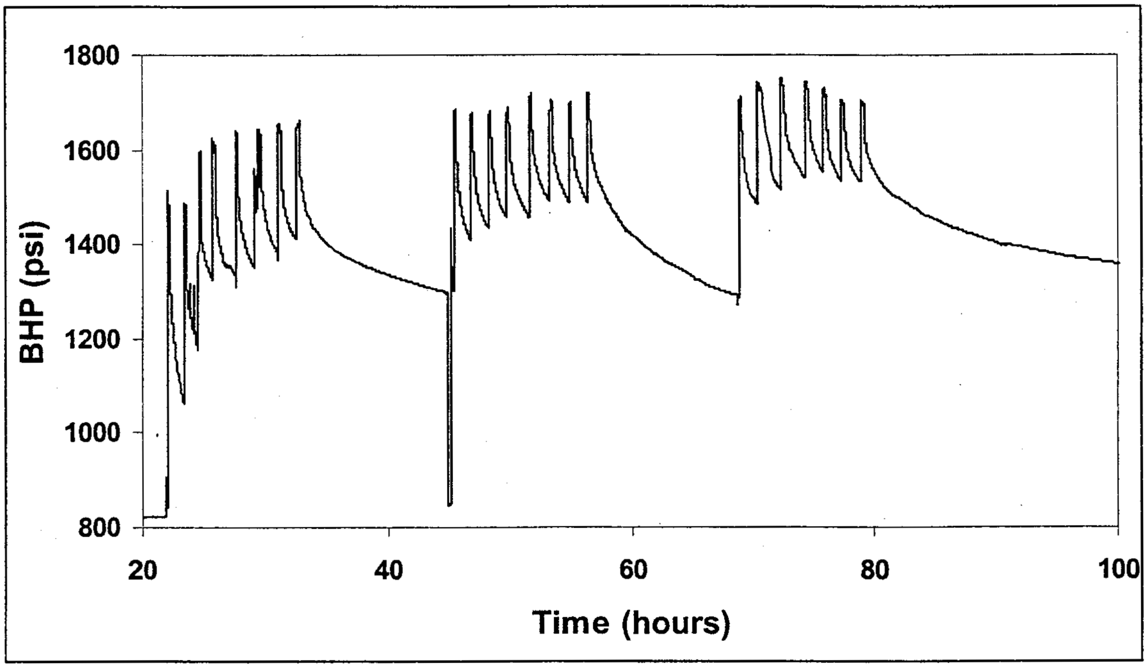

Figure 6. Atoka bottom-hole pressure data.

Other diagnostic results that can be compared to the downhole-tiltmeter data include microseismic images of the fractures, surface tiltmeter surveys, and deviated coreholes through the disposal zone. The deviated corehole data give an absolute ground-truth result showing fracture azimuth and dip and minimum values for length and height on one wing (side). There were two coreholes through the Wilcox disposal zone and a third intentionally placed above the zone. One corehole was placed through the Atoka disposal zone. Individual microseismic images were generated for each of the injections in the Wilcox sandstone, but for the Atoka tests there were very few microseisms detected and the best that could be obtained was a general image of all of the injections in this zone. The surface tiltmeters were used to obtained azimuth and dip information on both zones.

TILTMETER DATA

Examples of the tilt data for each of the zones are given in this section. An assessment of the tiltmeter operation can be made by examining the consistency of the response. Other issues such as the tiltmeter coupling are more complicated and can only be evaluated by modeling and comparison.

Wilcox Interval

The tiltmeters in the Wilcox interval were run on a wireline with centralizers and positioned at depths of 2466, 2538, 2613, 2665, 2717, 2769, 2844 and 2919 ft. Each of these tiltmeters is a bi-axial device measuring the tilts in two unknown orientations from which a total tilt magnitude can be computed (e.g., vector sum). To illustrate the quality of the data and the types of noise, the raw tiltmeter measurements from the first day of the Wilcox monitoring are shown in Figures 7-14.

Figure 7 shows the two traces from the tiltmeter at 2466 ft (shallowest tiltmeter). Being far from the fractures, it records only small signals and has a very low noise level. However, the series of injections conducted during the first day of testing can be seen in the bumps occurring on the top trace. When expanded (as will be shown later), there is a clear time-dependent response to the fracture opening in most of these features (the bumps). The arrows on the plot identify which axis scale pertains to the adjacent curve.

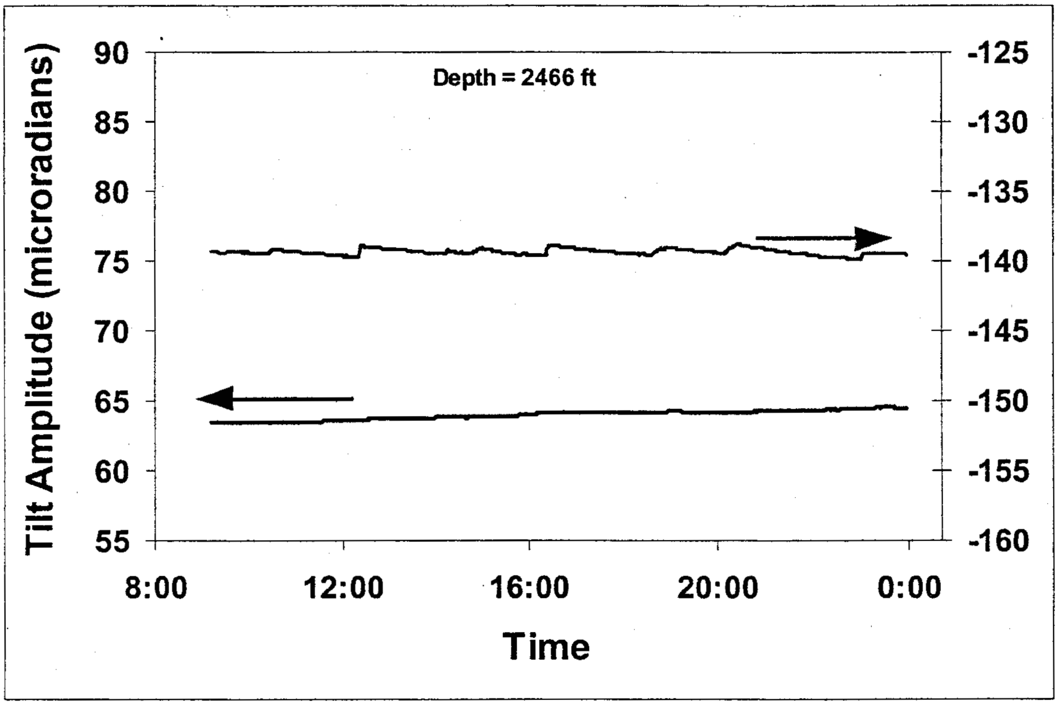

Figure 7. Tiltmeter data for tiltmeter at 2466 ft during first day of Wilcox testing.

The data for the tiltmeter at 2538 ft are shown in Figure 8. In this case, the signal is also relatively small, but some types of noise are evident. The most obvious noise features are the sharp discontinuities that occur at two locations on the lower curve and one location on the top curve (at about 1300 and 1700 hrs). These discontinuities are typically instantaneous jumps in the amplitude (e.g., across one sample point) and can be easily distinguished from the response due to the fracture when the scale is expanded. Although it is not clear exactly what is causing these features, they generally result in a step change in the amplitude of the signal at that point. In such cases, the step can be removed and the rest of the data analyzed as usual. Such a feature was seen on a few occasions in the cemented tiltmeters used at M-Site and were called "tears" (as in rip) to emphasize that they appeared to be due to some sudden offset movement in the tiltmeter, possibly due to stress on the cement. In this particular case, it is not clear if they are due to a similar movement in the cement around the wellbore or due to a movement of the tiltmeter itself. Most of the time they occur during an injection or just after, implying that there is some relation between the tears and the injection process (e.g., due to the stress induced by the injection fracture). A second type of noise seen here is a random fluctuation of approximately 1 microradian that occurs on both channels. It probably illustrates the noise associated with this particular tiltmeter due to either electrical or mechanical effects. A third type of noise is the moderate drift associated with the lower curve. It is not always clear how much of the change is instrument drift, tidal variations, or cumulative tilt, but in this case the tides are not evident and there is very little tilt to accumulate at this location. By elimination, the drift appears to be a feature of the instruments.

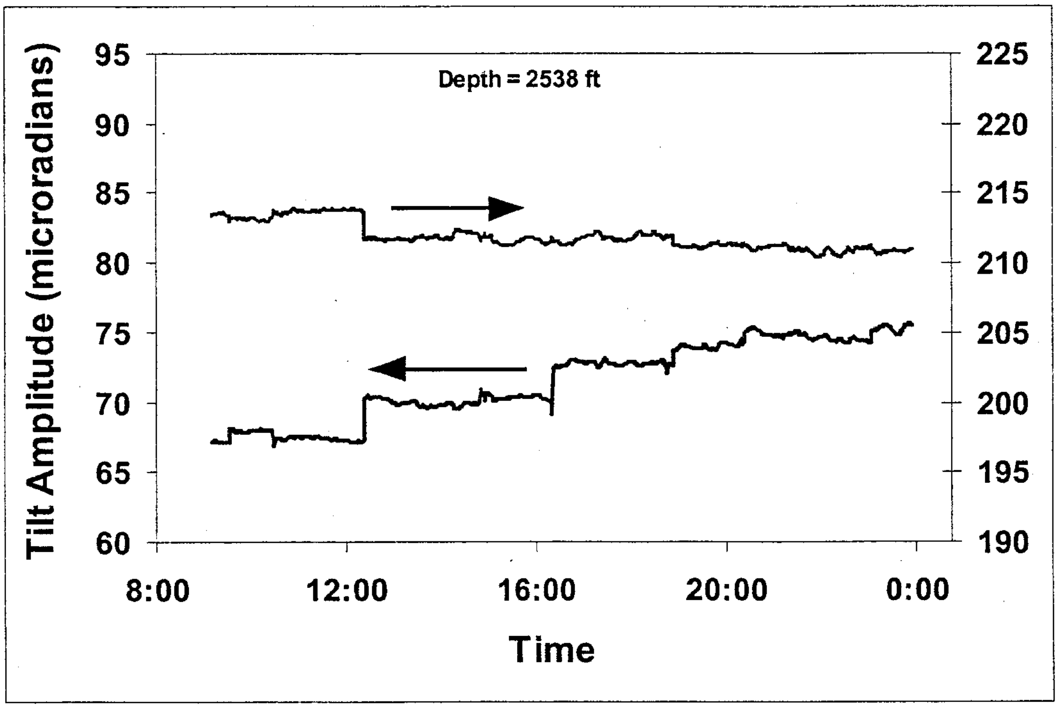

Figure 8. Tiltmeter data for tiltmeter at 2538 ft during first day of Wilcox testing.

Figure 9 shows the tiltmeter data for the instrument at 2613 ft. This level has the noisiest data of the entire set with fluctuations of as much as 2 microradians, several "tears", and relatively large drift occurring throughout the test. Nevertheless, estimates of the tilt changes can be made for many of the injections.

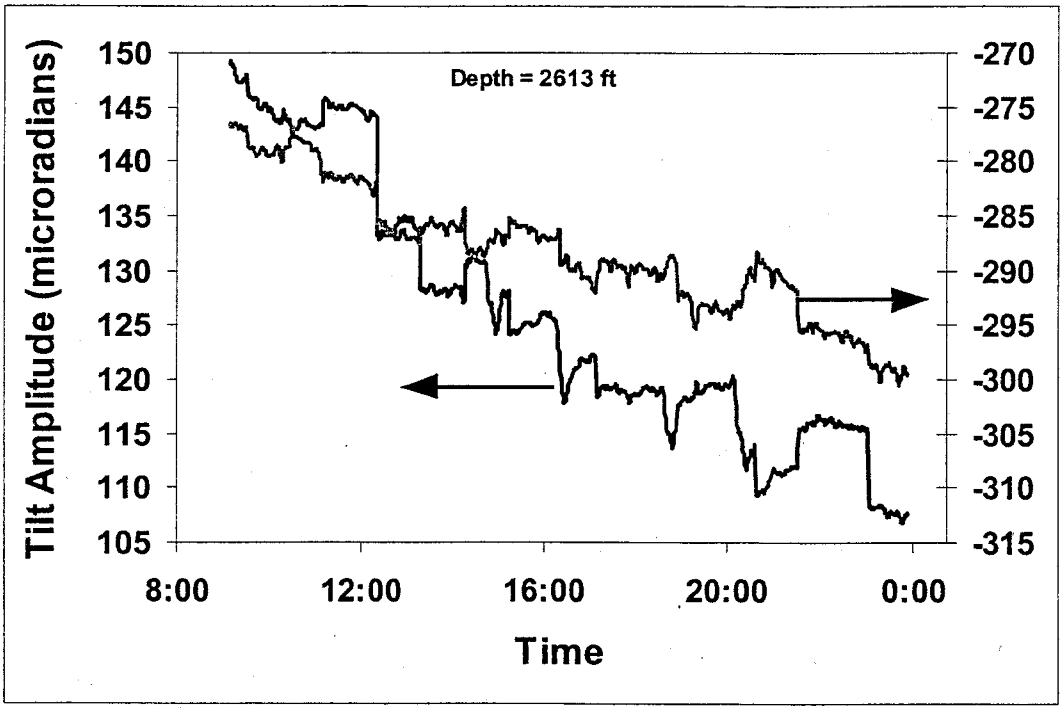

Figure 9. Tiltmeter data for tiltmeter at 2613 ft during first day of Wilcox testing.

The data from the tiltmeter at 2665 ft for the first day of Wilcox testing is shown in Figure 10. With the exception of a few tears on both traces and the large spike on the lower channel, the data are relatively noise free and the tilt responses during the injections can be seen.

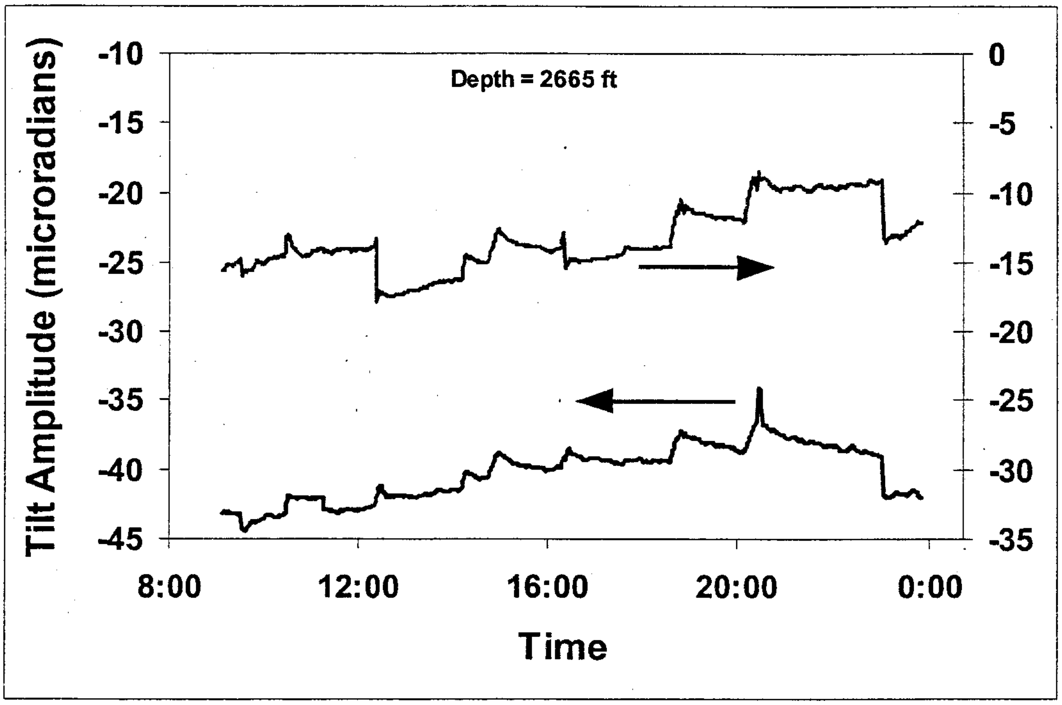

Figure 10. Tiltmeter data for tiltmeter at 2665 ft during first day of Wilcox testing.

Figure 11 shows data for the tiltmeter at 2717 ft, which had one of the two largest tilt responses during this series of tests. There is an extremely large tear occurring just after noon and a small one at the end of the day, but otherwise the data are quite good and clearly show the expected tilt responses as the fractures are inflated and then allowed to deflate during shut in.

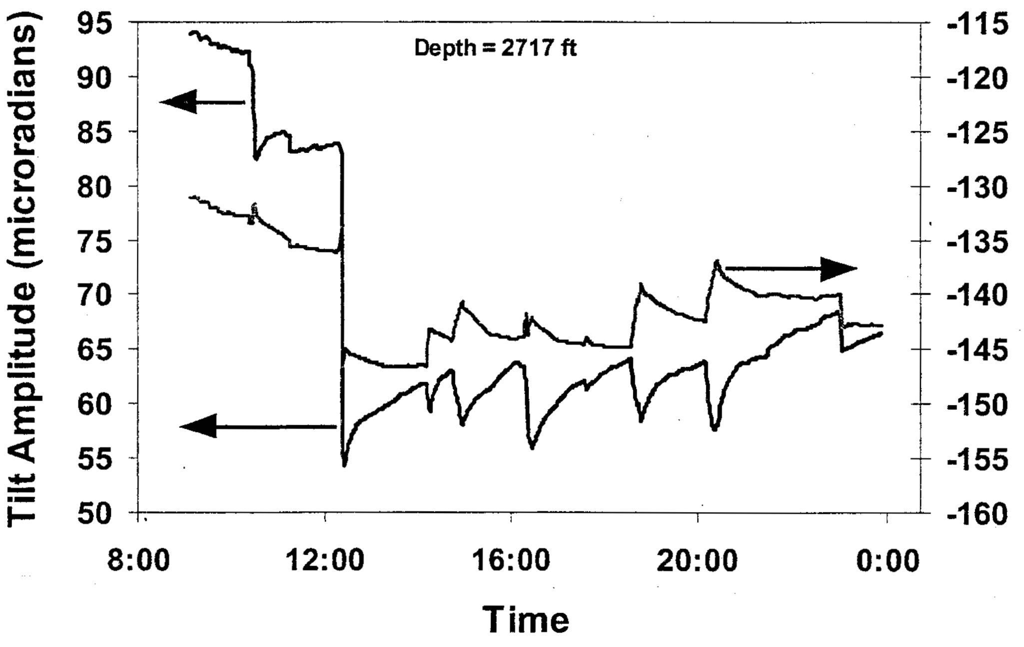

Figure 11. Tiltmeter data for tiltmeter at 2717 ft during first day of Wilcox testing.

The tiltmeter data for the instrument at 2769 ft during the first day of testing are shown in Figure 12. The lower trace shows some degree of random noise, a relatively large drift and several tears. The upper trace is reasonably quiet with the exception of a few small tears. The tilt responses due to the fracturing are quite clear on the upper trace and can be seen on the lower trace for several of the injections.

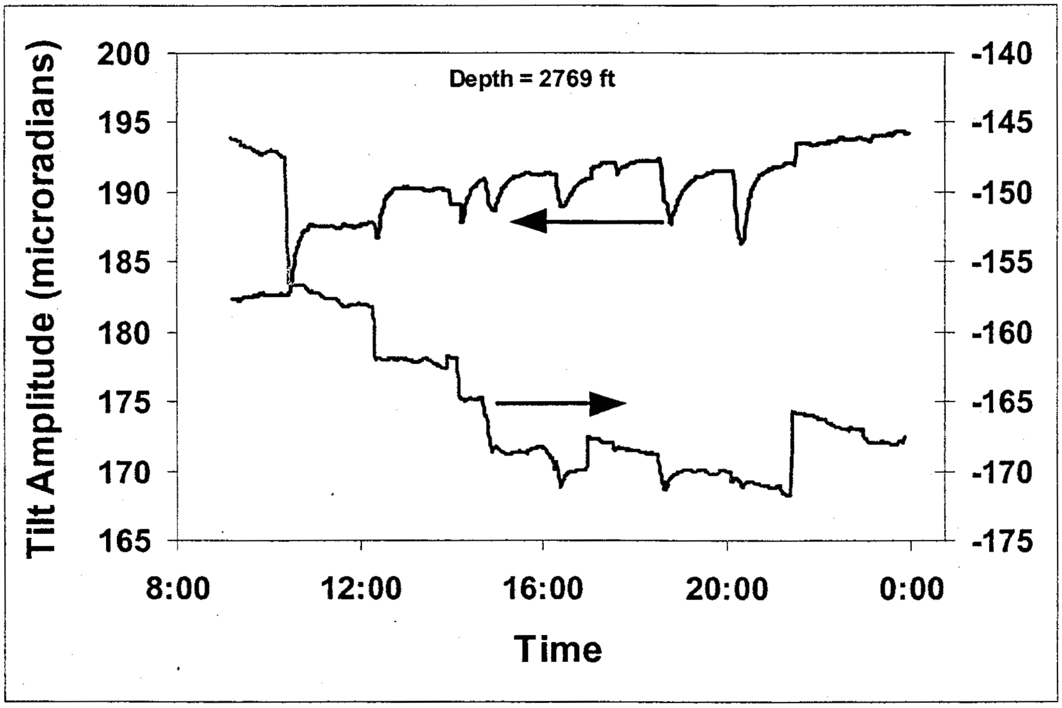

Figure 12. Tiltmeter data for tiltmeter at 2769 ft during first day of Wilcox testing.

The largest tilt response during the Wilcox testing was seen on the instrument at 2844-ft depth. The data from this tiltmeter during the first day of testing is seen in Figure 13. Most of the signal is seen on the lower trace, which suggests that this sensor is pointing nearly orthogonal to the fracture. There is very little noise of any kind on this channel. Since there is no significant drift on this channel, the accumulated tilt that occurs during the suite of injections also becomes apparent. The other channel of this instrument has a relatively large drift, but little noise and no tears.

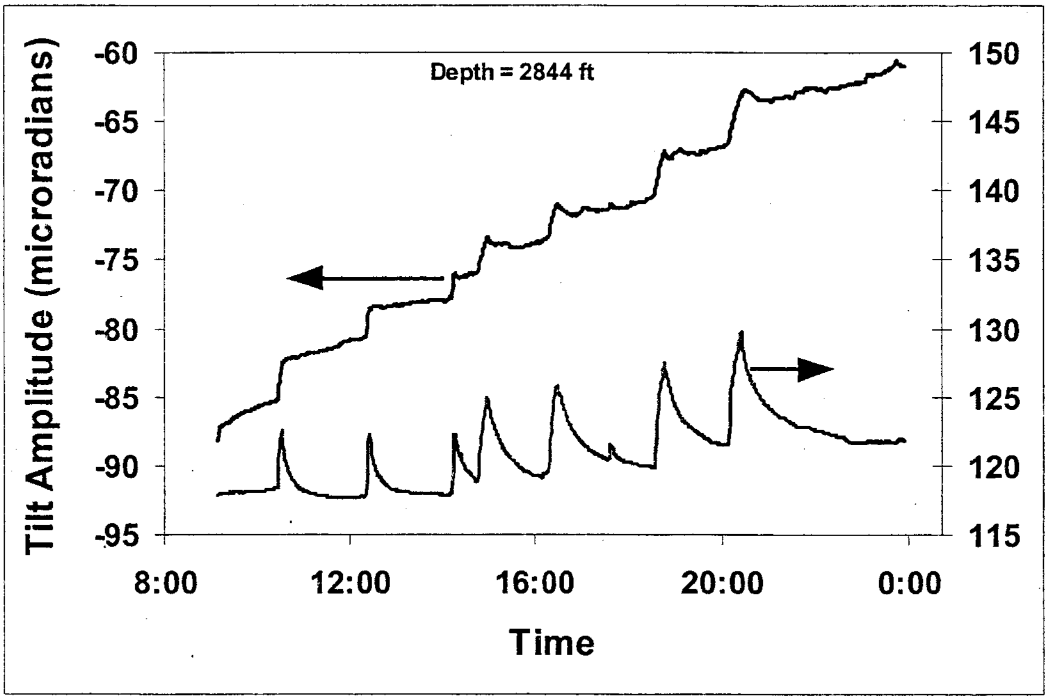

Figure 13. Tiltmeter data for tiltmeter at 2844 ft during first day of Wilcox testing.

The data for the lowest tiltmeter, at 2919 ft, are shown in figure 14. This tiltmeter has a relatively small signal, several tears on the top trace and some small random noise on both channels (about 0.5 microradians).

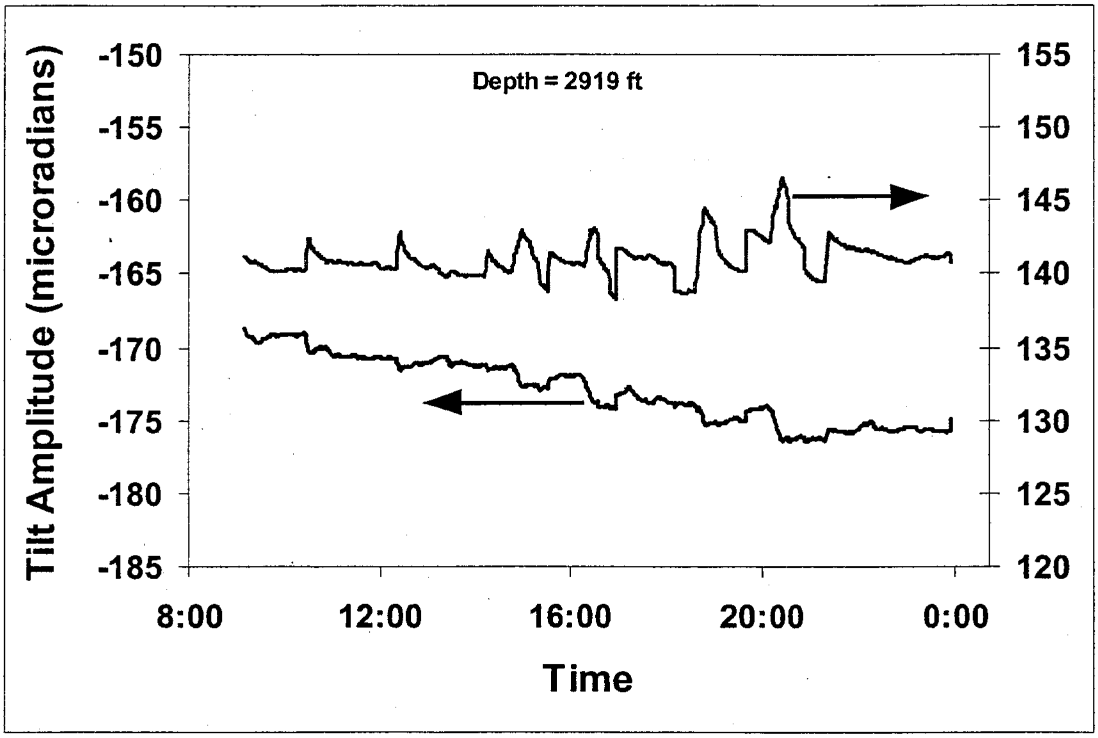

Figure 14. Tiltmeter data for tiltmeter at 2919 ft during first day of Wilcox testing.

In using these types of tilt data, it is first necessary to extract the part of the response due to the fracture. This can be done by either finding some initial response (e.g., an average over several minutes) prior to injection and subtracting out this response or by fitting a linear trend and subtracting the linear trend from the fracture response. In this test, the injections were so short (10-20 min) that the effect of drift was considered negligible compared to the noise levels and the first approach was used for nearly all of the data.

Since the tiltmeters are not oriented and the magnitude of the tilt is used for the analysis, the magnitude of the tilt must be found correctly. While it is convenient to simply take the magnitude of the two orthogonal components, find the initial value of this magnitude, and subtract it out to get a fracture-induced magnitude, it would result in the wrong value. The correct approach is to zero each channel independently (or find the linear trend) and subtract out the zero value (or the trend) to get fracture-induced responses for each channel. The total magnitude response can then be correctly found by using the two zeroed channels (or the two trend-subtracted channels) to calculate the magnitude.

When there are multiple injections in the same interval, a valuable assessment of the tiltmeter operation can be obtained by examining the phase behavior of the two channels. When the test configuration is such that the monitoring well is close to the fracture and nearly normal to the centerline of the fracture, the extracted phase angle at the end of each injection should zero in on nearly the same value from test to test. Figure 15 shows the phase angle for each tiltmeter for all 17 injections. This angle is the inverse tangent of the ratio of the y-axis magnitude to the x-axis magnitude. In general, the data are very consistent and the largest variations are due to already described tears. If these tears are removed from the data, most of the channels would have a very consistent phase for all tests. The only instrument that does not follow this behavior is the one at 2769 ft. Thus, the phase results suggest that all of the channels, with the possible exception of the instrument at 2769 ft, are working properly and are responding in the same way throughout the test. However, this does not mean that all of the tiltmeters are necessarily well coupled, Coupling is a more complex issue that cannot easily be resolved by examining just the tilt responses.

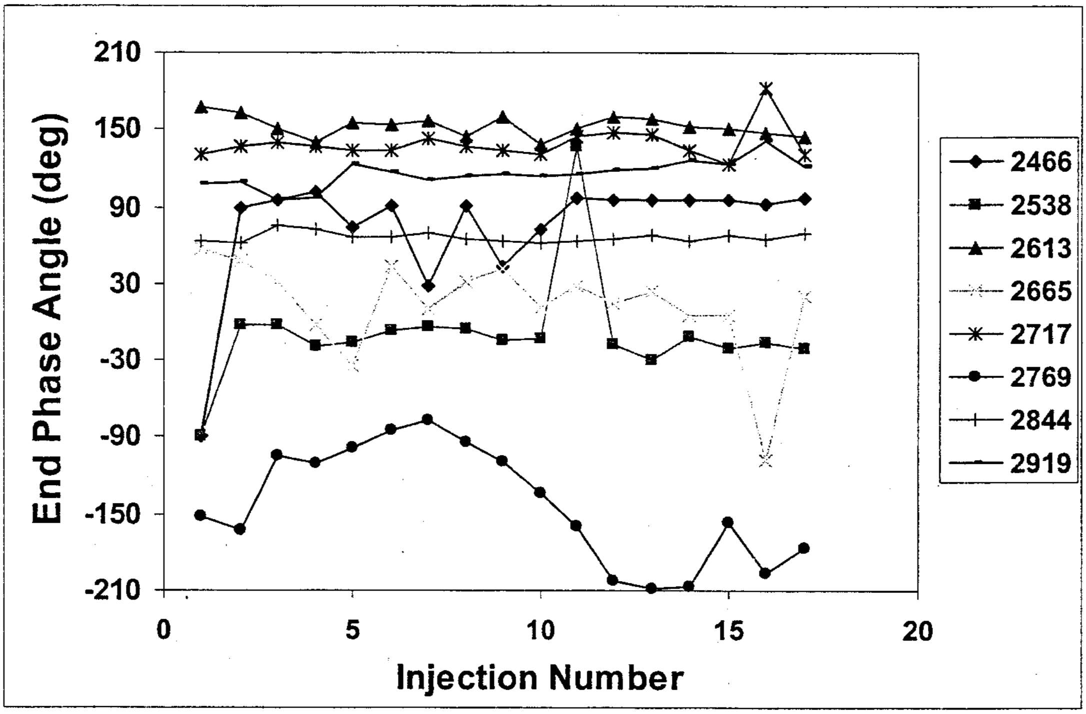

Figure 15. Phase angles at the end of the injections for Wilcox tests.

Atoka Interval

After the completion of operations in the Wilcox sandstone, the tiltmeters were pulled up hole and situated in positions straddling the Atoka interval. The locations of the eight tiltmeters were 1724, 1796, 1871, 1923, 1975, 2027, 2102, and 2177 ft. Since the tiltmeters were not brought out of the well, the operation of these instruments in the Atoka interval could be compared with the Wilcox results to assess whether questionable channels were functioning properly.

The data for the shallowest tiltmeter (1724 ft) during the first day of testing are shown in Figure 16. This instrument, being far from the fracture, has a relatively small response to most of the injections. The large discontinuities in the morning and at the end of the day are probably the tears described in the Wilcox section.

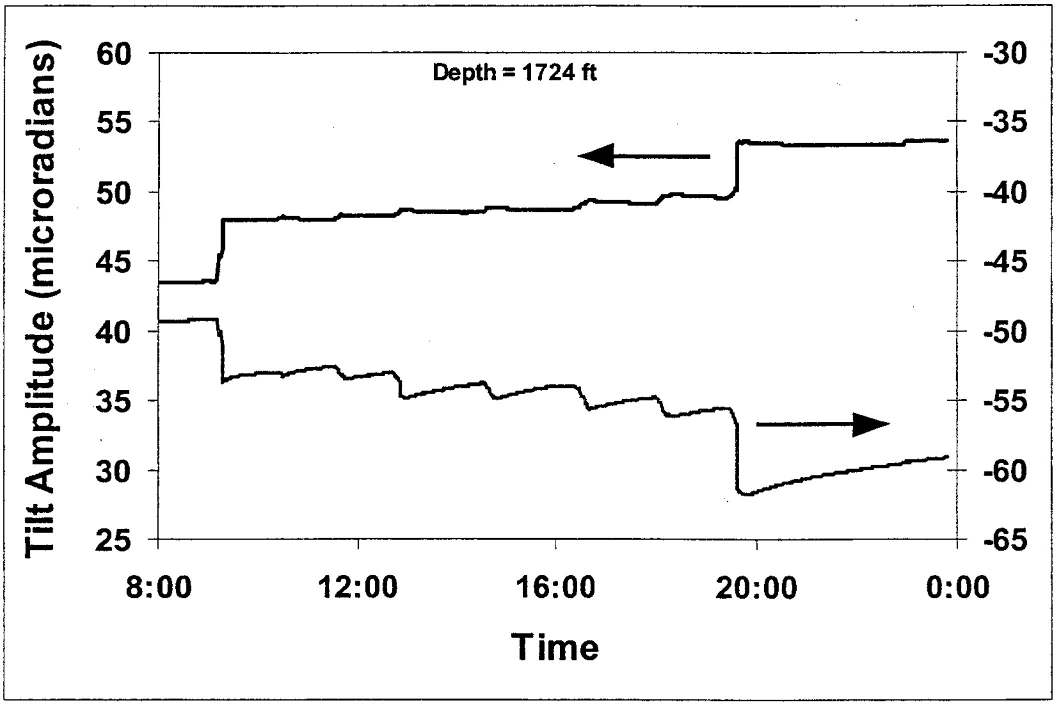

Figure 16. Tiltmeter data for tiltmeter at 1724 ft during first day of Atoka testing.

The data for the tiltmeter at 1796 ft are shown in Figure 17. Although the noise levels are 1-2 microradians, the signal strength is large enough that good quality data can probably be obtained from this level. Given that all of the signal is on one of the channels, it suggests that this channel (the upper trace) is oriented normal to the fracture.

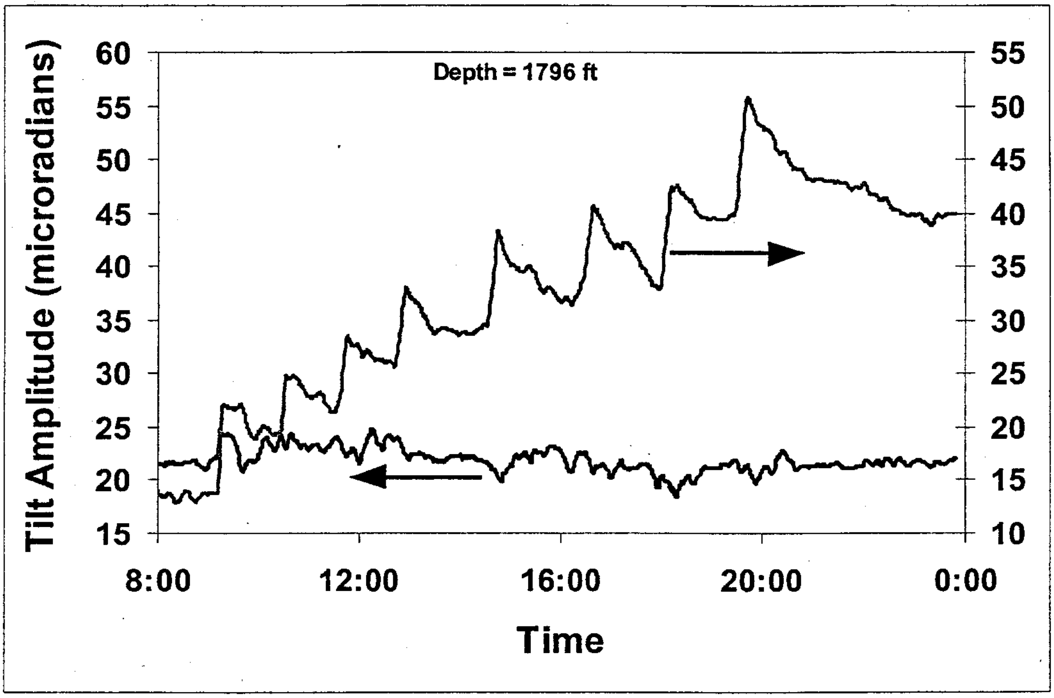

Figure 17. Tiltmeter data for tiltmeter at 1796 ft during first day of Atoka testing.

Figure 18 shows the tiltmeter data for the instrument at 1871 ft for the first day of testing. With the exception of the tear that occurred during the first injection and another one that might have occurred during the last injection, this level has good quality data and a large signal response to the injections.

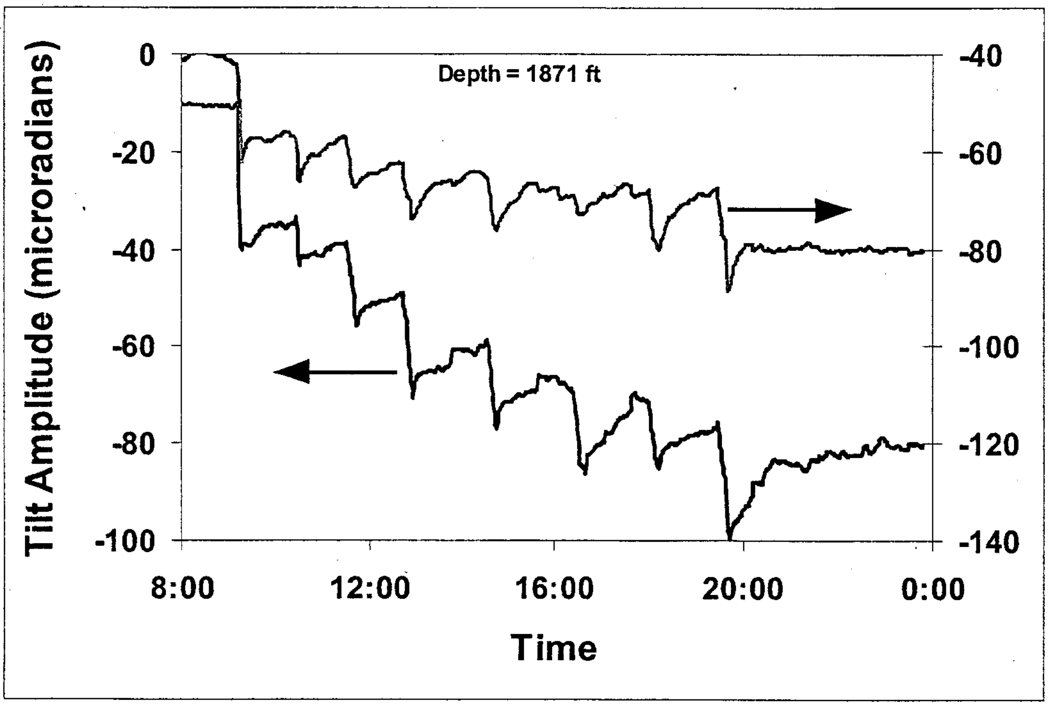

Figure 18: Tiltmeter data for tiltmeter at 1871 ft during first day of Atoka testing.

The results for the tiltmeter at 1923 ft, shown in Figure 19, are perhaps the most unusual of all of the data. Most of the response is on one trace (top), suggesting that it is oriented nearly normal to the fracture. However, the response early in the day is entirely negative while the response later in the day starts out negative and rapidly switches to a large positive response. This behavior suggests that the fracture center starts out on one side of this tiltmeter, but later in the day height growth moves the fracture center to the other side of this tiltmeter. Since the depth of this tiltmeter is about 20 ft above the perforated interval, it is assumed that the initial negative response is due to a fracture whose center is below the 1923-ft depth. Presumably, the fracture begins to grow upward in the later injections, thus switching the response.

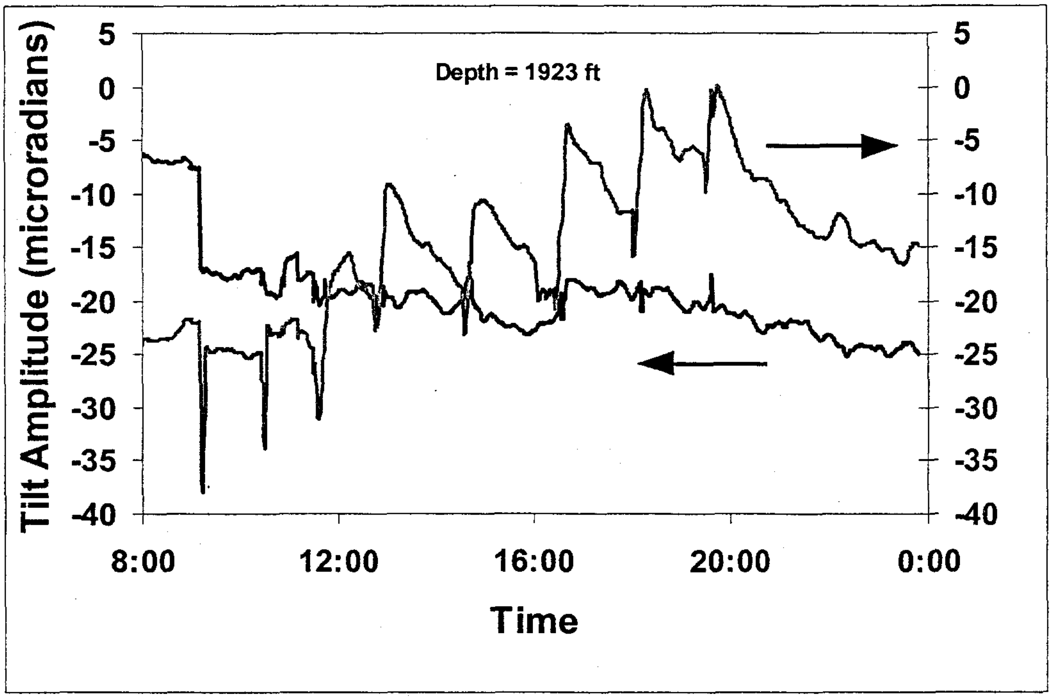

Figure 19. Tiltmeter data for tiltmeter at 1923 ft during first day of Atoka testing.

The data from the tiltmeter at 1975 ft are shown in Figure 20. The response has excellent quality with the largest amplitude of all of the tiltmeters.

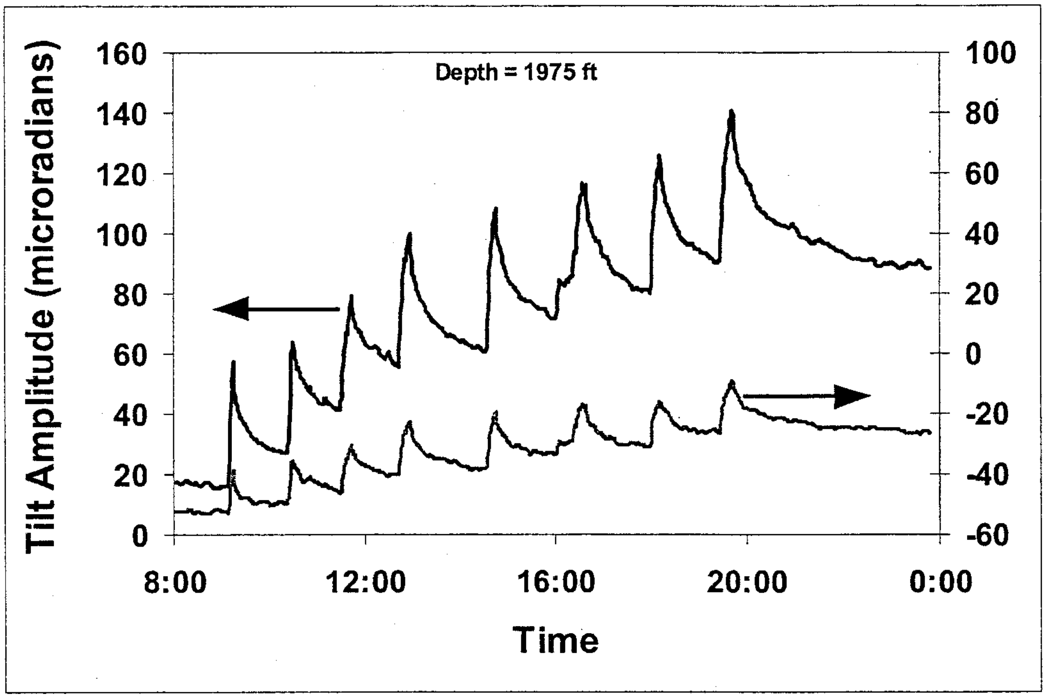

Figure 20. Tiltmeter data for tiltmeter at 1975 ft during first day of Atoka testing.

Figure 21 shows the tilt data for the instrument at 2027 ft. Most of the signal is again on only one channel suggesting that it is oriented nearly normal to the fracture. However, the possibility of having three of these instruments oriented nearly normal to the fracture seems somewhat remote and the question arises whether one or more of these axes may not be coupled very well or functioning properly.

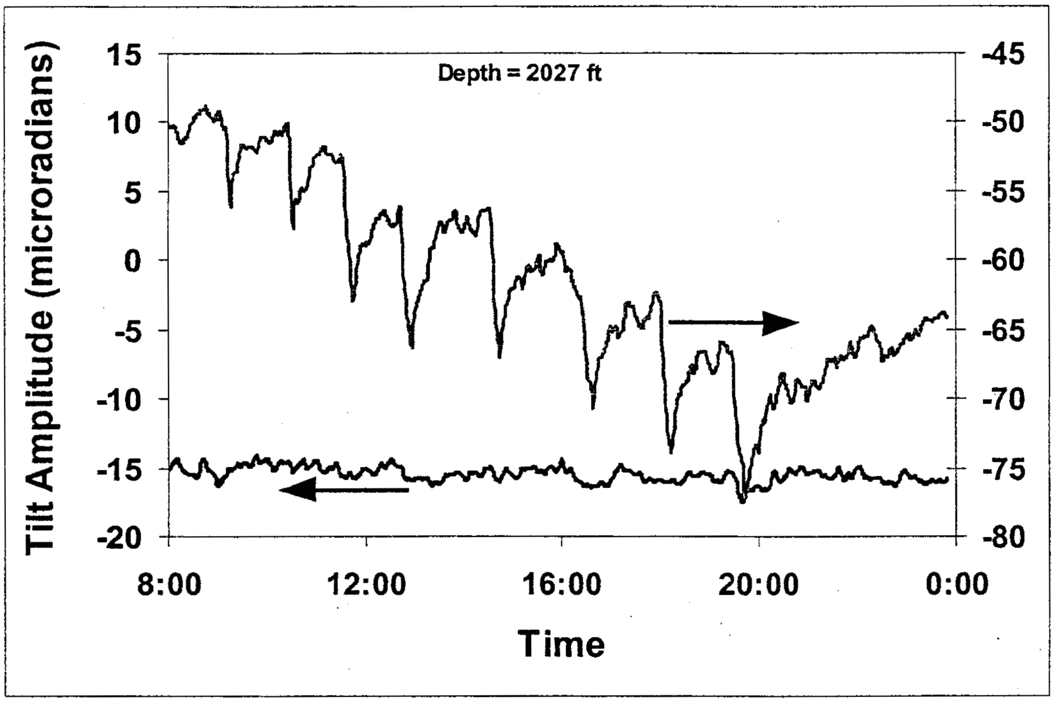

Figure 21. Tiltmeter data for tiltmeter at 2027 ft during first day of Atoka testing.

Figure 22 shows the data for the tiltmeter at 2102 ft. There is very little signal on this level and the signal that is present is obscured by the noise level. The response of the instrument at 2177 ft, shown in Figure 23, is very similar and the fracture signal is generally lost in the noise.

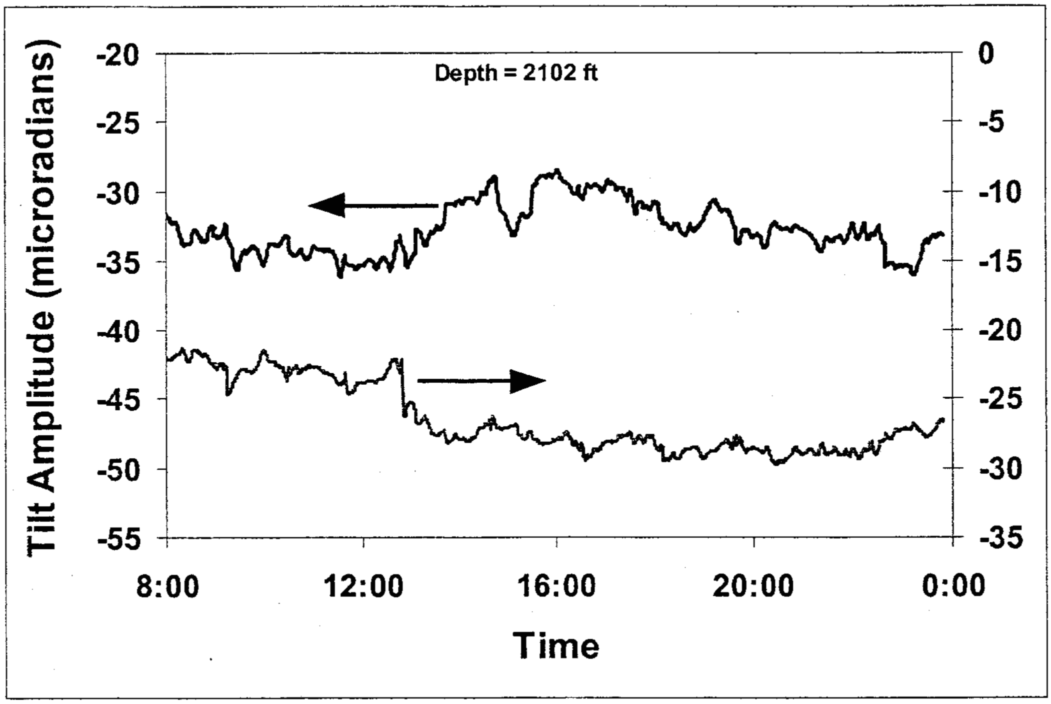

Figure 22. Tiltmeter data for tiltmeter at 2102 ft during first day of Atoka testing.

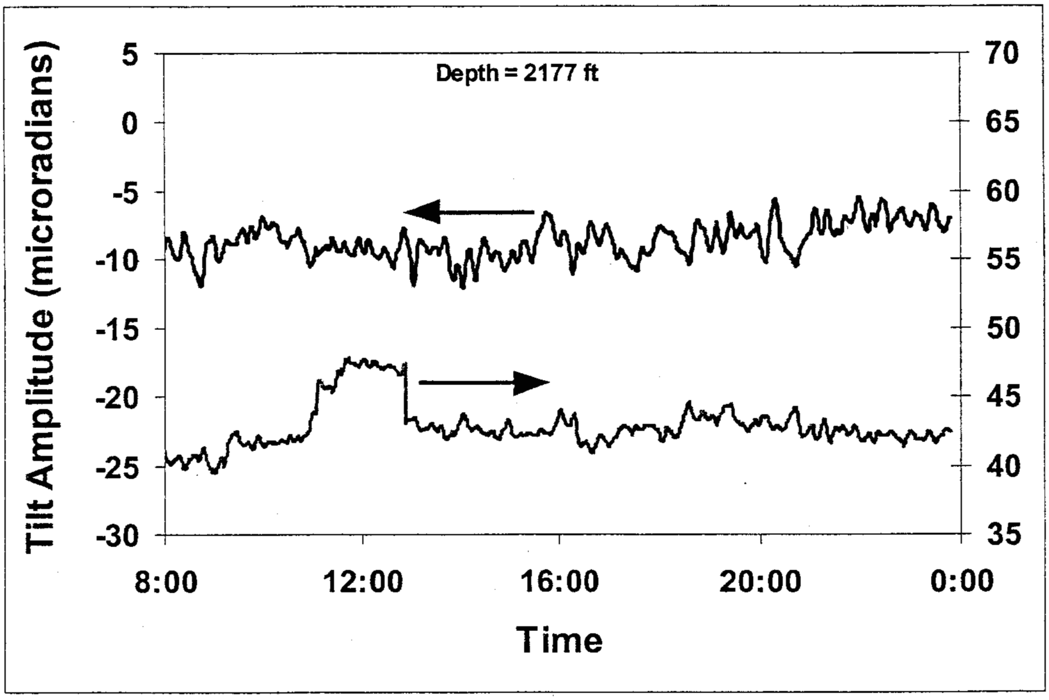

Figure 23. Tiltmeter data for tiltmeter at 2177 ft during first day of Atoka testing.

The phase plot for the Atoka data is shown in Figure 24. With the exception of the lowest two levels and the tiltmeter at 1923 ft, the data are quite consistent. The lowest two levels have very small signals so the scatter seen in Figure 24 is to be expected. The behavior of the instrument at 1923 ft is probably due to the fracture center moving from one side of the tiltmeter to the other side.

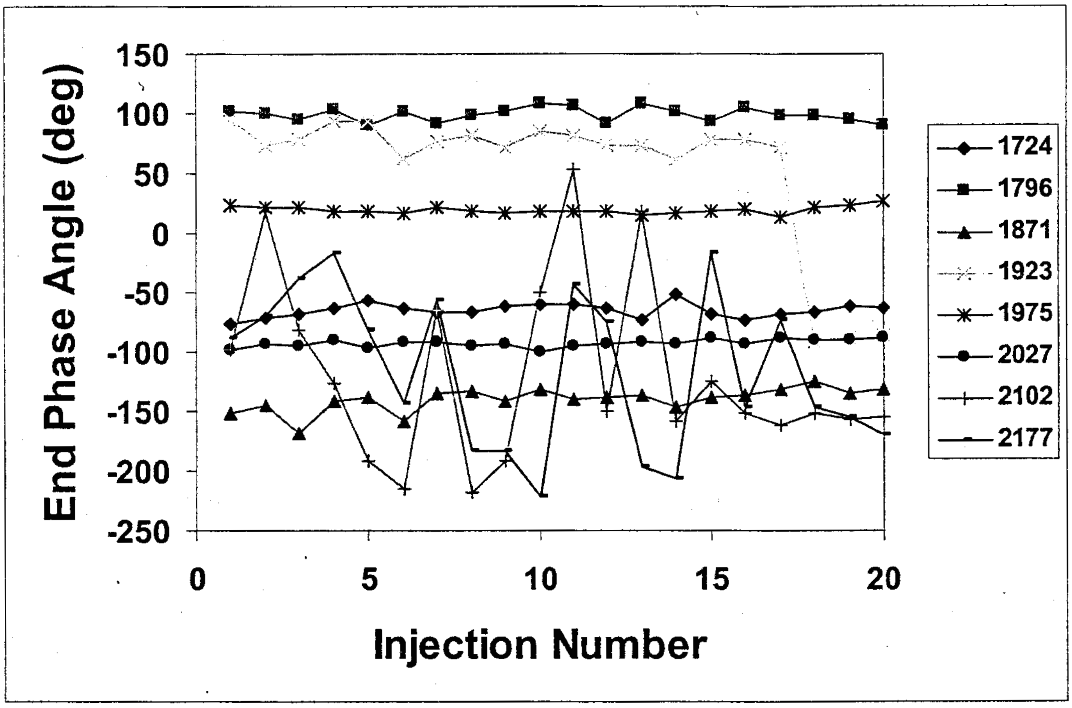

Figure 24. Phase plot for Atoka injections.

Assembled Data Sets

When the data from each tiltmeter are processed for vector magnitude and assembled into data sets for each injection, the result is a trace plot of the kind shown in Figure 25. This particular example is from the first drill-cuttings slurry injection into the Wilcox sandstone. It shows the clear response of six of the tiltmeters to an injection starting at 18:35 and ending at 18:48. The two tiltmeters with minimal response may be nonfunctioning or may be far enough away that the signal is in the noise. The effects of the tears (e.g., on the 2919 ft tiltmeter) are clear, although none happen during the injection. Also evident is a large amount of noise on the 2613 ft tiltmeter.

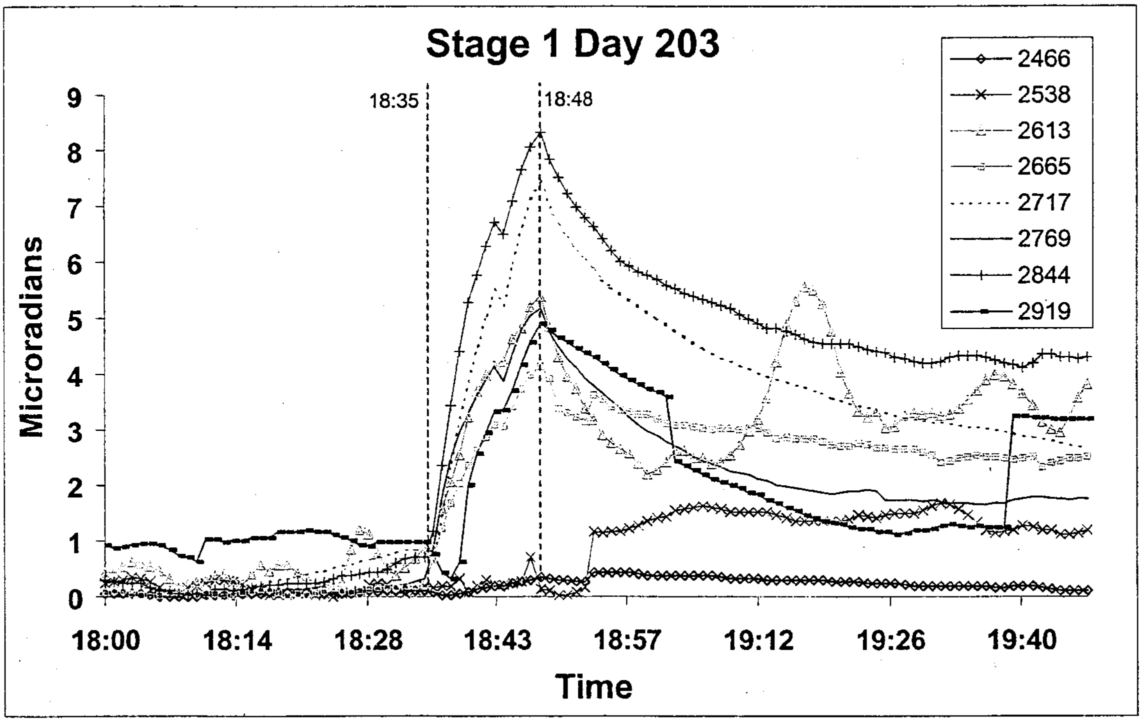

Figure 25. Example data from the first slurry injection in the Wilcox sandstone.

This form of the data is generally too complex to process and the standard procedure is to take the magnitude of the tilt at the end of the treatment and plot the magnitude at this one time as a function of depth, giving eight points. In doing so, it is also possible to compensate for the tears and other noise features in order to get the cleanest data set. Figure 26 shows the amplitude at shut-in as a function of the tiltmeter location. Note that all of the data are positive and the "S-shaped" curve shown in Figure 1 is not present. This is because there is no simple method to discern which levels have positive tilt and which have a negative tilt when the total magnitude is used (although this can be deciphered in some cases, as discussed later).

This particular example looks nothing like the standard tilt distributions, as the tilt field should tend towards zero near the center of the fracture (somewhere around 2700 ft) and have large amplitude lobes above and below it. Methods used to handle these types of results and fit some reasonable tilt distribution will be discussed in the section describing the inversion results.

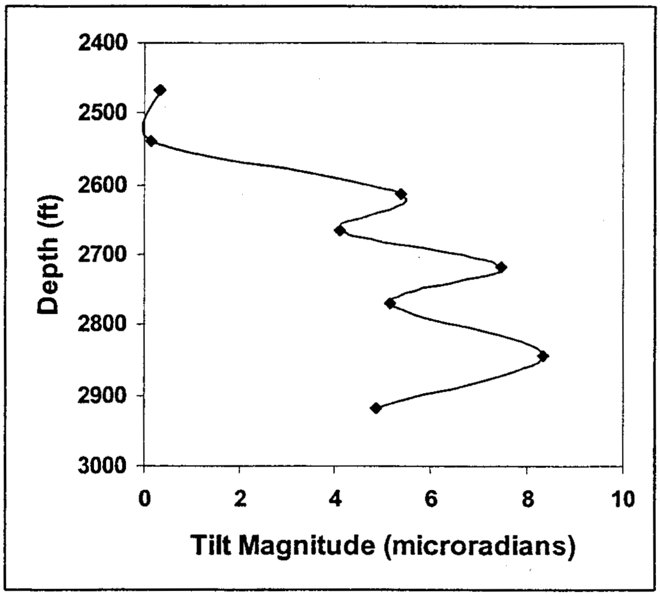

Figure 26. Amplitude vs. depth plot for tilt data, first injection, Wilcox sandstone.

The amplitude plots for all of the Wilcox injections are shown in order from left to right in Figure 27. In general, the classic double-lobed shape is not apparent in the data. Instead, there is usually a broad trough between 2650 and 2800. The scale in microradians is shown for every third injection. The challenge is to try to interpret this unusual character and obtain a reasonable image of the fracture.

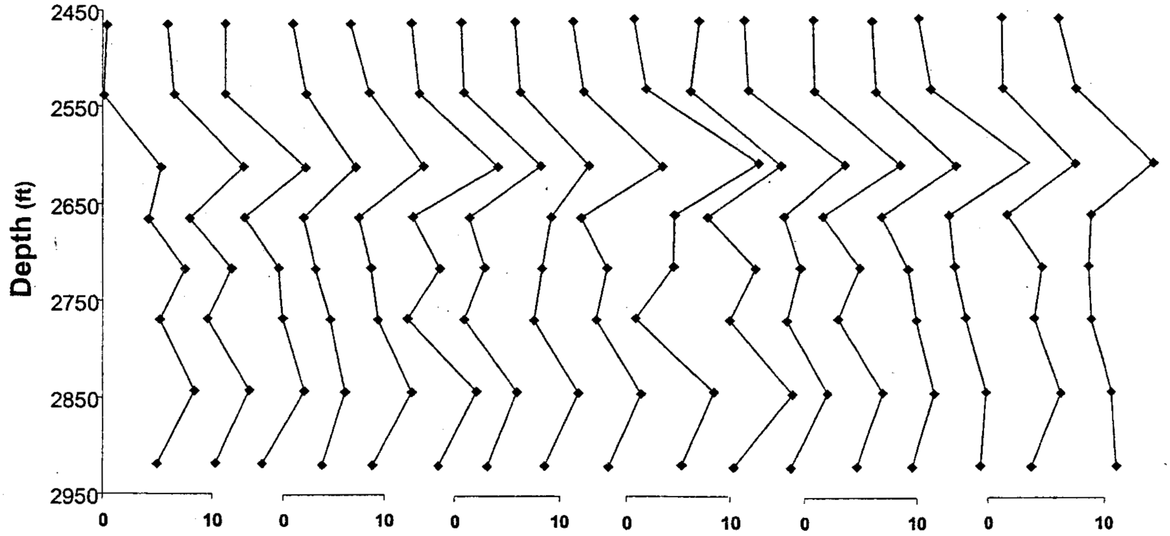

Figure 27. Amplitude plots for all Wilcox injections (amplitude in microradians).

Figure 28 shows an example of the assembled trace magnitudes for the first slurry injection in the Atoka shale. The Atoka tests generally resulted in one large-amplitude tilt trace, as seen in this example.

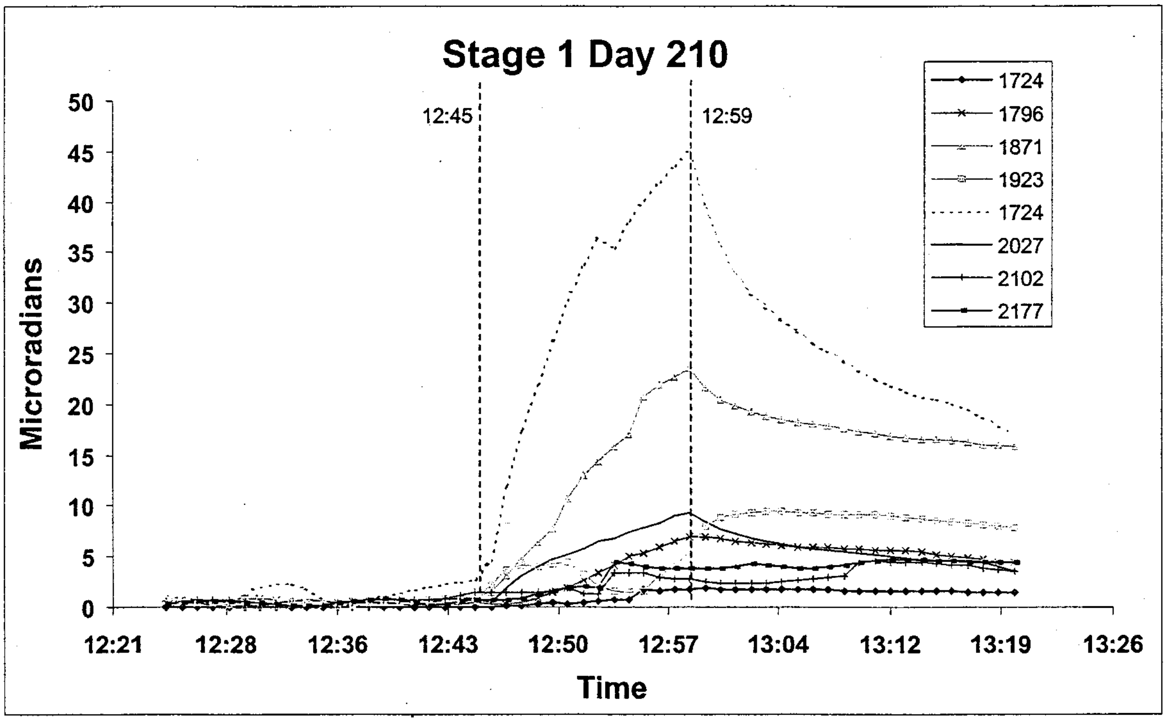

Figure 28. Example data from the first slurry injection in the Atoka shale.

The amplitude plots for all of the Atoka injections are shown in Figure 29. The Atoka data generally shows a single large peak below the perforated interval, except for the last 3-4 injections. The last few injections show considerably smaller magnitudes of tilt, but more symmetry about the perforated interval. The scale in microradians is associated with every fourth injection.

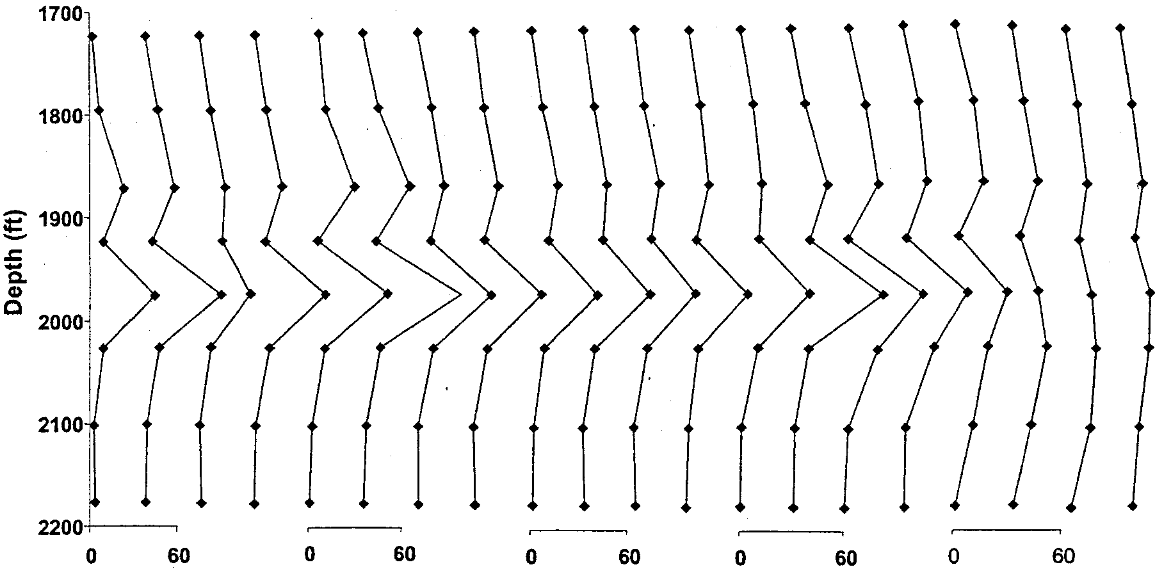

Figure 29. Amplitude plots for all Atoka injections (amplitude in microradians).

TILT INVERSION

Most inversions of tiltmeter data have used a dislocation model[29] because of its simplicity of use. Pinnacle Technology's inversion of these data used just such a model and their results are detailed in their paper at the 1999 Rock Mechanics meeting.[17] However, the dislocation approach has two drawbacks that limit its application in tests such as these. First, the dislocation model is only accurate when the monitoring location is farther away than the total height of the crack. It is not clear that such is the case here. Second, there is no simple way to tie the pressure into the dislocation inversion for any geometry other than an infinitely long 2D fracture or a penny-shaped fracture. Thus, dislocation inversions may produce results with dislocation widths greater than anything that can be supported by the pressure.

To avoid these problems, this analysis uses an inversion that makes use of Sneddon and Green's 3D flat elliptic crack solution.[30] This model has its own limitations (homogenous isotropic material, constant internal pressure), but it allows for close monitoring stations and has a direct pressure constraint.

3D Crack Model Inversion

The equations associated with the 3D crack model are given in Appendix A. Essentially, the tilt distribution as a function of distance away and vertical sensor location (y) are given as

$$tilt(y) = F(h, L, \Delta P, y_c, \alpha_f, \delta_f, w_{dis}, E, v)\ ,$$

where h is the fracture total height, L is the wing length (symmetry is assumed), ΔP is the net pressure, y_c is the vertical depth to the center of the fracture, α_f is the azimuth of the fracture relative to the monitoring position, δ_f is the inclination of the fracture (complement of the dip), w_{dis} is the separation between the monitor well and the injection well, E is Young's modulus, and v is Poisson's ratio. It is generally expected that w_{dis}, E, and v are known and are not free parameters in the inversion. The sense of α_f is such that a fracture azimuth normal to the line between the monitor and injection wells is 0° while a fracture directly approaching the monitor well is 90°. Any of the first six parameters may be known, but the general inversion solves for six free parameters.

The inversion of the tilt equation uses a general Levenberg/Marquardt non-linear solver[31] and the details are not given here. However, to constrain the solution to physically reasonable results (e.g., positive values for height, length, pressure, and center depth), the six free parameters are mapped into a limited range using the arctan function. For example, the height of the fracture should be constrained to values between 0 and some realistic maximum that is a function of the depth, yet the solver allows all values from $-\infty$ to $+\infty$. The use of negative values will cause the model to diverge and cannot be allowed. To avoid this problem, the height is mapped into a new parameter, x_i, through the function

$$h = C_h\left[\tan^{-1}(x_i) + \frac{\pi}{2}\right].$$

This mapping insures that $h \rightarrow 0$ as $x_i \rightarrow -\infty$ and $h \rightarrow \pi C_h$ as $x_i \rightarrow +\infty$. The parameter is called x_i here because any of the six free parameters can be constrained and the actual ith parameter will change depending on the set up of the inversion. However, this form is further modified to constrain the solution between two values by adding a second constant such that

$$h = C_h\left[\tan^{-1}(x_i) + \frac{\pi}{2} + C_{ho}\right].$$

By a proper selection of C_h and C_{ho}, the solution for h can be constrained between two limits. This choice can be useful if the least-square solution tends towards numbers that are unrealistically small or large. For $C_{ho} = 0$, the mapping is from 0 to $C_h\pi$ as given in the first mapping. Similarly, the mappings for L, ΔP and y_c are given by

$$L = C_L \left[\tan^{-1}(x_i) + \frac{\pi}{2} + C_{Lo} \right],$$

$$\Delta P = C_P \left[\tan^{-1}(x_i) + \frac{\pi}{2} + C_{Po} \right],$$

and

$$y_c = C_c \left[\tan^{-1}(x_i) + \frac{\pi}{2} + C_{co} \right].$$

For the azimuth and dip, the arctan function is also used to map the parameters, but in this case the angles only need to be constrained between -π and +π, the normal range of the arctan function. However, to add a further constraint of limiting these angles between two selected values, the final mappings used here are. of the form

$$\alpha_f = C_\alpha \left[\tan^{-1}(x_i) + C_{\alpha o} \right],$$

and

$$\delta_f = C_\delta \left[\tan^{-1}(x_i) + C_{\delta o} \right].$$

The two constants can be determined from the selection of a center angle and a ± deviation about that angle.

Note that this mapping is only used as a convenience. Rather than alter the regression routine to account for the range of applicability, it is simpler to map the parameters into new parameters that allow the regression routine to utilize its full range. In practice, the inversion algorithm first queries for absolute constraints (e.g., if the pressure is measured or the azimuth has been determined from a corethrough) and sets the number of regression parameters (x_i) based on the remaining unknowns. The user can then specify ranges or maximum values for the remaining free parameters. These constraints limit the range over which the regression is allowed to proceed.

Example Inversions – Check of the Model

To check the accuracy of the inversion routine, two cases were simulated using the elliptical forward model and then inverted. The first case, shown in Figure 30 is that of a vertical fracture of 120 ft height and 500 ft length, opened by an internal pressure of 800 psi, centered at 6000 ft, monitored from 300 ft away, and directly normal to the fracture (azimuth = 0) in a formation of modulus 5×10^6 psi and Poisson's ratio = 0.2. In this example, the inversion code obtains the correct results within the specified error tolerances of the algorithm. The actual inversion results are written on Figure 30 on the right side (last six of the parameters). The initial conditions were a height of 100 ft, length of 400 ft, pressure of 800 psi, center at 5980 ft, dip of 0° and azimuth of 0°.

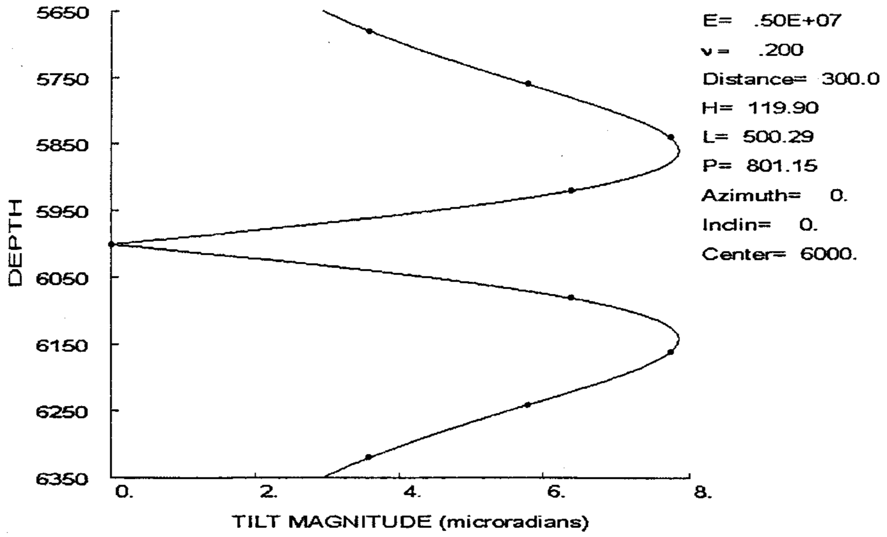

Figure 30. Test inversion case for a vertical fracture.

A second case, shown in Figure 31, is for a shorter fracture (300 ft) that is inclined 15° from the vertical. Otherwise, the rest of the parameters are the same. Figure 31 shows that the inversion correctly obtains the true answers starting with the same initial conditions as previous example.

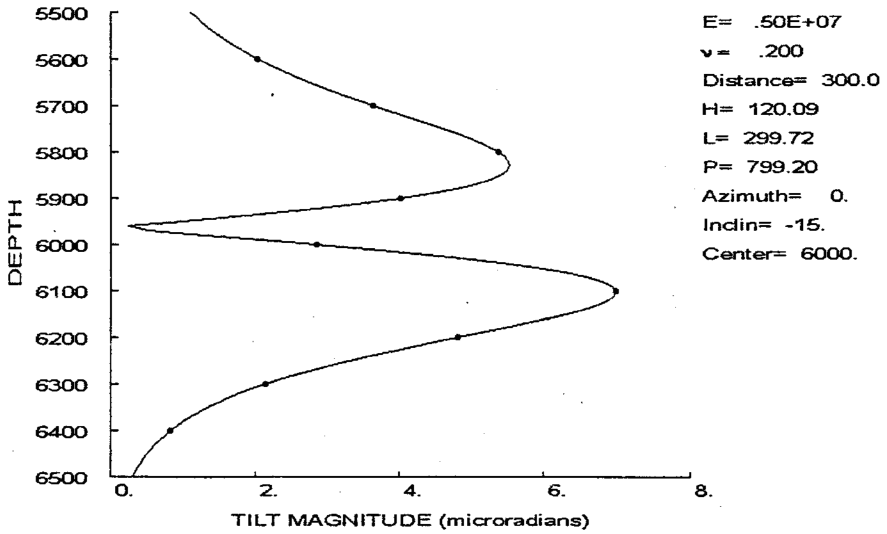

Figure 31. Test inversion case for a fracture with dip.

These test cases show that the tiltmeter inversion is able to exactly deduce the true fracture geometry for cases of perfect data (no noise) and a reasonable initial estimate. With the addition of noise, layers, uncertainty in the initial estimates, and deviations from the model assumptions, the ability of the inversion scheme to deduce the fracture geometry is considerably reduced. To determine the effect of noise, a random number generator was used to arbitrarily add a value between –0.5 and +0.5 microradians to each of the data points for the vertical fracture test case shown in Figure 30 for a noise level of about ±7%. This procedure was applied four times to get examples of the errors that might be generated by random noise. These examples are shown in Figures 32-35. As a result of the asymmetry added by the noise, the best inversion is seldom close to the original calculation, even though the fits look very good. It is clear that the presence of even small noise levels can seriously hamper the results. A value of 0.5 microradian noise was chosen in this case because it is about half of the typical Mounds data and this test case has amplitudes that are about half of the Wilcox amplitudes (the Atoka should be better because of the larger amplitudes).

The first noise case, shown in Figure 32, has an excellent fit, yet gives a height that is nearly three times too large, a length that is one-fifth of the original value, a pressure that is 1.5 times too high, and an azimuth that is drastically different. However, the confidence limits on these results are quite good because the inversion assumes that all of the misfit is due to the model and hence gives good confidence values when the match is as good as shown here. The linearized standard error (estimated one standard deviation for this nonlinear regression) is about ±85° on the azimuth, about ±3° on the dip, ±177 ft on height, ±200 ft on length, unbounded on pressure, and ±8 ft on the center of the fracture. The standard error is considered unbounded when it is larger than the maximum limit allowed by the regression (e.g., ±180° on azimuth or $\pm H_{max}$ on height). With so many free parameters (e.g., length, height, pressure, center, azimuth and dip), it is easy to match the data, but there is no certainty that the answer is even close to being correct. The solution to this problem is to reduce the number of free parameters by obtaining some independent diagnostic data to add other constraints.

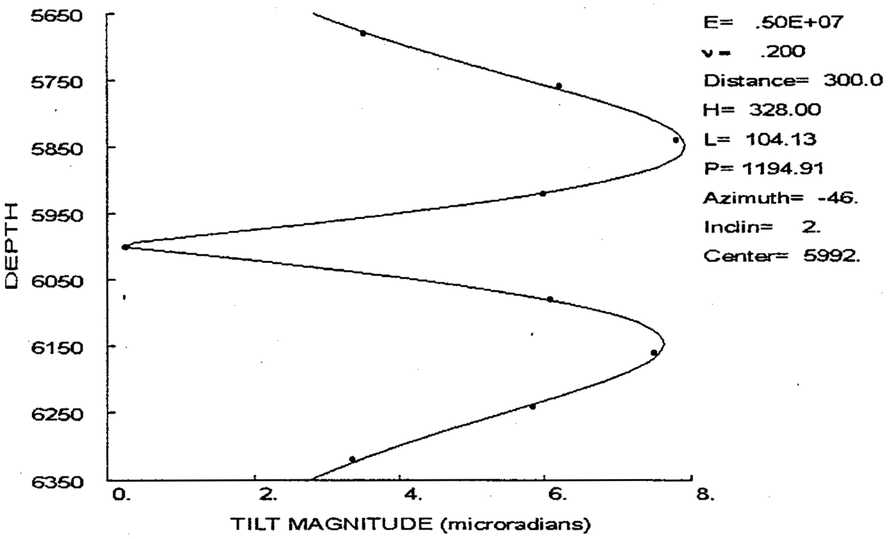

Figure 32. Test inversion case 1 for a vertical fracture with ±0.5 microradian random noise.

The second noise case, shown in Figure 33, has the closest solution to the original model. In this example, the height is within 10 ft, the length is 140 ft greater and the pressure is 150 psi less than the original calculation, while the azimuth, dip and center are all essentially correct. The standard errors are unbounded on the azimuth, about ±3° on the dip, unbounded on height, length, and pressure, and ±8 ft on the center of the fracture. The reason for the large uncertainties in several of the parameters is that they can be modified in many coupled ways to give nearly similar changes in the inversion; this makes the standard error large.

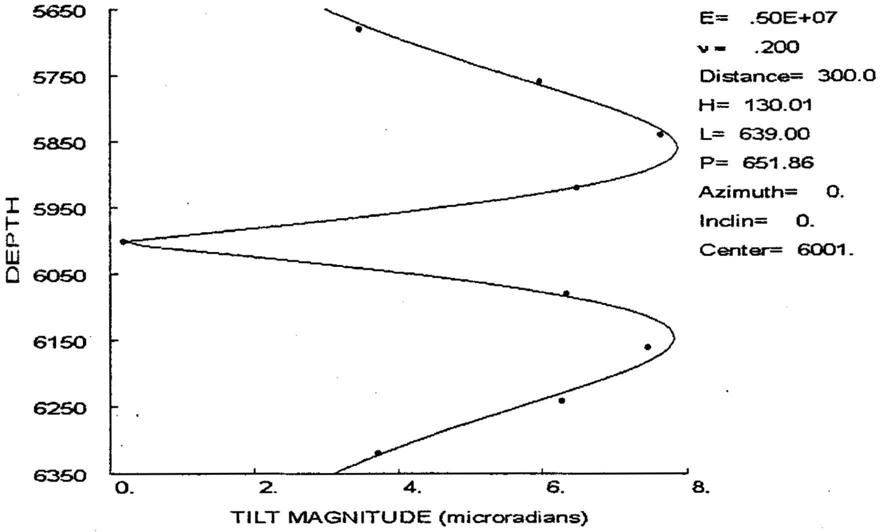

Figure 33. Test inversion case 2 for a vertical fracture with ±0.5 microradian random noise.

The third noise case, shown in Figure 34, is the worst of the cases and results in fracture lengths and pressures that reached the limits set by the code in the mapping (see the earlier discussion on the inversion). These two parameters are unbounded, as are the azimuth and height, and no standard errors can be given. The dip has a standard error of ±6° and the center has an uncertainty of ±18 ft. Again, it should be emphasized that the inversion has provided an excellent fit of the data, but it is an inaccurate one compared to the original model.

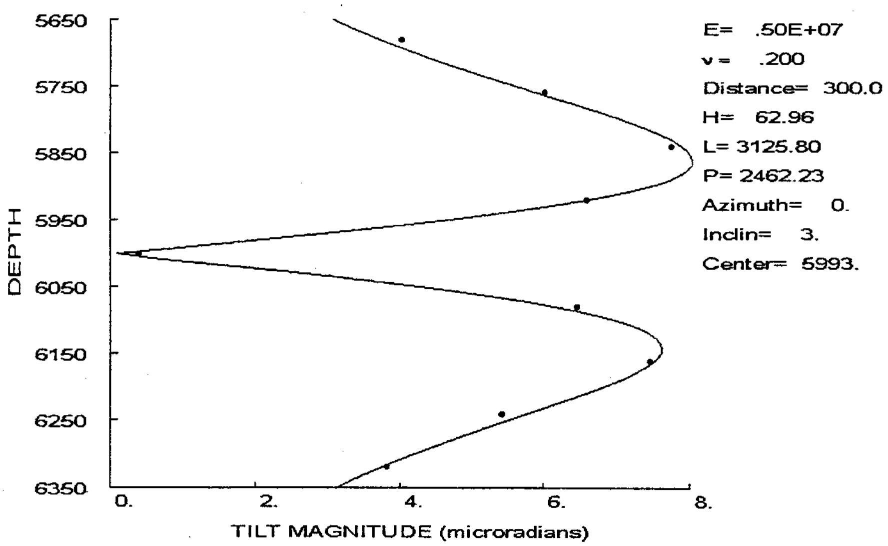

Figure 34. Test inversion case3 for a vertical fracture with ±0.5 microradian random noise.

The final noise case is shown in Figure 35. In this example, the length, height and pressure are unbounded, while the azimuth and dip have uncertainties of ±138° and ±6°, respectively, and the center has an uncertainty ±17 ft. The noise-evaluation results given here show that there must be a detailed noise analysis in order to understand the accuracy and value of the tiltmeter results. Furthermore, any independent constraints will help to improve the inversion.

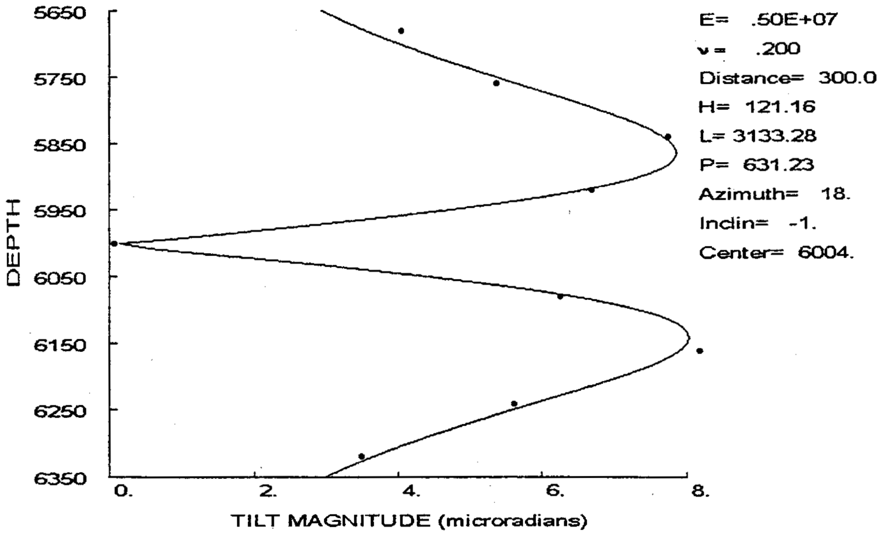

Figure 35. Test inversion case 4 for a vertical fracture with ±0.5 microradian random noise.

Inversion of Wilcox Data

The inversion of the Wilcox data was expected to be the more difficult inversion (compared to the Atoka) because of the large variations of modulus in this zone. In addition, it is not clear what the average modulus should be in this situation. However, after some experimentation with the inversion, a value of 3 x 10^6 psi was chosen as a reasonable value of Young's modulus and a value of 0.22 was chosen for Poisson's ratio. The monitoring distance to the fracture was found to be 140 ft and the line between the injection point and the center of the monitoring array was nearly a right angle to the average fracture orientation observed in the two lateral intersection coreholes. Thus the correct answer for azimuth should be 0° or 180°. Likewise the correct inclination (from the corehole data) is 0° and the measured pressure varied from 225 to 350 psi depending on the injection number. All other parameters were unknown, although they could be inferred from microseismic data.

Although many different inversions with varying constraints were tried, this report will not attempt to show them all. Instead, an example of the different types of results will be shown for the first injection in each zone and then one or two inversions, including a "best case", will be given for all of the subsequent injections. There is some subjectivity in choosing this best case, but in general the choice is governed by known data (e.g., from the coring).

Figure 36 shows the unconstrained inversion of the first Wilcox injection. In this case the fit to the data is very good and residuals are within the 1-2 μradian noise level. However, the azimuth of the fracture is nearly 90°(directed right at the monitor well) and the fracture height is an unlikely 352 ft.

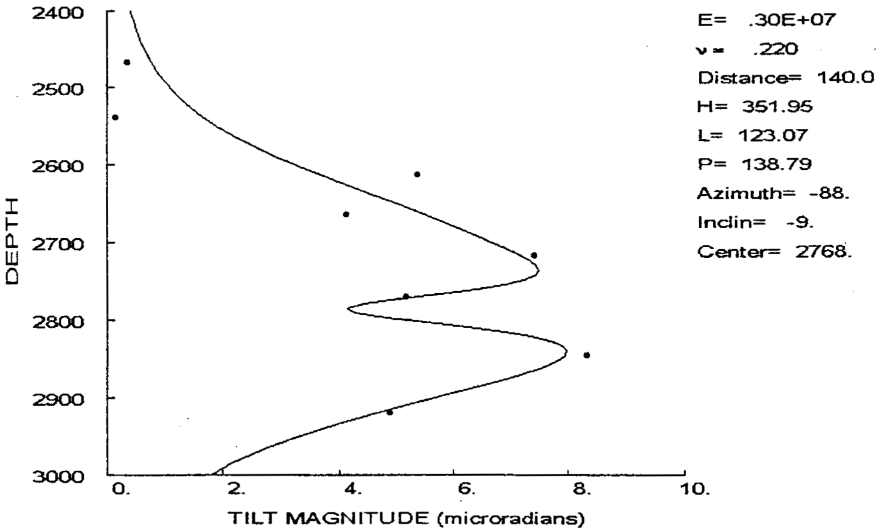

Figure 36. Unconstrained inversion for Wilcox injection #1.

This inversion can be improved upon by constraining the pressure to the measured value of 225 psi, resulting in the fit shown in Figure 37. In this case, the azimuth of -28° and the dip of -13° are almost acceptable and the height of 73 ft is very reasonable. The length of 3000 ft is misleading, since any fracture greater than about 400 ft length will give almost identical results. The actual value of 3130 ft is approximately the limiting length used in the code. The insensitivity to length occurs because any length greater than about 3 times the monitoring distance looks like an infinite 2D fracture and it is impossible to distinguish any differences. In this case, the result could be given with a length of 400 ft with the same accuracy.

In this particular case, the residuals are greater than the noise levels seen in Wilcox sandstone testing. However, the enlarged residuals could be due to other effects, such as modulus variations and imperfect coupling of the instruments. Thus, the size of the residuals do not rule out the possibility that this inversion is a reasonable answer.

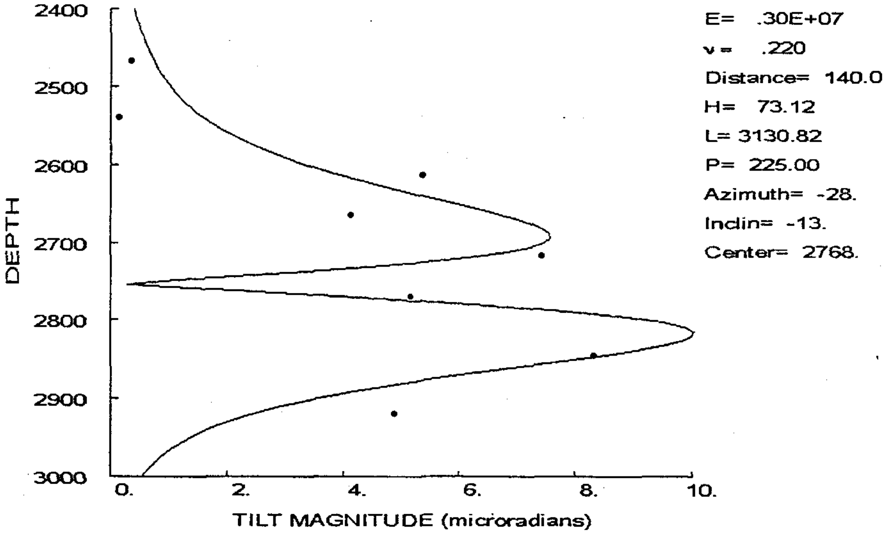

Figure 37. Inversion of Wilcox injection #1 with pressure constraint.

If the azimuth is constrained to the known direction, the fit is relatively good but the answer requires a short, fat fracture with unrealistic pressure. This fit is shown in Figure 38. The unrealistically large pressure immediately eliminates this possible solution.

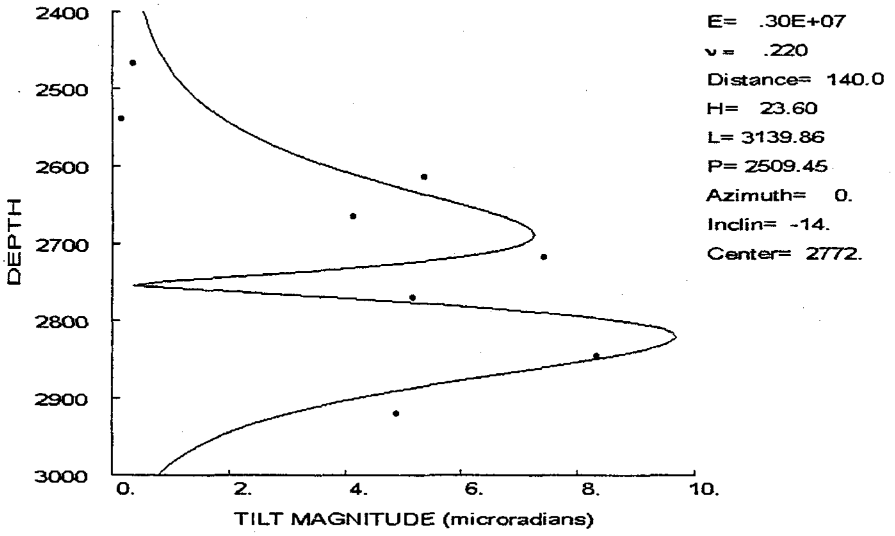

Figure 38. Inversion of Wilcox injection #1 with azimuth constraint.

If the pressure and azimuth are constrained to their measured values, the results shown in Figure 39 are obtained. In this case, the height is a reasonable 80 ft, the length is at least 400 ft (see preceding discussion on long lengths), and the inclination is a not unreasonable -13°.

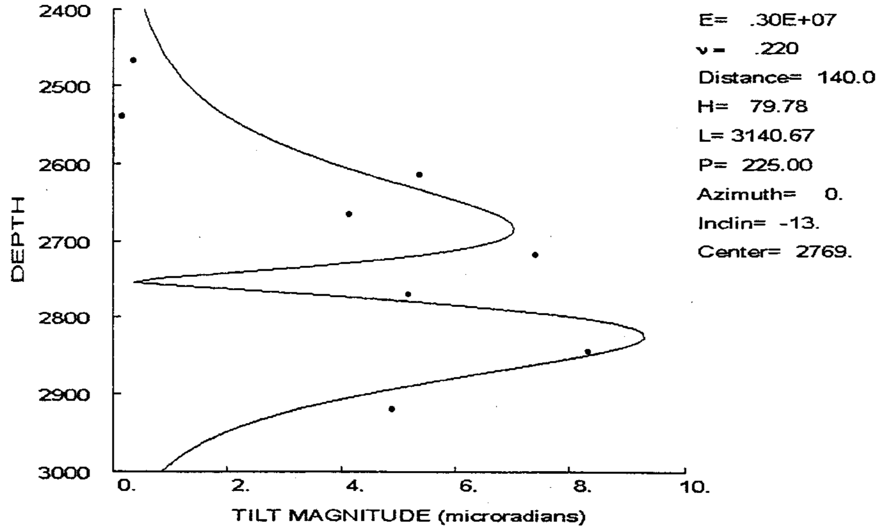

Figure 39. Inversion of Wilcox injection #1 with pressure and azimuth constraints.

Finally, if the solution is constrained with all of the measured parameters (pressure, azimuth, inclination), the results of Figure 40 are obtained. The fracture height is again about 80 ft while the length is greater than 400 ft. The fracture center is just about in the middle of the Wilcox sandstone. This case appears to be a reasonable solution to the problem. The residuals are within the noise limits for all but one point, which may be a reflection of other effects. The standard error for the height is 48 ft and for the center depth is 15 ft. The length, of course is unbounded.

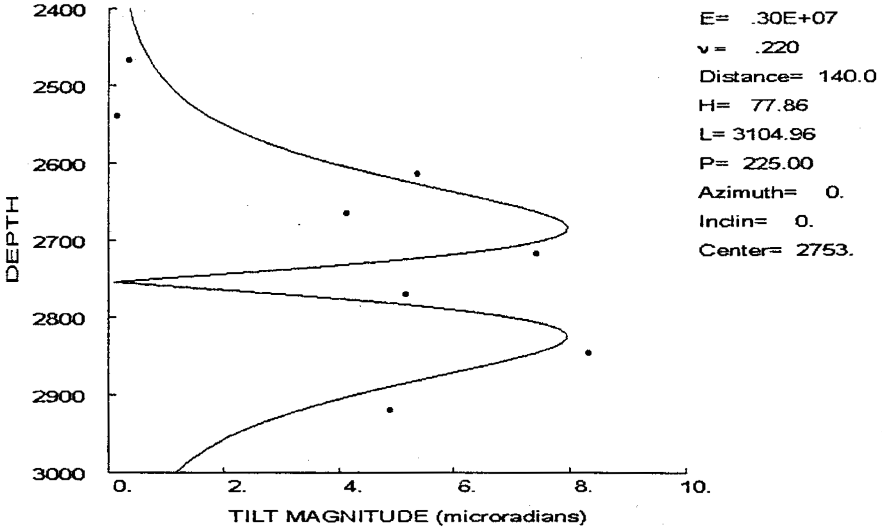

Figure 40. Inversion of Wilcox injection #1 with pressure, azimuth & inclination constraints.

The constrained inversion for injection #2 is shown in Figure 41. Constraints included pressure, azimuth and inclination. The results suggest that a long fracture with a height of 76 ft (±73 ft standard error) was created with a center point of 2685 ft (±26 ft). In this case, the residuals are much larger than the estimated noise and suggest a poor match of the model to measured data.

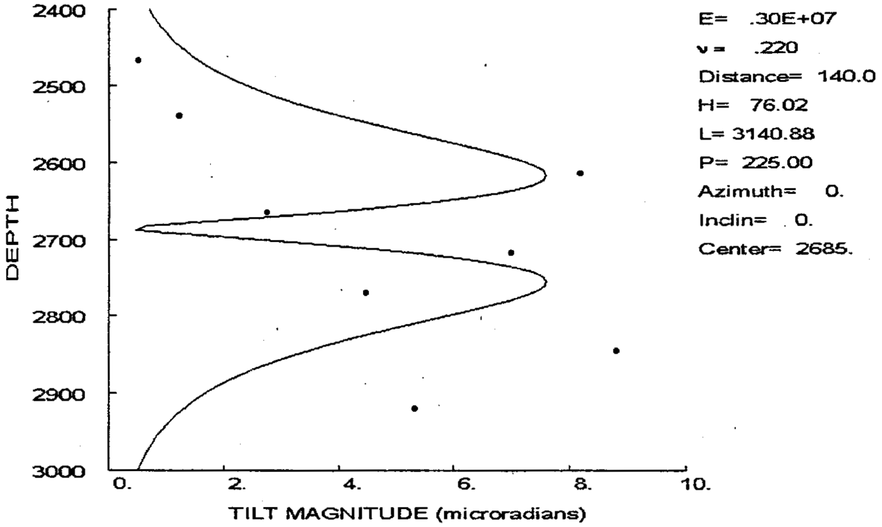

Figure 41. Inversion of Wilcox injection #2 with pressure, azimuth & inclination constraints.

The results for the third Wilcox injection using all known constraints is shown in Figure 42. In this case the fracture height is a reasonable 81 ft (±ft) and the center is at 2743 ft (±20 ft), in the center of the sandstone. The fracture length would appear to be greater than 400 ft. Some of the residuals are greater than the estimated noise, suggesting that the application of a model using a single fracture in a homogeneous material is not correct or that there is some other systematic error in the measurements (e.g., due to coupling).

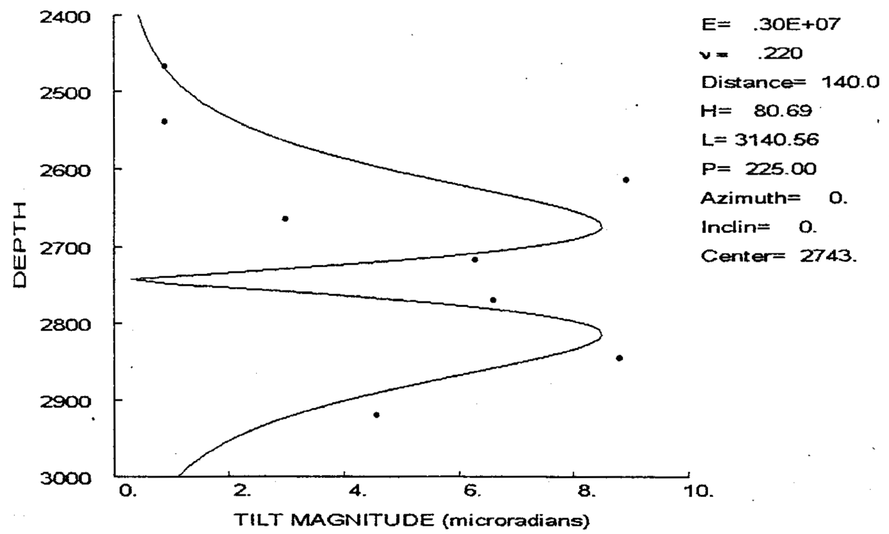

Figure 42. Inversion of Wilcox injection #3 with pressure, azimuth & inclination constraints.

The inversion for Wilcox injection #4 is shown in Figure 43. All known constraints are used, yielding a height of 68 ft (±ft) and a center of 2691 ft (±ft). In this case the fit at the bottom of the array is poor with very large residuals.

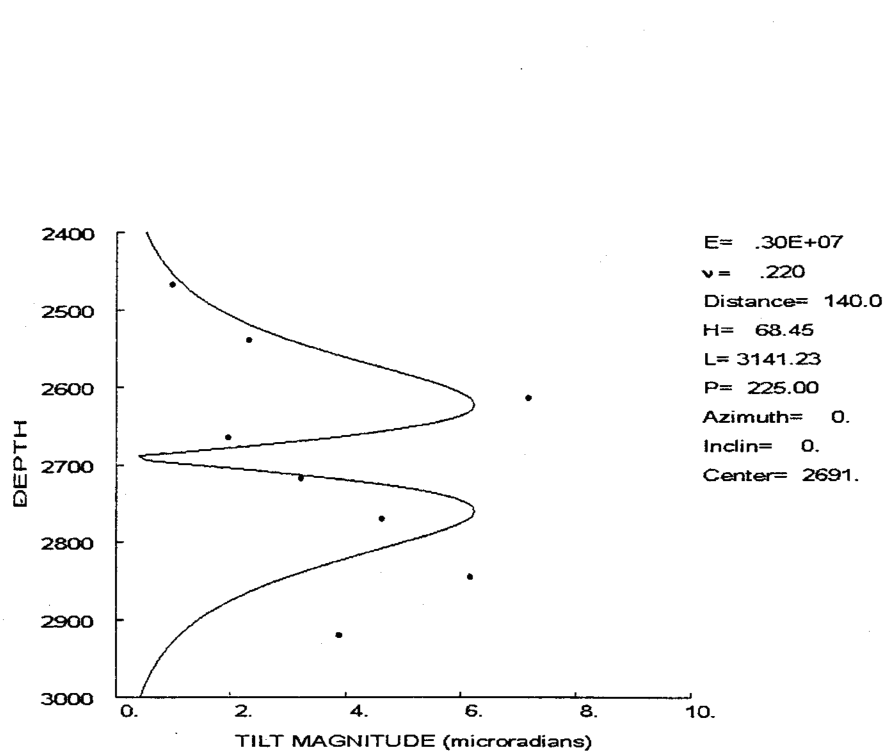

Figure 43. Inversion of Wilcox injection #4 with pressure, azimuth & inclination constraints.

The constrained inversion results for Wilcox injection #5 are shown in Figure 44. The height of the fracture is 65 ft (±52 ft) and the fracture center is at 2688 ft (±24 ft). As in most of these inversions, a long fracture is needed to obtain the best fit. Similarly, the large residuals in this match again suggest that the misfit is due to more than just the random noise.

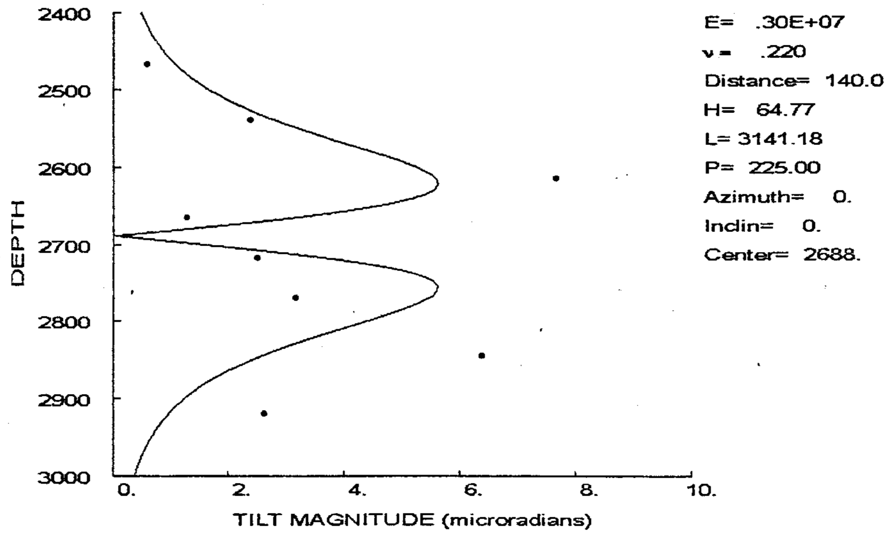

Figure 44. Inversion of Wilcox injection #5 with pressure, azimuth & inclination constraints.

The inversion result for Wilcox injection #6 is shown in Figure 45. The fracture height is 64 ft (±75 ft) and the center is at 2682 ft (±36 ft). As in pervious examples, the fit is poor.

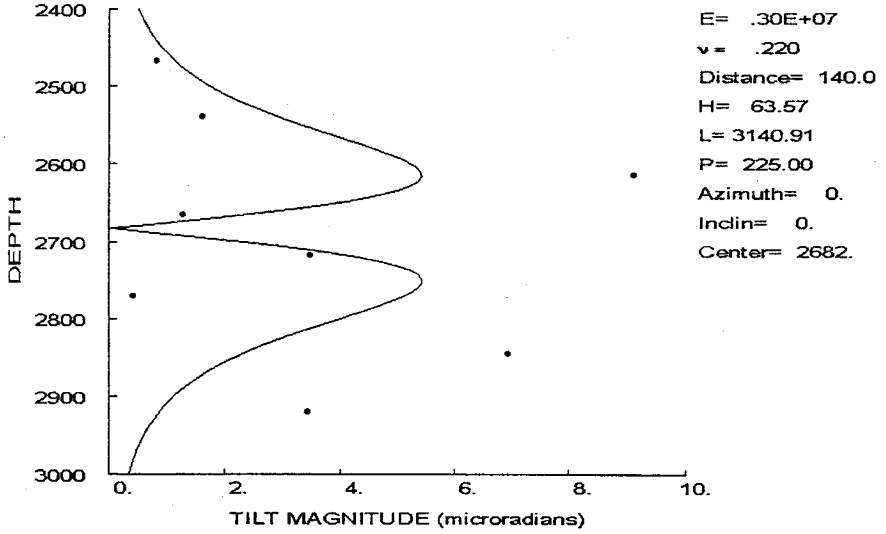

Figure 45. Inversion of Wilcox injection #6 with pressure, azimuth & inclination constraints.

The inversion for Wilcox injection #7 is shown in Figure 46. As with the previous tests the fit is not very good and yields a height of 57 ft (±60 ft) and a center of 2686 ft (±34 ft). The pressure is constrained at 250 psi because the pressure has been elevated somewhat with continued pumping. Subsequent matches will show successively higher pressures because of the steadily increasing pressures measured during the testing.

Although it might appear that the reason for the misfit is that the pressure is constrained at a value that is much too low (so that the peaks are matched better), this is not actually the case. Figure 47 shows this same injection without the pressure constraint (only azimuth and dip). The fit is very similar to Figure 45, except it is achieved through an increased height using a relatively small pressure. The difficulty with fitting these data is that the two peak points are so large relative to the other points that the curves cannot decay fast enough above and below the peaks.

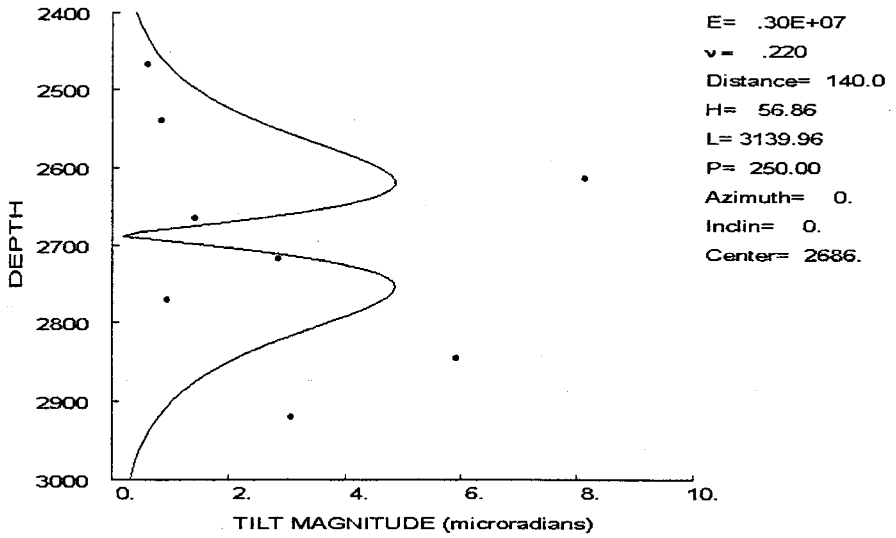

Figure 46. Inversion of Wilcox injection #7 with pressure, azimuth & inclination constraints.

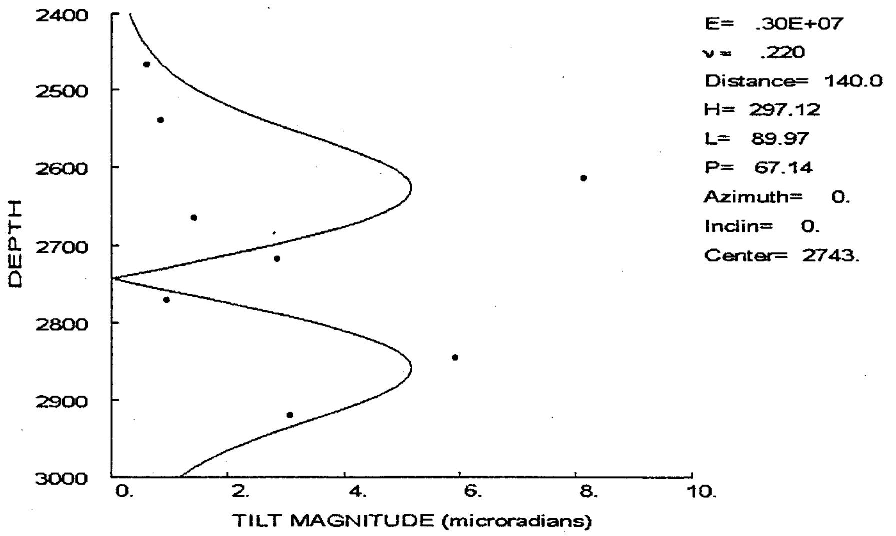

Figure 47. Inversion of Wilcox injection #7 with azimuth & inclination constraints.

The inversion for Wilcox injection #8 is shown in Figure 48. The match appears to be improving because the tilt values surrounding the peak locations have increased in magnitude, allowing the match to more closely approach the peak amplitudes. The fracture height is 62 ft (±46 ft) and the center is at 2700 (±23 ft).

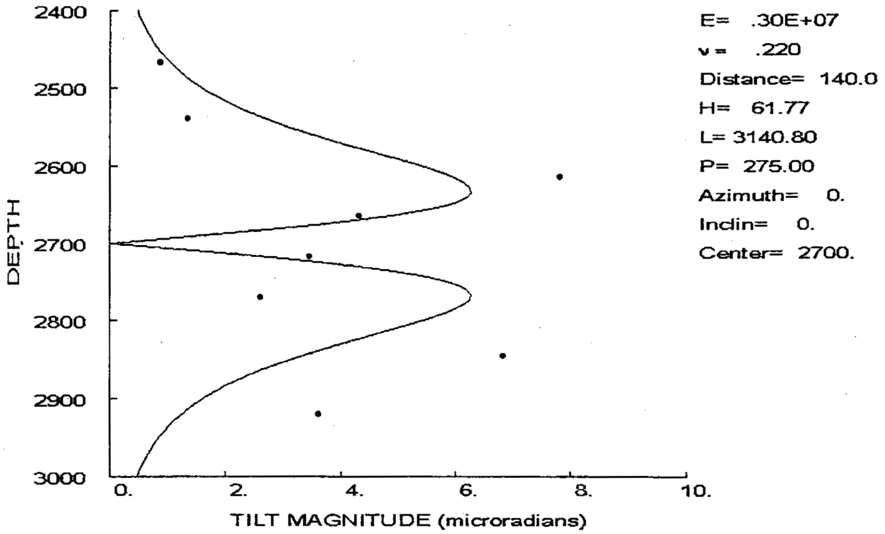

Figure 48. Inversion of Wilcox injection #8 with pressure, azimuth & inclination constraints.

The inversion for Wilcox injection #9 is shown in Figure 49. The height of the fracture is 58 ft (±49 ft) and the center is at 2684 ft (±28 ft).

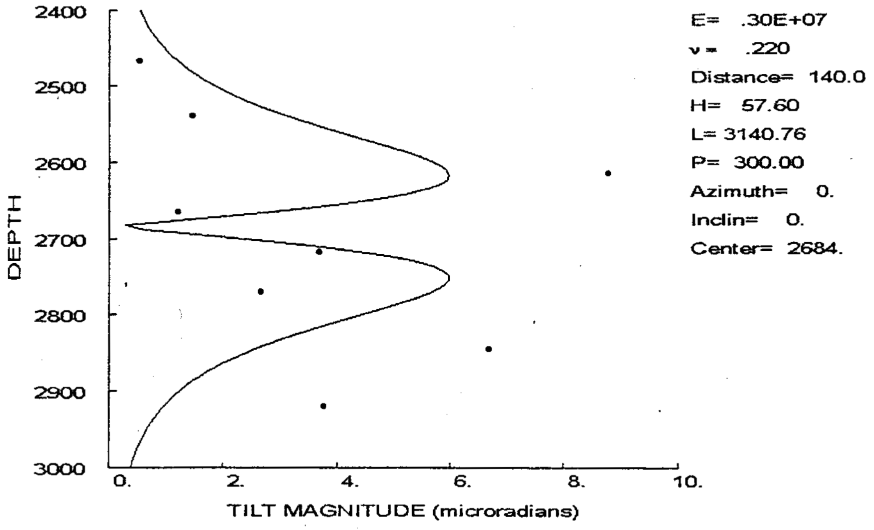

Figure 49. Inversion of Wilcox injection #9 with pressure, azimuth & inclination constraints.

For Wilcox injection #10, the inversion results are probably the worst of the entire data set because of the anomalously large tilt magnitude at the 1613 ft tiltmeter. However, this was the last injection of the day and it is possible that cumulative effects are causing additional problems. The fracture height for this inversion is 63 ft (±88 ft) and the center is at 2660 ft (±41 ft).

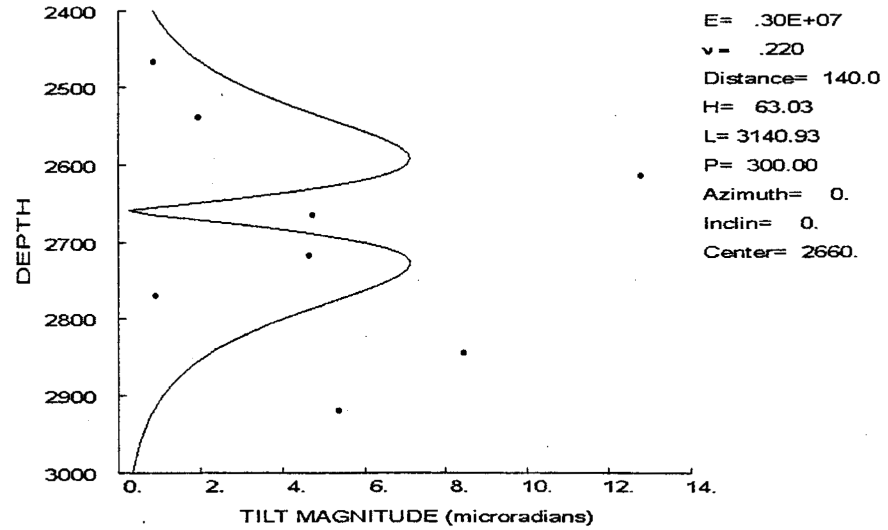

Figure 50. Inversion of Wilcox injection #10 with pressure, azimuth & inclination constraints.

The inversion for Wilcox injection #11 is shown in Figure 51. This result is considerably better than the previous test, possibly because it is the first test of the day and the formation has equilibrated. The fracture height is 69 ft (±55 ft) and the center is 2684 ft (±30 ft).

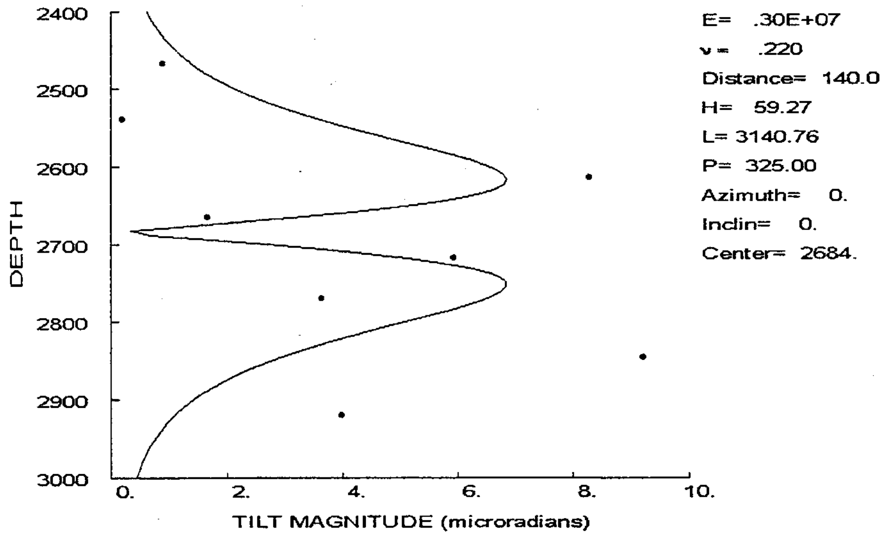

Figure 51. Inversion of Wilcox injection #11 with pressure, azimuth & inclination constraints.

The inversion for Wilcox injection #12 is very similar to #11 and gives a fracture height of 65 ft (±47 ft) and a center of 2692 ft (±22 ft). As in most other tests, the residuals are quite large and the fit is poor.

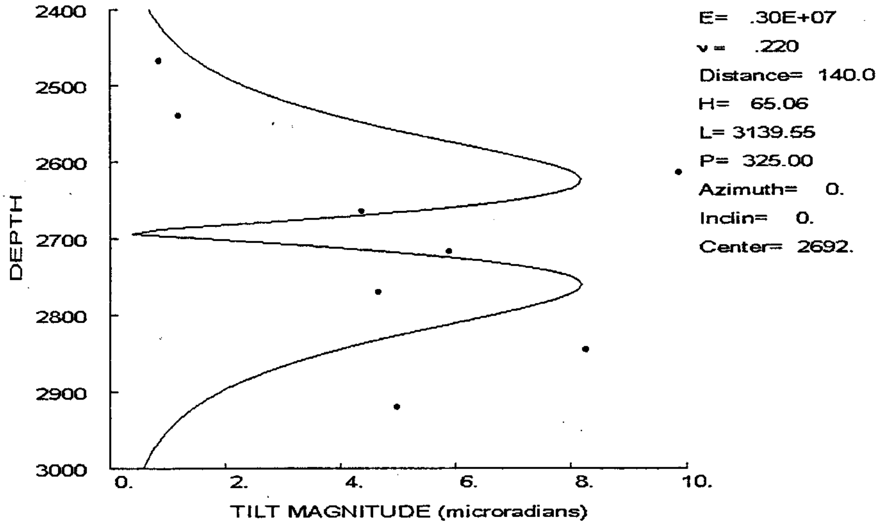

Figure 52. Inversion of Wilcox injection #12 with pressure, azimuth & inclination constraints.

The inversion of Wilcox injection is again similar to the previous tests and yields a height of 57 ft (±47 ft) and center of 2683 ft (±27 ft).

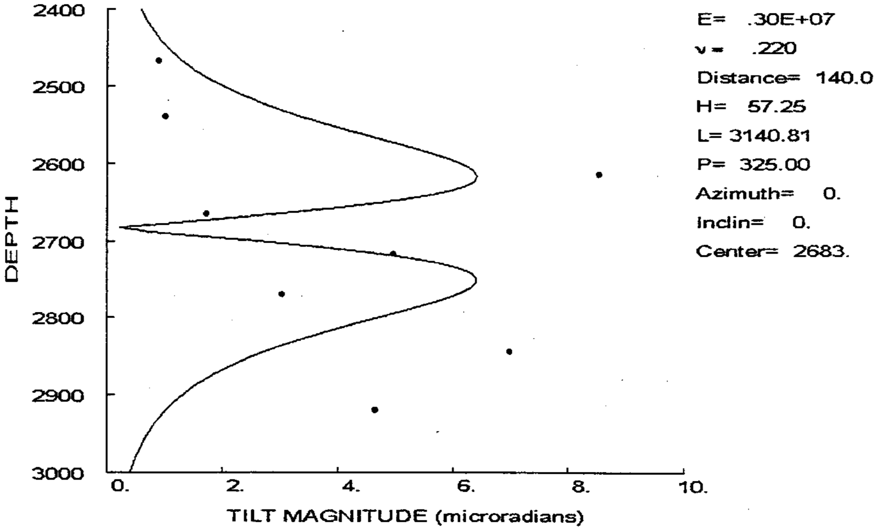

Figure 53. Inversion of Wilcox injection #13 with pressure, azimuth & inclination constraints.

Similarly, the inversion for Wilcox injection #14 yields a poor fit giving a height of 55 ft (±36 ft) and a center of 2687 ft (±22 ft).

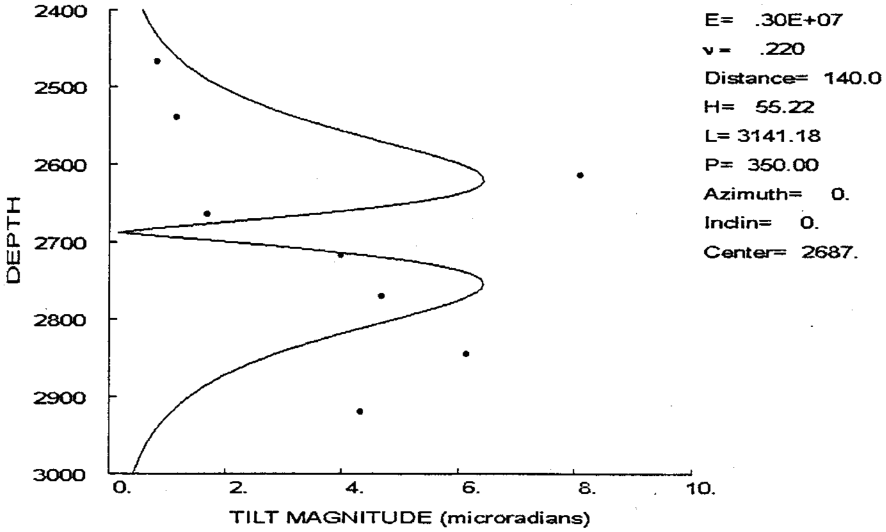

Figure 54. Inversion of Wilcox injection #14 with pressure, azimuth & inclination constraints.

The inversion of Wilcox injection #15 is shown in Figure 55. At this injection, the data are starting to change somewhat, resulting in a very non-symmetric amplitude of the peaks. The triply constrained fit shown here is rather poor and yields a height of 61 ft (±43 ft) with a fracture center at 2694 ft (±22 ft). Since the data have changed considerably, it is worthwhile to show in Figure 56 an inversion where only the pressure is constrained. Such a case can be matched more adequately by a fracture with dip, but this result is not supported by the coring.

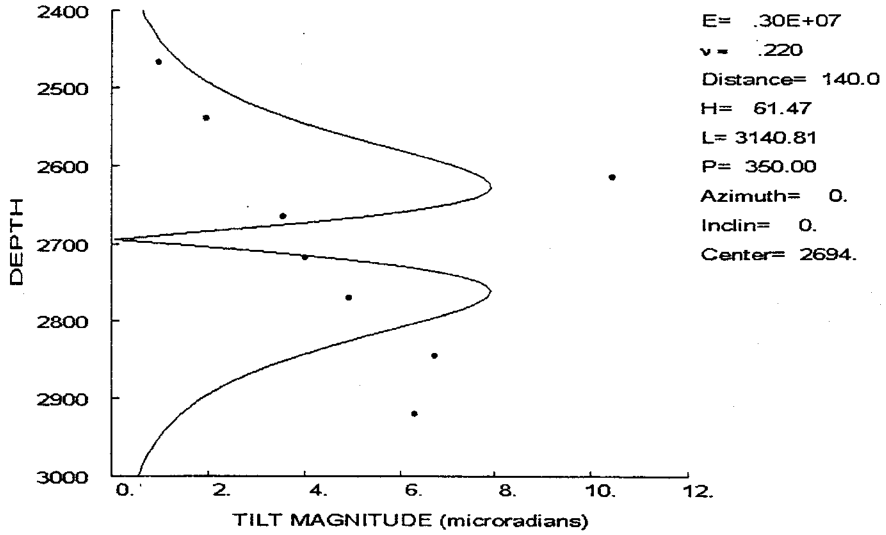

Figure 55. Inversion of Wilcox injection #15 with pressure, azimuth & inclination constraints.

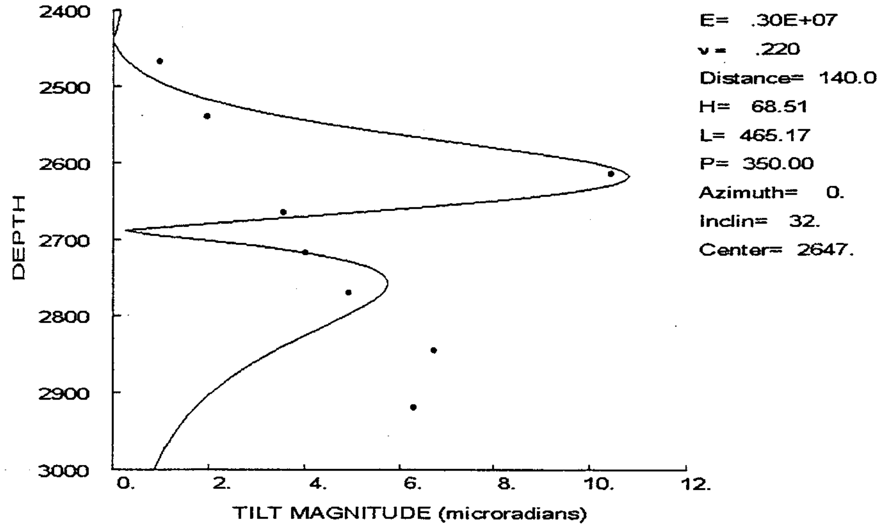

Figure 56. Inversion of Wilcox injection #15 with pressure constraint.

The inversion result for Wilcox injection #16 is shown in Figure 57. The fracture height is 54 ft (±35 ft) and the center is at 2683 ft (±22 ft).

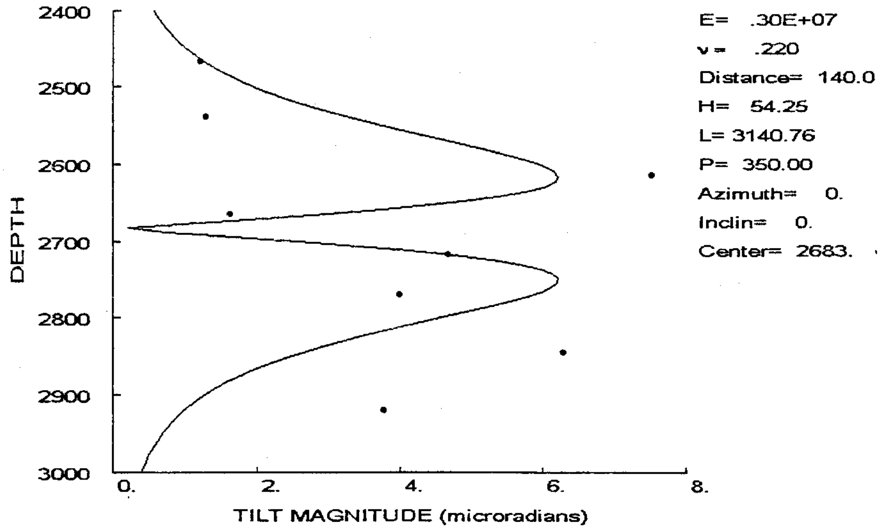

Figure 57. Inversion of Wilcox injection #16 with pressure, azimuth & inclination constraints.

The inversion for Wilcox injection #17 is also a poor fit, as shown in Figure 58. The height is 63 ft (±45 ft) and the center is at 2694 ft (±22 ft).

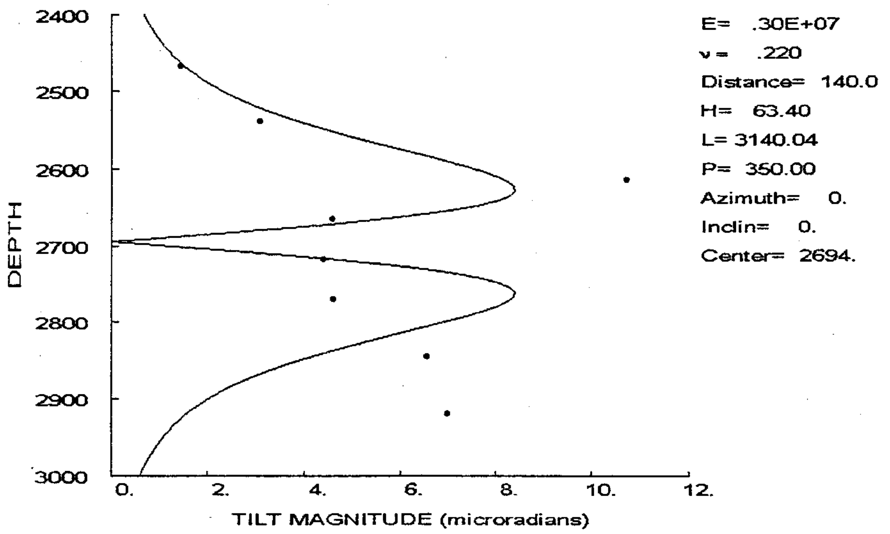

Figure 58. Inversion of Wilcox injection #17 with pressure, azimuth & inclination constraints.

Given the constrained inversion results shown in the previous figures, the fracture height appears to vary from 50-80 ft, but with a very large uncertainty for each of the tests. However, the large number of tests having similar results suggests that numbers may be reasonable. If we were to use fully unconstrained inversions or inversions constrained only by the pressure, we would have had many fractures directed at the monitor well and many with a significant amount of dip. Clearly, the availability of the additional contraints is essential to obtaining a meaningful tiltmeter inversion. However, even with the constraints it is not clear that the results are accurate because of the significant and consistent misfits of the data. These misfits might be due to inadequacy of the model, as in the case of multiple fracture strands, horizontal fracture components, layered materials with different moduli and stress, and many other possible effects. The misfits might also be due to the measurement system, as in the case of unreliable coupling. One other method to better constrain the results is to have more tiltmeter wells.

One comparison that can be made is the tiltmeter geometry with the microseismic geometry. Figures 59-75 show those comparisons for each of the injections. Each of these figures shows a side view of the microseismic locations relative to the injection wellbore and the Wilcox sandstone (solid lines) along with a superposed outline of the inversion result. Note that the inversion actually determines an elliptic fracture, but since it is a very long fracture in every case it is shown as a rectangle on the plot. In general, the microseismic and tiltmeter images are offset vertically, although a few of the tests coincide. This mismatch could be due to the velocity structure affecting the microseisms or it could be due to layering or complex fracturing affecting the tiltmeters (or some combination of both). The microseismic points generally outline a short fracture that is often asymmetric. The downhole tiltmeters cannot distinguish asymmetry and the long fracture lengths may be a modulus amplification of the tiltmeter data at one or two levels that requires a much greater length (since pressure and azimuth are fixed) to match. In the later fractures, the microseismic data show evidence of downward activity, but this is not obtained in the tiltmeter inversion. The Pinnacle dislocation inversion matched some of these later tests using two fractures, but that is not done in this inversion algorithm because a first fracture will significantly perturb the boundary conditions on the second fracture (and the second on the first, as well). As a result, both fractures will have additional tractions on their boundaries that cannot correctly be accounted for and the analysis will have a possibility of being significantly in error.

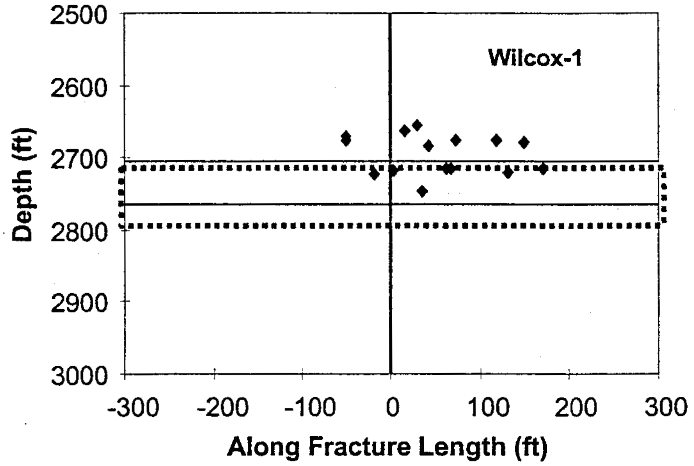

Figure 59. Comparison of microseismic and downhole-tiltmeter results for Wilcox injection #1.

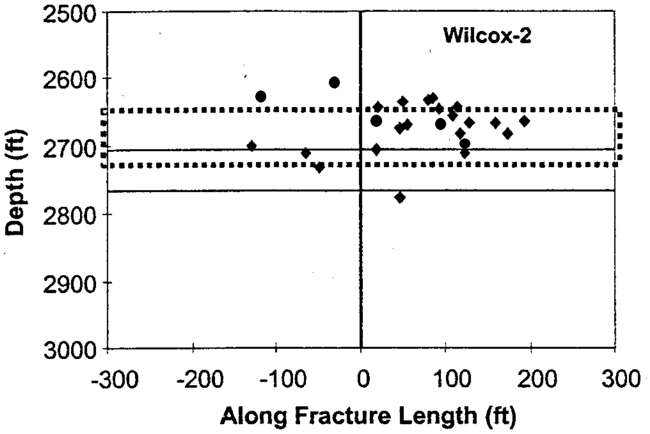

Figure 60. Comparison of microseismic and downhole-tiltmeter results for Wilcox injection #2.

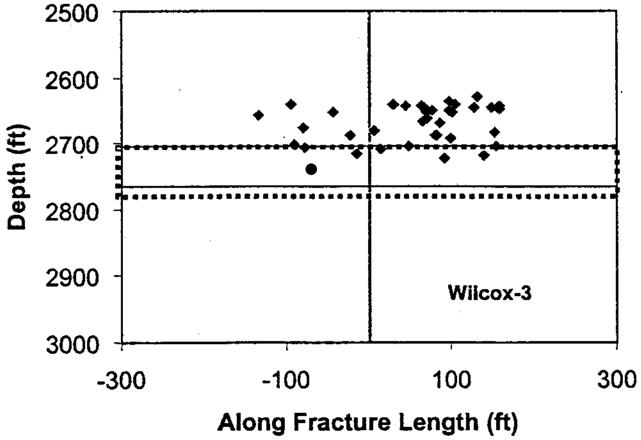

Figure 61. Comparison of microseismic and downhole-tiltmeter results for Wilcox injection #3.

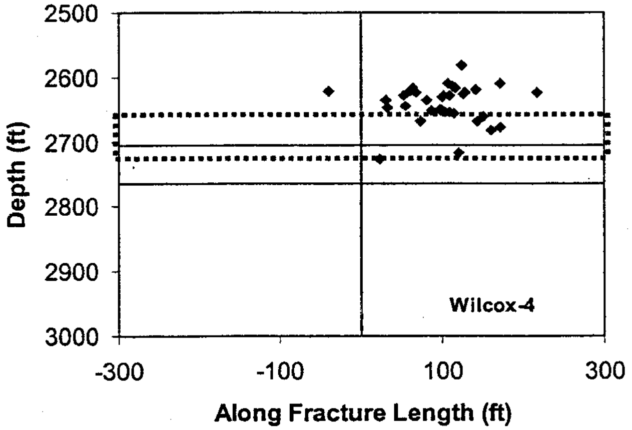

Figure 62. Comparison of microseismic and downhole-tiltmeter results for Wilcox injection #4.

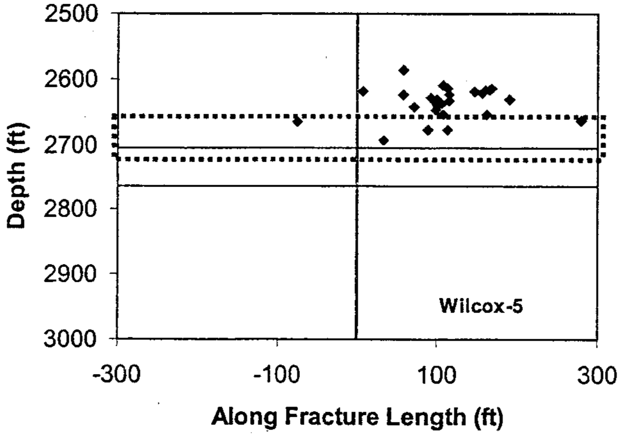

Figure 63. Comparison of microseismic and downhole-tiltmeter results for Wilcox injection #5.

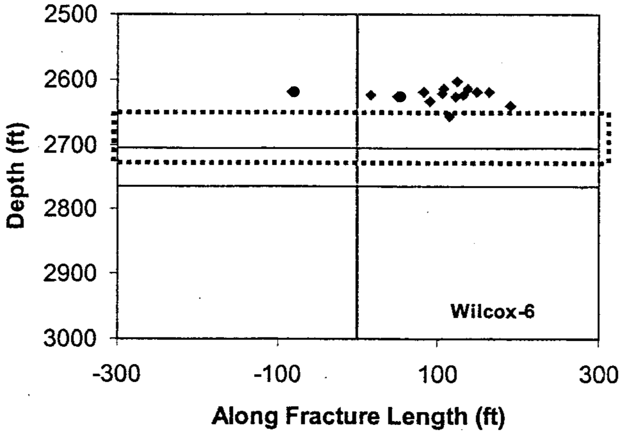

Figure 64. Comparison of microseismic and downhole-tiltmeter results for Wilcox injection #6.

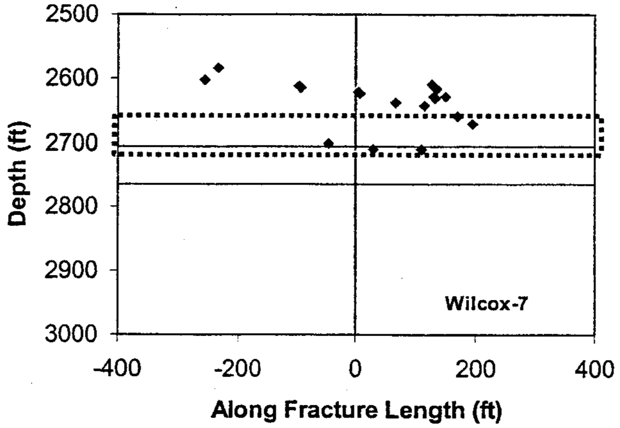

Figure 65. Comparison of microseismic and downhole-tiltmeter results for Wilcox injection #7.

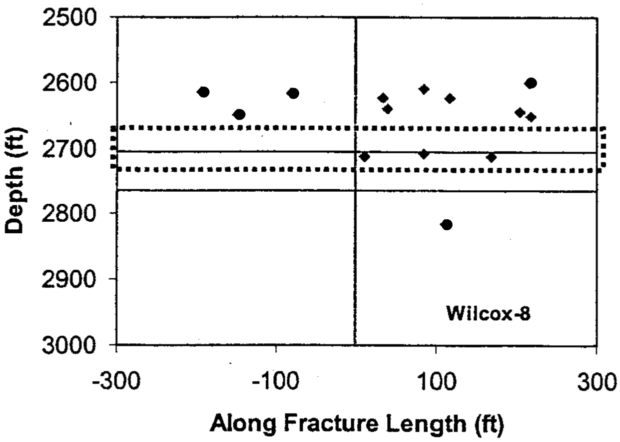

Figure 66. Comparison of microseismic and downhole-tiltmeter results for Wilcox injection #8.

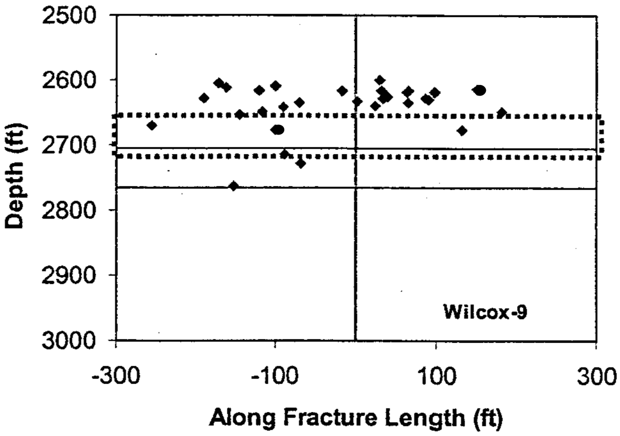

Figure 67. Comparison of microseismic and downhole-tiltmeter results for Wilcox injection #9.

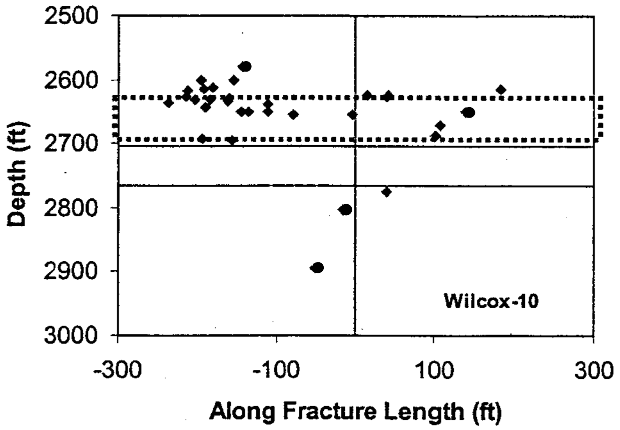

Figure 68. Comparison of microseismic and downhole-tiltmeter results for Wilcox injection #10.

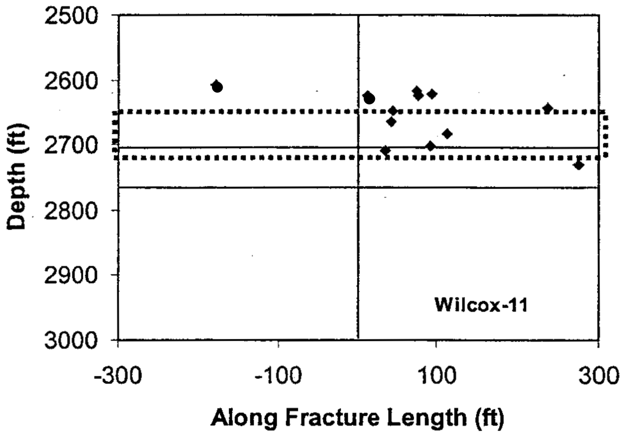

Figure 69. Comparison of microseismic and downhole-tiltmeter results for Wilcox injection #11.

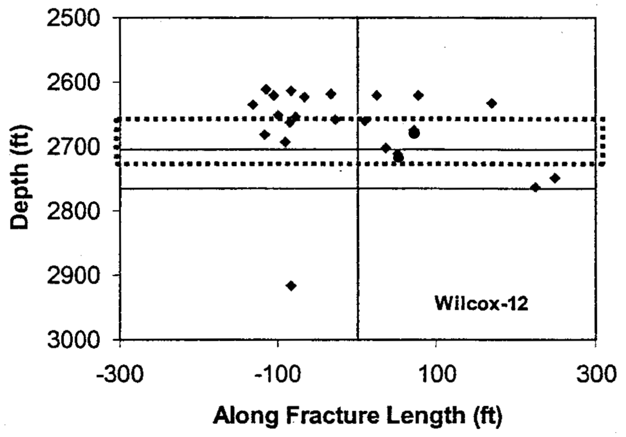

Figure 70. Comparison of microseismic and downhole-tiltmeter results for Wilcox injection #12.

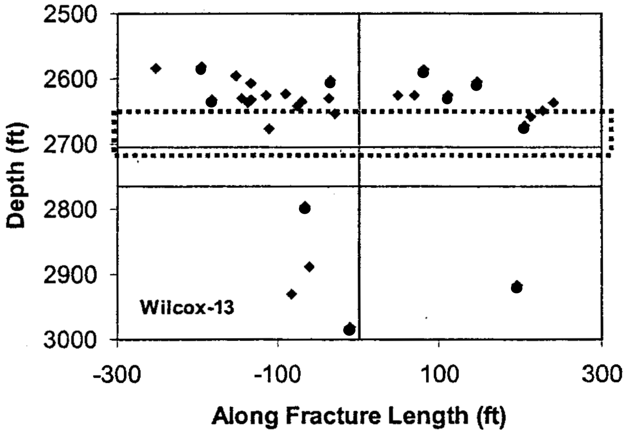

Figure 71. Comparison of microseismic and downhole-tiltmeter results for Wilcox injection #13.

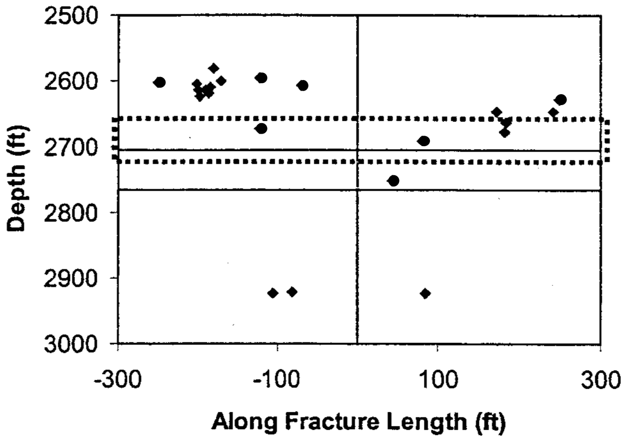

Figure 72. Comparison of microseismic and downhole-tiltmeter results for Wilcox injection #14.

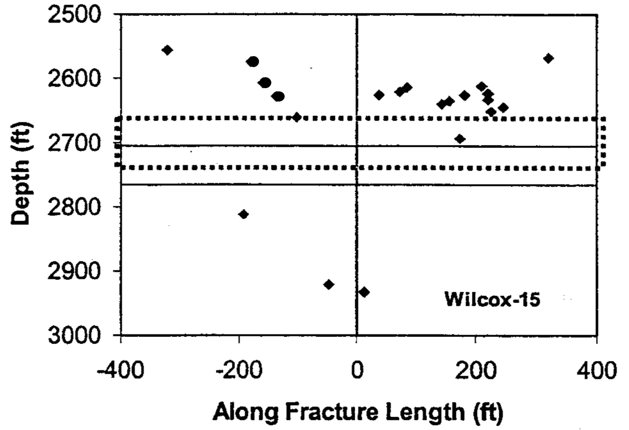

Figure 73. Comparison of microseismic and downhole-tiltmeter results for Wilcox injection #15.

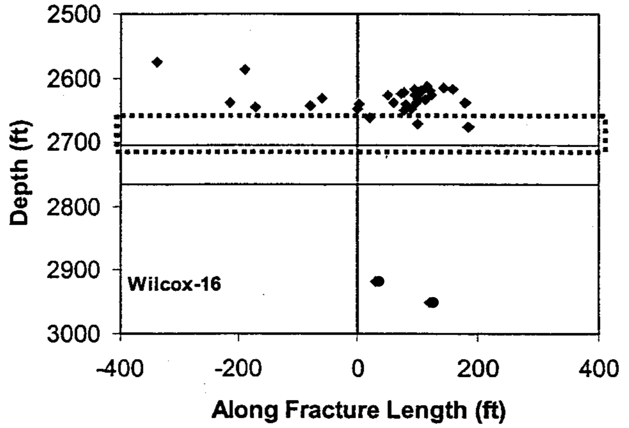

Figure 74. Comparison of microseismic and downhole-tiltmeter results for Wilcox injection #16.

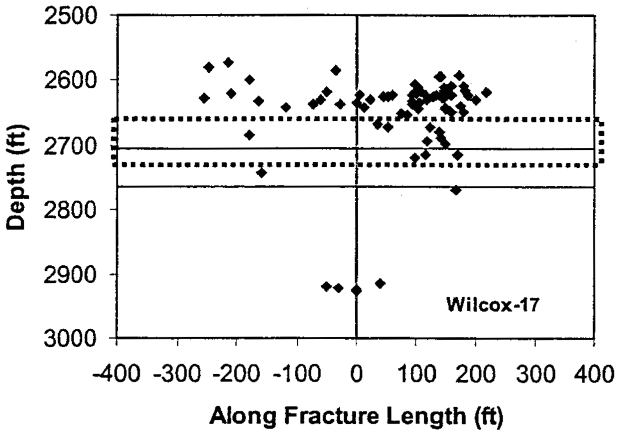

Figure 75. Comparison of microseismic and downhole-tiltmeter results for Wilcox injection #17.

Inversion of Atoka Data

The inversion of the Atoka data would appear to be easier because the massive shale eliminates any possibility of layering inducing complex tilt responses. However, the geometry is somewhat more complex because the downhole location of the downhole-tiltmeter monitor-well location is offset somewhat to the west (only the surface location is shown in Figure 2). As a result, the perpendicular between the monitor well and the fracture azimuth (as determined from core, surface tiltmeter, and microseismic data) does not intersect the injection point. Using a downhole distance of 130 ft between the injection point and the tiltmeter array, the measured azimuth of the fracture would be 15° relative to the normal to this line (e.g., the inversion geometry is constructed so that a 0° fracture is normal to line between the monitor and injection wells, so a 15° fracture is slightly off from this line). Thus, a 15° fracture azimuth was used for constrained inversions.

In this zone, the average Young's modulus was taken to be 2 x 10^6 psi and Poisson's ratio is 0.25. The fracture center is presumably somewhere near the perforated interval (1920-1940 ft) and the inclination is generally near zero based on surface tiltmeter data. As with the Wilcox inversions, successively increasing pressure were measured during the Atoka testing and the appropriate pressure for each test will be used as the pressure constraint.

Similar to the results shown in the Wilcox experiments, several differently constrained inversions are shown for the first injection. Subsequent injections will generally show the "best" match of the data with the known constraints. The fully unconstrained inversion for the first injection is shown in Figure 76. This inversion very accurately fits the data, but it yields fracture parameters that are not consistent with other known data. The inclination of −12° is not unreasonable, but the azimuth of -69° would have the fracture closely approaching the monitor well. The core through the fracture, surface tiltmeter data, and microseismic locations all suggest that this is not occurring. The fracture height of 68 ft, length of 95 ft, and center at 1942 ft are all reasonable, but the pressure would need to be extremely large to create a fat fracture. The uncertainties for this inversion are ±11° for the azimuth, ±6° for the dip, ±54 ft for the length, ±7 ft for the center, and unbounded for height and pressure (e.g., uncertainties larger than the values).

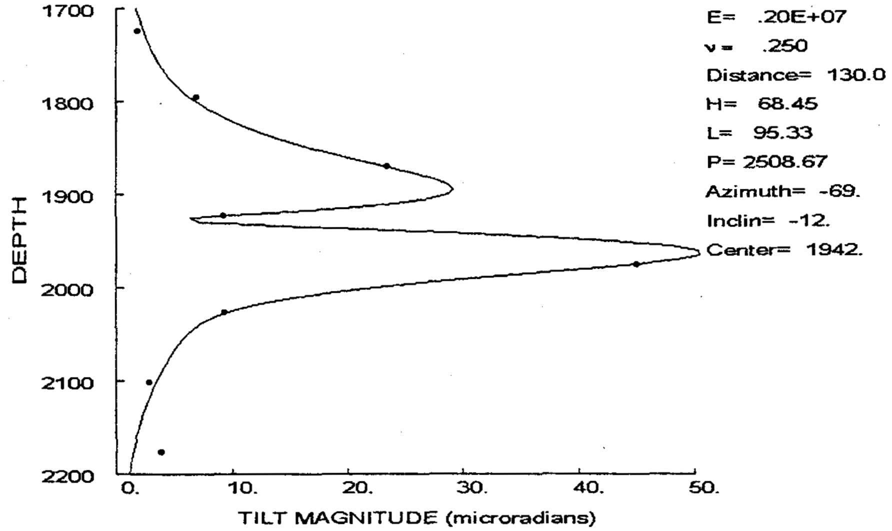

Figure 76. Inversion of Atoka injection #1 with no constraints.

The inversion using the measured pressure of 360 psi shows an equally good result which is obtained by increasing the height and changing the direction to compensate for the pressure. The azimuth of 72° (±7°) is inconsistent with the known data and suggest that the fracture is approaching close to the monitor well. The 167 ft height has an uncertainty of 36 ft, the114 length is ±2 ft, the center is at 1941 ±4 ft, the inclination is -11° ±5°.

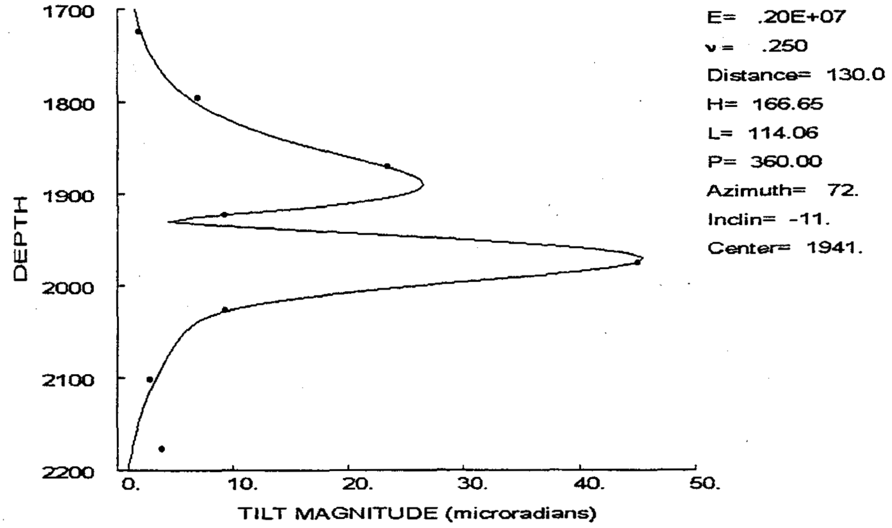

Figure 77. Inversion of Atoka injection #1 with pressure constraint.

If just the azimuth is constrained to the measured 15° orientation, the inversion produces the somewhat unusual results shown in Figure 78. The highly inclined, fat fracture gives a reasonable match of the data but is not consistent with known data.

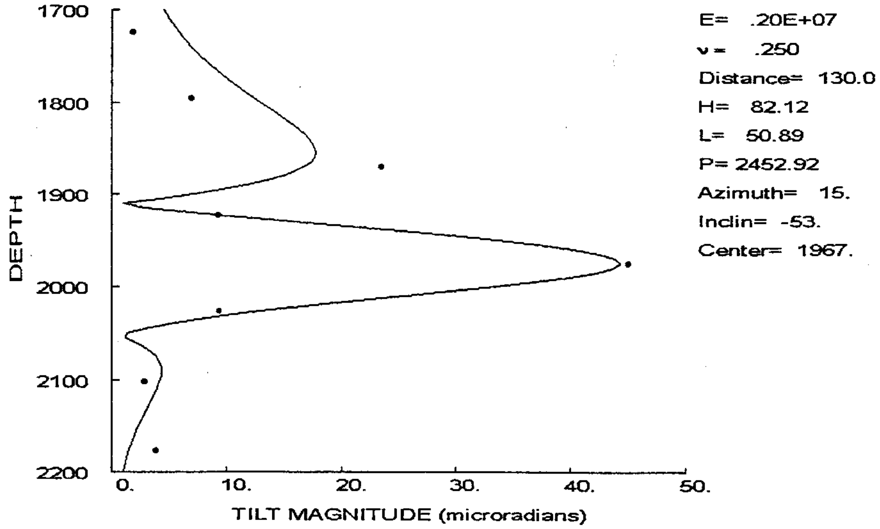

Figure 78. Inversion of Atoka injection #1 with azimuth constraint.

Constraining both azimuth and dip, the inversion yields the results shown in Figure 79. The match is not very good and uncertainties on height, length and pressure are all unbounded.

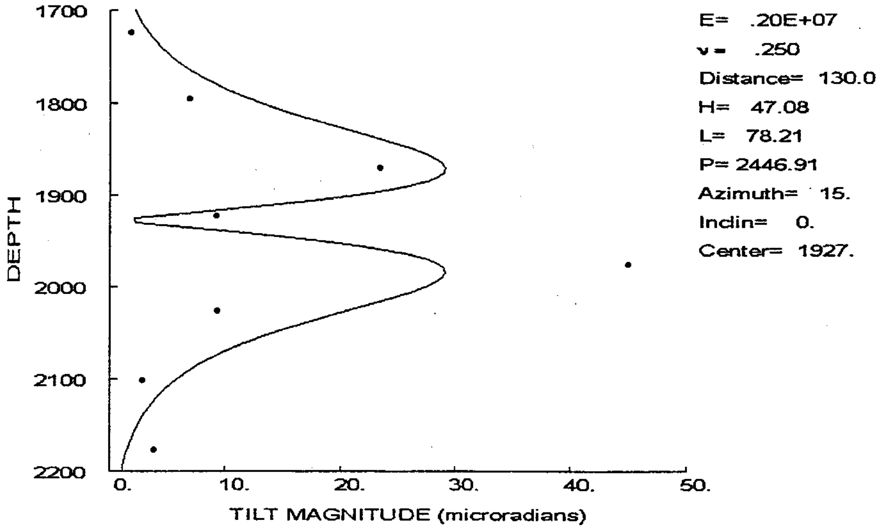

Figure 79. Inversion of Atoka injection #1 with azimuth and dip constraints.

The final inversion of this injection, using pressure, azimuth and dip constraints, is shown in Figure 80. The center at 1925 ft has an uncertainty of ±23 ft, but height and length are both unbounded because of the poor fit of the model to the data. Like the Wilcox data, these results show that the additional constraints are absolutely necessary for a correct interpretation of the tiltmeter results. This relatively poor fit is only chosen because the azimuth, dip and pressure are known and are prescribed. Otherwise, the much better fits of Figures 76 and 77 would have been chosen, yielding incorrect azimuths and uncertain lengths and heights.

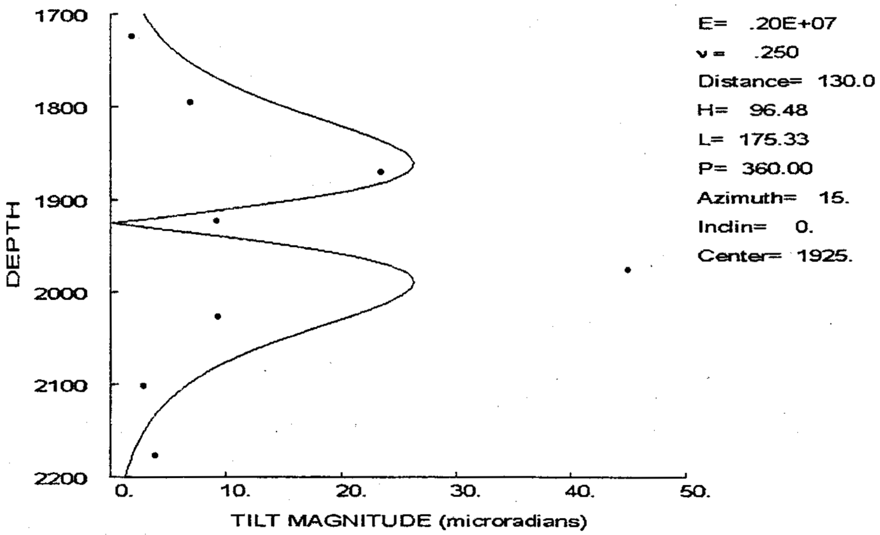

Figure 80. Inversion of Atoka injection #1 with pressure, azimuth and dip constraints.

Finally, if some small amount of fracture inclination is allowed to try and match the asymmetric peaks, then the results shown in Figure 81 can be obtained. In this case, the inclination of the fracture was constrained to a maximum absolute value of 15° and the results do show some asymmetry that makes the match look better. However, the actual values of height and length change little (96 ft to 102 ft for height, 175 ft to 171 ft for length), so there is only a small effect on the fracture dimensions. Based upon the core results and the surface tiltmeter data, it is unlikely that fracture inclination were greater than 10°, so any effect of small dip will be ignored for the rest of the Atoka cases.

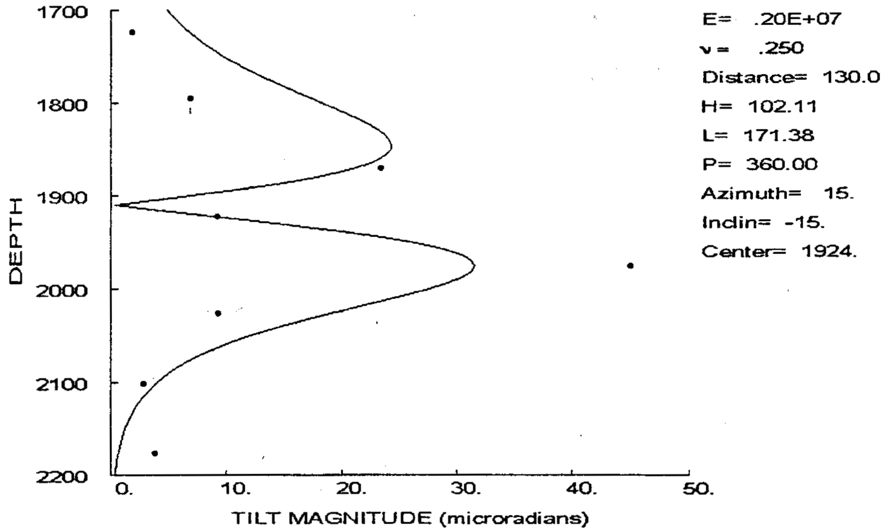

Figure 81. Inversion of Atoka injection #1 with pressure & azimuth constraints and dip limits.

For the second Atoka injection, the inversion results with pressure, azimuth and dip constraints are shown in Figure 82. The length and height values look very reasonable, but the uncertainties are unbounded because of the large misfit of the model to the data. The center at 1912 ft has a standard error of ± 21 ft.

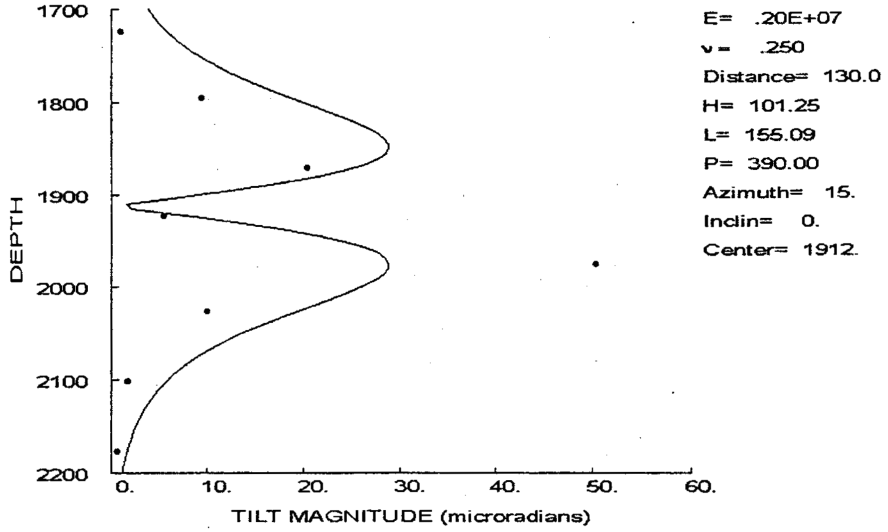

Figure 82. Inversion of Atoka injection #2 with pressure, azimuth and dip constraints.

The constrained results for the third Atoka injection are shown in Figure 83. As with the previous Atoka tests, the poor fit of the data results in unbounded length and height standard errors, even though the 86 ft height and 160 ft length are very reasonable values. The center at 1934 ft has a standard error of ± 22 ft.

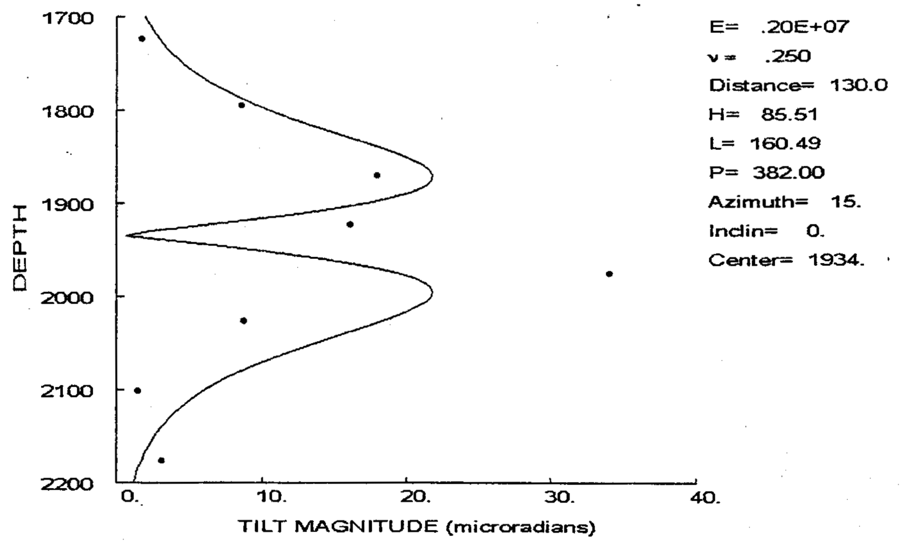

Figure 83. Inversion of Atoka injection #3 with pressure, azimuth and dip constraints.

The data for injection number 4 are very similar to those of the previous injections and the inversion results are likewise similar. The height of 93 ft and length of 157 ft have unbounded standard errors and the center of 1923 has a ±23 ft standard error.

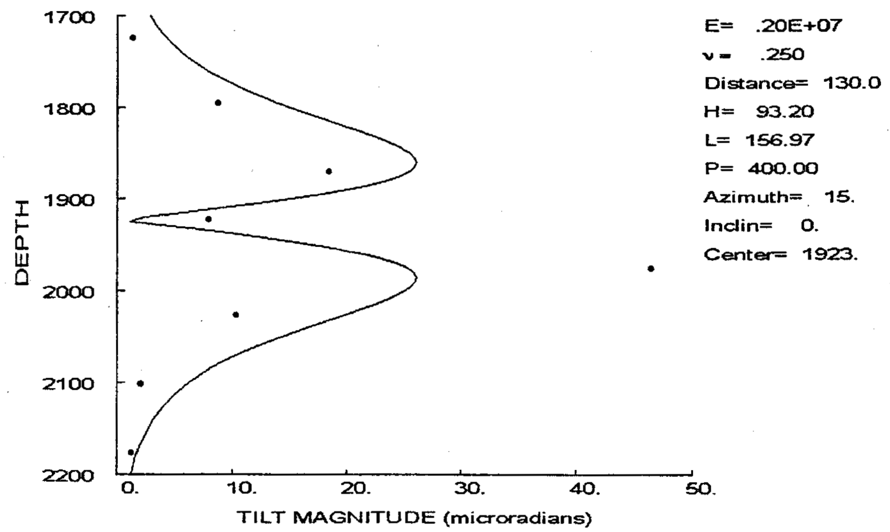

Figure 84. Inversion of Atoka injection #4 with pressure, azimuth and dip constraints.

Atoka injection #5 has similar results, as shown in Figure 85. The height of 101 ft and length of 173 ft have unbounded standard errors and the center at 1914 ft has a standard error of 17 ft.

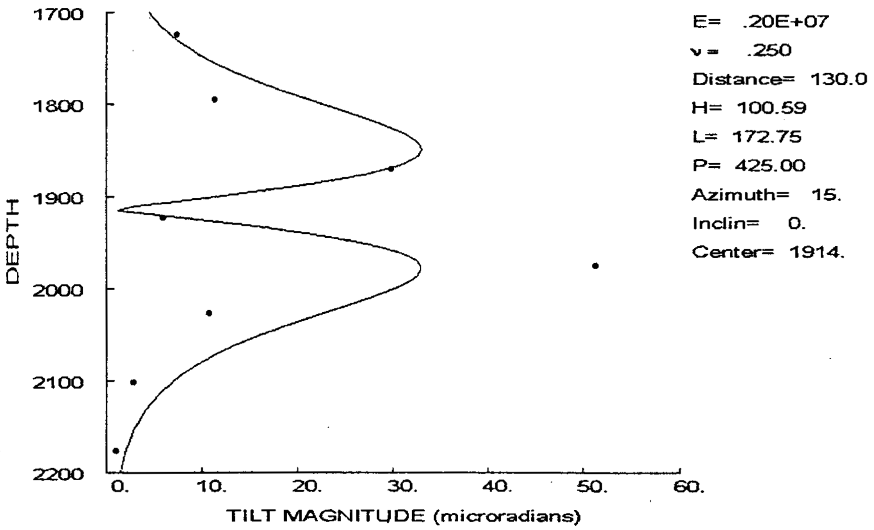

Figure 85. Inversion of Atoka injection #5 with pressure, azimuth and dip constraints.

Atoka injection #6 had the largest asymmetry of all of the tests in this interval. Figure 86 shows that the inversion model is able to quite adequately fit the data with no constraints with quite reasonable parameters and small standard errors, including a height of 200 ft (± 74 ft), a length of 144 ft (±31 ft), a center of 1934 ft (±5 ft), a dip of -17° (±8), and a pressure of 161 psi (± 87 psi). Unfortunately, the azimuth of 69° (±11°) is clearly wrong based on the coring results.

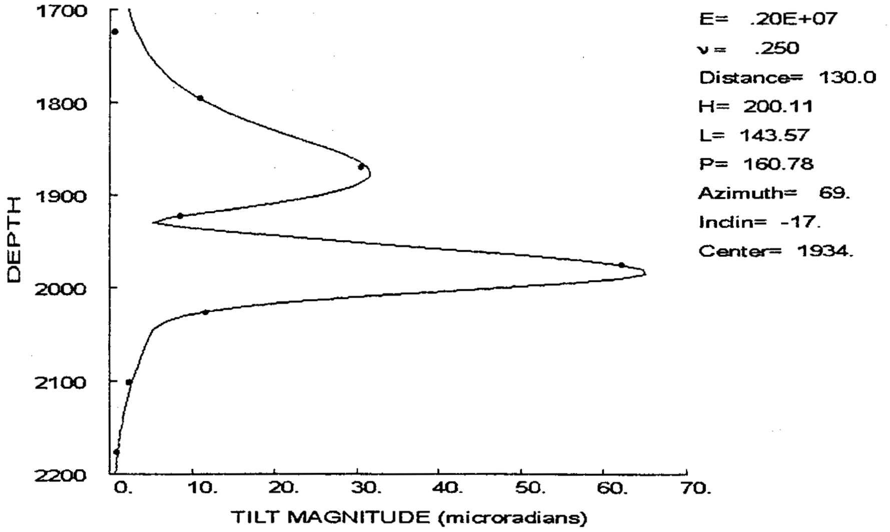

Figure 86. Inversion of Atoka injection #6 with no constraints.

The constrained inversion results for this same injection are shown in Figure 87. In this case the residuals are very large and standard errors are unbounded. The 95 ft height and 179 ft length are reasonable values, but there is no confidence in their accuracy. The center at 1934 ft has a standard error of 27 ft.

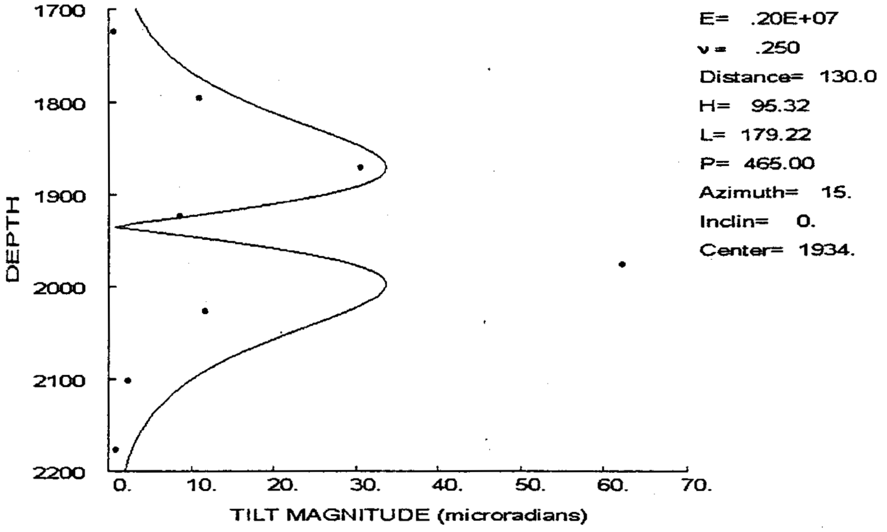

Figure 87. Inversion of Atoka injection #6 with pressure, azimuth and dip constraints.

The constrained inversion results for injections 7-16 are all very similar and are shown in Figures 88-97. These injections all have similar lengths and heights and have unbounded standard errors for these two parameters. The centers consistently remain near the perforated interval for all these inversions.

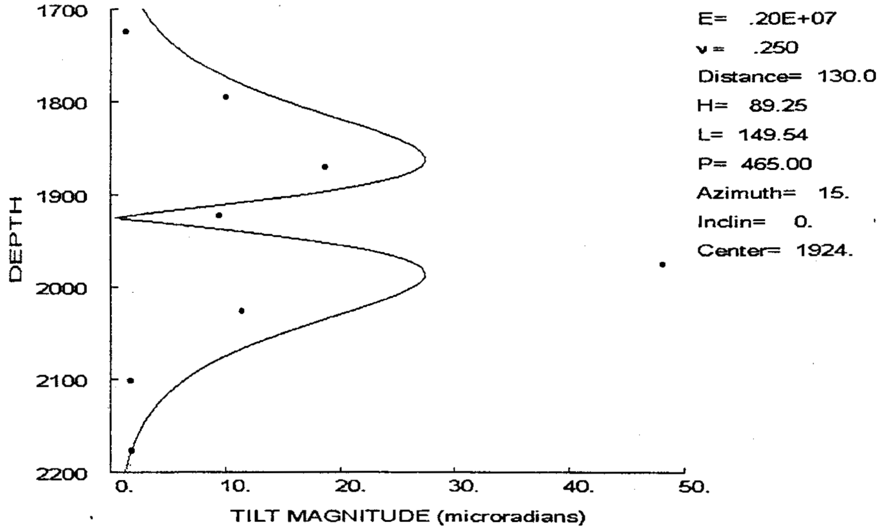

Figure 88. Inversion of Atoka injection #7 with pressure, azimuth and dip constraints.

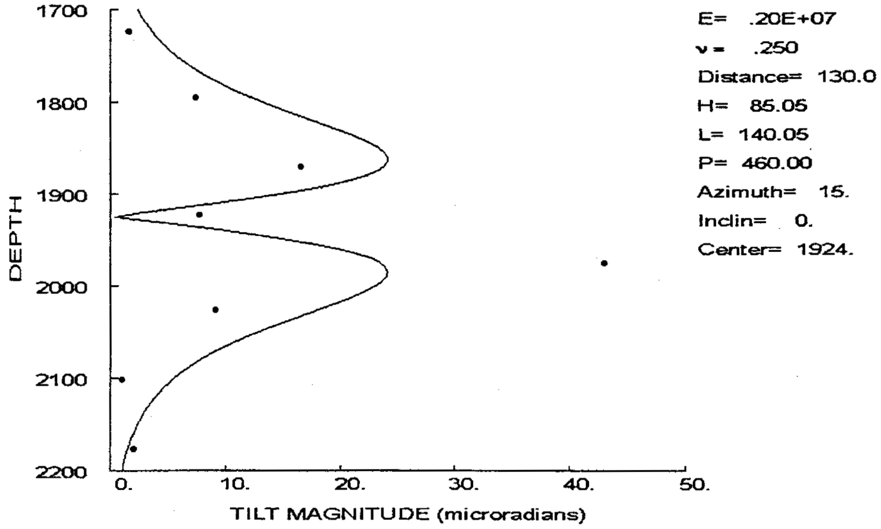

Figure 89. Inversion of Atoka injection #8 with pressure, azimuth and dip constraints.

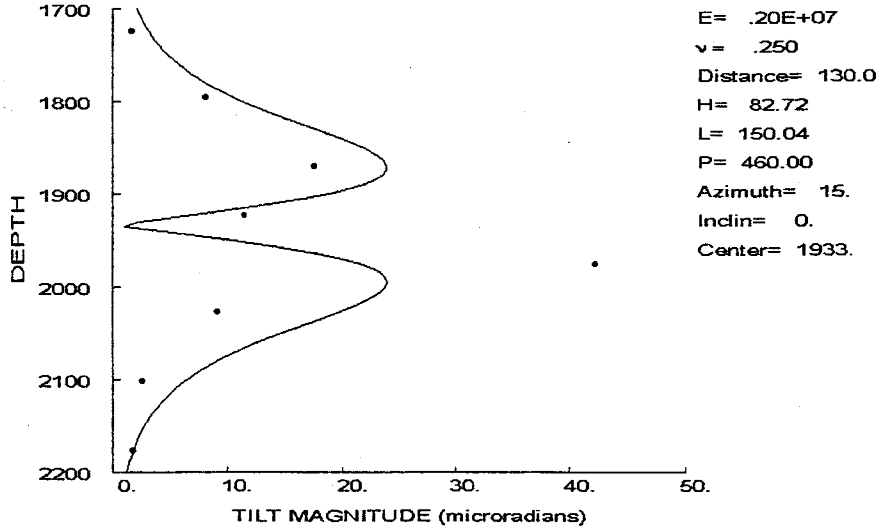

Figure 90. Inversion of Atoka injection #9 with pressure, azimuth and dip constraints.

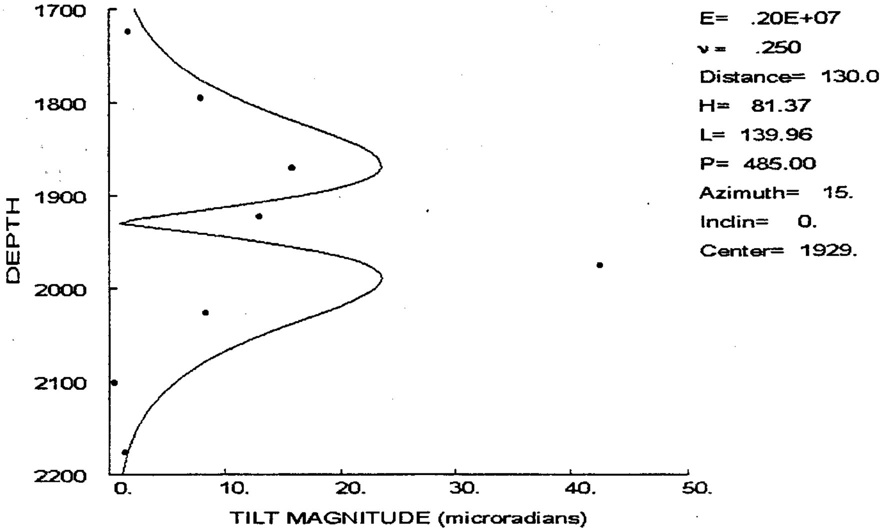

Figure 91. Inversion of Atoka injection #10 with pressure, azimuth and dip constraints.

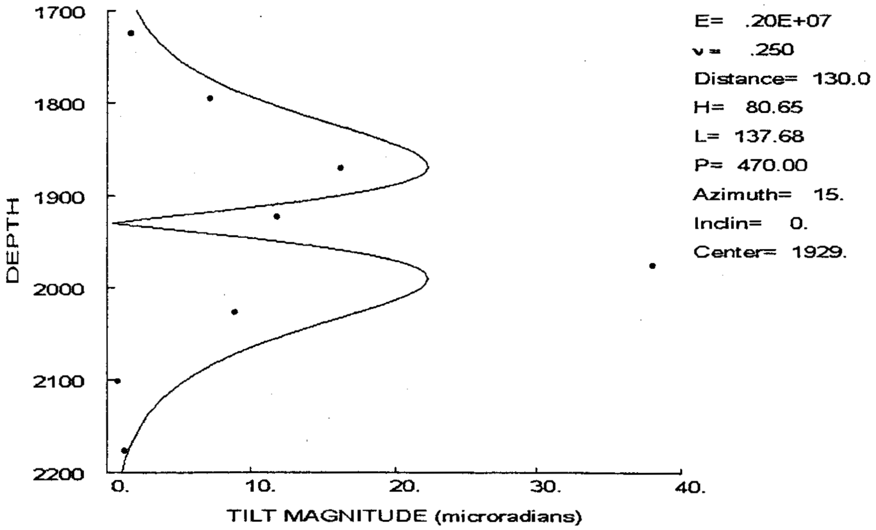

Figure 92. Inversion of Atoka injection #11 with pressure, azimuth and dip constraints.

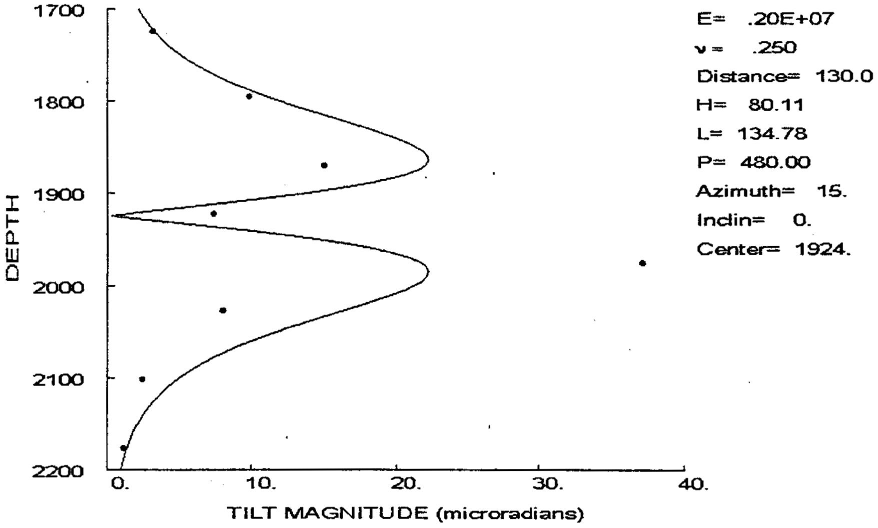

Figure 93. Inversion of Atoka injection #12 with pressure, azimuth and dip constraints.

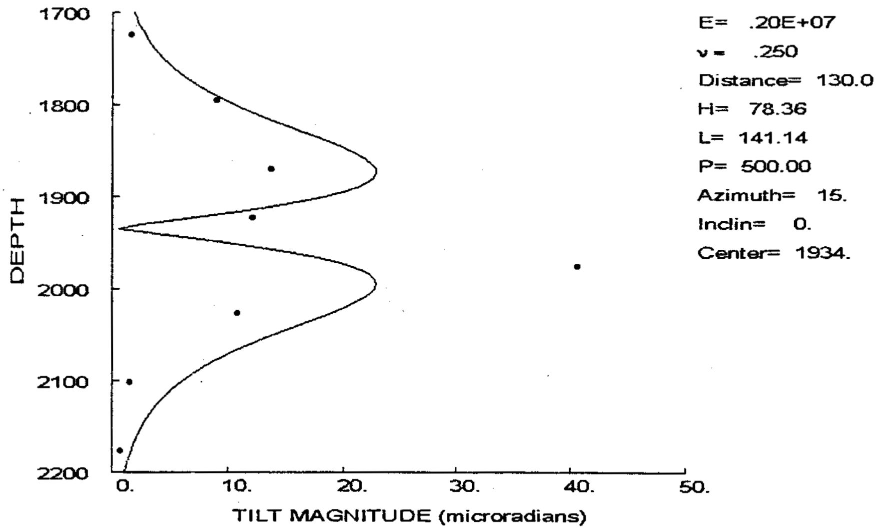

Figure 94. Inversion of Atoka injection #13 with pressure, azimuth and dip constraints.

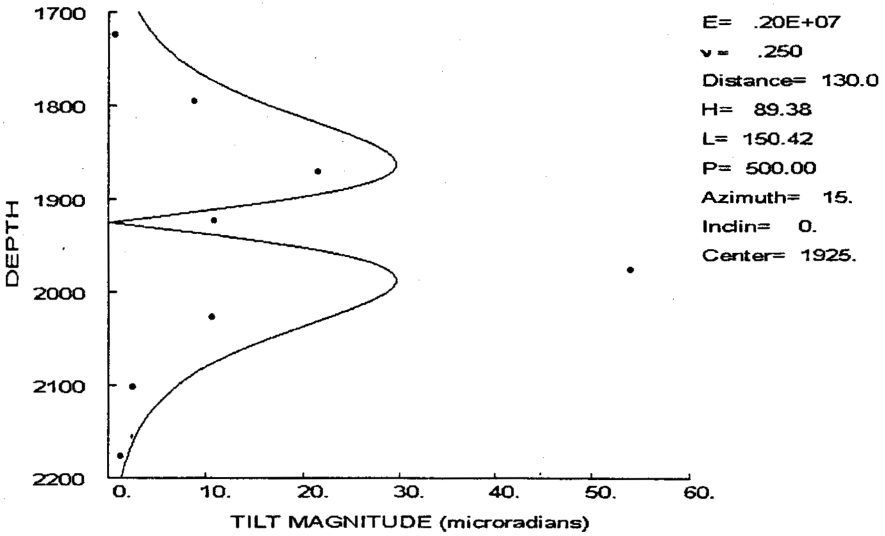

Figure 95. Inversion of Atoka injection #14 with pressure, azimuth and dip constraints.

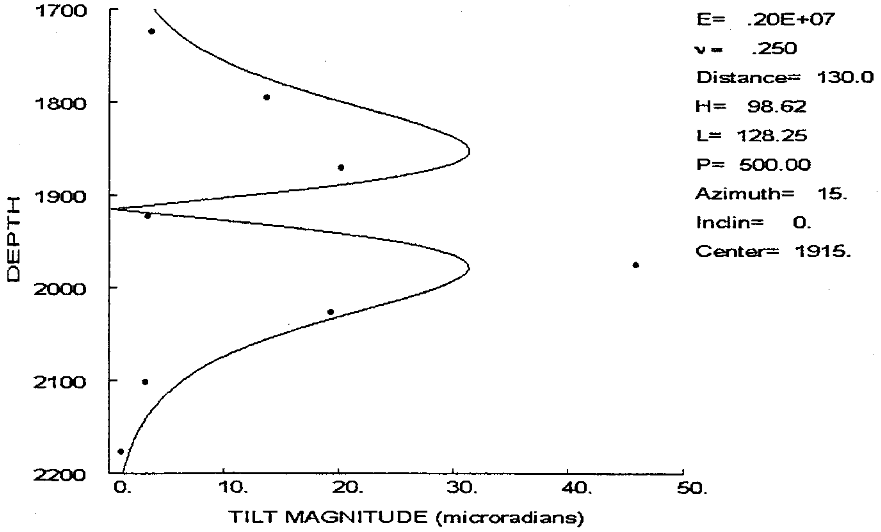

Figure 96. Inversion of Atoka injection #15 with pressure, azimuth and dip constraints.

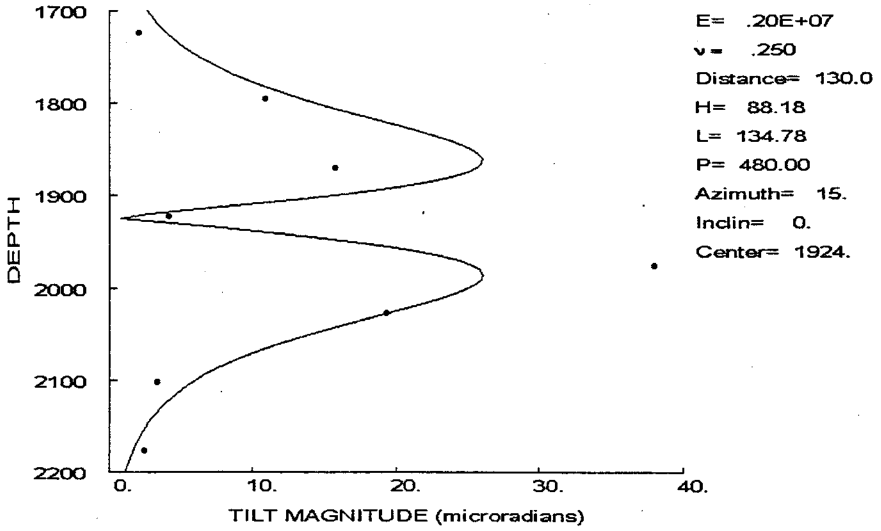

Figure 97. Inversion of Atoka injection #16 with pressure, azimuth and dip constraints.

At Atoka injection #17 the tilt profile becomes more symmetric and the inversion fit begins to look very reasonable, as shown in Figure 98. In this case, the fracture height of 69 ft has a standard error of only 32 ft, although the length is unbounded and wants to be as large as possible. As with the Wilcox results, lengths greater than about 400 ft are essentially indistinguishable from the large lengths found in the inversion. The center at 1926 ft has a standard error of 10 ft.

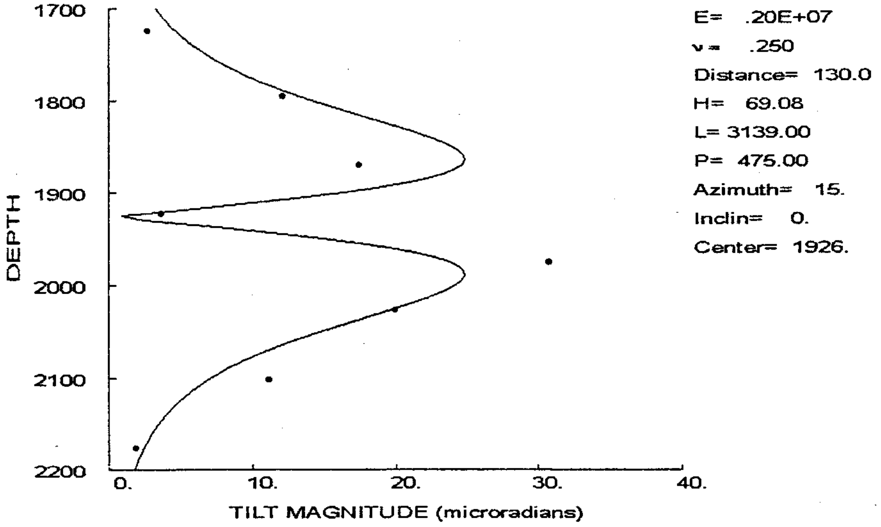

Figure 98. Inversion of Atoka injection #17 with pressure, azimuth and dip constraints.

Atoka injection #18 has become nearly symmetric and is fit relatively well by the model. It requires a 62 ft high fracture (± 23 ft) and a long fracture length, with the center at 1940 ft (± 9 ft). This case is a very adequate inversion of the data and suggests that the fracture is remaining near the perforated interval even as its length extends far into the formation.

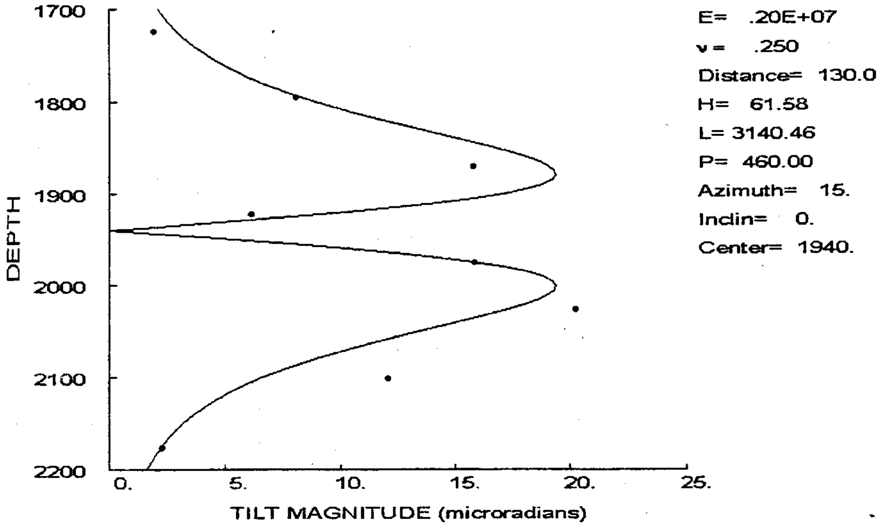

Figure 99. Inversion of Atoka injection #18 with pressure, azimuth and dip constraints.

The inversion results for injection #19 and #20 are very similar to those of injection #18, giving heights of 60 ft (± 30-33 ft), a long fracture length, and centers at 1944 ft (± 12 ft) and 1954 ft (± 14 ft), respectively. These inversions are shown in Figures 100 and 101.

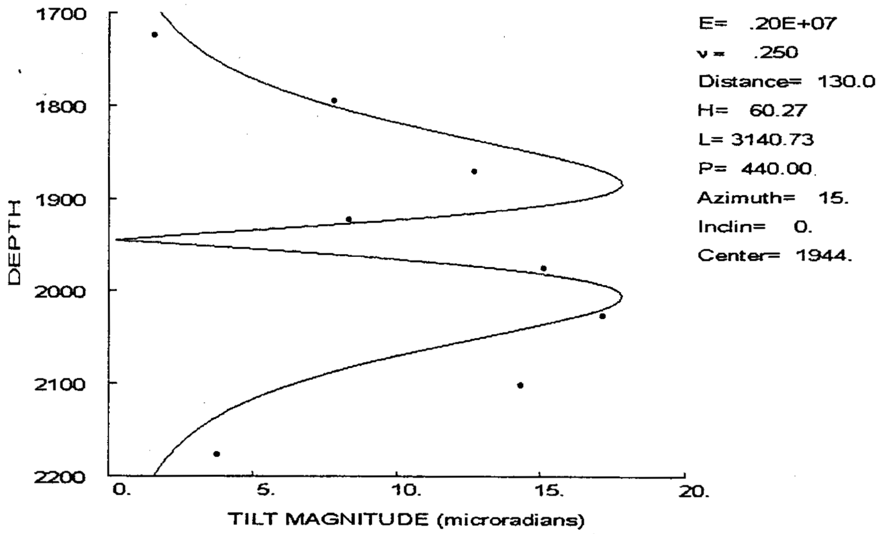

Figure 100. Inversion of Atoka injection #19 with pressure, azimuth and dip constraints.

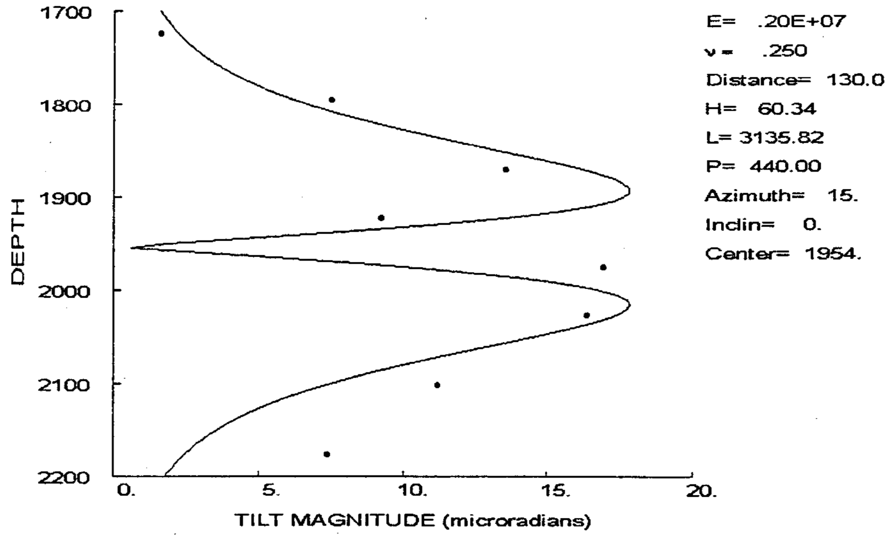

Figure 101. Inversion of Atoka injection #20 with pressure, azimuth and dip constraints.

The Atoka inversions are similar to the Wilcox results in that the asymmetry of the data cannot be readily fit by a fracture with minimal dip, as was determined in the coring process. As a consequence, the standard errors for these inversions are large and the accuracy of the numbers is a question. There is considerable consistency to the results, however, with the height varying between 78 and 101 ft in the first sixteen injections and between 60 and 69 ft in the last four. The lengths are between 128 and 179 ft for the first sixteen injections and are large for the last four. The centers of the fractures are mostly within the perforated intervals, although a few migrate outside this zone by as much as 15 ft.

Because there was very limited microseismic activity during the Atoka injections, it is not possible to do a test-by-test comparison of the microseisms and the tiltmeter results, as was done in the Wilcox sandstone. However, a day-by-day comparison of the results has enough microseisms to provide useful information. Figure 102 shows the comparison for the first day of testing. Both of the imaging technologies indicate that the fracturing is mostly around the perforated interval (1920-1940 ft), but there are only microseisms on one side of the well. The lack of microseisms on the other side is probably due to the extremely low energy of the microseisms and the greater distance from the monitor receivers to the west wing of the fractures, making it very difficult to detect those microseisms. The microseisms on the east wing of the disposal domain suggest that the fracture is somewhat longer and extends deeper than the tiltmeters indicate, but the difference is not significant.

Similar plots for the second-day and third-day microseisms are shown in Figures 103 and 104. On the second day, the microseismic results suggest that the fractures are much longer than indicated by the tiltmeters, at least on the east wing, but both technologies suggest that the height is quite limited. The third day, when there were more microseisms due to the increased energy of larger volume injections, the major discrepancy is in height. The tiltmeter inversions indicate that the fractures are still very limited, but the microseisms show downward growth of about 200 ft.

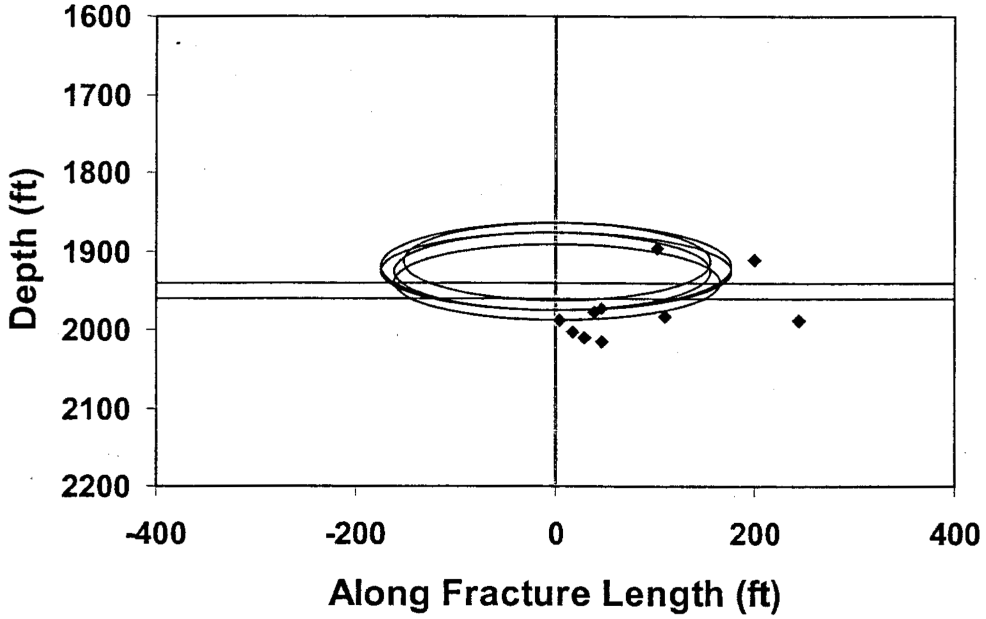

Figure 102. Comparison of first-day microseisms with tiltmeter inversion ellipses.

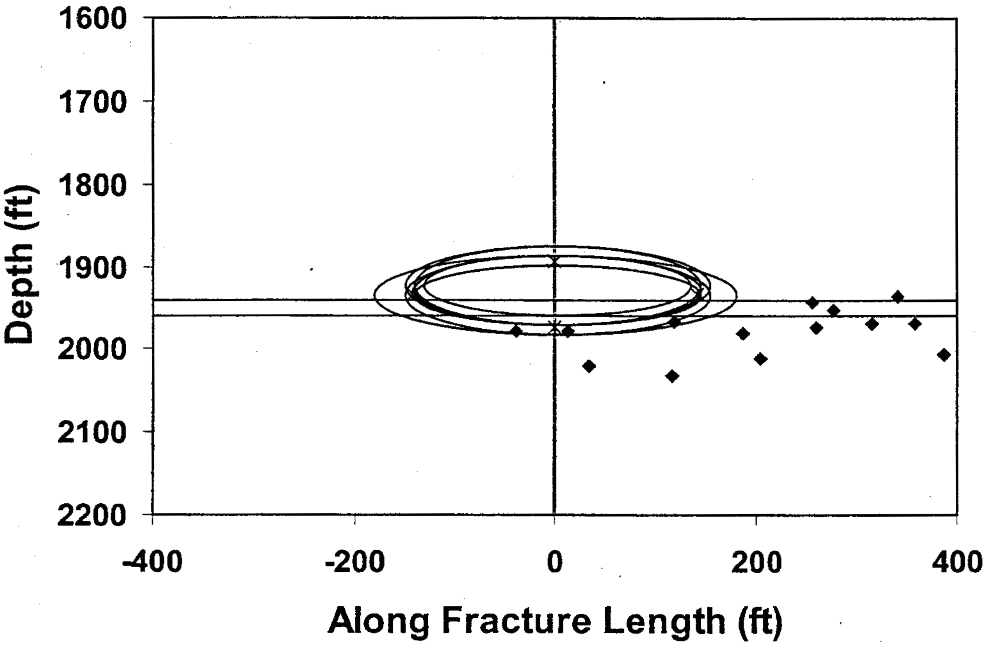

Figure 103. Comparison of second-day microseisms with tiltmeter inversion ellipses.

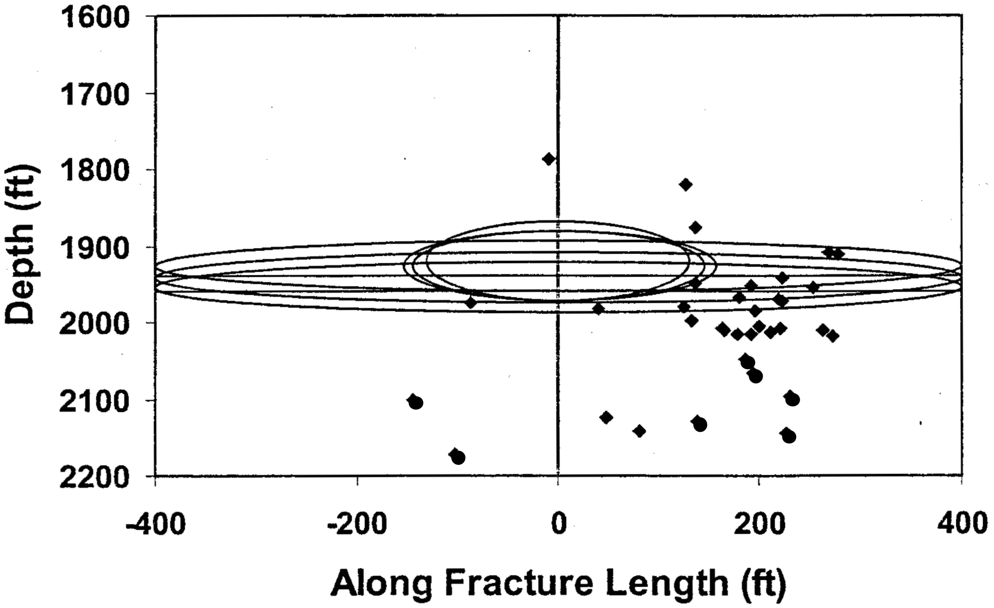

Figure 104. Comparison of third-day microseisms with tiltmeter inversion ellipses.

ASSESSMENT OF THE LACK OF FIT

As noted in the results section for both intervals, the downhole-tiltmeter data can usually be fit quite accurately, but only with parameters that do not agree with other reliable diagnostic data (such as the azimuth and dip from the core throughs). When the inversions are constrained with these known parameters, as well as with the pressure, then the fits are not as good, the residuals are relatively large, and the standard errors of the inversion are large. The two major problems are the asymmetry of the peak amplitudes in the data, which can only be modeled with some degree of fracture dip, and the relatively narrow depth interval over which the tilt amplitudes are large, which suggests that the fracture is very close (thus, the wrong azimuth).

Of course, the most obvious source of the discrepancy is the heterogeneous nature of the earth, particularly the large variations in modulus that can occur in adjacent layers. In the Wilcox zone, the variations in Young's modulus may have been as much as 4:1, a very significant amount. On the other hand, there were no large variations in material properties in the Atoka interval on a scale that would likely affect the tiltmeter inversion. The Atoka shale is a laminated sequence with many shaley, silty and muddy layers that might have considerably different properties, but the thickness of the laminations is at most a few feet and the overall material probably "looks" relatively homogeneous to a large fracture.

A second possible source of errors is due to fracture complexity, which is not accounted for by a simple planar fracture with constant internal pressure. Such complexity, due to offsets, secondary fractures, opening of horizontal bedding layers, and other such effects could produce considerable amplitude variations that would not be accounted for by a simple model.

This section attempts to investigate the effects of some of these parameters using finite element models and other techniques.

Investigation of Layering Effects in the Wilcox Sandstone Interval

To investigate the effects of layering, a large number of finite element calculations (using the code JAC2D[32]) were performed to attempt to match the Wilcox downhole-tiltmeter data. JAC2D is a finite element analysis program that is used for solving large deformation, temperature-dependent quasi-static mechanics problems in two dimensions. A nonlinear conjugate gradient technique is used to solve the governing nonlinear equations.

JAC2D is written in modular form allowing the use of any one of seven continuum material models presently developed to be incorporated within the analysis. When combined with these and other ancillary capabilities, this program allows for the solution to linear or nonlinear problems that involve time-dependent and/or time-constant loads, kinematic boundary constraints, element birth and death, thermal history and fixed and/or sliding contacting surfaces. In this application, a linear elastic material model with constant boundary conditions was used for all cases.

The rock mechanical properties were obtained in some intervals from two different organizations and at different times during the study. Unfortunately, at times there were discrepancies between property data from different tests. An attempt was made to try both sets of data and select the data that provided the best fit to the data. Nevertheless, some questions remain about the adequacy of the values used here. The plan was to use a 2D finite-element model first and then to finalize the results with a 3D finite element model. However, the lack of agreement with the 2D model was discouraging and no attempt was made to use the 3D capabilities.

The 2D cases were run using a grid of 1200 ft height and 1000 ft width with fracture height varying depending on the case run. Numerous calculations with different parameters and conditions were run, of which 29 particularly useful ones are listed in Table 3. Different grid models were employed in these cases and various fracture intervals and numbers of intervals were also used. Part way through the analysis, other rock property data became available and these data were used in several calculations.

Case #	Fracture Zone	Fracture Depth (ft)	Pressure (psi)	Modulus (10^6 psi)	Model #	Miscellaneous
1	2 - Wilcox	2706 - 2775	500	3.500	1	
2	2 - Wilcox	2706 - 2775	500	7.122	1	
3	2 - Wilcox	2706 - 2775	100	7.122	1	
4	2 - Wilcox	2706 - 2775	300	7.122	1	
5	2 - Wilcox	2706 - 2775	300	7.122	1	
	5	2618 - 2650	200	2.000		
6	2 - Wilcox	2706 - 2775	500	7.122	1	
	3	2682 - 2706	800	5.000		
	4	2650 - 2682	200	5.445		
7	2 - Wilcox	2706 - 2775	300	7.122	1	
	3	2682 - 2706	600	5.000		
	4	2650 - 2682	200	5.445		
8	2 – Wilcox	2706 - 2775	300	7.122	2	
	5	2618 – 2650	300	2.000		
	6	2600 – 2618	300	2.000		
9	2 - Wilcox	2706 – 2775	300	7.122	2	Zone 5,6 Stress Inc to 1800
	7	2550 – 2600	300	2.000		Zone 7 Stress Dec to 1500
10	2 - Wilcox	2706 – 2775	300	7.122	2	Zone 5,6 Stress Inc to 1800
	8	2500 – 2550	300	2.000		Zone 8 Stress Dec to 1500
11	2 - Wilcox	2706 – 2775	200	7.122	2	Zone 5,6 Stress Inc to 1800
	8	2500 – 2550	400	2.000		Zone 2 Stress Inc to 1700
						Zone 8 Stress Dec to 1500
12	2 - Wilcox	2706 – 2775	300	7.122	2	Zone 5,6 Stress Inc to 1800
	8	2500 – 2550	400	2.000		Zone 2 Stress Dec to 1600
						Zone 8 Stress Dec to 1500
13	2 - Wilcox	2706 – 2775	300	7.122	2	Zone 5,6 Stress Inc to 1800
	8	2500 – 2550	400	1.000		Zone 2 Stress Dec to 1600
						Zone 8 Stress Dec to 1500
14	2 - Wilcox	2706 – 2775	300	7.122	2	Zone 5,6 Stress Inc to 1800
	8	2500 – 2550	300	2.000		Zone 8 Stress Dec to 1500
						Zone 5 Mod Inc to 4.0E+06
15	2 – Wilcox	2706 – 2775	300	7.122	2	Zone 5,6 Stress Inc to 1800
	8	2500 – 2550	300	2.000		Zone 8 Stress Dec to 1500
						Zone 5 Mod Inc to 4.0 E+06
						Zone 9 Mod Inc to 4.0 E+06
16	2 – Wilcox	2706 – 2775	300	7.122	2	Zone 5,6 Stress Inc to 1800
	8	2500 – 2550	300	2.000		Zone 8 Stress Dec to 1500
						Zone 5 Mod Inc to 4.0 E+06
						Zone 10 Mod Inc to 4.0 E+06
17	2 - Wilcox	2706 – 2775	300	7.122	2	Zone 5,6 Stress Inc to 1800
	8	2500 – 2550	300	1.000		Zone 2 Stress Inc to 1500
						Zone 8 Stress Dec to 1500
						Zone 5 Mod Inc to 4.0 E+06
						Zone 10 Inc to 4.0 E+06
18	2 – Wilcox	2706 – 2775	300	7.122	2	Zone 5,6 Stress Inc to 1800
	8	2500 - 2550	400	1.000		Zone 2 Stress Dec to 1600
						Zone 8 Stress Dec to 1500
						Zone 5 Mod Inc to 4.0 E+06
						Zone 10 Mod Inc to 4.0 E+06

19	2 – Wilcox 8	2706 – 2775 2500 – 2550	300 600	7.122 1.000	2	Zone 5,6 Stress Inc to 1800 Zone 2 Stress Inc to 1800 Zone 8 Stress Dec to 1500 Zone 5 Mod Inc to 4.0 E+06 Zone 10 Mod Inc to 4.0 E+06
20	2 – Wilcox 8	2706 – 2775 2525 – 2575	300 600	7.122 1.000	3	Shift Zone 8 Down 25 ft. Zone 5 Inc. to 4.0 E+06 Zone 10 Inc. to 4.0 E+06
21	2 - Wilcox 8	2706 – 2775 2525 – 2575	300 600	7.122 1.000	3	Shift Zone 8 down 25 ft. Zone 5 Inc. to 6.0 E+06 Zone 10 Inc. to 4.0 E+06
22	2 - Wilcox 7	2706 – 2775 2550 – 2600	300 600	7.122 1.000	2	Zone 5 Inc. to 6.0 E+06 Zone 10 Inc. to 4.0 E+06
23	2 – Wilcox 7	2706 – 2775 2550 – 2600	300 600	7.122 1.000	2	Zone 3 Inc. to 11.741 E+06
24	2 – Wilcox 8	2706 – 2775 2500 – 2550	300 600	7.122 1.000	2	Zone 3 Inc. to 11.741 E+06
25	2 – Wilcox 9	2750 - 2775 2530 - 2550	250 250	7.122 2.000	4	Wilcox split into Zones 2,3 Zone 4 Inc. to 11.741 E+06
26	2 – Wilcox 9	2750 - 2775 2530 - 2550	250 250	7.923 2.000	4	Wilcox split into Zones 2,3 Zone 2,3 Poisson Ratio = 0.182 and Mod Inc as noted. Zone 4 Dec. to 4.984 E+06 Poisson Ratio = 0.394
27	2 – Wilcox 9	2730 - 2775 2530 - 2570	250 250	7.122 2.000	5	Wilcox split into Zones 2,3 Zone 4 Inc. to 11.741 E+06
28	2 – Wilcox 9	2730 - 2775 2530 - 2570	250 250	7.923 2.000	5	Wilcox split into Zones 2,3 Zone 4 Dec. to 4.984 E+06 Poisson Ratio = 0.394 Zone 5 Dec. to 2.000 E+06 Poisson Ratio = 0.26
29	2 – Wilcox 9	2730 - 2775 2530 - 2570	300 300	7.122 2.000	5	Wilcox split into Zones 2,3 Zone 4 Inc. to 11.741 E+06

Figure 105 shows the grid and the layering properties that were intially chosen for use with the model. These properties were based on initial stress information and core data from previous wells at the site. The major question was the value of Young's modulus for the carbonate just above the Wilcox sandstone. Values ranged from 5 x 10^6 psi to 11 x 10^6 psi. However, because it is a relatively thin zone, the effect of the difference was relatively small. In addition, the Wilcox sandstone had some relatively large variations in modulus because of the large number of deformation bands in the bottom half of the zone. The number used is reflective of the harder, lower porosity basal section of the Wilcox.

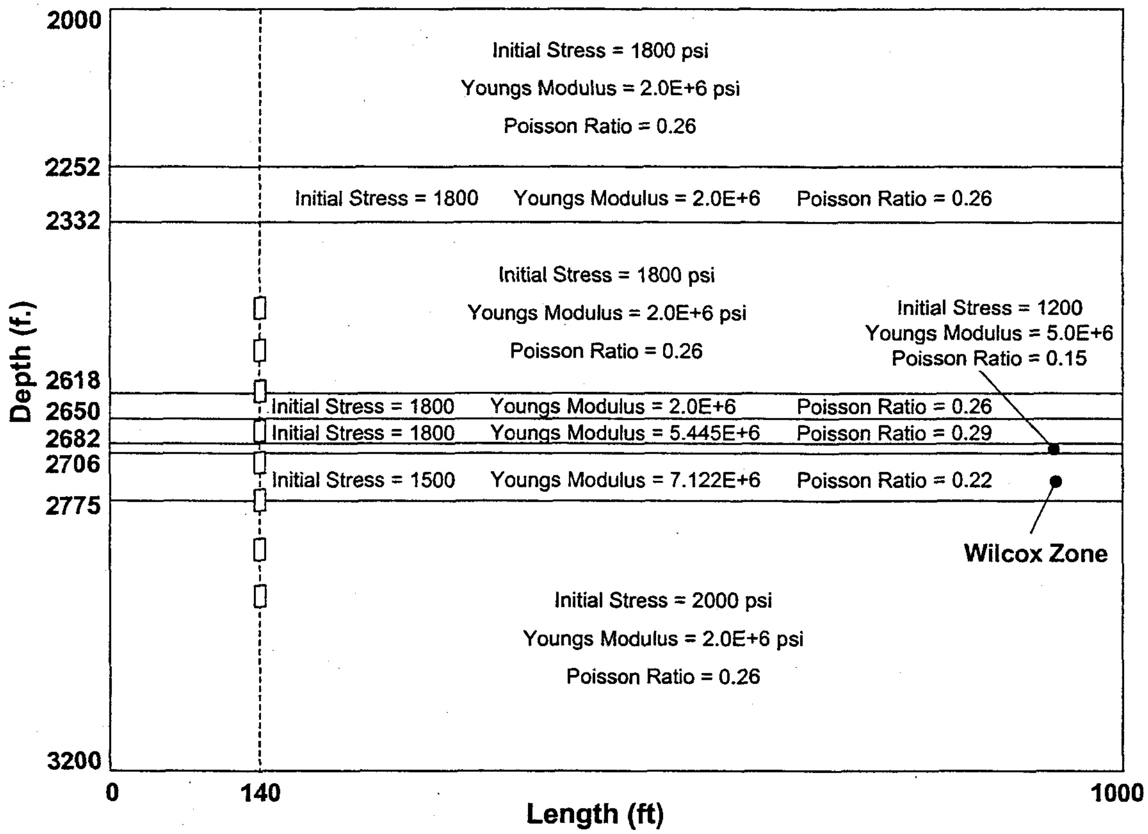

Figure 105. Initial layering and grid for Wilcox finite-element calculations (Model 1).

Figure 106 shows a one of the initial calculations that is typical of the results that were obtained throughout this work. It shows a calculation of a long 2-D fracture (as suggested by the tilt inversion results in this zone) with internal pressures of 100, 300 and 500 psi for comparison. The height of the fracture is 69 ft, the thickness of the Wilcox sandstone in the model. It is compared to three of the stages of testing, with these particular stages chosen for their variety of symmetry and undulations. As can be seen, the 300 psi net-pressure case best matches the amplitude of the measured tilts, as it should since most of the net pressures in the Wilcox interval were in the 250-350 psi range. The layering adds a small degree of asymmetry to the results, but not nearly enough to match the results obtained with the tiltmeters. In addition, it was found that no amount of layering could give the character of the tilt data measured above the Wilcox sandstone, where the tilt amplitudes undulate.

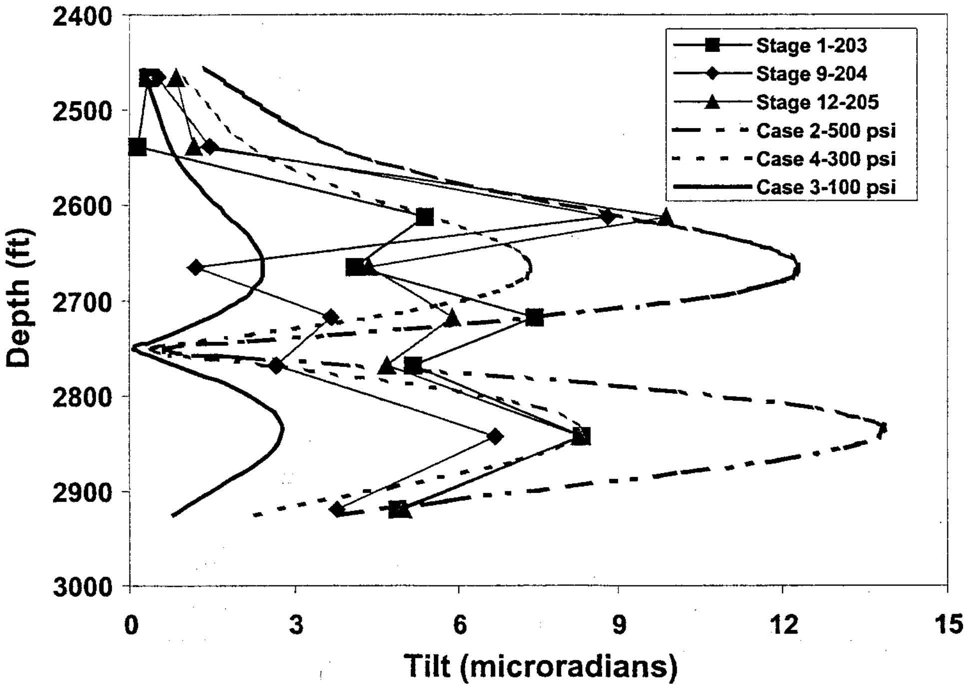

Figure 106. Example calculations using Model 1 with a single 69 ft fracture and various pressures.

In Figure 107, the 300 psi case is compared with three measured data sets with which it best matches. While the amplitudes are relatively close, the upper peak is poorly matched and the center undulations cannot be reproduced. Increasing the fracture height upward serves to raise the peak location, but it also increases the amplitudes too much and results in a complete mismatch in the center.

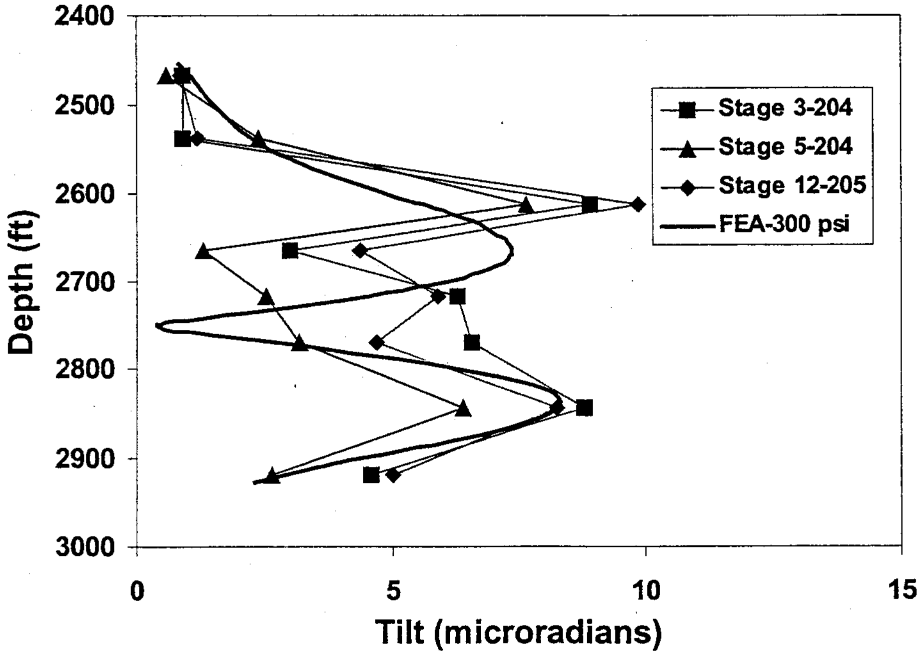

Figure 107. Comparison of 2D finite-element calculations and measured downhole tilt data.

It appeared that the only method available to add more "character" to the calculated tilt response (within the framework of known data, such as minimal fracture dip and measured fracture strike) was to add other fracture intervals that could be pressurized separately or jointly. The model (Model 2) that was constructed for doing this is shown in Figure 108. The region above the Wilcox sandstone was subdivided to provide zones for additional pressurized fractures, in keeping with the microseismic data showing upward fracture growth. Model 2 was used in cases 8-19 of Table 3 for calculations with two or three pressurized intervals.

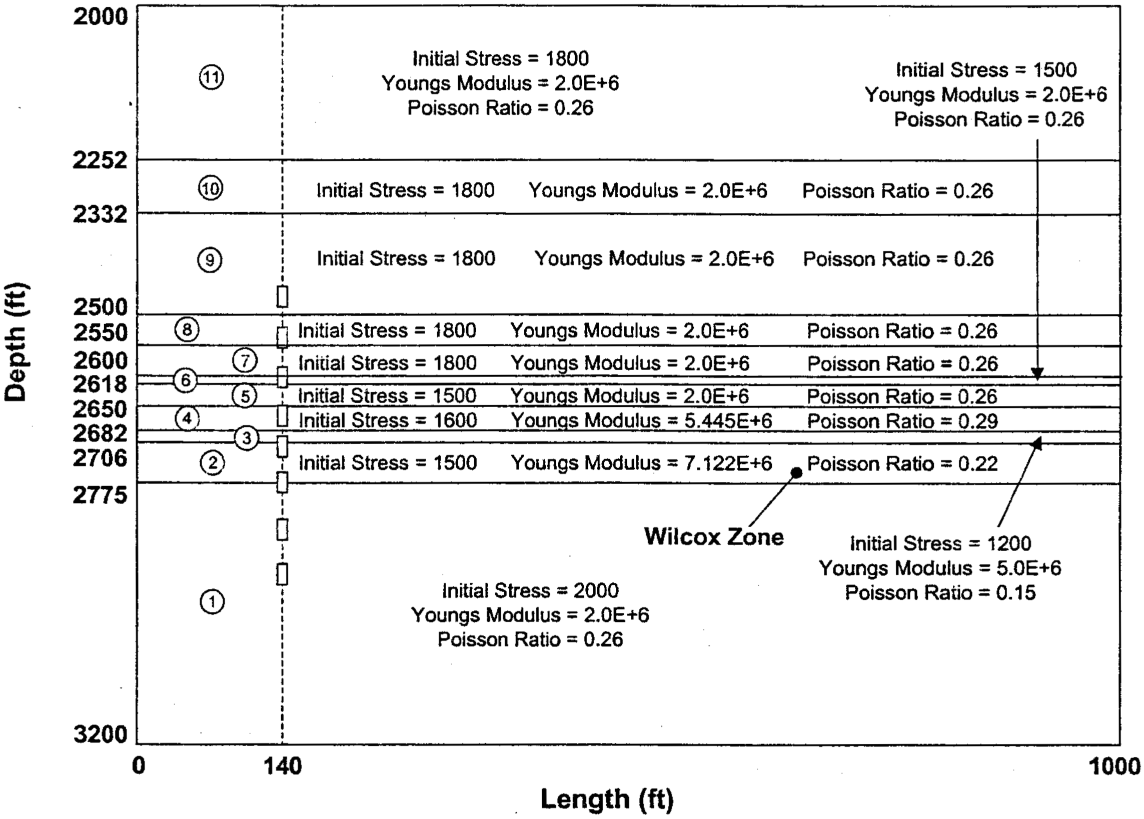

Figure 108. Model 2 layering and grid for Wilcox finite-element calculations.

Figure 109 shows three calculated cases where two fractures were constructed. As given in Table 3, Case 5 is for two fractures (but still using Model 1), one of which is in the Wilcox sandstone (height = 69 ft) and the other is in the shale above the Wilcox sandstone at a depth of 2618-2650 ft (height=32 ft). The additional fracture only affects the upper peak and does not increase the tilt variations in the center of the array. Case 9 is a two-fracture case with the upper fracture placed higher (at 2550-2600 ft) with a 50 ft height while the lower fracture is still in the Wilcox sandstone. In this case, the upper fracture is far enough away from the lower fracture that the undulation in the tilt field in the center region are reproduced, but the upper peak is far too high. Case 10 has the upper fracture at 2500-2550 ft and results in more undulations in the center region but is much too high on the location of the upper peak. Within the scope of reasonable pressures and fracture locations, it was not possible to match the measured Wilcox results with a two fracture system.

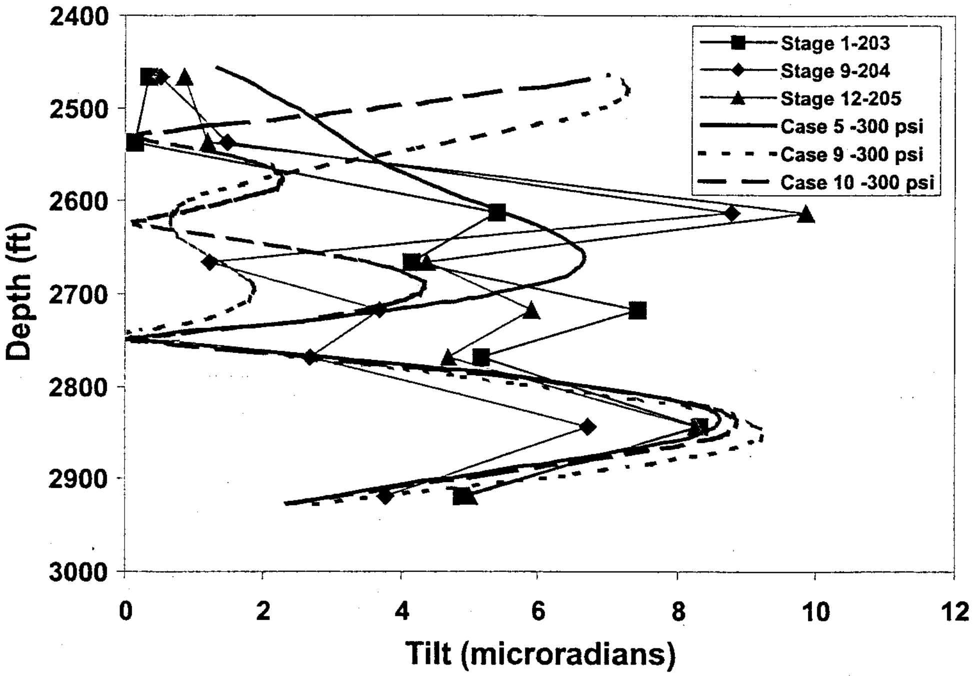

Figure 109. Comparison of two-fracture calculations using Models 1 & 2 with measured tilts.

Cases using additional pressurized intervals (besides the Wilcox sandstone) are shown in Figure 110. Cases 6 and 7 use Model 1 and have a fracture running from the bottom of the Wilcox up to 2650 ft, but they have different levels of pressurization in the three separate regions to try to account for possible changes in stress state. The legend in the figure gives the pressure within the Wilcox sandstone (e.g., net fracture pressure). Both of these cases result in tilts that are much too large. Case 8 has the fracture separated into two intervals, one of which is in the Wilcox sandstone and the other is located from 2600-2650 ft (but it is in two regions, as seen in Table 3 and Figure 108). Pressures for both of these intervals are 300 psi. While the peak amplitudes are much closer, the tilt distribution does not match the measure results.

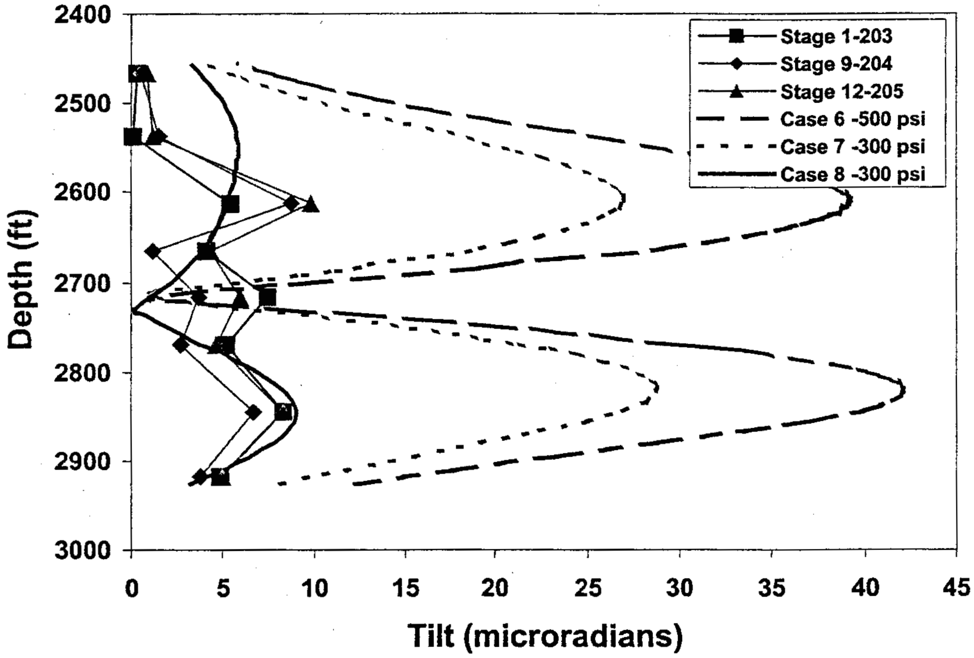

Figure 110. Comparison of multi-zone-fracture calculations using Models 1 & 2 with measured tilts.

Figure 111 shows four calculations using two fractures, one of which is in the Wilcox sandstone and the other is located from 2500-2550 ft. In these cases, the stresses and moduli of the various intervals were changed to determine if uncertainty in these parameters could be responsible for the mismatch with the measured data. As can be seen, the stress and moduli do have a significant effect on the results, but the experimental data still cannot be matched with reasonable parameters. Values for the parameters used in the different cases are shown in the last column of Table 3 and refer to regions of Model 2 (Figure 108).

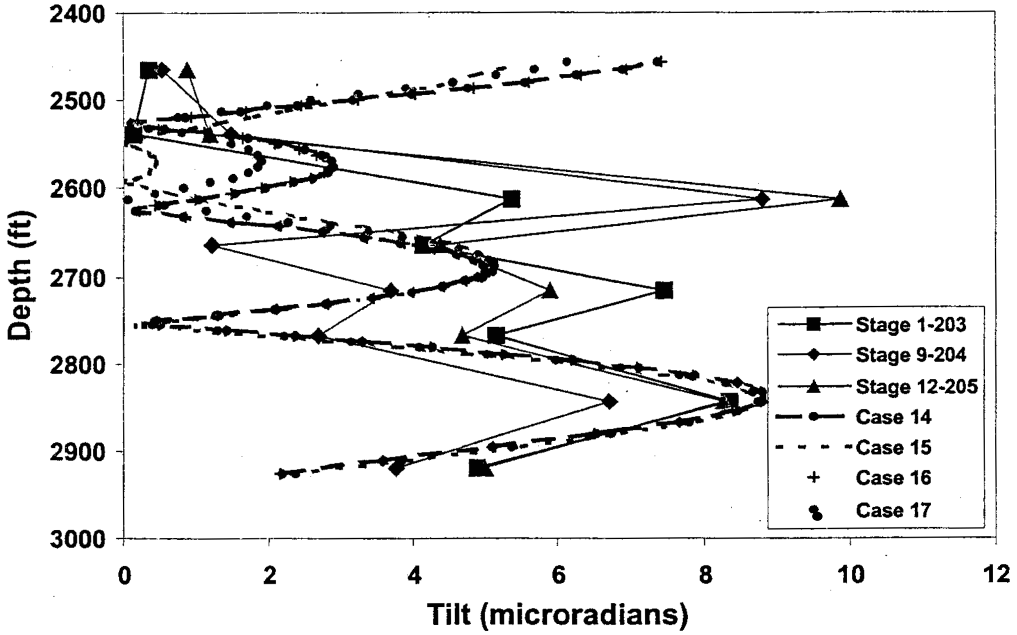

Figure 111. Comparison of various two-fracture calculations (Model 2) with measured tilts.

Using the same fracture intervals as used in the previous figure, the pressure in the upper fracture was altered along with the moduli and stresses to obtain the results shown in Figure 112. Case 18 had an upper fracture pressure of 400 psi while case 19 had 600 psi. Case 19 in particular does a good job of matching the measured tilts, with the exception of the upper point. If the upper tiltmeter were broken, then it could be argued that the large tilts above 2500 ft were not recorded and a two-fracture system with a lower stress in the upper fracture interval would match the data fairly well. However, there is no information that would suggest that the upper tiltmeter is broken.

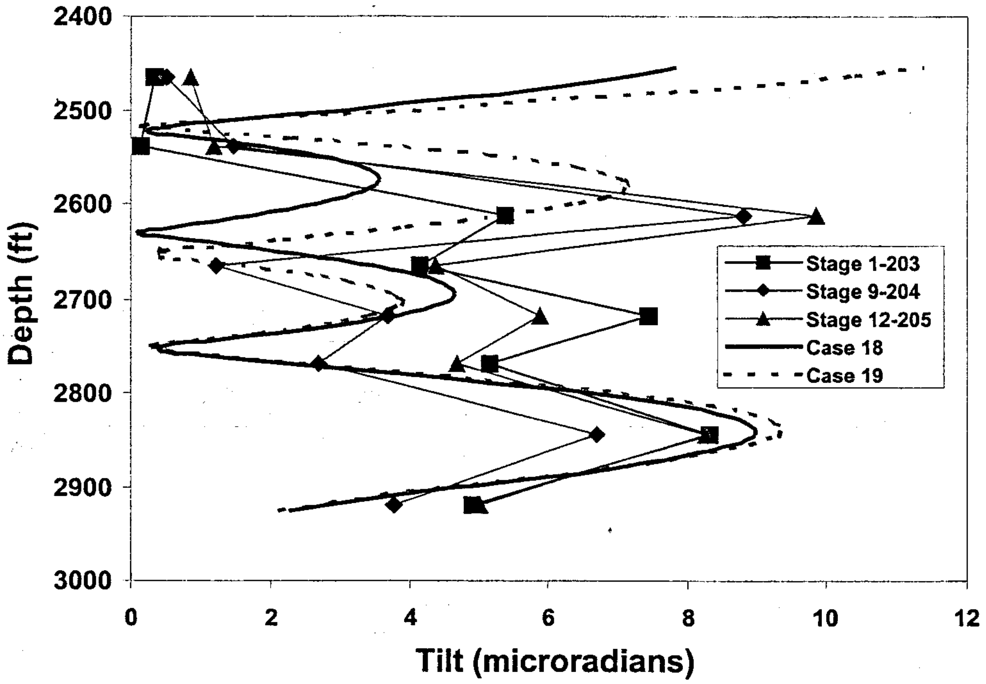

Figure 112. Comparison of variable-pressure, two-fracture calculations (Model 2) with measured tilts.

In order to assess other multiple-zone combinations, Model 3 was constructed with the shale broken into different intervals that could be separately pressurized or have stresses and moduli altered. This model is shown in Figure 113.

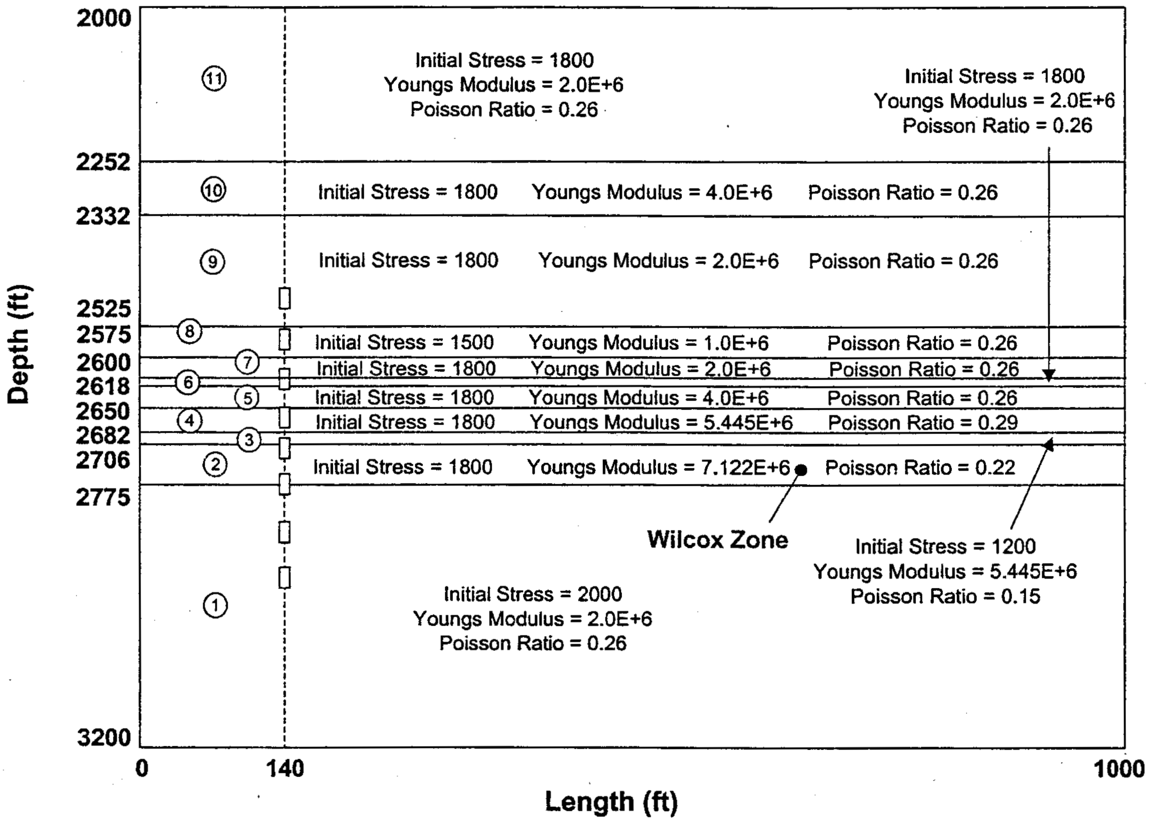

Figure 113. Model 3 layering and grid for Wilcox finite-element calculations.

Figure 114 shows a comparison of three cases using the Model 3 configuration with fractures in the Wilcox sandstone and in an interval from 2525-2575 ft in cases 20 and 21 and from 2550-2600 in case 22. These results show that by moving the upper fracture interval it is possible to reproduce the triple peak configuration, but with the problem of having a large tilt region at the top of the array that was not measured.

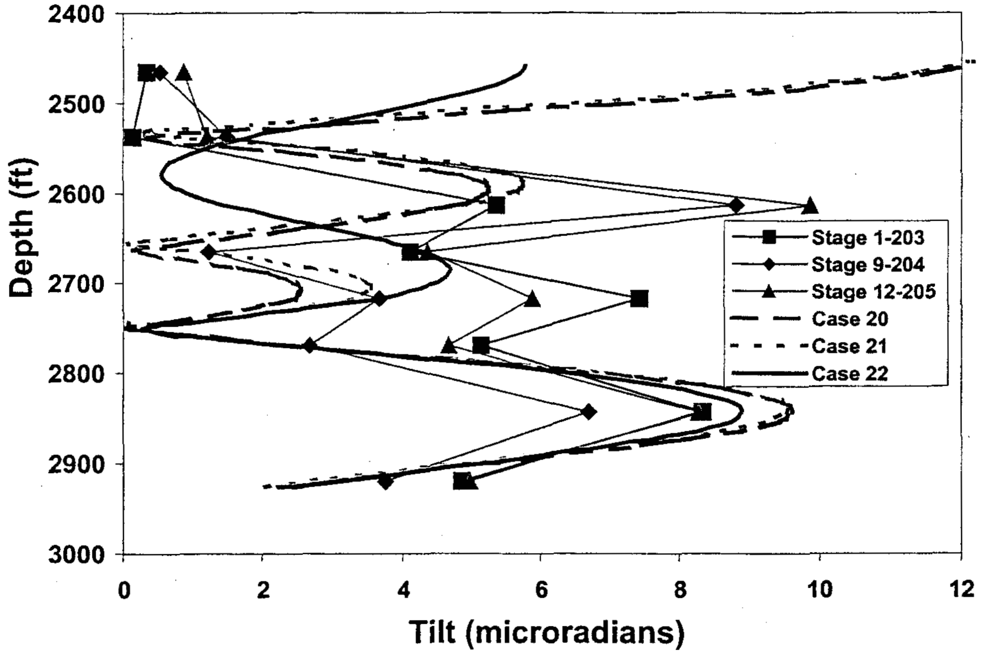

Figure 114. Comparison of various two-fracture calculations (Model 3) with measured tilts.

Finally, two additional models were constructed that had new material property data and that split the Wilcox into upper and lower intervals. These two models (4 and 5) are shown in Figures 115 and 116.

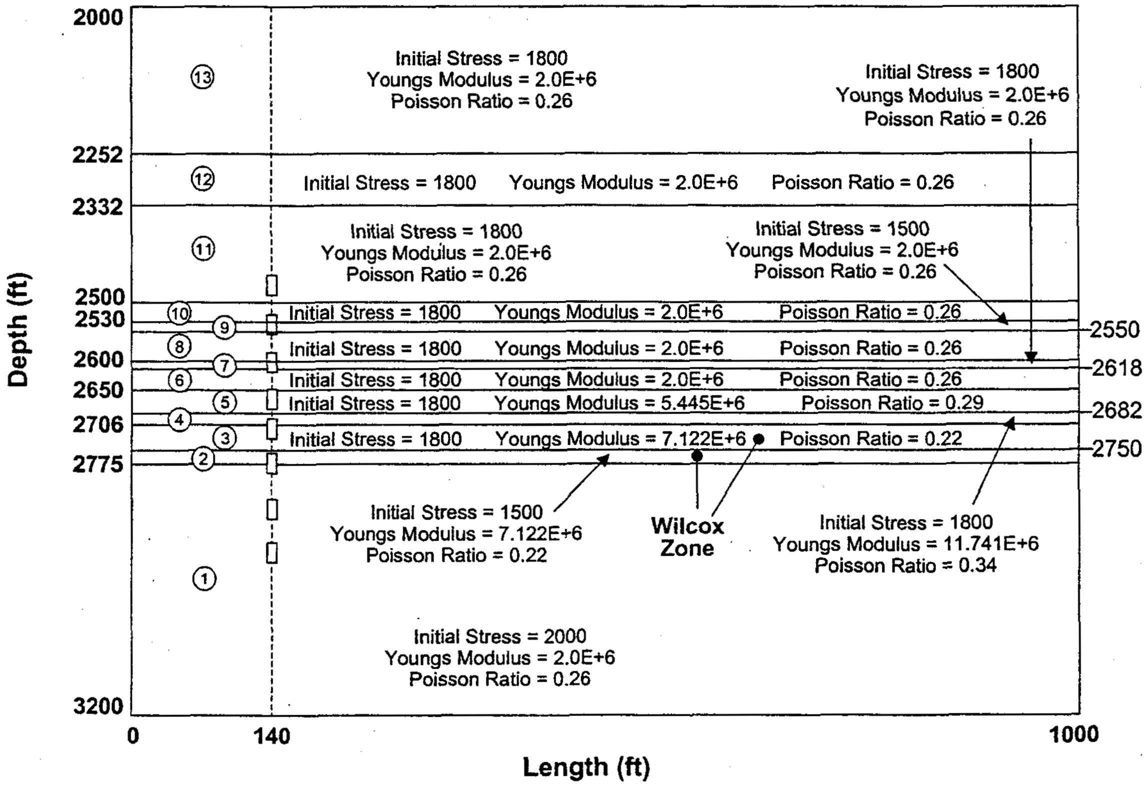

Figure 115. Model 4 layering and grid for Wilcox finite-element calculations.

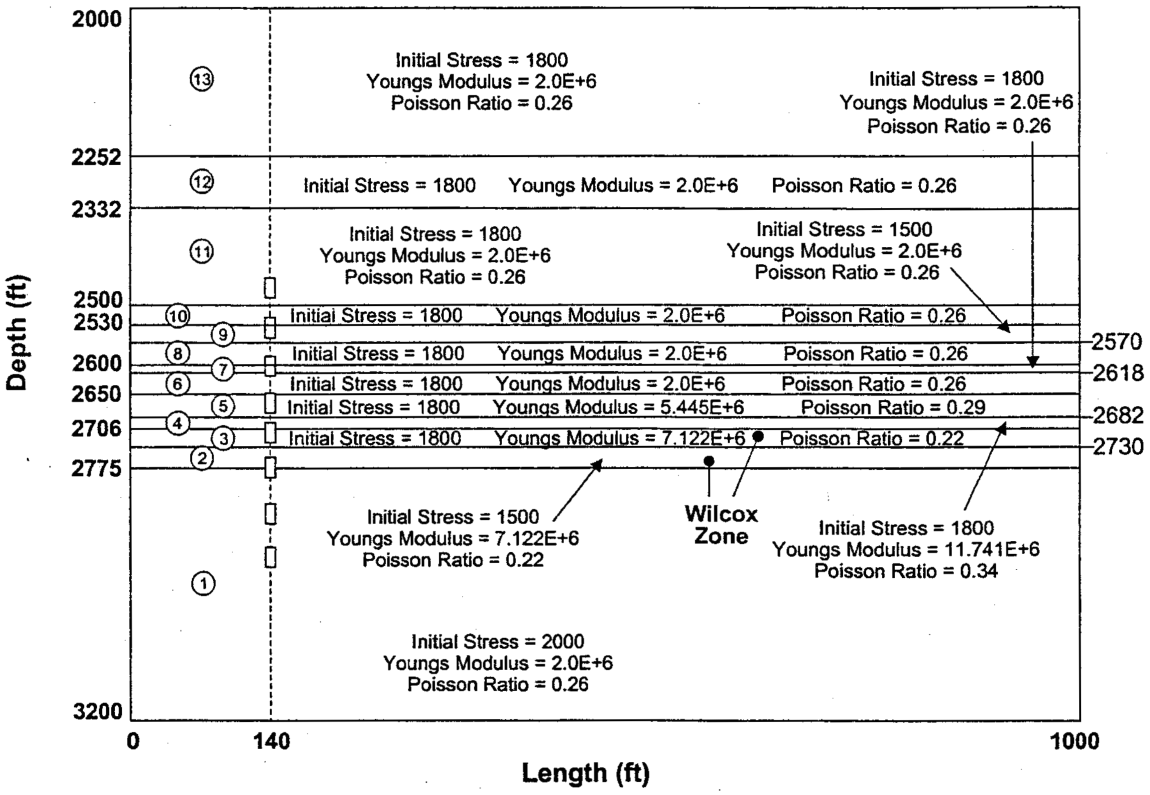

Figure 116. Model 5 layering and grid for Wilcox finite-element calculations.

These two models were used to evaluate the differences between two sets of material property data that had some considerably different values for the carbonate layers. Figure 117 shows the comparison between two cases run with Amoco-derived data (low modulus for the carbonate) and Terra Tek-derived data (high modulus for the carbonate). In addition, the Wilcox sandstone was split differently for cases 25 and 26 (Model 4) relative to cases 27 and 28 (Model 5). The split in the Wilcox sandstone was an attempt to match the tiltmeter and microseismic data that seemed to indicate that only the part of the Wilcox may have been fractured, yet still keep the lower peak location in the proper place. The Model-5 geometry with the larger fracture in the Wilcox sandstone is clearly a better solution, but all cases have tilt magnitudes that are too low. The final best fit of these cases, but with higher pressures, is shown in Figure 118. Some of the character of the data is again reconstructed, but the amplitudes are off without much higher pressures.

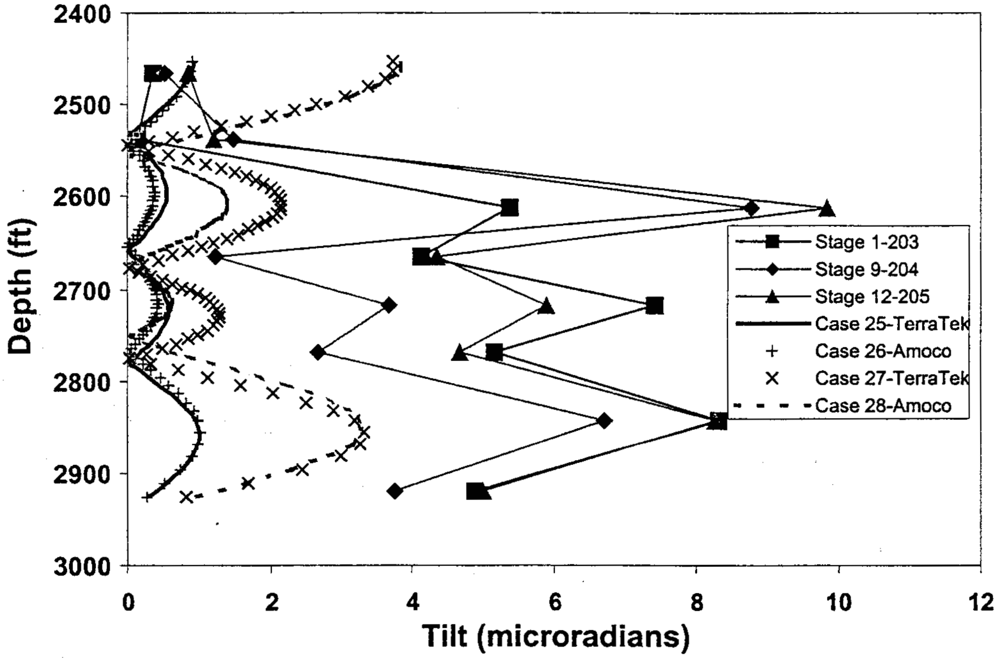

Figure 117. Comparison of various two-fracture calculations (Models 4 & 5) with measured tilts.

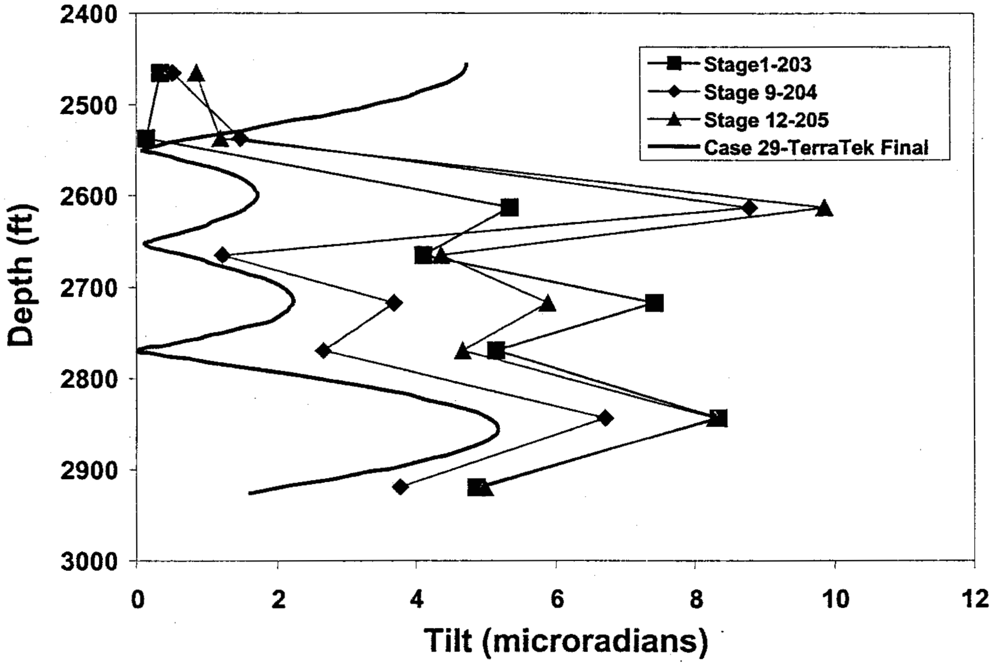

Figure 118. Comparison of two-fracture calculation (Models 5, Terra Tek data) with measured tilts.

In summary, the finite element calculations show that layering alone cannot be responsible for the complex tilt distribution and other factors such as multiple fractures, possibly within some low stress zones, would be required to produce the measured tilt distribution. In some circumstances parts of the tilt field can be reproduced, but not the entire tilt field.

Since the actual distributions of the downhole-tiltmeter data could not be reproduced using layering alone, these results were not very useful for assessing the effects of modulus variations. In order to gain some understanding of the accuracy of inverting data that were perturbed by layers, some finite element cases were run using the grid of Figure 105 and then inverted to assess the capability of the simple models to accurately process complex data. For this assessment, the relatively simple case of a single fracture in the Wilcox sandstone was used (height =69 ft, center at 2740.5 ft, dip=0°, azimuth = 0° and infinite length). Figure 119 shows the match that is obtained, which is actually quite good. However, the height of 307 ft is in error by a factor of 4.4, the azimuth is perpendicular to the correct azimuth and the length is much too short.

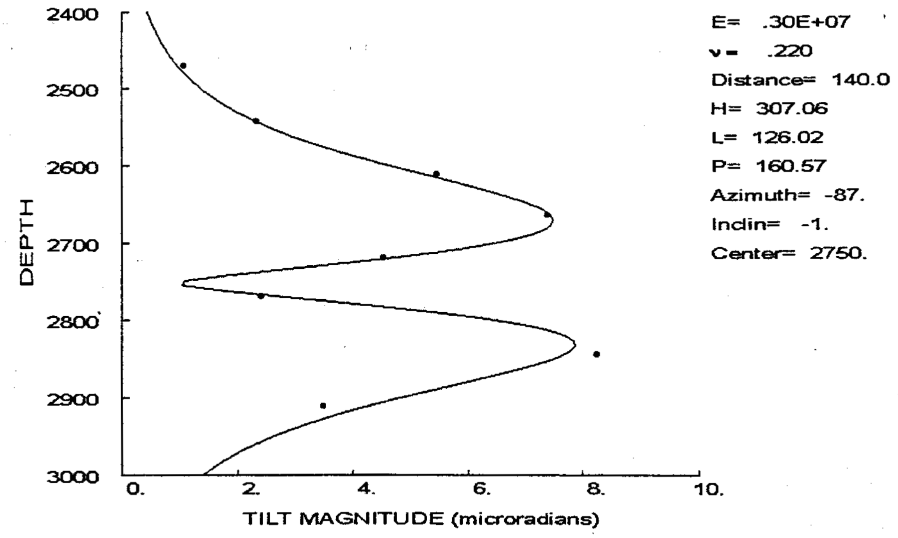

Figure 119. Inversion of layered finite-element calculation with no constraints.

If the azimuth is known and constrained, the inversion shown in Figure 120 is obtained. This inversion provides another excellent fit to the data, but the fracture is tall, short, fat and slightly inclined, all of which are incorrect. Of particular concern is the error in the height (nearly a factor of 3).

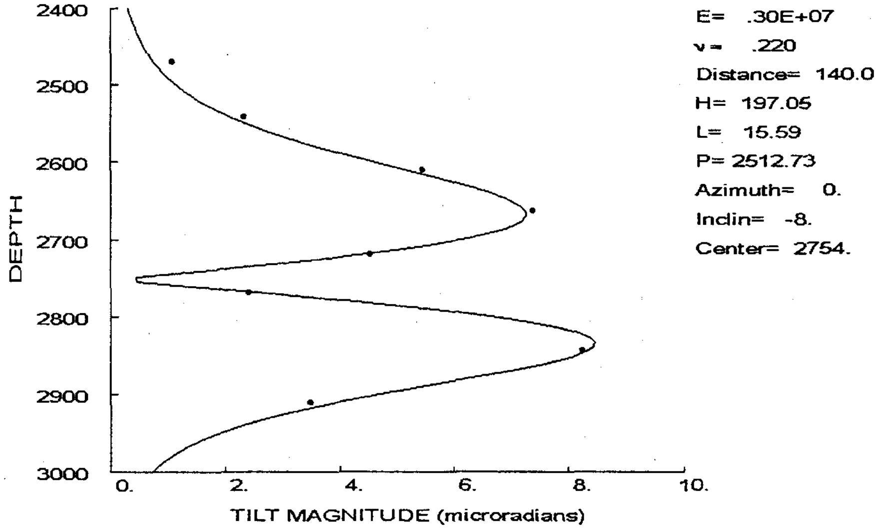

Figure 120. Inversion of layered finite-element calculation with azimuth constraint.

If both the pressure and the azimuth are constrained, the inversion can finally find a good fit to the actual model, as shown in Figure 121. In this case, the model matches the data quite well, the height is almost exact, and the length is very long (as it should be to match the 2D results). The asymmetry is matched by having the fracture inclined 9°. Standard errors are ± 16° on the inclination, ±12 ft on the height, and ± 20 ft on the center location

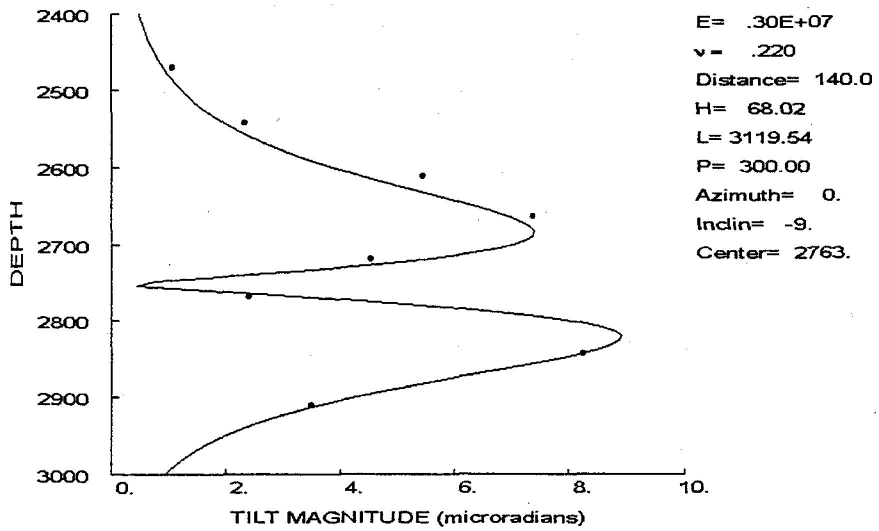

Figure 121. Inversion of layered finite-element calculation with azimuth & pressure constraints.

Finally, if there is some knowledge of the fracture inclination (e.g., equal to 0), then the inversion constrained by azimuth, inclination and pressure is shown in Figure 122. In this case the fit is not as good, but the long fracture is extracted and the height of 65 ft is not much different from the true value of 69 ft. The standard error on the height increases to 33 ft because of the larger misfit.

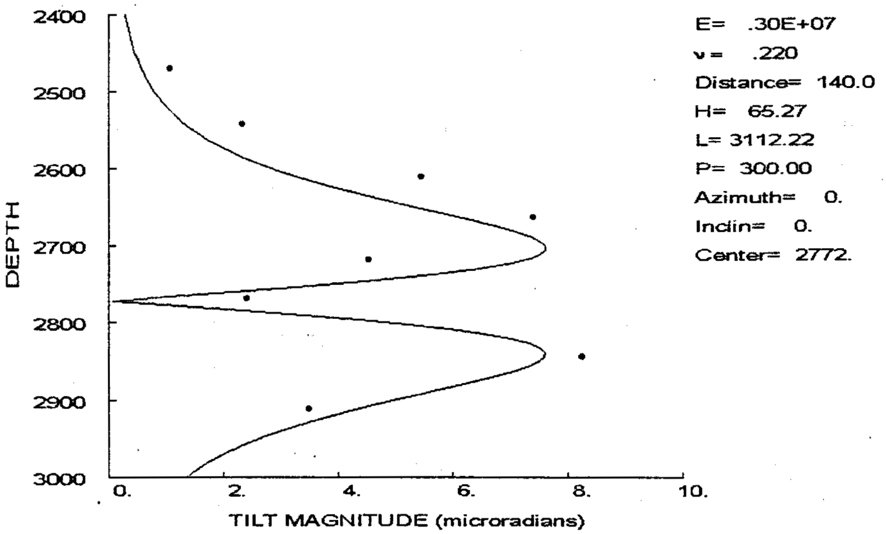

Figure 122. Inversion of layered finite-element calculation with azimuth, pressure & inclination constraints.

One of the difficulties with doing the previous calculations is that it is not clear what modulus to use. The value of 3 x 10^6 psi was chosen as an approximate average over the interval in which tiltmeters were emplaced, but it is possible that different values would provide a better fit. The results obtained from an inversion using a Young's modulus of 4 x 10^6 psi is shown in Figure 123. The fit of the data is considerable better than that shown in Figure 122, but the height value of 78 ft (± 20 ft) is a worse estimate of the true height. Examples for modulus values of 2 x10^6 and 5 x 10^6 psi are shown in Figures 124 and 125. The case with the lower modulus has a worse fit of the data and a height that is much smaller than the true value. The higher modulus value has the best data fit (smallest sum of residuals squared) of all four cases shown here, but its height value of 88 ft is off by 28%.

This series of calculations on the effect of modulus also shows that it may not help to add modulus to the list of regression parameters. The smallest residuals (which is where a regression would want to push the solution) are found for modulus values that give incorrect height data and the net effect would likely be additional uncertainties. Furthermore, all of the analyses shown so far indicate that the more free parameters there are, the more likely it is that the solutions will be wrong. No attempt was made to show the changes induced by Poisson's ratio variations because its general effect is small.

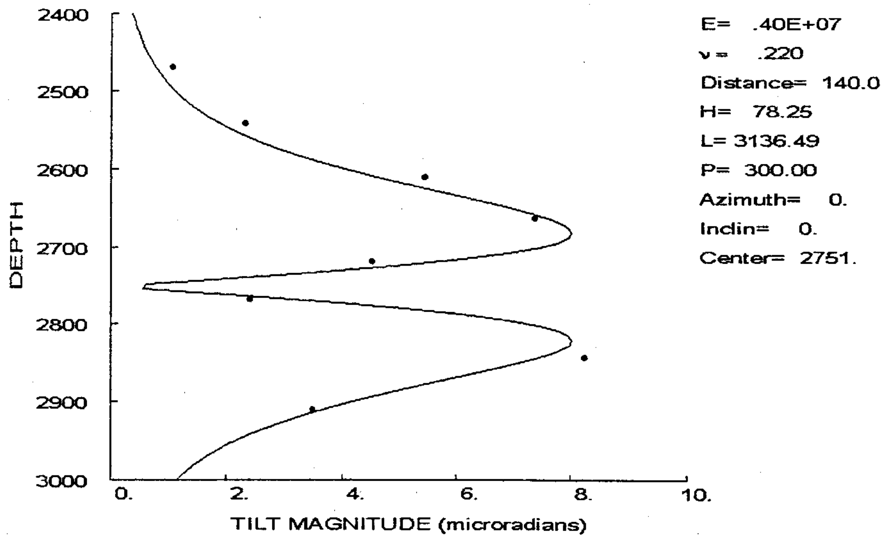

Figure 123. Inversion of layered finite-element calculation with azimuth, pressure & inclination constraints and modulus of 4.e+06 psi.

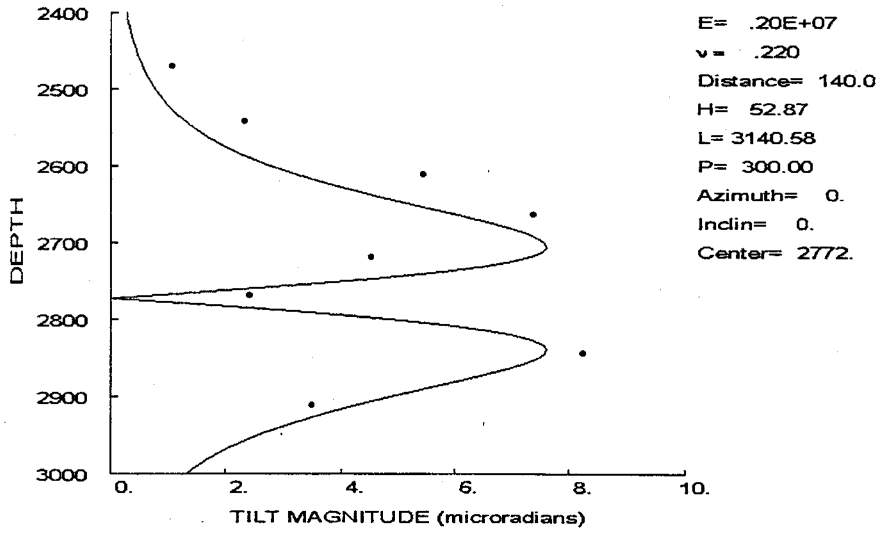

Figure 124. Inversion of layered finite-element calculation with azimuth, pressure & inclination constraints and modulus of 2.e+06 psi.

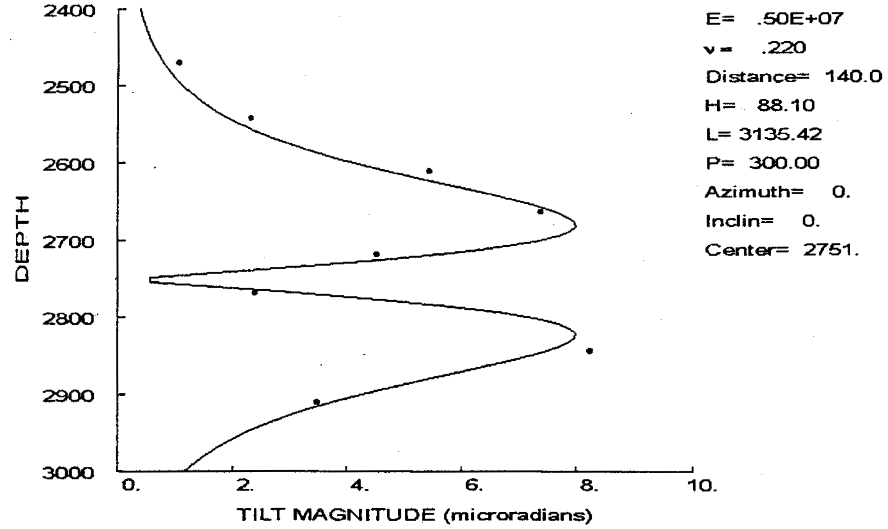

Figure 125. Inversion of layered finite-element calculation with azimuth, pressure & inclination constraints and modulus of 5.e+06 psi.

These calculations show that the amplitude changes induced by the possible layering at Mounds are relatively small and probably do not induce the large asymmetries found in the downhole-tiltmeter data. However, even though the changes are small, they can cause large errors when a homogeneous-material regression model is used to invert the data. It is only when the fracture is highly constrained and a suitable average modulus is chosen that the regression determines the correct values of the remaining unknown parameters.

Effect of Crack Geometry

The effect of crack complexity is a very difficult problem to examine since solutions for nearby cracks do not superpose (one crack influences the other, changes the boundary conditions). In addition, solutions for non-simple crack geometries are not readily available. One feature that can be examined is the difference between a fracture clamped at top and bottom (e.g., the pressurized crack model used here) and one with full slip at the top and bottom. The full-slip case is essentially that of a very long dislocation of constant width, the same solution typically used for most tiltmeter inversions. If the fracture is relatively tall and the monitoring location is close, the difference between the two models may become significant and might explain some of the misfit observed at Mounds. Details of the dislocation model used here are given in Appendix B.

Figure 126 shows a comparison between a 50 ft height pressurized fracture and a 50 ft height dislocation at the Mounds Wilcox monitoring distance of 140 ft. This monitoring distance is nearly three times the height, and this relative far location has almost identical results for the two models. Figure 127 shows the comparison for a 100 ft height fracture. At this monitoring-distance to height ratio of 1.4, there is about a 10% difference in peak amplitudes, but the locations of the peaks are fairly close. Figure 128 show the comparison for a 200 ft height fracture. The difference in amplitudes is about 15% and the peaks show a noticeable shift. The monitoring-distance to height ratio here is about 0.7. Finally, for a 300 ft fracture height, the comparison is shown in Figure 129. At a distance to height ratio of less than 0.5, the amplitude discrepancy remains about 15%, but the shift in peak locations is about 20 ft on both top and bottom.

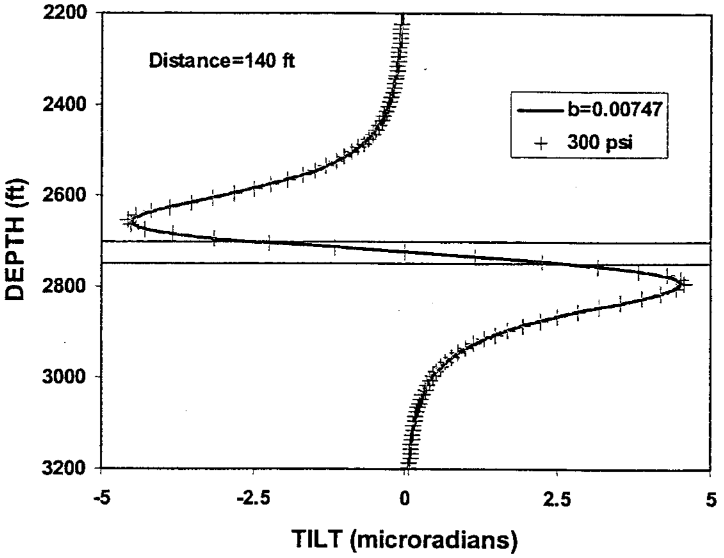

Figure 126. Comparison of dislocation and pressurized crack for a 50 ft height fracture.

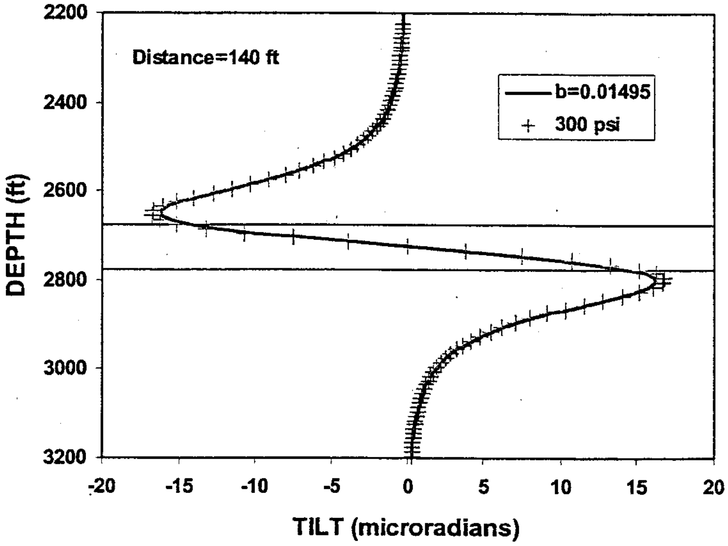

Figure 127. Comparison of dislocation and pressurized crack for a 100 ft height fracture.

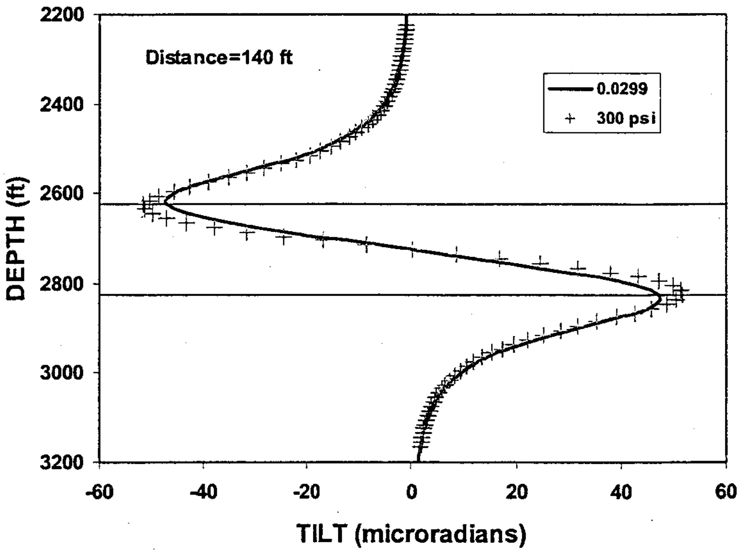

Figure 128. Comparison of dislocation and pressurized crack for a 200 ft height fracture.

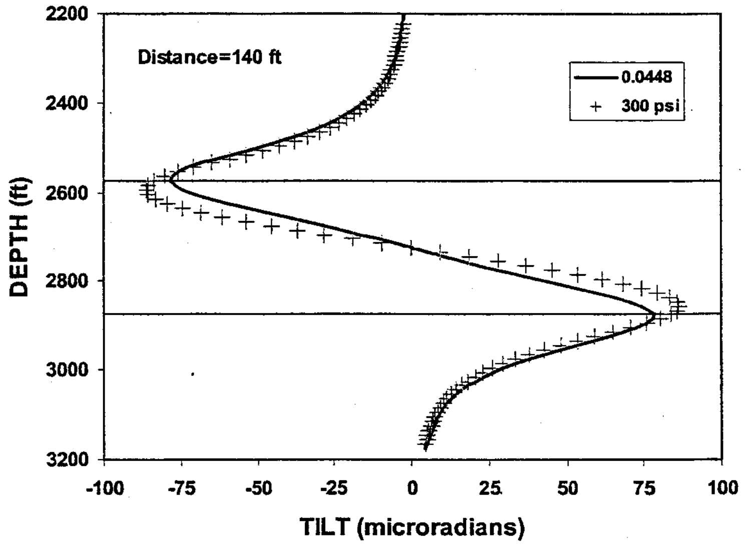

Figure 129. Comparison of dislocation and pressurized crack for a 300 ft height fracture.

It appears that a fracture with full slip at the top and bottom of the fracture will be indistinguishable from a normal pressurized crack if the monitoring distance is greater than the height of the fracture. If the monitoring distance is closer (or the fracture height greater), then a constant width fracture (full slip at top and bottom) will generate peak locations that are farther apart then those generated by a pressurized crack. This is the opposite direction to that needed to improve the match of the Mounds results and it suggests that the slip condition is not likely part of the problem.

Effect of Two Fractures

While the finite element calculations were used to examine the effect of more than one fracture, an analytical solution exists for two symmetric fractures having the same internal pressure. The solution to this problem is given in Appendix E. This solution is useful for examining the effect of distance from two fractures and separation of the two fractures. However, it is somewhat limited because the two fractures must be the same height, have the same internal pressure, and have their axes aligned. In the case that will be shown here, the internal pressure in the fracture is 300 psi, Young's modulus is 3 x 10^6 psi and Poisson's ratio is 0.22.

Figure 130 shows a comparison of the effect of separation for two fractures having heights of 70 ft. In this case, the center of the two fractures is at 2700 ft (top of the Wilcox) and the center of the upper fracture is either 80, 120, 150 or 200 ft above the center of the lower fracture. Since the fracture heights are 70 ft, the undisturbed separation between the fractures is 10, 50, 80 and 130 ft, respectively. This figure shows that at the Wilcox monitoring distance of 140 ft, two fractures separated by 10 ft (case 80) would look like a single fracture with a lower pressure. If the separation distance is 50 ft (case 120), there is a kink in the data that probably would not be observable on a typical tiltmeter array. Only if the fracture separation exceeds 80 ft (case 150) does the reversal in the tilt field occur.

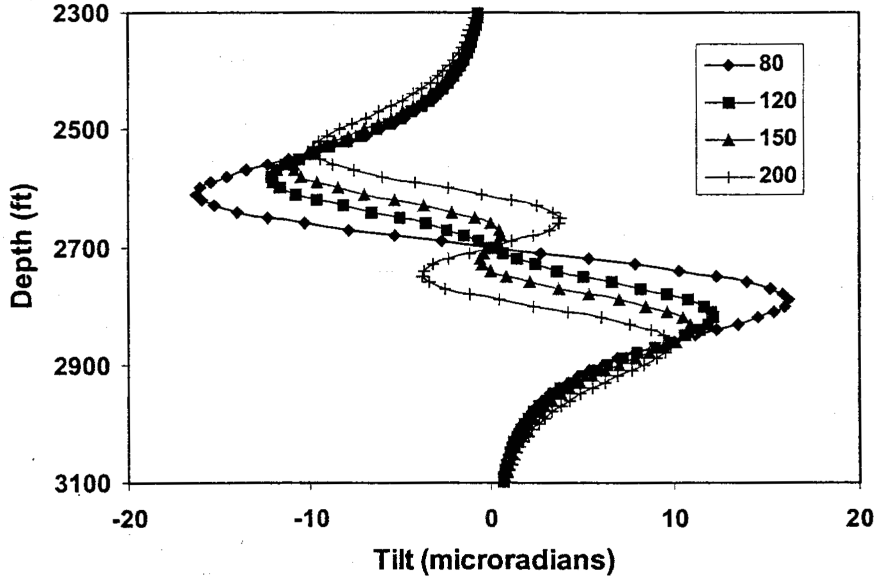

Figure 130. Effect of crack separation for two 70 ft fractures at 140 ft monitoring distance.

If the fractures are smaller (40 ft height) and the centers of the fractures are separated by 50, 100, 150 and 200 ft, then the results shown in Figure 131 are obtained. The undisturbed separated distance between the fractures for these cases are 10, 60, 110 and 160 ft. At the Mounds monitoring distance, having smaller fractures does not particularly increase the tilt reversal. It merely decreases the amplitude of the tilts.

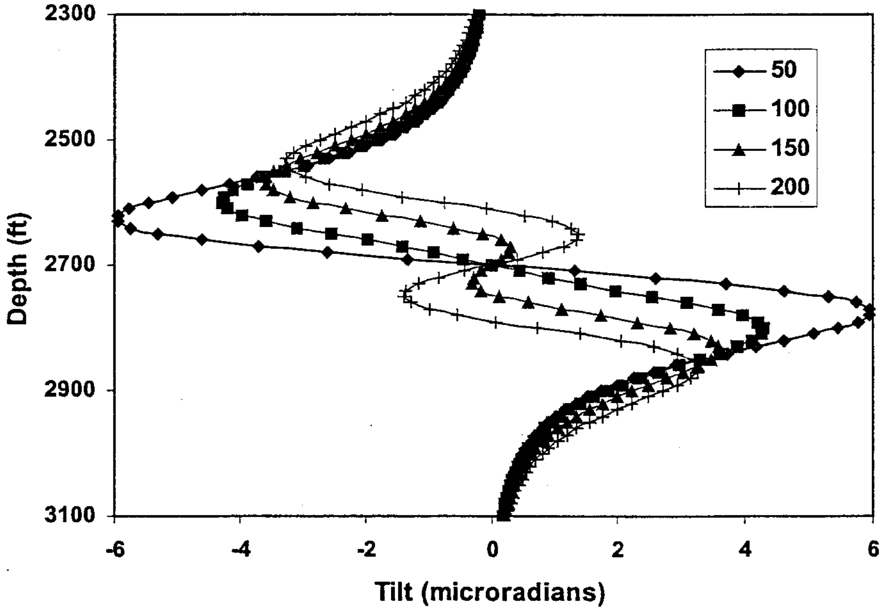

Figure 131. Effect of crack separation for two 40 ft fractures at 140 ft monitoring distance.

Although these results cannot be used to match the Wilcox data, they do show that two fractures can increase the character of the tilt profiles. In addition, it helps to visualize the situation if there were two fractures having different heights and pressures. In such a case, the symmetry would disappear and an upper secondary fracture having shorter height and lower pressure could reduce the top peak of a lower larger fracture. This is one situation that could cause the observed asymmetry at Mounds.

These examples also provide an opportunity to investigate the errors caused by attempting to add two solutions to obtain a tilt field due to some complicated multi-crack geometry. Since the crack and dislocation solutions normally used for tilt analysis assume that there is only a single crack in a uniform medium, any attempt to add solutions (e.g., put two cracks in together) causes interference that is not accounted for in the constructed solutions. However, the two crack solutions given above are exact.

Figure 132 shows a comparison of the two crack tilt field from the exact solution with the tilt field obtained by simply adding the tilts for two cracks. This particular case is for 70 ft fracture heights with 80 ft spacing on centers, so the cracks are relatively close and interfere. All other parameters are the same as given previously above. It can be seen that the difference in the maximum tilt is about 15% (2.5 microradian difference). This is a sizable difference and it would appear to suggest that solutions should not be added unless the two cracks are far apart. However, the important effect is the difference that results after inversion.

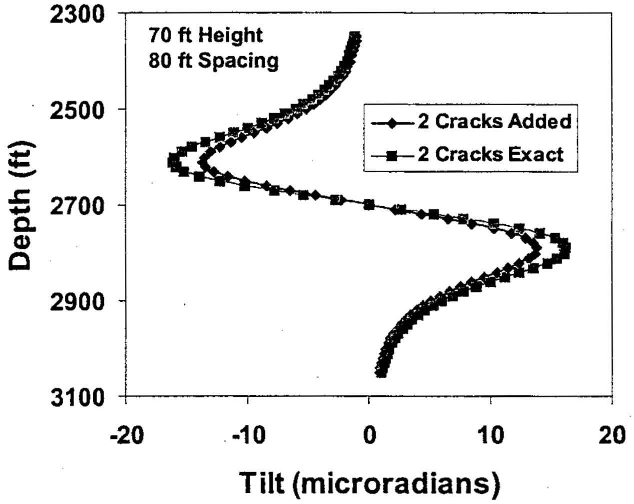

Figure 132. Difference in tilt results using exact two-crack solution and the simple addition of the tilt fields for two cracks.

Figure 133 shows the inversion obtained by taking the exact solution for two cracks and inverting it using the single-fracture model. No attempt is made to use a dual-fracture inversion because in normal field operations the number of fractures will never be known (except in cases where there may be two nearby zones stimulated at the same time). This inversion is only performed here to show the difference in the inversion for the exact and superposed solutions. In Figure 133, the inverted height was 182 ft, which is actually close to the total fracture height of 150 ft for this case (two 70 ft fractures with a 10 ft separation). The height is very long, corresponding to the 2D solution. The pressure is low, at 112 psi, but this is to be expected for this solution. The important comparison is with the inversion of two superposed cracks, which is shown in Figure 134. There is little difference in the two solutions, as the amplitude discrepancy is accounted for in a slightly lower pressure. However, the shapes are sufficiently similar that the height, which is the important parameter in this inversion, is essentially the same. These calculations suggest that superposition of fractures may be a good approximation for many cases where the two fractures are co-aligned. No attempt is made here to investigate other geometries.

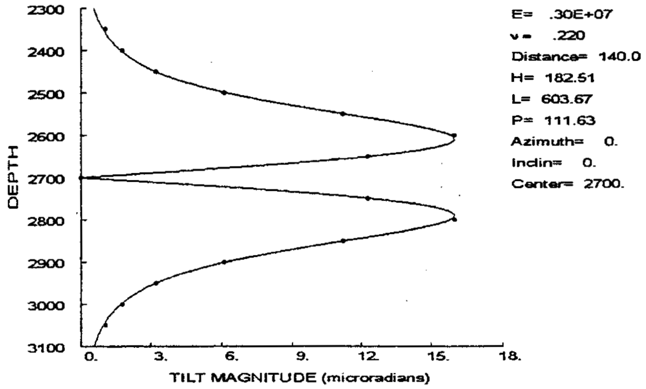

Figure 133. Inversion of two-crack solution.

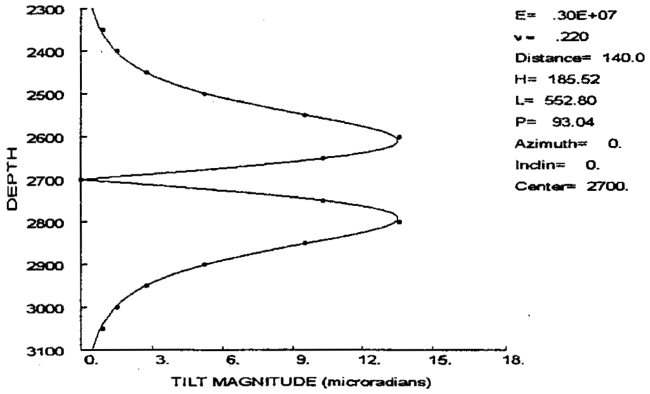

Figure 134. Inversion of superposed two-crack solution.

Effect of Pore Pressure Changes

Hydraulic fractures created in gas reservoirs are not expected to induce much of a poro-mechanical tilt response because the zone of pressure perturbation is very limited. However, in a fluid saturated reservoir the pressure coupling extends much farther[33] and the mechanical response might be significant. A simple solution for the poro-elastic effect of fluid leakoff due to fractures created in permeable fluid-saturated reservoirs is given in Appendix F. The solution requires knowledge of both the mechanical and reservoir properties of the zone of interest. Only the Wilcox zone is considered here because it is the only highly permeable interval and the poroelastic contributions only arise from pressurization of the Wilcox sandstone. For this case the same mechanical properties were used as in the regression analyses of the Wilcox data. The reservoir properties used were

Porosity = 0.15
Permeability = 10 md
Fluid viscosity = 1 cp
Fluid compressibility = 3.3×10^{-6} psi^{-1}
Leakoff time (injection time) = 0.33 hrs
Biot's parameter = 0.9
Pressure level above reservoir pressure = 1000 psi
Zone thickness = 70 ft
Fracture length = 200 ft

Figure 133 shows the tilt response induced by the leakoff of high pressure fluid from a 20 minute injection with a pressure level 1000 psi above the reservoir pressure for a 200 ft fracture length. This example has no filter cake formation and is a worst-case calculation. The tilt response is very similar to that induced by a fracture without leakoff effects and the magnitude is comparable to the mechanical response of the fracture by itself.

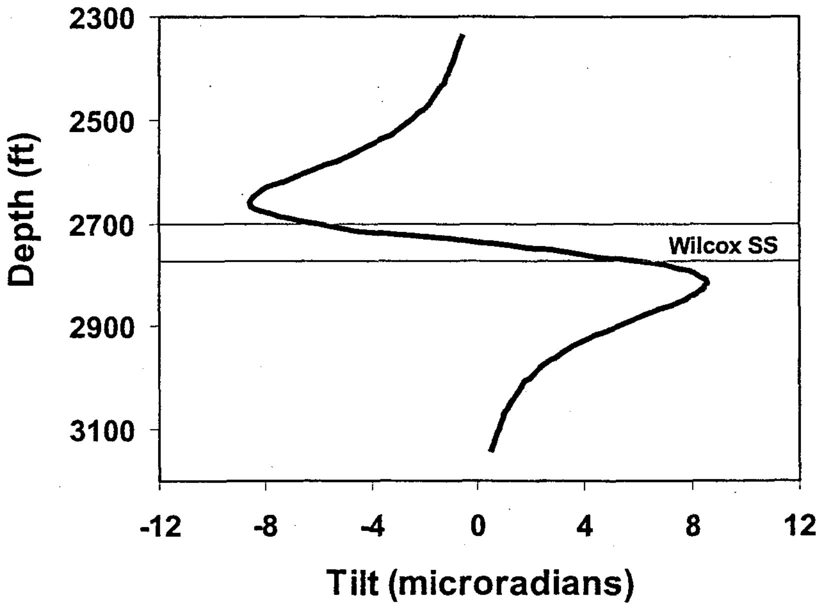

Figure 135. Tilt response due to poroelastic effect for a single injection.

Unfortunately, this poroelastic response can not be superposed on the elastic solution because the pore pressurization significantly alters the purely mechanical response. Smith's analysis[33] of the change in closure stress as a function of leakoff can be used to estimate the increase in closure stress that occurs in this environment. The equation for stress increase is

$$\Delta\sigma = \frac{A\Delta p}{2+\varsigma}$$

where ζ is given by

$$\varsigma = \frac{1}{2}\left(a\frac{H}{2}\sqrt{\pi} + \sqrt{a^2\left(\frac{H}{2}\right)^2 \pi + 4} \right)$$

a is

$$a = \sqrt{\frac{\varphi\mu c}{kt}}$$

and A is a plane-strain poroelastic coefficient given by

$$A = \frac{(1-2\nu)\alpha_B}{1-\nu}$$

where α_B is Biot's parameter.

At Mounds, the reservoir pressure was about 1200 psi, the closure stress about 1900 psi and the fracturing pressure about 2200 psi. The porosity is about 15%, the permeability about 10 md, the fluid viscosity is 1 cp, the reservoir compressibility is about 3.3 x 10^{-6} psi^{-1}, and the leakoff time is about 20 min. Using elastic parameters of the previous calculations, the change is stress is 167 psi, more than half of the net fracturing pressure. Adding the poroelastic component plus the reduced elastic component due to a net pressure of 300 psi – 167 psi = 133 psi, the calculated theoretical poroelastic response is shown in Figure 134. Clearly, the poroelastic component should not be neglected in these analyses. However, this simple analysis requires many assumptions about the leakoff behavior and the net effect on the reservoir. What is needed for advanced analysis of the Mounds data is a complete integrated poroelastic model of a fracture in a liquid saturated medium.

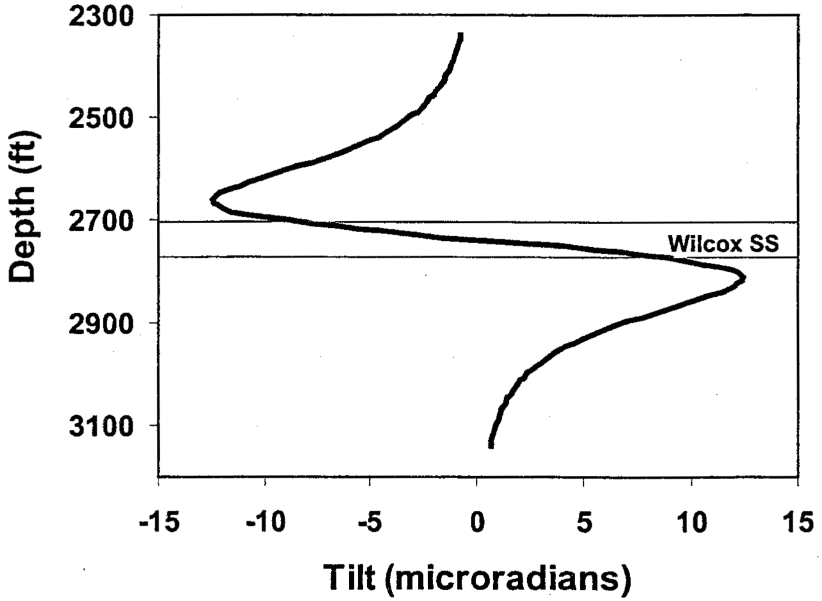

Figure 136. Combined mechanical and pore-pressure induced theoretical tilt field for a single injection.

The response shown in Figure 134 is that due to a fracture and a poroelastic zone that have the same height. However, the poroelastic tilt due to pressurization of the Wilcox sandstone, when superposed on the fracture response that may have much greater height or be over a different interval, may be partially responsible for the complicated tilt profiles measured at Mounds. This effect only applies to the Wilcox injections since the permeability and porosity of the Atoka interval is so low that the poroelastic effects should be very small.

The combined leakoff/mechanical effect can be investigated partially using Smith's analysis.[33] However, this 2D analysis assumes that the leakoff occurs in the full 2D space, rather than just in the Wilcox sandstone. Nevertheless, this approach should still be useful for evaluating whether the prior summation of two separate mechanisms yields reasonable results. *Smith* assumed a 2D fracture having a leakoff-induced elliptical pressure distribution of the form

$$p(\alpha,\beta) = p_o + \Delta p\, e^{-\varsigma\alpha}$$

where α and β are the elliptic coordinates, p_o is the initial reservoir pressure, Δp is the fracturing pressure above the reservoir pressure level, and ζ is a leakoff depth parameter found by matching this elliptical distribution with the linear flow solution from a 2D fracture. Writing the equations in terms of a Goodier potential, the solution of this problem is given by

$$\nabla^4\Phi = -A\nabla^2 p$$

Solutions to the general homogeneous equation are well known and the solution of the subsidiary equation in elliptical coordinates,

$$\nabla^2\Phi = -Ac^2\left(\sinh^2\alpha + \sin^2\beta\right)p(\alpha,\beta)$$

was found by *Smith* to be

$$\Phi = -\frac{Ac^2\Delta p}{2}\left[\frac{1}{4-\varsigma^2}e^{-\varsigma\alpha}\cos 2\beta + \frac{e^{(2-\varsigma)\alpha}}{2(2-\varsigma)^2} + \frac{e^{-(2+\varsigma)\alpha}}{2(2+\varsigma)^2}\right] - \frac{Ac^2 p_o}{8}\left[\cosh 2\alpha + \cos 2\beta\right]$$

$$+\left[\frac{Ac^2\Delta p}{2\left(4-\varsigma^2\right)} + \frac{Ac^2 p_o}{8} - \frac{c^2 p_f}{4}\right]\cos 2\beta\cosh 2\alpha - \frac{Ac^2\varsigma\Delta p}{4\left(4-\varsigma^2\right)}\cos 2\beta\sinh 2\alpha + \frac{Ac^2\varsigma\Delta p}{2\left(4-\varsigma^2\right)}\alpha$$

where c is the fracture half-height (or half length, depending on the geometry) and p_f is the fracture pressure. Although *Smith* was interested primarily in the induced stress changes and did not obtain displacements, they can be obtained and then differentiated to give the tilt field as

$$\frac{\partial v}{\partial x} = \frac{\sinh\alpha\cos\beta}{c\left[\sinh^2\alpha + \sin^2\beta\right]}\frac{\partial v}{\partial \alpha} - \frac{\cosh\alpha\sin\beta}{c\left[\sinh^2\alpha + \sin^2\beta\right]}\frac{\partial v}{\partial \beta}.$$

The results are quite tedious and are not given here.

Figure 135 shows the poro-mechanical tilt field induced by a 2D crack with leakoff into the entire surrounding space. The maximum value is about 11 microradians, which is slightly smaller than the previously constructed solution (about 12 microradians). The good agreement of these two solutions gives confidence that the results are valid and that the poro-elastic component of the response can indeed be quite large in the absence of any filter cake formation. Unfortunately, without better knowledge of the leakoff, it is difficult to attempt to analyze the Wilcox results from a poro-elastic perspective.

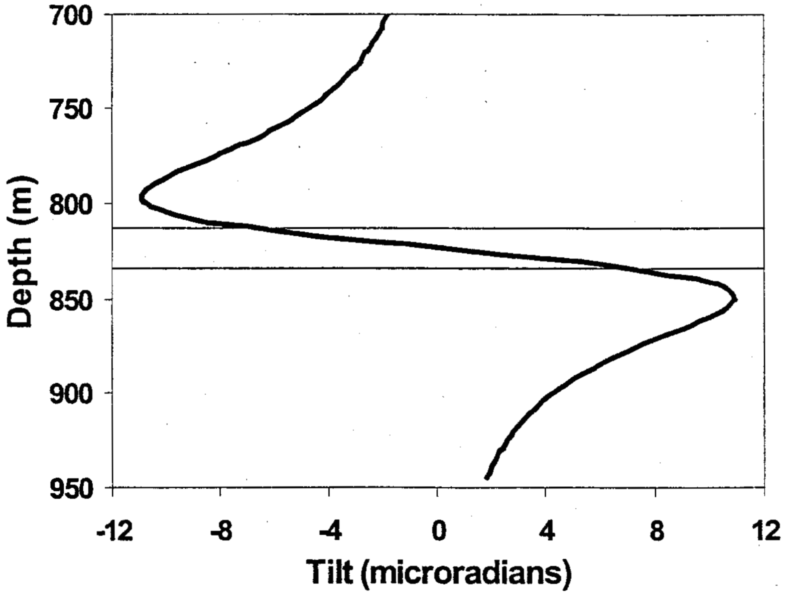

Figure 137. Example calculation of poro-mechanical tilt field using Smith's analysis.

DISCUSSION

The Mounds Drill Cuttings Injection Experiments demonstrated that the downhole tiltmeters can respond to even the small cuttings injections produced in these tests. Amplitudes as large as 10 and 50 microradians were observed in the Wilcox and Atoka injections, respectively, at a distance of 130-140 ft. Given a noise level that averaged about 1 microradian, the signal-to-noise ratio (SNR) of 10 to 50 would appear to be excellent, although this good SNR only applies to one or two tiltmeters.

Nevertheless, some noise features were apparent and they do have a significant impact on the interpretation of the results. The "tears" (discontinuous jumps in the data) are easily correctable if it can be clearly determined that they are not associated with any data trend. If they are part of a "stick/slip" process, then the effect of the discontinuous behavior is minimal if the analyst avoids selecting data sets at a jump location. The difficulty lies in deciding which tear is a real response and which is an anomaly. Furthermore, it is not obvious what could be causing the anomaly and the temptation is to use all data. For example, the third Wilcox injection had a tear in one of the tiltmeters that would have resulted in a maximum amplitude of about 16 microradians. The tear was subtracted out in that case because it would have resulted in a maximum amplitude that was nearly twice that of any of the other injections in the Wilcox. In many other cases, however, the tear is only 1 or 2 microradians and the correct treatment of the tear is not as certain.

The general noise level without the tears varied from sensor to sensor with noise levels ranging from about 0.25 microradians to more than 1 microradian. This noise is probably electronic for the most part, but it may have a cable component as well (e.g., due to wind blowing the cable at the surface). The tiltmeters were downhole for relatively long periods prior to the injection, so it is likely that they were in thermal equilibrium with the wellbore, at least in their power-off state. Some of the drift observed on various levels is most likely due to internal heating when the instruments are turned on. Given the short duration of the Mounds injections, the drift was relatively insignificant and drift problems on longer tests could have been subtracted out using a linear-trend analysis.

The most difficult feature to explain was the large amplitude asymmetry observed in the Atoka injections and to some extent in the Wilcox tests. The factor of two asymmetry in the amplitude of the peaks is most easily explained by fracture dip, but all evidence from coring, microseismic imaging, and past stress history at the site show that the fractures are vertical. In addition, the Atoka tests show this asymmetry starting at the first cuttings injection, so it is not likely to be some complex fracturing (e.g., horizontal or deviated component) that results after cuttings have plugged the first fracture. While some of the asymmetry could be due to modulus changes in the Wilcox zone, the finite-element solutions suggest that the effect of layers is not nearly as large as the observed asymmetry. Furthermore, the Atoka interval had very little variation in modulus over the entire range of the tiltmeters, so modulus effects do not appear to be responsible for the behavior in that zone. Another possible cause of the asymmetry is two fractures that are vertically aligned, but having different pressures and heights. However, this is an impossible situation to model because there is absolutely no information about the location or characteristics of these fractures. Nevertheless, because the asymmetry is so large, it is not likely that an accurate mapping of the fractures can be made without understanding the cause of this feature.

The process of interpreting the data requires an inversion of the data to fit a model. There are two parts to this process, inversion and model, and both may affect the answer that is obtained. The model chosen here is that of a 3D flat elliptic crack with constant internal pressure. It is a rather complex model, but it is felt to be the one analytic model that most accurately represents a fracture. Other models, such as the popular dislocation approach, may also be realistic under appropriate conditions (e.g., far from the fracture), but the conditions of application need to be checked for each application. Even so, there is no guarantee that a flat elliptic crack is the most appropriate model, as the conditions of full slip at the top and bottom of the fracture may occur in some intervals, in which case the dislocation model would be more appropriate close to the fracture (but it would still have end effects if the fracture was short).

The inversion methodology is also very important for extracting the correct solution. The general approach is to use a least-squares methodology to fit the data to a model. For complex, non-linear problems such as this one, the least-squares approach can only be applied approximately. The method used here is the Levenberg-Marquardt approach[31] that linearizes the equations and applies the regression analysis to the linearized equations. However, this approach is not guaranteed to find the best fit for complex topologies. It merely finds the best fit in the vicinity of the initial guess. Thus, the method of providing an initial guess becomes an important part of the solution.

As shown in the examples, the availability of independent constraints is absolutely essential for obtaining meaningful results. In this analysis there are six possible free parameters: azimuth, inclination, height, length, center depth and pressure. If the data are perfect, then the model can extract all six parameters. However, the addition of small amounts of noise will lead to serious errors if all six parameters are free. Adding two or three constraints was very significant in reducing the error. In the case of the Mounds data, the application of the regression with all six parameters free would have resulted in fractures with significant inclination and incorrect azimuths that were directed at the monitoring well. These parameters needed to be constrained to the known values in order to obtain useful interpretive data from the tiltmeters. Additionally, the fracture pressure (corresponding to the width in the dislocation model) was seldom extracted correctly and the inversion results typically gave extremely large pressures. Since large pressures were not measured, the inversion results obtained here required that the measured pressure be used. As a result, the Mounds data could only be used to extract height, length and center depth.

In these Mounds results, the standard errors associated with the regression were quite large and thus the accuracy of the tiltmeter results was very poor. The size of the standard error for an individual component has two components: the size of the sum the residuals squared and the size of the inverse of the gradient of tilt with respect to the parameter. The first component is obvious and is a direct reflection of the ability of the model to fit the data. Because of the large misfits in these results, the first component was generally large. The second component reflects the "strength" of the extremum. If the small changes in the parameter result in large changes in the tilt, then the minimum is a deep well and the corresponding large gradient surrounding the "well" results in a small standard error. If the minimum is shallow and the tilt changes only slightly with changes in the parameter, then the resultant small gradient makes the standard error even larger. For this data set and configuration, the dip and center depth are the two parameters with strong extrema because no other parameters will give the tilt shift that the center depth will and no other parameters give the asymmetry that the dip (or inclination) does. Unfortunately, the height, azimuth, pressure and length are all tied together and thus the uncertainty of these values is very large. Even with the three constraints, the uncertainties still remain large for the height and length.

A limited attempt was made to deduce the effect of some complexities on the inversion. As seen in the original inversion example, the addition of small amounts of noise resulted in very poor fracture estimates. Similar results were obtained when an inversion of a finite-element case was attempted. In this case, the asymmetry caused by layering sufficiently perturbed the tilt distribution that poor results were generated unless the fracture was highly constrained. In addition, it was also found that uncertainties in the modulus can result in moderate errors in the geometry parameters. Other complexities, such as multiple or complex fracturing, are likely to produce additional errors. Poroelastic tilts due to leakoff were calculated to be about the same order as the measured tilts, suggesting that much of the complexity in the Wilcox sandstone could be due to the pressurization effects. In the Atoka interval, however, there should be only a small poroelastic effect due to the low permeability.

In evaluating the tiltmeter results at Mounds, a comparison with other data is as useful as the standard error analysis. In this case, the other diagnostic data included bottom-hole pressure measurements, the core throughs of the fracture, the surface tiltmeter results, and the microseismic imaging. Unfortunately, the bottom-hole pressure, core-throughs, and surface tiltmeter results were used to provide data constraints and thus are not useful for any comparisons. The microseismic data is available and provides a useful comparison, but it is limited somewhat by some uncertainty in the velocity structure of the shear wave (a compressional wave tomographic survey was run, but no shear wave tomogram was obtained). Comparisons of the microseismic images and the tiltmeter maps show reasonable agreement on some tests, but large discrepancies on others. During the early Wilcox injections when the fracture was in or above the Wilcox sandstone, there is relatively good agreement between the two techniques. In the later Wilcox injection, however, the microseismic images showed considerable activity well below the Wilcox sandstone to which the tiltmeter inversion did not respond. Comparisons in the Atoka are much less certain because of the paucity of microseisms detected during those injections, but results from the third day of testing show considerable discrepancies between the tiltmeter and the microseismic heights.

It should be stressed that the inversion results given here are those resulting from the application of a 3D flat elliptic crack using the Levenberg-Marquardt regression algorithm. Pinnacle Technologies provided their own inversion of the data using a dislocation model and their own regression technique and obtained some quite dissimilar results. A comparison of the two inversions for all injections are shown in Appendix D. While many of the Atoka results are relatively close, most Wilcox injections and the later Atoka injections are quite different. Some of this is undoubtedly due to the correction of "tears" that was performed to the data sets analyzed here, but many of the different cases are for data sets in which no correction was made. Other discrepancies are obtained by different methods for zeroing the tilt data; these changes could offset the tilt values by as much as 0.5 microradians on a few sensors. In general, however, these effects are not large enough to cause the observed differences and the most likely cause is the difference in the two inversion models. For example, Pinnacle's standard inversion procedure is to extract a horizontal fracture component in addition to the vertical fracture (this is done because all of their surface tiltmeter results indicate that some horizontal fracturing occurs in all tests). Thus, Pinnacle is extracting vertical and horizontal fracture components, while the analysis used here only extracts parameters associated with a vertical fracture.

The other source of error not thoroughly discussed in this report is the functioning and coupling of the tiltmeters. This factor has been largely ignored because of a lack of access to the tiltmeters and no known test data on the centralized positioning technique. To give some comparison, the tiltmeter data from the B-sandstone experiments at M-Site are included in Appendix C. Since these tiltmeters were cemented in place, there is perfect coupling between the tiltmeters and the rock. In addition, noise levels and drift were well characterized and easily eliminated from the data sets. The noise levels for the cemented tiltmeters was about 2 orders of magnitude smaller than the wireline run tiltmeters at Mounds, but the signals at M-Site were also smaller for most of the tests. The asymmetry at M-Site was clearly smaller (even with a highly layered sandstone/shale sequence), but it cannot be fully evaluated because there were not enough tiltmeters to extend fully below the lower peak location. Using similar constraints to those used here at Mounds, the fits of the M-Site data are clearly better, but by no means perfect. However, most of the misfit at M-Site could be explained by the layering effects and finite-element studies showed good agreement with the measured data when all of the layers were added. Thus, the M-Site data would suggest that fully coupled tiltmeters provide data that can be interpreted within the framework of a single pressurized crack in a layered structure. As result, the possibility that the Mounds data asymmetry and resulting misfit are due to coupling or other hardware issues cannot be ruled out.

CONCLUSIONS

These tests show that downhole tiltmeters provide a large signal response to the injection of cuttings in nearby wells. However, the interpretation of these data is still quite difficult and the uncertainties associated with the interpretations are quite large.

Noise levels are a critical issue, as small amounts of noise can result in significant errors. One of the most important things that can be done is to perform a detailed noise analysis and noise uncertainty test.

Interpreting the tiltmeter data is largely dependent upon assembling sufficient independent constraints to obtain a reasonable inversion. In the Mounds tests it was necessary to constrain the azimuth, inclination and pressure. Thus, it is important that other diagnostics be run in order to assure a reasonable result.

Since the inversion is nonlinear and nonlinear regression routines are not necessarily guaranteed to find the best fit of the data, it is important to provide good initial guesses because the nonlinear inversions will find the best fit in the vicinity of that initial guess. It is also quite possible that another inversion approach could be advantageous in extracting the best-fit parameters.

The error analyses are an important part of the tiltmeter interpretation process as they show the reliability of the answer. Unfortunately, the uncertainty associated with height and length are often quite large.

The misfits between the crack model and the Mounds data do not appear to be due to layering, fracture azimuth, or fracture dip. At the present time, the cause of the large asymmetry in the peaks is unknown and, thus, the answers obtained in these tests have a large amount of uncertainty.

ACKNOWLEDGMENTS

The authors would like to acknowledge the support of the DOE Natural Gas and Oil Recovery Technology Partnership for this project. In addition, the authors would like to thank the companies and the representatives of the Mounds Drill Cuttings Experiment Executive Committee for their funding and assistance of project field operations. The companies include BP Exploration, Azerbaijan Oil Co., Schlumberger, Shell E&P Tech., Chevron, MSD, Halliburton Energy Services, Amoco, Mobil, Hughes-Christensen, Exxon Production Research, Arco, Gas Research Institute, Pinnacle Technologies and UPRC. A particular acknowledgement is made to GRI for its management of the project and funding of the microseismic diagnostics, the results of which were used for comparison in this study. Special thanks to the field support crew of Branagan & Associates, Rich Peterson for planning and management of many of the field activities, and Ed Chesney for his dedicated work at site management. Finally, the authors thank Pinnacle Technologies, Inc. (particularly Eric Davis) for its efforts to obtain the surface and downhole-tiltmeter data and provide the initial analyses of those data. They were funded by the NGOTP through Sandia National Labs to obtain these data, and they were able to gather both downhole and surface tiltmeter results for every one of the injections.

REFERENCES

1. Albright, J.N. & C.F. Pearson 1982. Acoustic emissions as a tool for hydraulic fracture location. *SPE Journal* 22(4): 523-530.
2. Thorne, B. J., "An Assessment of Borehole Seismic Fracture Diagnostics," SPE 18193, Proceedings, 63rd Annual Technical Conference of the SPE , Houston, TX, pp. 123-132, October 2-5, 1988.
3. Keck, R.G. & R.J. Withers 1994. A field demonstration of hydraulic fracturing for solids waste injection with real-time passive seismic monitoring. SPE 28495, *Proc SPE Annual Tech. Conf. & Exh.*, New Orleans, LA: 319-334.
4. Warpinski, N.R., P.T. Branagan, R.E. Peterson, S.L. Wolhart & J.E. Uhl 1998. Mapping hydraulic fracture growth and geometry using microseismic events detected by a wireline retrievable accelerometer array. SPE 40014, Proc. *SPE Gas Tech. Symp.*, Calgary, AB, Canada: 335-346.
5. Pollard, D.D. and Holzhausen, G., "On the Mechanical Interaction Between a Fluid-Filled Fracture and the Earth's Surface," *Tectonophysics*, **53**, pp. 27-57, 1979.
6. Sun, R.J., "Theoretical Size of Hydraulically Induced Horizontal Fractures and Corresponding Surface Uplift in an Idealized Medium," *Journal of Geophysical Research*, **74**, No. 25, , pp. 5995-6011, November 15, 1969.
7. Davis, P.M., "Surface Deformation Associated with a Dipping Hydrofracture," *Journal of Geophysical Research*, **88**, No. B7, pp. 5829-5834, July 10, 1983.
8. Palmer, I.D., "Uplifts and Tilts at Earth's Surface Induced by Pressure Transients from Hydraulic Fractures," *SPE Production Engineering*, Aug. 1990, 324.
9. Wright, C.A., Davis, E.J., Minner, W.A., Ward, J.F., Weijers, L., Schell, E.J. and Hunter, S.P., "Surface Tiltmeter Fracture Mapping Reaches new Depths – 10,000 Feet and Beyond?," SPE 39919, Proceedings, 1998 SPE Rocky Mountain Regional Conference, Denver, CO, April 5-8, 1998.
10. Warpinski, N.R., Branagan, P.T., Engler, B.P., Wilmer, R., and Wolhart, S.L.: "Evaluation of a Downhole Tiltmeter Array for Monitoring Hydraulic Fractures", Proc. 36th U.S. Rock Mechanics Symposium, Columbia University, NY, June 29 - July 2, 1997.
11. Branagan, P.T., Warpinski, N.R., Engler, B.P., Wilmer, R., "Measuring the Hydraulic Fracture-Induced Deformation of Reservoir and Adjacent Rocks Employing a Deeply Buried Inclinometer Array: GRI/DOE Multi-Site Project," SPE 36451, SPE Annual Tech. Conf. & Exhibition, Denver, CO, Oct. 6-9, 1996.
12. Wright, C.W., "Tiltmeter Fracture Mapping: From the Surface and Now Downhole, " *Petroleum Engineer International*, January 1998.
13. Wright, C.A., Davis, E.J., Golich, G.M., Ward, J.F., Demetrius, S.L., Minner, W.A. and Weijers, L., "Downhole Tiltmeter Fracture Mapping: Finally Measuring Hydraulic Fracture Dimensions," SPE 46194, SPE Western Regional Conference, Bakersfield, CA, May 10-13, 1998.
14. Warpinski, N.R., "Interpretation of Hydraulic Fracture Mapping Experiments," SPE 27985, proceedings of the Tulsa Centennial Petroleum Engineering Symposium, Tulsa, OK, pp. 291-300, August 29-31, 1994.
15. Moschovidis et al., "The Mounds Drill Cuttings Injection Field Experiment," Proceedings, 37th U.S. Rock Mechanics Symposium, Vail Colorado, pp. 1017-1024, June 6-9, 1999.
16. Warpinski, N.R., Branagan, P.T., Wolhart, S.L., Moschovidis, Z.A. and Mahrer, K.D., "Microseismic Monitoring of the Mounds Drill Cuttings Injection Tests," Proceedings, 37th U.S. Rock Mechanics Symposium, Vail Colorado, pp. 1025-1032, June 6-9, 1999.
17. Griffin, L.G., Wright, C.A., Davis, E.J., Weijers, L. and Moschovidis, Z.A., "Tiltmeter Mapping to Monitor Drill Cuttings Disposal," Proceedings, 37th U.S. Rock Mechanics Symposium, Vail Colorado, pp. 1033-1040, June 6-9, 1999.
18. Moschovidis, Z.A., Steiger, R.P., Weng, X. and Abou-Sayed, A.S., "The Mounds Drill Cuttings Experiment: Determining Placement of Cuttings by Hydraulic Fracturing Injection," SPE 48987,

Proceedings, 1998 SPE Annual Technical Conference and Exhibition, New Orleans, Sept. 27-30, 1998.

19. Abou-Sayed, A.S., D.E. Andrews & I.M. Buhidma 1989. Evaluation of oily waste injection below the permafrost in Prudhoe Bay field. SPE 18757, *Proc. SPE California Regional Mtg.*, Bakersfield CA: 129-142.
20. Bruno, M.S., R.A. Bilak, M.B. Dusseault & L. Rothenburg 1995. Economic disposal of solid oil field wastes through slurry fracture injection. SPE 29646, *Proc. SPE Western Regional Mtg.*, Bakersfield, CA: 313-320.
21. Hainey, B.W., R.G. Keck, M.B. Smith, K.W. Lynch & J.W. Barth 1997. On-site fracturing disposal of oilfield waste solids in Wilmington field, Long Beach unit, CA. SPE 38255, *Proc. SPE Western Regional Mtg.*, Long Beach, CA: 77-84.
22. Louviere, R.J. & J.A. Reddoch 1993. Onsite disposal of rig-generated waste via slurrification and annular injection. SPE 25755, *Proc. SPE/IADC Drilling Conf.*, Amsterdam: 737-751.
23. Moschovidis, Z.A., D.C. Gardner, G.V. Sund & R.W. Veatch 1994. Disposal of oily cuttings by downhole periodic fracturing injections, Valhall, North Sea: case study and modeling concepts. SPE Drilling & Completion 9(4): 256-262.
24. Malachosky, E., B.E. Shannon, J.E. Jackson & W.G. Aubert 1993. Offshore disposal of oil-based drilling-fluid waste: an environmentally acceptable solution. *SPE Drilling & Completion* 8(4):283-287.
25. Weng, X., A. Settaro & R.G. Keck 1997. A field demonstration of hydraulic fracturing for solids waste disposal – injection pressure analysis. *Int. J. Rock Mech. & Min. Sci.* 34:3-4, paper No. 331.
26. Wilson, S.M., M. Rylance & N.C. Last 1993. Fracture mechanics issues relating to cuttings re-injection at shallow depth. SPE 25756, *Proc. SPE/IADC Drilling Conf.* Amsterdam, 753-762.
27. Smith, M.B., N.-K. Ren, G.G. Sorrells & L.W. Teufel 1985. A comprehensive fracture diagnostics experiment: part II – comparison of seven fracture azimuth measurements. SPE 13894, *Proc. SPE Low Permeability Gas Reservoirs Symp.*, Denver, CO: 443-458.
28. CD, "Mounds Drill Cuttings Injection Project", S. Wolhart (manager), Gas Research Institute, Chicago, IL, 1999.
29. Okada, Y., "Internal Deformation Due to Shear and Tensile Faults in a Half-Space," *Bulletin of the Seismological Society of America*, **82**, No. 2, pp. 1018-1040, April 1992.
30. Green, A.E. and Sneddon, I.N., "The Distribution of Stress in the Neighbourhood of a Flat Elliptic Crack in an Elastic Solid," *Proc. Camb. Phil. Soc.*, **46**, pp. 159-163, 1950.
31. Draper, N.R. and Smith, H., *Applied Regression Analysis*, John Wiley & Sons, New York, NY, 1981.
32. Biffle, J.H. and Blanford, M.L., "JAC2D-A Two-Dimensional Finite Element Computer Program for the Nonlinear Quasi-Static Response of Solids with the Conjugate Gradient Method," SAND93-1891, Sandia National Laboratories Report, May 1994.
33. Smith, M.B., "Stimulation Design for Short Precise Hydraulic Fractures," *Society of Petroleum Engineers Journal*, pp. 371-379, June 1985.

APPENDIX A
3D ELLIPTIC CRACK MODEL

Considering a 3-dimensional flat elliptic crack opened by internal pressure and having the geometry shown in Figure A1, Green and Sneddon[A1] found an analytical solution for the following assumptions:

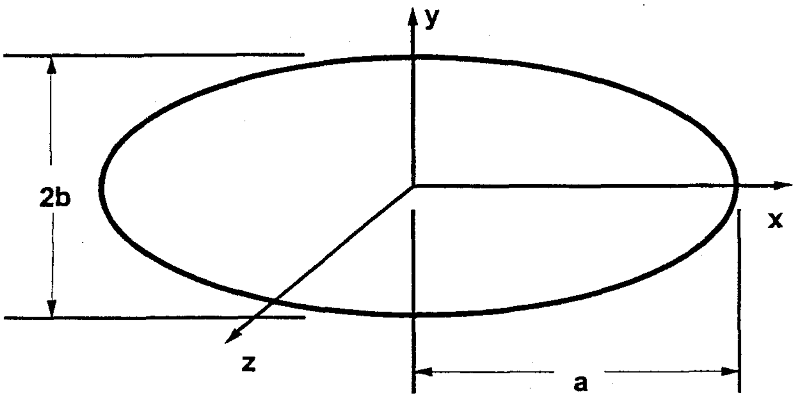

Figure A1. Geometry of fracture for tilt and stress calculations

- infinite medium
- homogeneous isotropic material
- linear elastic behavior
- uniform pressure
- length > height (a > b).

Given these restrictions, the displacements and stresses can be given by

$$D = 8\frac{\partial}{\partial \bar{z}}\left\{(1+2\nu)\phi + Z\frac{\partial \phi}{\partial Z}\right\} ,$$

$$u_Z = -8(1-\nu)\frac{\partial \phi}{\partial Z} + 4Z\frac{\partial^2 \phi}{\partial Z^2} ,$$

$$\Theta = -8G\left\{(1-2\nu)\frac{\partial^2 \phi}{\partial Z^2} + Z\frac{\partial^3 \phi}{\partial Z^3}\right\} ,$$

$$\Phi = 32G\frac{\partial^2}{\partial \bar{z}^2}\left\{(1-2\nu)\phi + Z\frac{\partial \phi}{\partial Z}\right\} ,$$

$$\sigma_Z = -8G\frac{\partial^2 \phi}{\partial Z^2} + 8GZ\frac{\partial^3 \phi}{\partial Z^3} \text{ , and}$$

$$\Psi = 16GZ\frac{\partial^3 \phi}{\partial \bar{z}\partial Z^2} ,$$

with

$$D = u_x + iu_y ,$$

$$\Theta = \sigma_x + \sigma_y ,$$

$$\Phi = \sigma_x - \sigma_y + 2i\tau_{xy} \text{ ,and}$$

$$\Psi = \tau_{xz} + i\tau_{yz} .$$

In these equations, G is the shear modulus of the material and ν is Poisson's ratio. Additionally, Z is the third coordinate while z is the complex variable given by $z = x + iy$ and $\bar{z}$ is its complex conjugate. Given such forms of the equations, Green and Sneddon[16] found a solution of the problem by converting to an ellipsoidal coordinate system, λ, μ, ε, given by

$$\begin{aligned} a^2\left(a^2-b^2\right)x^2 &= \left(a^2+\lambda\right)\left(a^2+\mu\right)\left(a^2+\varepsilon\right) \\ b^2\left(b^2-a^2\right)y^2 &= \left(b^2+\lambda\right)\left(b^2+\mu\right)\left(b^2+\varepsilon\right) \\ a^2b^2Z^2 &= \lambda\mu\varepsilon \end{aligned}$$

where

$$\infty > \lambda \geq 0 \geq \mu \geq -b^2 \geq \varepsilon \geq -a^2 \ .$$

In this coordinate system, the solution can be found as an integration of combined coordinates as

$$\phi = \frac{ab^2 p}{32G \ E(k)} \int_\lambda^\infty \left\{ \frac{x^2}{a^2+s} + \frac{y^2}{b^2+s} + \frac{Z^2}{s} - 1 \right\} \frac{ds}{\sqrt{s\left(a^2+s\right)\left(b^2+s\right)}} \ ,$$

where *E(k)* is an elliptic integral of modulus *k*, with

$$k = \frac{\sqrt{a^2-b^2}}{a}$$

and with a complementary modulus, *k' = 1 - k*

Application to a Vertical Fracture (Length > Height)

The tilts normal to the face of a long vertical fracture can be found as

$$\begin{aligned} \frac{\partial u_Z}{\partial y} = \frac{-8AZ}{ab^2}\Bigg[& -\left(1-2\nu\right)\left\{k'^2\frac{\operatorname{sn}^2 u}{\operatorname{cn}^2 u}\right\}\frac{du}{d\lambda}\frac{\partial\lambda}{\partial y} \\ & + Z\left\{2k'^2\frac{\operatorname{sn}u\,\operatorname{dn}u}{\operatorname{cn}^3 u}\right\}\left(\frac{du}{d\lambda}\right)^2\frac{\partial\lambda}{\partial y}\frac{\partial\lambda}{\partial Z} \\ & + Z\left\{k'^2\frac{\operatorname{sn}^2 u}{\operatorname{cn}^2 u}\right\}\left(\frac{d^2u}{d\lambda^2}\frac{\partial\lambda}{\partial y}\frac{\partial\lambda}{\partial Z} + \frac{du}{d\lambda}\frac{\partial^2\lambda}{\partial y\partial Z}\right)\Bigg], \end{aligned}$$

where sn, dn and cn are Jacobian elliptic functions, *A* is given by

$$A = -\frac{ab^2P}{16GE(k)} \ ,$$

u is defined as

$$\lambda = a^2\frac{\operatorname{cn}u}{\operatorname{sn}u}$$

and *E(k)* is the complete elliptic integral of the second kind. The additional derivatives are found from

$$\frac{du}{d\lambda} = \frac{-\operatorname{sn}^3 u}{2a^2\operatorname{cn}u\,\operatorname{dn}u} \ ,$$

$$\frac{d^2u}{d\lambda^2}=\frac{-\mathrm{sn}^2 u}{2a^2}\left[3+\frac{\mathrm{sn}^2 u}{\mathrm{cn}^2 u}+k^2\frac{\mathrm{sn}^2 u}{\mathrm{dn}^2 u}\right]\frac{du}{d\lambda} ,$$

$$\frac{\partial\lambda}{\partial y}=\frac{2y\lambda\left(a^2+\lambda\right)}{(\lambda-\mu)(\lambda-\varepsilon)} ;$$

$$\frac{\partial\lambda}{\partial Z}=\frac{2Z\left(a^2+\lambda\right)\left(b^2+\lambda\right)}{(\lambda-\mu)(\lambda-\varepsilon)} ,$$

$$\frac{\partial^2\lambda}{\partial y\partial Z}=\frac{yZ}{4\left(h_1^2\right)^2\lambda\left(b^2+\lambda\right)}\left[-\frac{1}{\lambda}-\frac{1}{b^2+\lambda}+\frac{1}{2h_1^2}\left\{\frac{x^2}{\left(a^2+\lambda\right)^3}+\frac{y^2}{\left(b^2+\lambda\right)^3}+\frac{Z^2}{\lambda^3}\right\}\right] ,$$

and

$$h_1^2=\frac{(\lambda-\mu)(\lambda-\varepsilon)}{4\lambda\left(a^2+\lambda\right)\left(b^2+\lambda\right)} .$$

More information about these derivatives and other characteristics of the ellipsoidal confocal coordinate system can be found in Whittaker and Watson.[A2] This same reference has extensive information about the Jacobian elliptic functions, as does Abramowitz and Stegun.[A3] In addition, Sih and Liebowitz[A4] provide some discussion on the 3D-elliptic-crack solution that is useful.

Similarly, the tilts parallel to the fracture face are found from

$$\begin{aligned}\frac{\partial u_x}{\partial y}&=\frac{8(1-2\nu)Ax}{a^3}\left\{\mathrm{sn}^2 u\right\}\frac{du}{d\lambda}\frac{\partial\lambda}{\partial y}\\&+\frac{8AZ^2}{ab^2}\left[\left\{2k'^2\frac{\mathrm{sn}\,u\,\mathrm{dn}\,u}{\mathrm{cn}^3 u}\right\}\left(\frac{du}{d\lambda}\right)^2\frac{\partial\lambda}{\partial x}\frac{\partial\lambda}{\partial y}\right.\\&\left.+\left\{k'^2\frac{\mathrm{sn}^2 u}{\mathrm{cn}^2 u}\right\}\left\{\frac{d^2u}{d\lambda^2}\frac{\partial\lambda}{\partial x}\frac{\partial\lambda}{\partial y}+\frac{du}{d\lambda}\frac{\partial^2\lambda}{\partial x\partial y}\right\}\right]\end{aligned}$$

where the additional derivatives are given by

$$\frac{\partial\lambda}{\partial x}=\frac{2x\lambda\left(b^2+\lambda\right)}{(\lambda-\mu)(\lambda-\varepsilon)}$$

and

$$\frac{\partial^2\lambda}{\partial x\partial y}=\frac{xy}{4\left(h_1^2\right)^2\left(a^2+\lambda\right)\left(b^2+\lambda\right)}\left[-\frac{a^2+b^2+2\lambda}{\left(a^2+\lambda\right)\left(b^2+\lambda\right)}+\frac{1}{2h_1^2}\left\{\frac{x^2}{\left(a^2+\lambda\right)^3}+\frac{y^2}{\left(b^2+\lambda\right)^3}+\frac{Z^2}{\lambda^3}\right\}\right] .$$

The calculation of the λ, μ, ν coordinates requires the solution of the cubic equation

$$\lambda^3+\lambda^2\left(a^2+b^2-x^2-y^2-Z^2\right)+\lambda\left(a^2b^2-b^2x^2-a^2y^2-a^2Z^2-b^2Z^2\right)-a^2b^2Z^2=0$$

for λ followed by solution of the quadratic equation

$$\mu^2\left(a^2\lambda+\lambda\right)+\mu\left(a^2b^2Z^2+b^2\lambda Z^2+a^4\lambda+a^2\lambda^2-a^2\lambda x^2+b^2\lambda x^2\right)+a^4b^2Z^2+a^2b^2\lambda Z^2=0$$

for μ and then

$$\varepsilon = \frac{a^2 b^2 Z^2}{\lambda \mu}$$

The procedure for using these equations is as follows:

1. Select point x,y,Z for which the calculation is to be made
2. Determine the appropriate λ,μ,ε for this point
3. Determine the value of u
4. Obtain tilts.

Non-Vertical Fracture or Height Greater than Length

The previous solution is for a vertical fracture whose height is greater than its length, which are quite limiting constraints. However, this model can be used to also extract the tilts for a fracture with dip and for one whose height is greater than its length. To obtain the tilts for these cases, it is necessary to obtain the displacement derivatives for the seven other components. These are given as:

$$\begin{aligned}
\frac{\partial u_x}{\partial x} = {} & \frac{8(1-2\nu)A}{a^3 k^2}\{u - E(u)\} \\
& + \frac{8(1-2\nu)Ax}{a^3}\{\mathrm{sn}^2 u\}\frac{du}{d\lambda}\frac{\partial\lambda}{\partial x} \\
& + \frac{8AZ^2}{ab^2}\Bigg[\left\{2k'^2 \frac{\mathrm{sn}\,u\,\mathrm{dn}\,u}{\mathrm{cn}^3 u}\right\}\left(\frac{du}{d\lambda}\right)^2\left(\frac{\partial\lambda}{\partial x}\right)^2 \\
& + \left\{k'^2 \frac{\mathrm{sn}^2 u}{\mathrm{cn}^2 u}\right\}\left\{\frac{d^2 u}{d\lambda^2}\left(\frac{\partial\lambda}{\partial x}\right)^2 + \frac{du}{d\lambda}\frac{\partial^2\lambda}{\partial x^2}\right\}\Bigg]
\end{aligned}$$

$$\begin{aligned}
\frac{\partial u_x}{\partial Z} = {} & \frac{8(1-2\nu)Ax}{a^3}\{\mathrm{sn}^2 u\}\frac{du}{d\lambda}\frac{\partial\lambda}{\partial Z} \\
& + \frac{8AZ}{ab^2}\Bigg[\left\{2k'^2 \frac{\mathrm{sn}^2 u}{\mathrm{cn}^2 u}\right\}\frac{du}{d\lambda}\frac{\partial\lambda}{\partial x} \\
& + Z\left\{2k'^2 \frac{\mathrm{sn}\,u\,\mathrm{dn}\,u}{\mathrm{cn}^3 u}\right\}\left(\frac{du}{d\lambda}\right)^2 \frac{\partial\lambda}{\partial x}\frac{\partial\lambda}{\partial Z} \\
& + Z\left\{k'^2 \frac{\mathrm{sn}^2 u}{\mathrm{cn}^2 u}\right\}\left\{\frac{d^2 u}{d\lambda^2}\frac{\partial\lambda}{\partial x}\frac{\partial\lambda}{\partial Z} + \frac{du}{d\lambda}\frac{\partial^2\lambda}{\partial x \partial Z}\right\} + \Bigg]
\end{aligned}$$

$$
\begin{aligned}
\frac{\partial u_y}{\partial x} = & \frac{8(1-2\nu)Ay}{a^3}\left\{\frac{\mathrm{sn}^2 u}{\mathrm{dn}^2 u}\right\}\frac{du}{d\lambda}\frac{\partial \lambda}{\partial x} \\
& + \frac{8AZ^2}{ab^2}\Bigg[\Bigg[\left\{2k'^2\frac{\mathrm{sn}\,u\,\mathrm{dn}\,u}{\mathrm{cn}^3 u}\right\}\left(\frac{du}{d\lambda}\right)^2\frac{\partial \lambda}{\partial y}\frac{\partial \lambda}{\partial x} \\
& + \left\{k'^2\frac{\mathrm{sn}^2 u}{\mathrm{cn}^2 u}\right\}\left\{\frac{d^2u}{d\lambda^2}\frac{\partial \lambda}{\partial y}\frac{\partial \lambda}{\partial x} + \frac{du}{d\lambda}\frac{\partial^2 \lambda}{\partial y \partial x}\right\}\Bigg]\Bigg]
\end{aligned}
$$

$$
\begin{aligned}
\frac{\partial u_y}{\partial y} = & \frac{8(1-2\nu)A}{a^3k^2k'^2}\left\{E(u) - k'^2u - \frac{k^2\,\mathrm{sn}\,u\,\mathrm{cn}\,u}{\mathrm{dn}\,u}\right\} \\
& + \frac{8(1-2\eta)Ay}{a^3}\left\{\frac{\mathrm{sn}^2 u}{\mathrm{dn}^2 u}\right\}\frac{du}{d\lambda}\frac{\partial \lambda}{\partial y} \\
& + \frac{8AZ^2}{ab^2}\Bigg[\left\{2k'^2\frac{\mathrm{sn}\,u\,\mathrm{dn}\,u}{\mathrm{cn}^3 u}\right\}\left(\frac{du}{d\lambda}\right)^2\left(\frac{\partial \lambda}{\partial y}\right)^2 \\
& + \left\{k'^2\frac{\mathrm{sn}^2 u}{\mathrm{cn}^2 u}\right\}\left\{\frac{d^2u}{d\lambda^2}\left(\frac{\partial \lambda}{\partial y}\right)^2 + \frac{du}{d\lambda}\frac{\partial^2 \lambda}{\partial y^2}\right\}\Bigg]\Bigg]
\end{aligned}
$$

$$
\begin{aligned}
\frac{\partial u_y}{\partial Z} = & \frac{8(1-2\nu)Ay}{a^3}\left\{\frac{\mathrm{sn}^2 u}{\mathrm{dn}^2 u}\right\}\frac{du}{d\lambda}\frac{\partial \lambda}{\partial Z} \\
& + \frac{8AZ}{ab^2}\Bigg[\Bigg[\left\{2k'^2\frac{\mathrm{sn}^2 u}{\mathrm{cn}^2 u}\right\}\frac{du}{d\lambda}\frac{\partial \lambda}{\partial y} \\
& + Z\left\{2k'^2\frac{\mathrm{sn}\,u\,\mathrm{dn}\,u}{\mathrm{cn}^3 u}\right\}\left(\frac{du}{d\lambda}\right)^2\frac{\partial \lambda}{\partial y}\frac{\partial \lambda}{\partial Z} \\
& + Z\left\{k'^2\frac{\mathrm{sn}^2 u}{\mathrm{cn}^2 u}\right\}\left\{\frac{d^2u}{d\lambda^2}\frac{\partial \lambda}{\partial y}\frac{\partial \lambda}{\partial Z} + \frac{du}{d\lambda}\frac{\partial^2 \lambda}{\partial y \partial Z}\right\} + \Bigg]
\end{aligned}
$$

$$
\begin{aligned}
\frac{\partial u_Z}{\partial x} = & \frac{8AZ}{ab^2}\Bigg[-(1-2\nu)\left\{k'^2\frac{\mathrm{sn}^2 u}{\mathrm{cn}^2 u}\right\}\frac{du}{d\lambda}\frac{\partial \lambda}{\partial x} \\
& + Z\left\{2k'^2\frac{\mathrm{sn}\,u\,\mathrm{dn}\,u}{\mathrm{cn}^3 u}\right\}\left(\frac{du}{d\lambda}\right)^2\frac{\partial \lambda}{\partial x}\frac{\partial \lambda}{\partial Z} \\
& + Z\left\{k'^2\frac{\mathrm{sn}^2 u}{\mathrm{cn}^2 u}\right\}\left\{\frac{d^2u}{d\lambda^2}\frac{\partial \lambda}{\partial x}\frac{\partial \lambda}{\partial Z} + \frac{du}{d\lambda}\frac{\partial^2 \lambda}{\partial x \partial Z}\right\}\Bigg]\Bigg]
\end{aligned}
$$

$$\begin{aligned}\frac{\partial u_z}{\partial z} &= \frac{8(1-2\nu)A}{ab^2}\left\{E(u)-\frac{\operatorname{sn}u\operatorname{dn}u}{\operatorname{cn}u}\right\}\\ &\quad \frac{8(1+2\nu)AZ}{ab^2}\left[\left\{k'^2\frac{\operatorname{sn}^2u}{\operatorname{cn}^2u}\right\}\frac{du}{d\lambda}\frac{\partial\lambda}{\partial Z}\right.\\ &\quad +Z\left\{2k'^2\frac{\operatorname{sn}u\operatorname{dn}u}{\operatorname{cn}^3u}\right\}\left(\frac{du}{d\lambda}\right)^2\left(\frac{\partial\lambda}{\partial Z}\right)^2\\ &\quad \left.+Z\left\{k'^2\frac{\operatorname{sn}^2u}{\operatorname{cn}^2u}\right\}\left\{\frac{d^2u}{d\lambda^2}\left(\frac{\partial\lambda}{\partial Z}\right)^2+\frac{du}{d\lambda}\frac{\partial^2\lambda}{\partial Z^2}\right\}\right]\end{aligned}$$

To calculate these derivatives, some additional partial derivatives of λ need to be calculated. These are given by

$$\frac{\partial^2\lambda}{\partial x\partial Z}=\frac{xZ}{4\left(h_1^2\right)^2\lambda\left(a^2+\lambda\right)}\left[-\frac{1}{\lambda}-\frac{1}{a^2+\lambda}+\frac{1}{2h_1^2}\left\{\frac{x^2}{\left(a^2+\lambda\right)^3}+\frac{y^2}{\left(b^2+\lambda\right)^3}+\frac{Z^2}{\lambda^3}\right\}\right],$$

$$\frac{\partial^2\lambda}{\partial x^2}=\frac{1}{2\left(a^2+\lambda\right)H_1^2}\left[1-\frac{x^2}{\left(a^2+\lambda\right)^2H_1^2}+\frac{x^2}{4\left(a^2+\lambda\right)H_1^4}\left\{\frac{x^2}{\left(a^2+\lambda\right)^3}+\frac{y^2}{\left(b^2+\lambda\right)^3}+\frac{Z^2}{\lambda^3}\right\}\right],$$

$$\frac{\partial^2\lambda}{\partial y^2}=\frac{1}{2\left(b^2+\lambda\right)H_1^2}\left[1-\frac{y^2}{\left(b^2+\lambda\right)^2H_1^2}+\frac{y^2}{4\left(b^2+\lambda\right)H_1^4}\left\{\frac{x^2}{\left(a^2+\lambda\right)^3}+\frac{y^2}{\left(b^2+\lambda\right)^3}+\frac{Z^2}{\lambda^3}\right\}\right],$$

and

$$\frac{\partial^2\lambda}{\partial Z^2}=\frac{1}{2\lambda H_1^2}\left[1-\frac{Z^2}{\lambda^2H_1^2}+\frac{Z^2}{4\lambda H_1^4}\left\{\frac{x^2}{\left(a^2+\lambda\right)^3}+\frac{y^2}{\left(b^2+\lambda\right)^3}+\frac{Z^2}{\lambda^3}\right\}\right].$$

For vertical fractures that are taller than they are long, the normal tilt is given by interchanging a and b (essentially switching the length and the height) and using $\partial u_Z/\partial x$. The parallel tilt is given by $\partial u_y/\partial x$.

For fractures with dip, it is necessary to rotate the displacement gradients into the correct orientation and it is necessary to find the correct spatial parameters. Considering the transformation first, Figure A2 shows the fracture with dip and the observation well and a rotated view of this geometry. It is observed that the two displacements of interest, the one normal to the fracture (u_n) and the one parallel to the fracture (u_p) are given by

$$u_n=u_Z\cos\gamma+u_y\sin\gamma$$

$$u_p=u_x\ ,$$

where θ is the angle of the fracture plane references to the vertical (e.g., zero is a vertical fracture). The tiltmeter array measures the variation of the displacement derivatives along the s direction,

$$\frac{\partial u_n}{\partial s} = \frac{\partial u_n}{\partial Z}\frac{dZ}{ds} + \frac{\partial u_n}{\partial y}\frac{dy}{ds}$$

and

$$\frac{\partial u_p}{\partial s} = \frac{\partial u_p}{\partial Z}\frac{dZ}{ds} + \frac{\partial u_p}{\partial y}\frac{dy}{ds}.$$

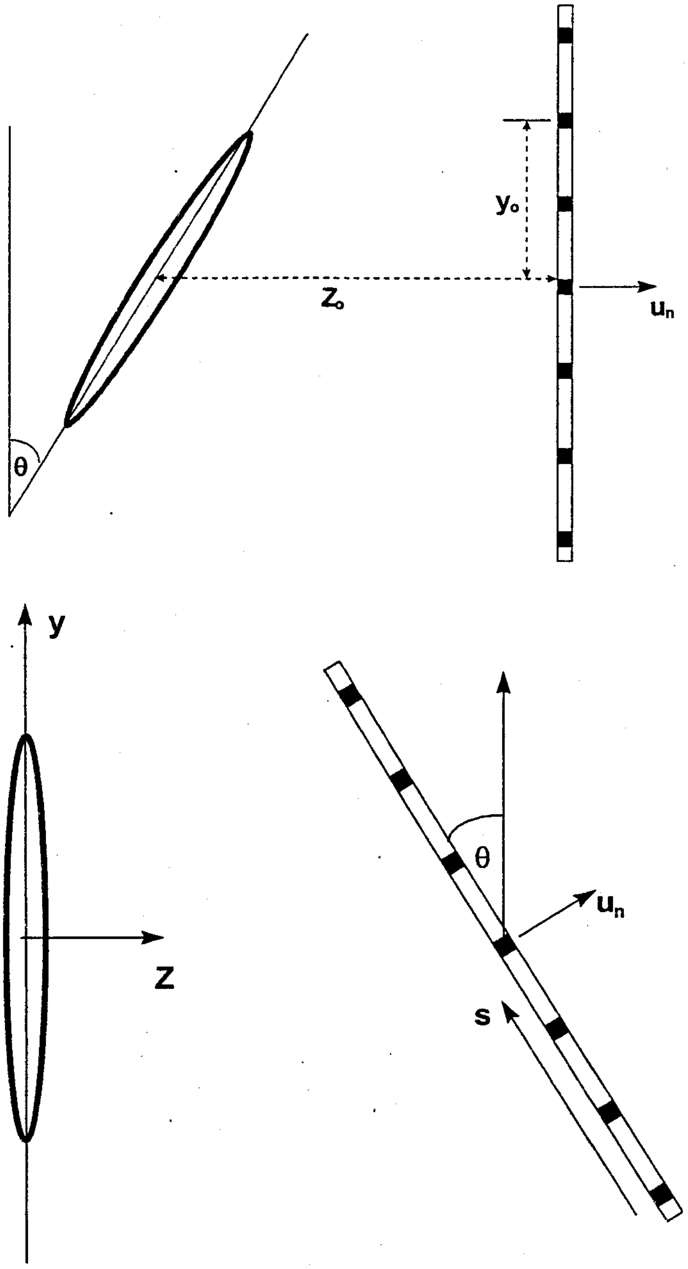

Figure 4 Geometry for fracture with dip.

Since the two spatial derivatives are given by

$$\frac{dZ}{ds} = -\sin\gamma$$

and

$$\frac{dy}{ds} = \cos\gamma$$

the tilt derivatives can be reduced to

$$\frac{\partial u_n}{\partial s} = \sin\gamma\cos\gamma\left[-\frac{\partial u_Z}{\partial Z} + \frac{\partial u_y}{\partial y}\right] - \sin^2\gamma\frac{\partial u_y}{\partial Z} + \cos^2\lambda\frac{\partial u_Z}{\partial y}$$

and

$$\frac{\partial u_p}{\partial s} = -\sin\gamma\frac{\partial u_x}{\partial Z} + \cos\gamma\frac{\partial u_x}{\partial y}\ .$$

If the fracture is taller than it is long, the a and b should be switched and the appropriate derivatives are

$$\frac{\partial u_n}{\partial s} = \sin\gamma\cos\gamma\left[-\frac{\partial u_Z}{\partial Z} + \frac{\partial u_x}{\partial x}\right] - \sin^2\gamma\frac{\partial u_x}{\partial Z} + \cos^2\gamma\frac{\partial u_Z}{\partial x}$$

and

$$\frac{\partial u_p}{\partial s} = -\sin\gamma\frac{\partial u_y}{\partial Z} + \cos\gamma\frac{\partial u_y}{\partial x}\ .$$

The final issue is the correct geometric parameters to characterize the distance from the fracture to the tiltmeters. Referring to the unrotated schematic in Figure A2, it can be found from geometry considerations that

$$\hat{x} = x$$

$$\hat{y} = Z_o \sin\gamma + y_o \cos\gamma$$

and

$$\hat{Z} = Z_o \cos\gamma - y_o \sin\varphi\ ,$$

where the variables with hats are the correct distances to use in the analysis. Of course, if the fracture is taller than it is long, then the x and y variable need to be reversed so that

$$\hat{x} = Z_o \sin\gamma + x_o \cos\gamma$$

$$\hat{y} = y\ ,$$

where the vertical distance from the crack centerline to the tiltmeter of interest is now x_o.

These equations complete the analysis of downhole tilt data for any fracture of any geometry, as long as it is far from the free surface.

Appendix A References

1. Green, A.E. and Sneddon, I.N., "The Distribution of Stress in the Neighbourhood of a Flat Elliptic Crack in an Elastic Solid," *Proc. Camb. Phil. Soc.*, **46**, pp. 159-163, 1950.
2. Whittaker, E.T. and Watson, G.N., *A Course of Modern Analysis*, Cambridge, 1927.
3. Abramowitz, M. and Stegun, I.A., *Handbook of Mathematical Functions*, Dover Publications, New York, 1970.
4. Sih, G.C. and Liebowitz, H., "Mathematical Theories of Brittle Fracture", in *Fracture*, Liebowitz, ed., **II**, Academic Press, New York, p.137, 1968.

APPENDIX B
DISLOCATION EQUATIONS

The solution for a tensile dislocation of any size and orientation in a semi-infinite medium is given by Okada[B1]. This expression is very useful, but it is relatively lengthy and complicated. A simple expression for use with downhole tiltmeters can be developed by considering an infinitely long dislocation in an infinite medium. This solution will be accurate whenever the depth to the fracture is considerably larger than the height of the fracture and the depth to the shallowest monitoring station is relatively large. The expression for a tensile dislocation in an infinite medium can be extracted fairly easily using Maruyama's expressions,[B2] as follows.

The displacement due to any appropriate dislocation in an infinite medium is given by

$$u_m(Q) = \iint_{\Sigma} \Delta u_k(P) T_{kl}^m(P,Q) n_l(P) d\Sigma \ ,$$

where $u_m(Q)$ is the displacement of the i^{th} direction at the monitoring point Q, $\Delta u_k(P)$ is the opening (or other movement) of the dislocation at some point P on the boundary Σ, $T_{kl}^m(P,Q)$ is the kl component of stress at P due to a unit body force in the m direction located at Q, and $n_l(P)$ is the outward normal of the dislocation surface at the point P. Maruyama[B2] gives

$$T_{kl}^m(P,Q) = \frac{1}{4\pi}\left\{(1-\alpha)\left(-\delta_{kl}\frac{r_m}{r^3} + \delta_{mk}\frac{r_l}{r^3} + \delta_{lm}\frac{r_k}{r^3}\right) + 3\alpha\frac{r_k r_l r_m}{r^5}\right\} ,$$

where δ is the Kronecker delta,

$$\alpha = \frac{1}{2(1-\nu)} ,$$

$$r_i = x_i - \xi_i ,$$

and

$$r = \sqrt{(x_1-\xi_1)^2 + (x_2-\xi_2)^2 + (x_3-\xi_3)^2}$$

for

$$P = P(\xi_1,\xi_2,\xi_3), \quad Q = Q(x_1,x_2,x_3) \ .$$

For the simple case of a vertical dislocation of constant width, b, in the x_2 direction, then

$$\Delta u_k = (0,b,0)$$

and

$$n_l = (0,1,0) \ .$$

For downhole tiltmeters monitoring a 2D vertical fracture, only the vertical derivative of the normal displacement is needed and T is simplified as

$$T_{22}^2 = \frac{1}{4\pi}\left\{(1-\alpha)\frac{r_2}{r^3} + 3\alpha\frac{r_2^3}{r^5}\right\}$$

Inserting all of these equations, the displacement of interest is given by

$$u_2(Q) = \frac{b}{4\pi}\int_{-H/2}^{H/2} d\xi_1 \int_{-L}^{L}\left[(1-\alpha)\frac{r_2}{r^3} + 3\alpha\frac{r_2^3}{r^5}\right] d\xi_3$$

Performing the integrations and simplifying in the limit as $L \to \infty$, the normal displacement at some distance, x_2, for a 2D vertical fracture is given by

$$u_2(Q) = \frac{b}{2\pi}\left\{\tan^{-1}\left[\frac{H/2 - x_1}{x_2}\right] + \tan^{-1}\left[\frac{H/2 + x_1}{x_2}\right]\right\}$$

$$+\frac{b\alpha}{2\pi}\left\{\frac{\left(H/2 - x_1\right)x_2}{\left(H/2 - x_1\right)^2 + x_2^2} + \frac{\left(H/2 + x_1\right)x_2}{\left(H/2 + x_1\right)^2 + x_2^2}\right\}$$

with H being the fracture height, x_2 being the normal distance (horizontally) to the monitoring station, and x_1 being the vertical location of the monitoring station relative to the center of the fracture. Taking the derivative, the tilt at some position (x_1,x_2) is

$$\frac{\partial u_2}{\partial x_1}(Q) = \frac{b}{2\pi}\left\{\frac{-x_2}{x_2^2 + \left(H/2 - x_1\right)^2} + \frac{x_2}{x_2^2 + \left(H/2 + x_1\right)^2}\right\}$$

$$+\frac{b\alpha}{2\pi}\left\{\frac{2x_2\left(H/2 - x_1\right)^2}{\left[x_2^2 + \left(H/2 - x_1\right)^2\right]^2} - \frac{2x_2\left(H/2 + x_1\right)^2}{\left[x_2^2 + \left(H/2 + x_1\right)^2\right]^2}\right\}$$

This equation is a relatively simple expression that can easily be used to check and compare results.

In comparing dislocation and crack models, one needs to find some basis to compare the crack pressure to the dislocation width. The most obvious solution is to equate the average displacement for both cases, or equivalently, the integrated displacement for both cases, assuming equal heights. Doing so results in a crack pressure given by

$$\Delta P = \frac{2Eb}{\pi\left(1 - \nu^2\right)H}$$

or in a dislocation width given by

$$b = \frac{\pi\left(1 - \nu^2\right)H\Delta P}{2E}.$$

Appendix B References

1. Okada, Y., "Internal Deformation Due to Shear and Tensile Faults in a Half-Space," *Bulletin of the Seismological Society of America*, **82**, No. 2, pp. 1018-1040, April 1992.
2. Maruyama, T., "Statical Elastic Dislocations in an Infinite and Semi-Infinite Medium," *Bulletin of the Earthquake Research Institute*, Tokyo University, **42**, pp. 289-368, 1964.

APPENDIX C
M-SITE B-SAND CEMENTED TILTMETER RESULTS

This appendix presents data similar to that shown in this report for the M-Site B-sandstone fracturing experiments. However, these tiltmeters were cemented in place and thus coupling can not be an issue relative to any difficulties in interpreting the data. Figure C1 shows the locations of the tiltmeters relative to the two sandstone intervals that were fractured. The data shown in this appendix are from the B-sandstone testing when the tiltmeters were new and there was little doubt that they were all functioning correctly. During the B-sandstone testing, there were 7 injections including a cross-linked gel breakdown (1B), a KCl step-rate test (2B), two KCl pump-in/shut-in tests (3B & 4B) of which the second was twice the volume of the first, two identical linear gel minifracs (5B & 6B), and a propped stimulation (7B).

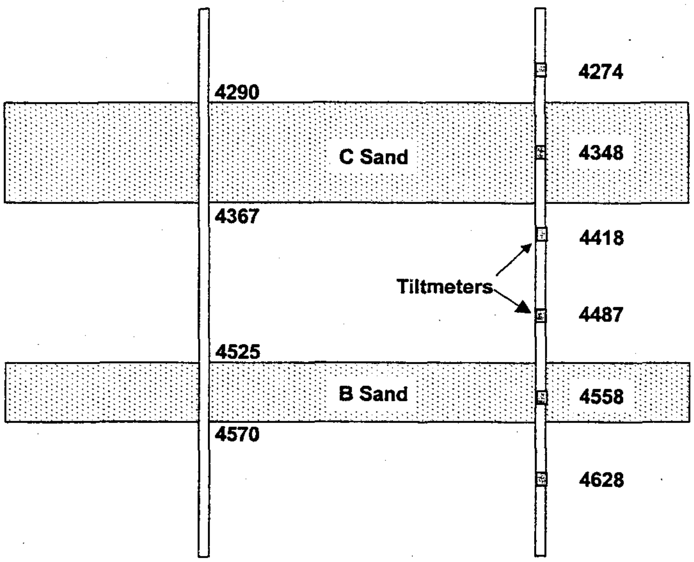

Figure C1. Tiltmeter geometry for M-Site testing

Figure C1 shows example data for the two axes of a tiltmeter located at a depth of 4487 ft during several days of testing. This particular example shows data from the four smallest injections because it is easy to see the noise levels and the tides. In general, the noise level was on the order of 10 nanoradians (0.01 microradians) and the tides were typically under 50 nanoradians. The wireline tiltmeters at Mounds had noise levels of 1-2 microradians.

The small initial injections had signal levels less than 1 microradian, while the larger KCl pump-in tests had levels of a few microradians. Later injections that were larger, higher rate, and more viscous had amplitudes that were 2-3 times these levels. Note that these tiltmeters were oriented so that separate components could be determined. In this case, the parallel component is small, as it should be since it is not directed at the fracture.

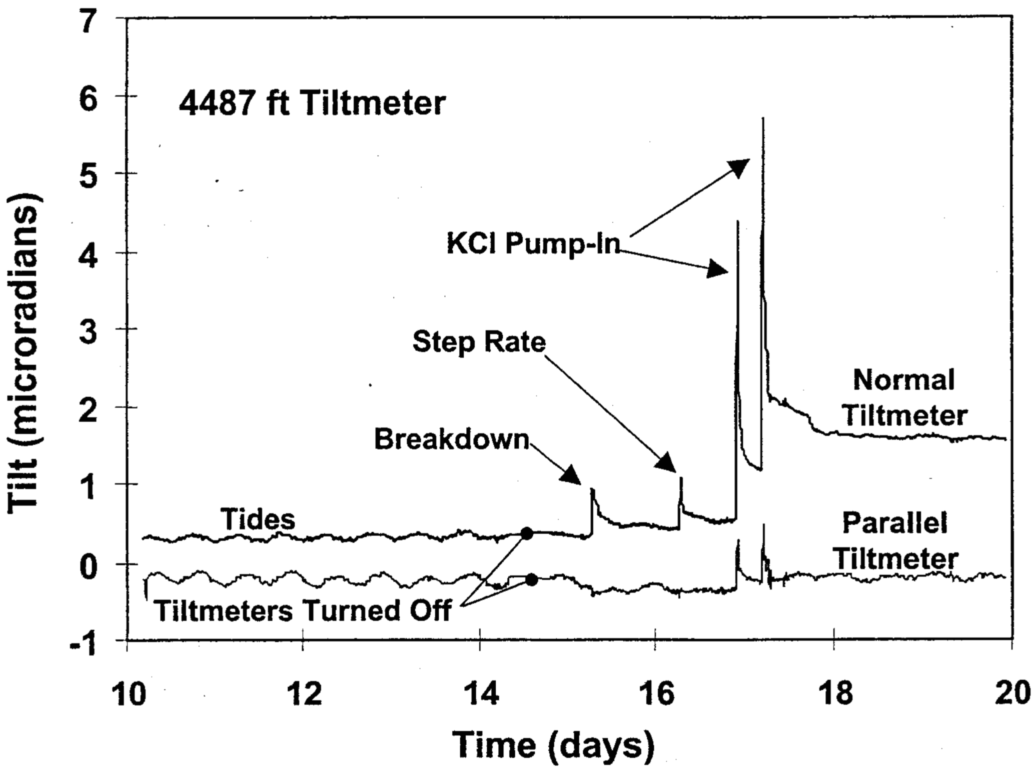

Figure C2. Example M-Site B-sandstone tiltmeter data over a 10 day period of testing

The phase information can also be examined to check the orientation of the tiltmeters. The phase is simply the angular relationship between the amplitude of the two channels. Figure C3 shows the phase development for the breakdown injection in the B sandstone. Prior to the 10 minute time location when pumping starts, the tiltmeters are responding to noise and tides and the phase is uncorrelated. Once a fracture is initiated, the tiltmeters quickly zero in on an orientation and hold it throughout the injection and during the shut in. If the fracture were very long, the phase would be 90° for all levels. Because (a) the monitor location is considerably offset from the normal line between the injection and monitor wells and (b) the fracture is small, the phase obtained here is within about 30° of the expected ±90° value. The lowest tiltmeter has a negative phase because it is the only one below the center of the fracture.

Figure C4 shows the phase at the end of each injection for all B sand tests and all tiltmeter levels. In general, the phases are within about 30° of the expected ±90° value. Because of the offset of the monitor well relative to the fracture, the phases do not quite reach the expected value. The variability of the top trace is probably because it is near the center of the fracture and has small amplitude that is easily perturbed by noise and by slight shifts in the center of the fracture. For the most part, these data are relatively consistent and they agree with the axes orienations.

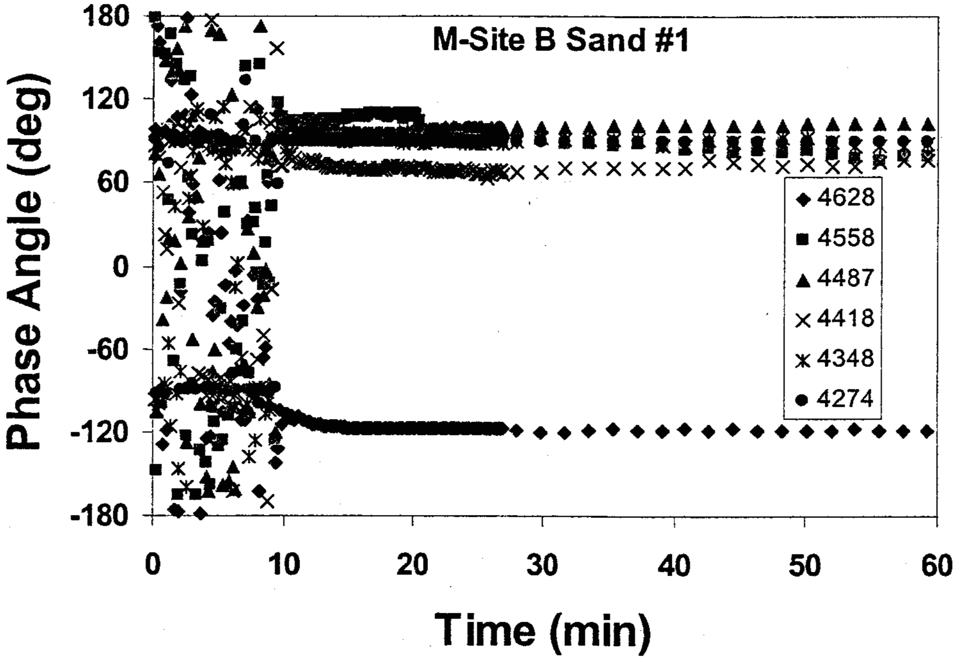

Figure C3. Phase development during injection (breakdown pump).

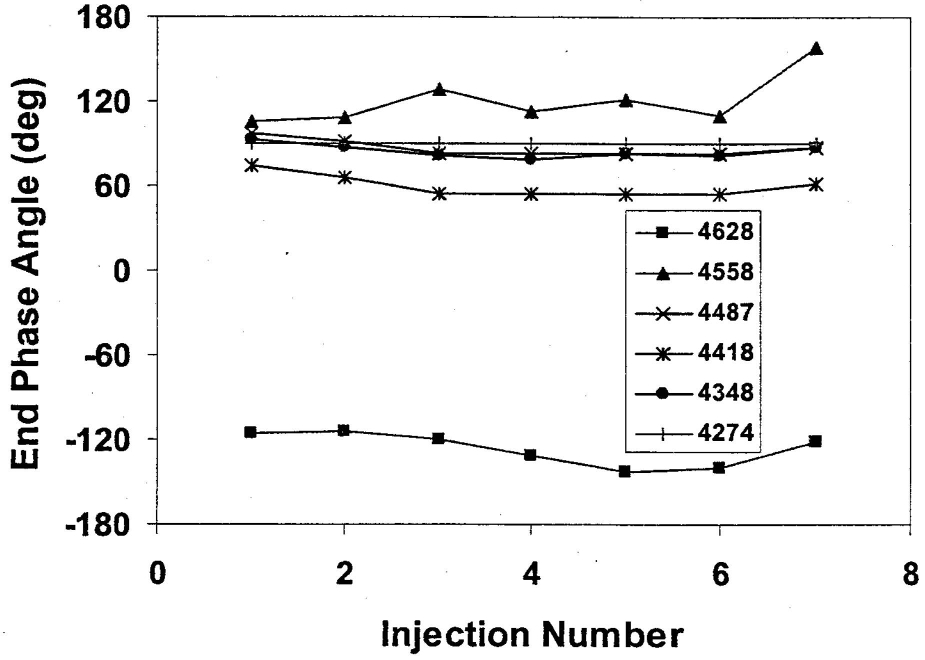

Figure C4. Phase data at the end of each injection in the B sandstone.

The correlated amplitude data for each of the B sand injections are shown in Figure C5. The first four injections are very small and it is difficult to see much movement in the amplitudes, but later expanded views of the data will show more contrast. The most important points here are:

- There are only six tiltmeters
- There is only one tiltmeter below the B sand fracture
- The second tiltmeter from the bottom is in the bottom of the B sandstone
- A clear progression of amplitudes can be seen with the increasingly larger injections.

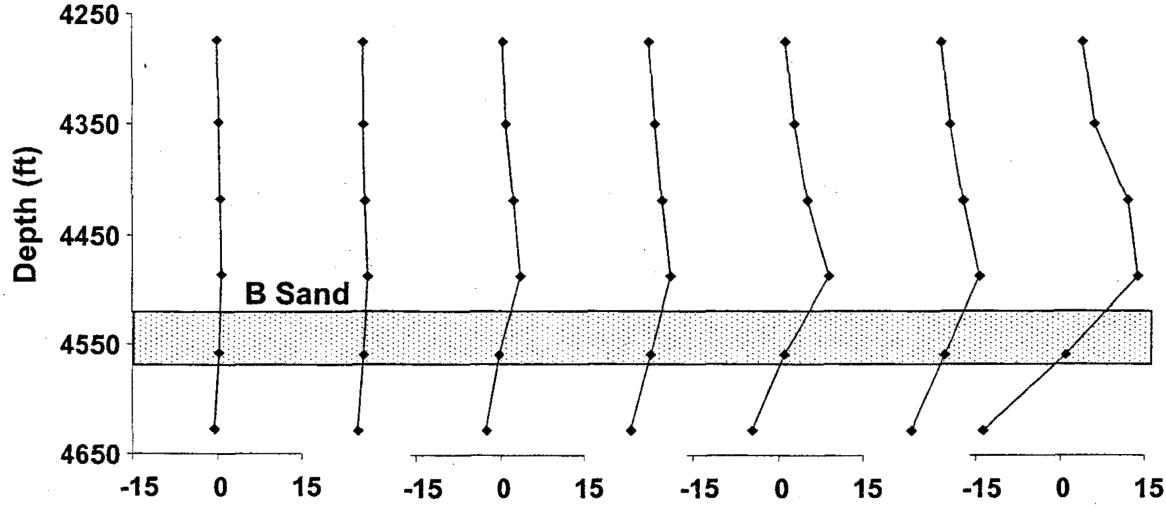

Figure C5. Maximum amplitude data for the seven B sandstone injections

The inversion results for the B sandstone injections are shown in Figures C6-C12. These inversions are all constrained by the pressure and the azimuth, which are known, and the last three inversions are also constrained by the inclination (since the best fit would have had about a 20° inclination from the vertical and this was not observed in the cored fractures at M-Site). In general, there are misfits of the data, but the misfits and the asymmetry are not as severe as in the Mounds results. Standard errors at M-Site were large, but this was primarily due to the smaller numbers of tiltmeters used. It is also clear that even one additional tiltmeter below the original array would have been very helpful in interpreting the data.

The heights for most of the injections are about 30 ft greater than the heights measured using the microseismic method and the lengths are all short by a factor of 2-3. The height for the last injection (the stimulation) is about 20 ft smaller than the maximum height measured with the microseismic technique, but is relatively close to the average height of the fracture, as measured by the microseisms. In a separate report on tiltmeter analyses at M-Site[C1], finite-element analyses were used to show that most of the misfit at that site could be explained by the complex layering in this fluvial environment.

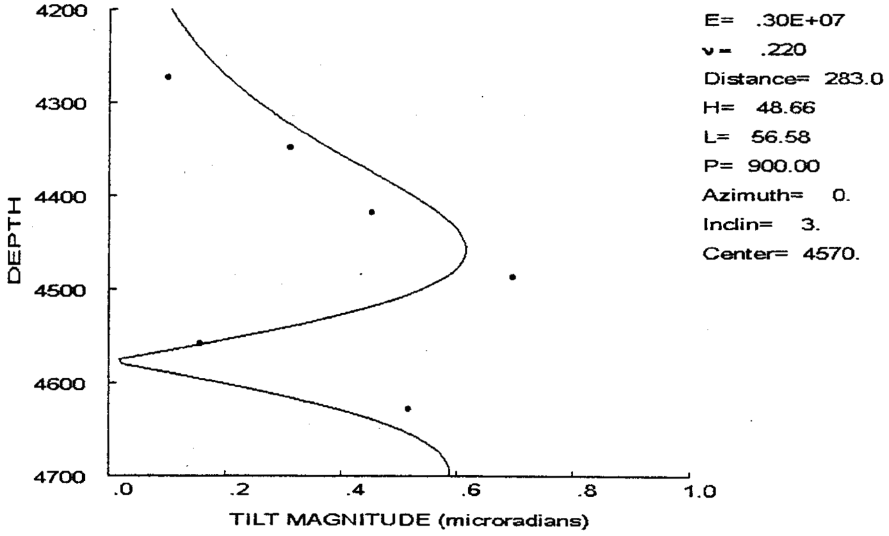

Figure C6. Inversion results for breakdown injection in B sandstone.

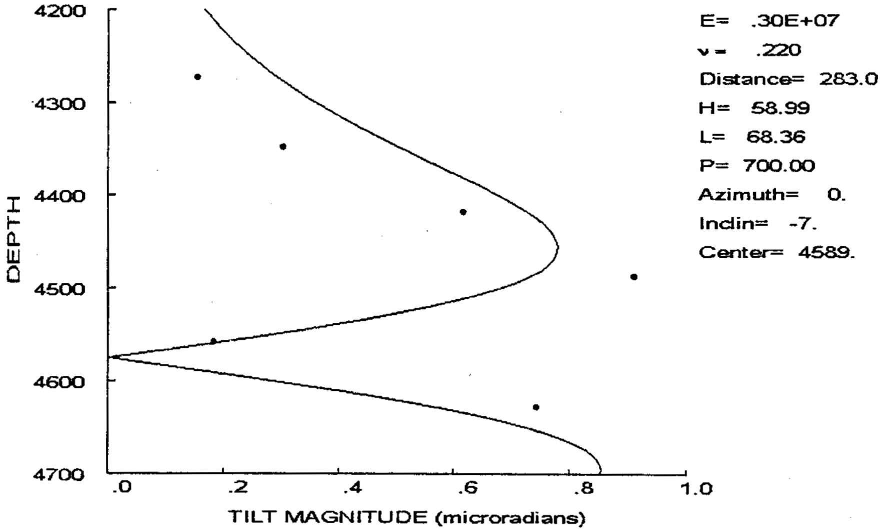

Figure C7. Inversion results for step-rate injection (#2) in B sandstone.

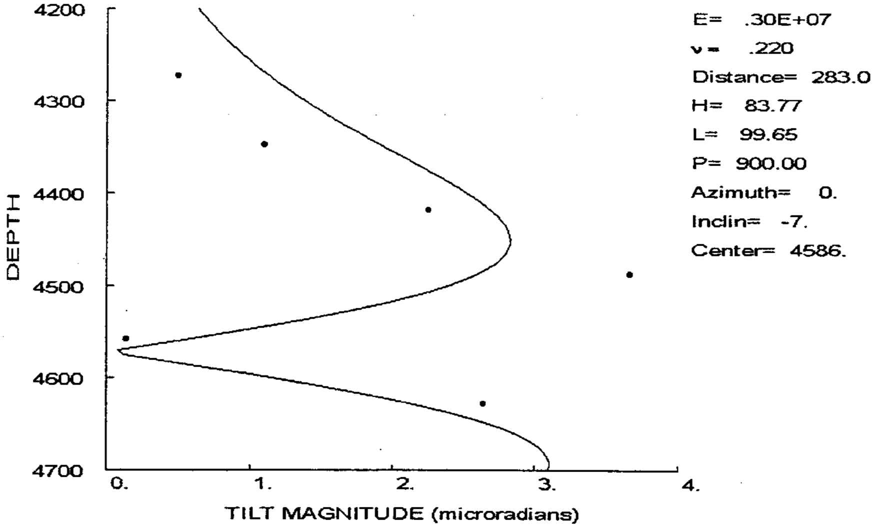

Figure C8. Inversion results for first pump-in injection (#3) in B sandstone.

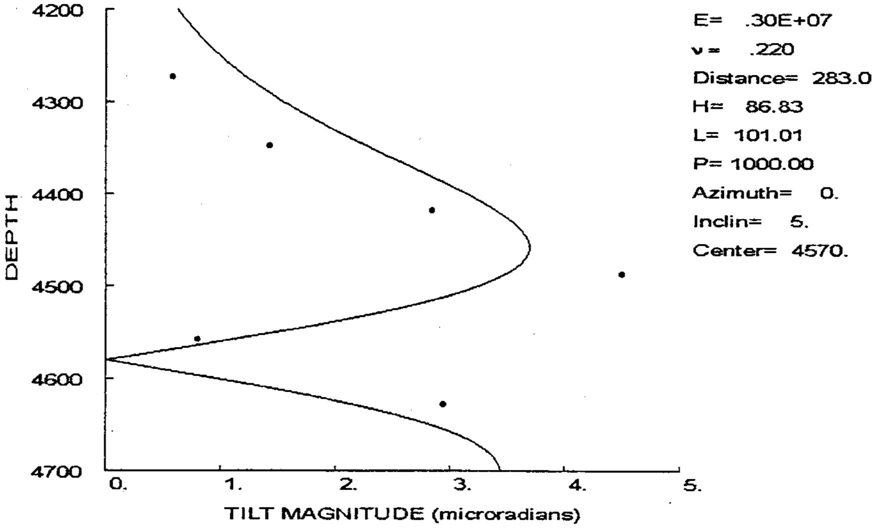

Figure C9. Inversion results for second pump-in injection (#4) in B sandstone.

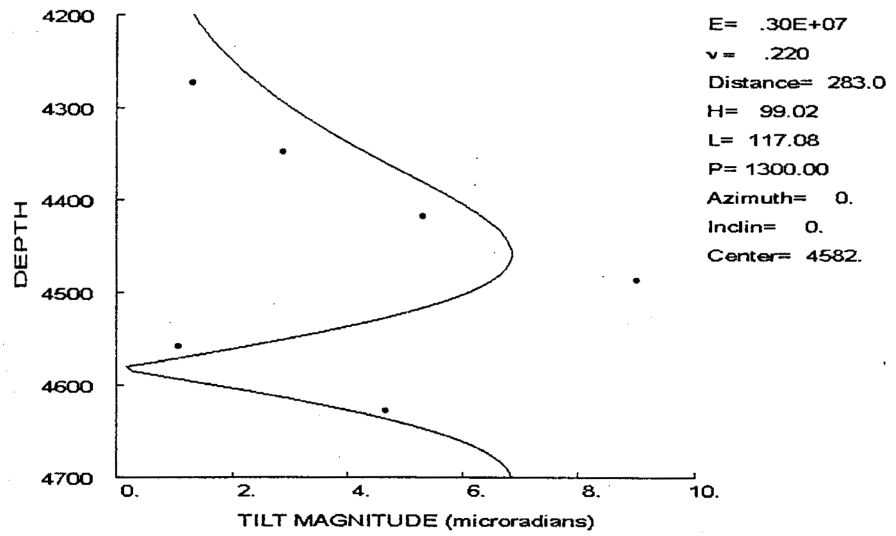

Figure C10. Inversion results for first minifrac injection (#5) in B sandstone.

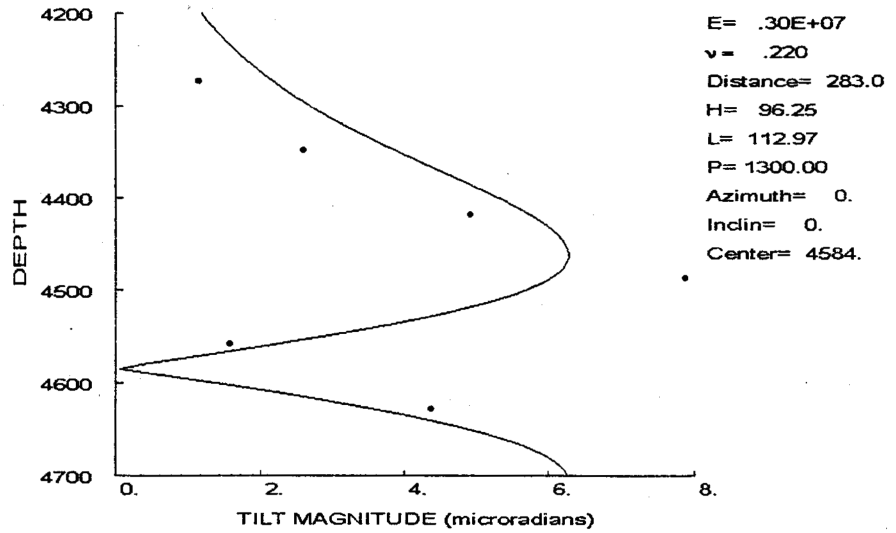

Figure C11. Inversion results for second minifrac injection (#6) in B sandstone.

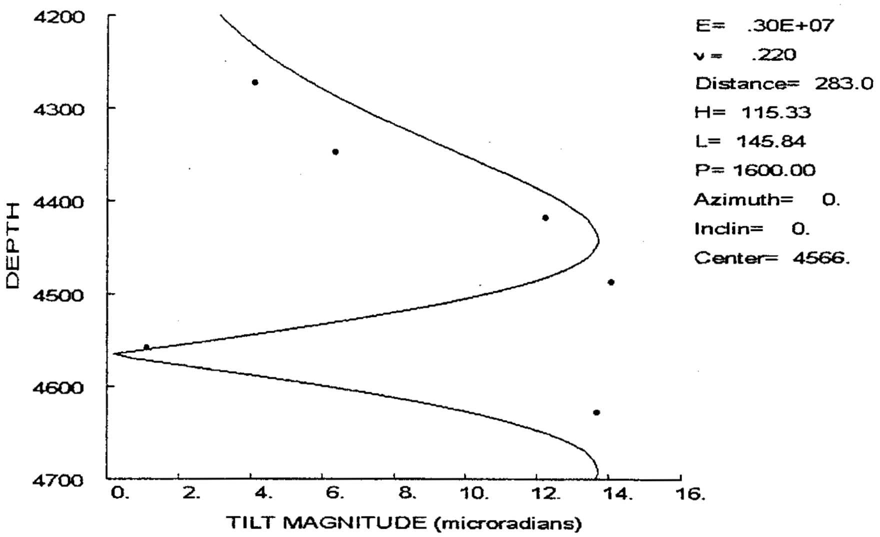

Figure C12. Inversion results for stimulation injection (#7) in B sandstone.

Appendix C References

1. Engler, B.P. and Warpinski, N.R., “Hydraulic Fracture Imaging Using Inclinometers at M-Site: Finite-Element Analyses of the B-Sandstone Experiments,” GRI Topical Report, GRI-97/0361, December 1997.

APPENDIX D
COMPARISON WITH PINNACLE DISLOCATION INVERSION

Pinnacle Technologies Incorporated fielded the downhole-tiltmeter arrays used during these tests (they also fielded the surface tiltmeter array, but those data are not considered here). Pinnacle's results are discussed in Griffin et al.[D1] and detailed information are provided in the Mounds project CD.[D2] As part of the service offered by Pinnacle, the data were inverted using Okada's[D3] dislocation model and fracture parameters were derived. This appendix shows an injection-by-injection comparison of the inversion results from this study using the 3D crack model with the Pinnacle inversion results using the rectangular dislocation model. All of the following figures show a side view of the fracture length and height with respect to the injection interval. For those crack results where the fracture length is greater than 500 ft, it is assumed that the length is 500 ft (since the effect of longer fractures is insignificant). In general, the comparison between results is better in the Atoka tests than in the Wilcox injections. The discrepancy may be partly due to the difference in models, to the correction of "tears" in this report, to different constraints used in the inversion process, or to the additional extraction of horizontal components in Pinnacle's inversion.

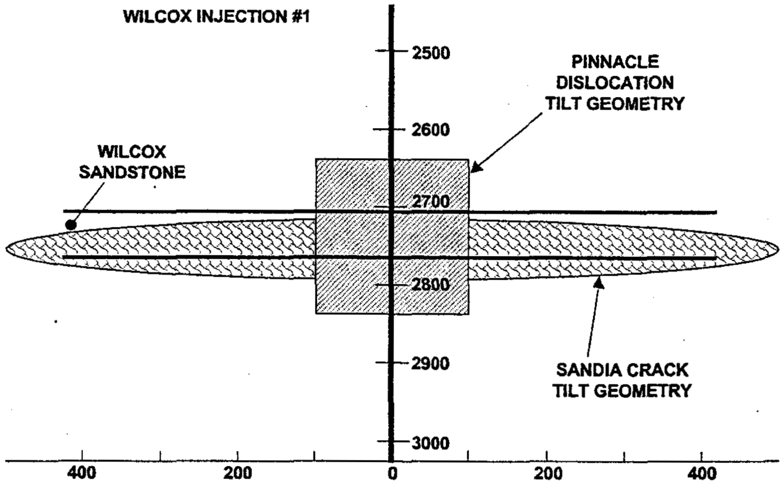

Figure D1. Comparison of Pinnacle dislocation and Sandia crack inversion, Wilcox #1.

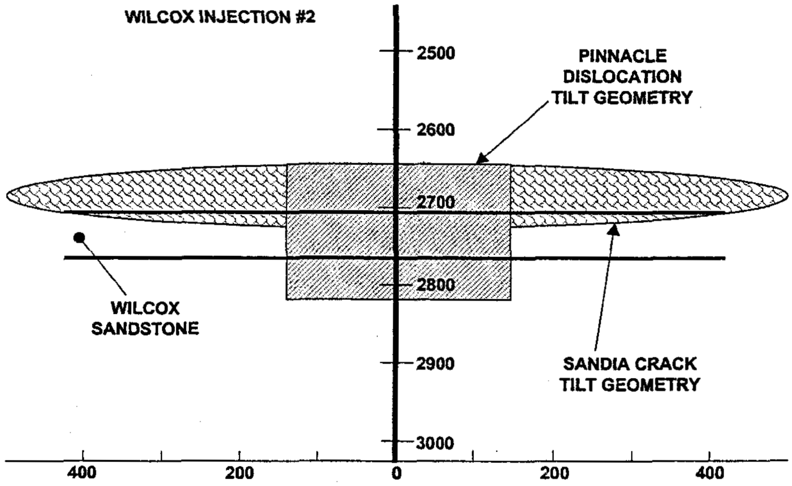

Figure D2. Comparison of Pinnacle dislocation and Sandia crack inversion, Wilcox #2.

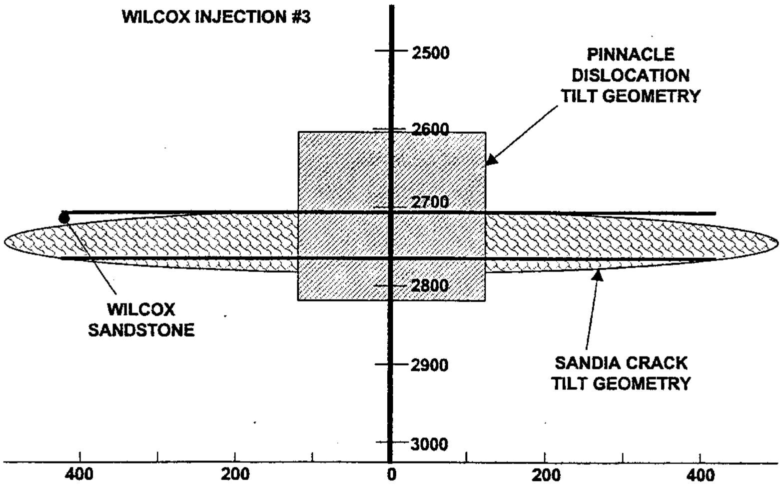

Figure D3. Comparison of Pinnacle dislocation and Sandia crack inversion, Wilcox #3.

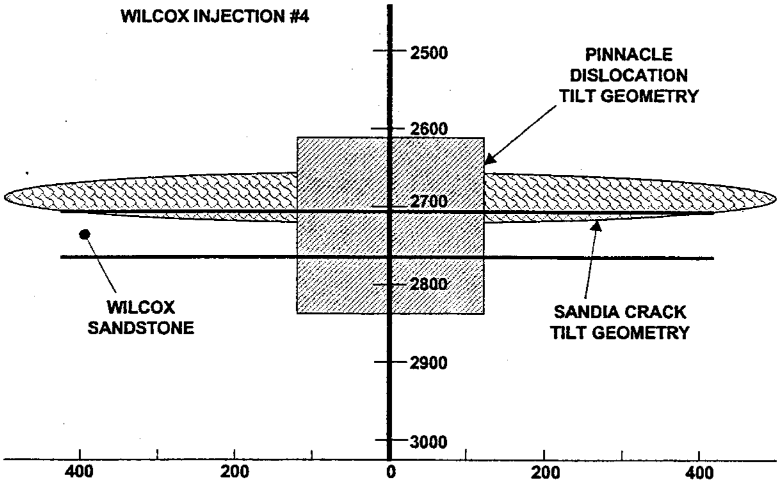

Figure D4. Comparison of Pinnacle dislocation and Sandia crack inversion, Wilcox #4.

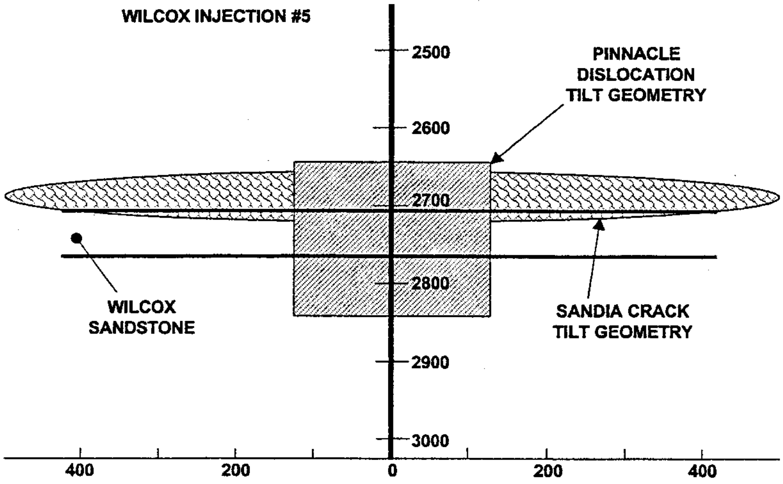

Figure D5. Comparison of Pinnacle dislocation and Sandia crack inversion, Wilcox #5.

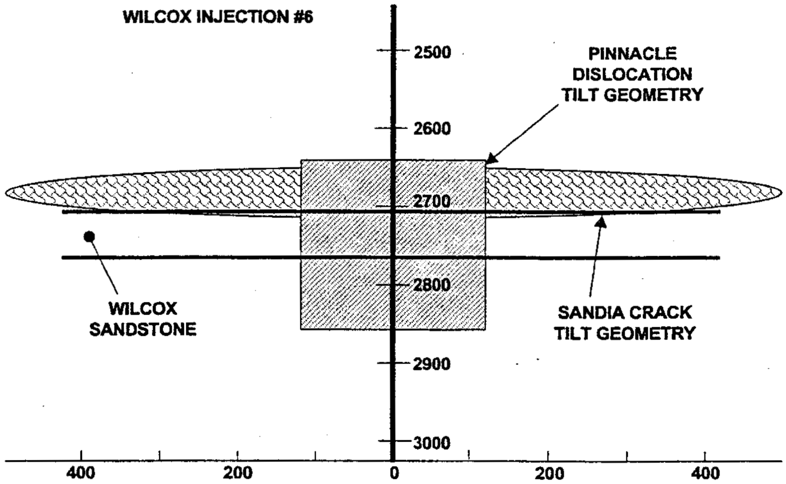

Figure D6. Comparison of Pinnacle dislocation and Sandia crack inversion, Wilcox #6.

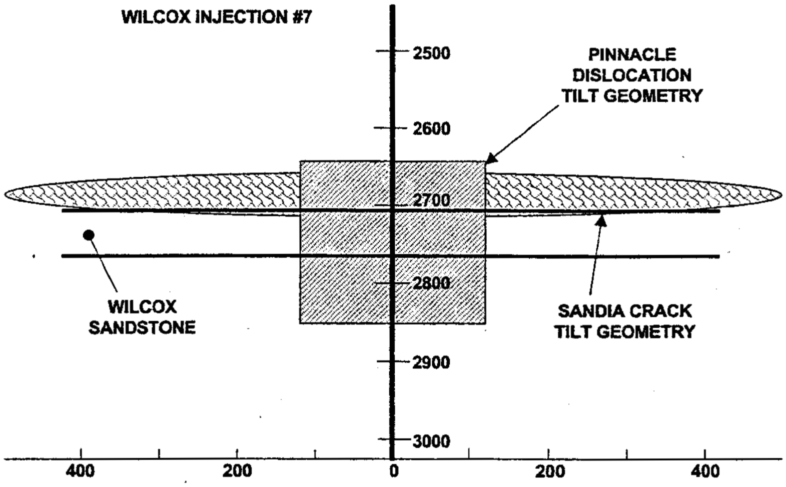

Figure D7. Comparison of Pinnacle dislocation and Sandia crack inversion, Wilcox #7.

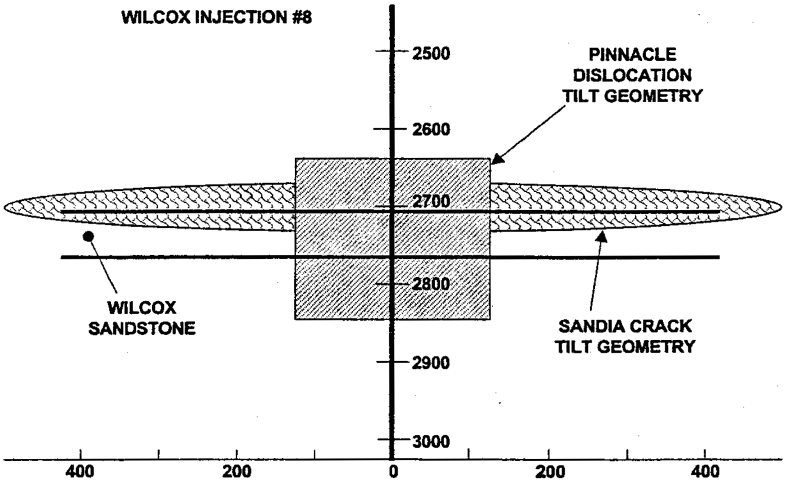

Figure D8. Comparison of Pinnacle dislocation and Sandia crack inversion, Wilcox #8.

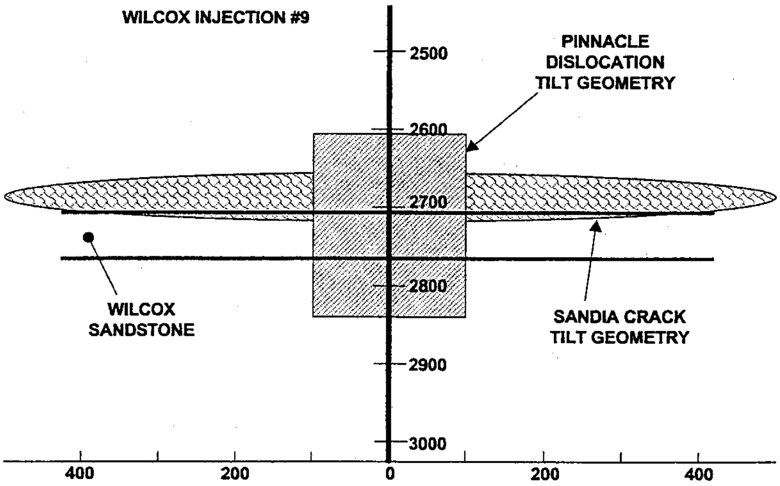

Figure D9. Comparison of Pinnacle dislocation and Sandia crack inversion, Wilcox #9.

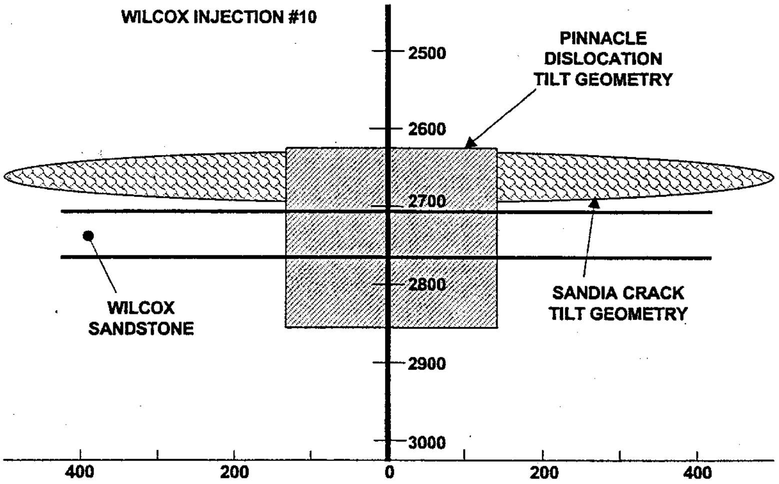

Figure D10. Comparison of Pinnacle dislocation and Sandia crack inversion, Wilcox #10.

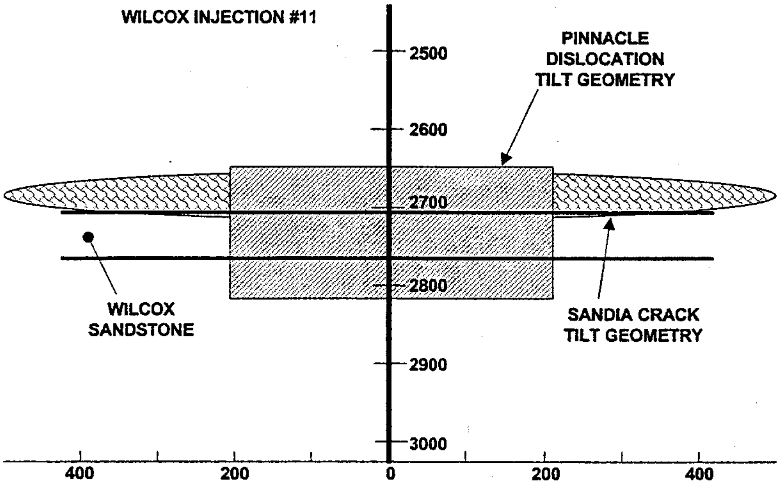

Figure D11. Comparison of Pinnacle dislocation and Sandia crack inversion, Wilcox #11.

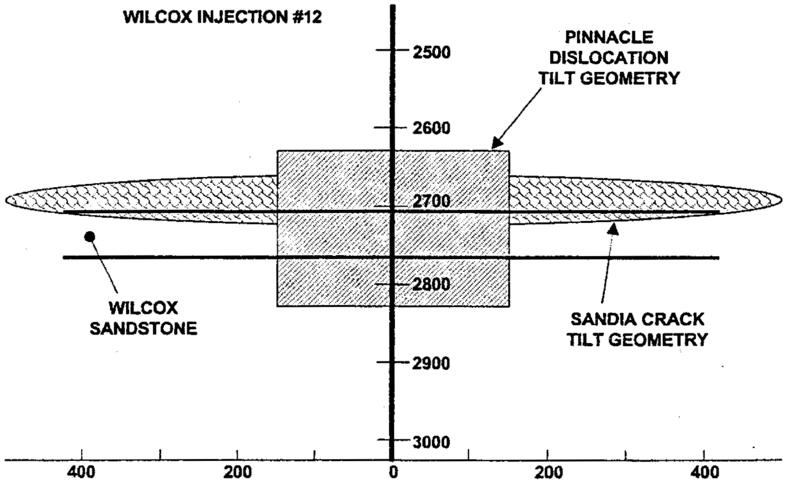

Figure D12. Comparison of Pinnacle dislocation and Sandia crack inversion, Wilcox #12.

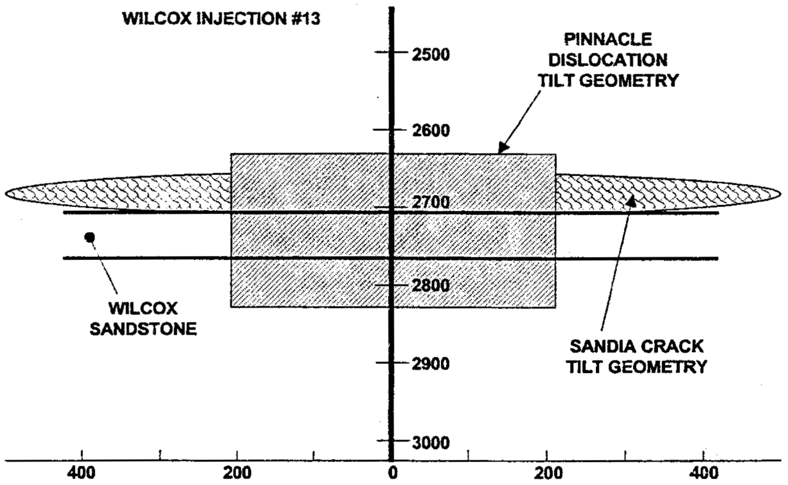

Figure D13. Comparison of Pinnacle dislocation and Sandia crack inversion, Wilcox #13.

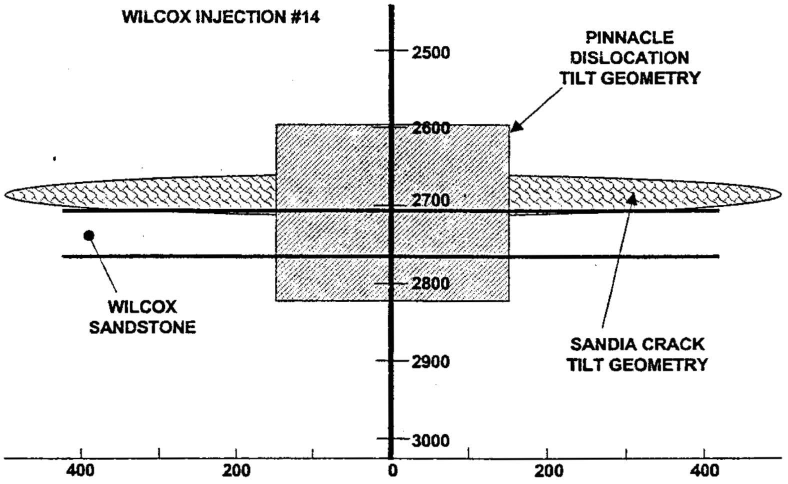

Figure D14. Comparison of Pinnacle dislocation and Sandia crack inversion, Wilcox #14.

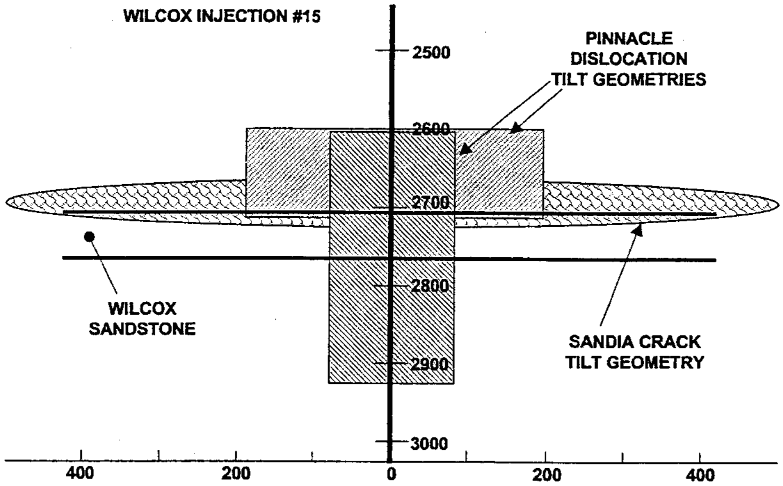

Figure D15. Comparison of Pinnacle dislocation and Sandia crack inversion, Wilcox #15.

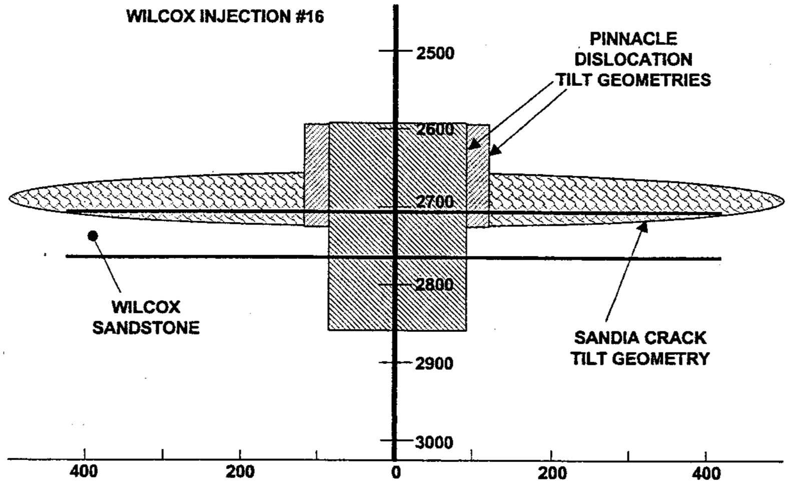

Figure D16. Comparison of Pinnacle dislocation and Sandia crack inversion, Wilcox #16.

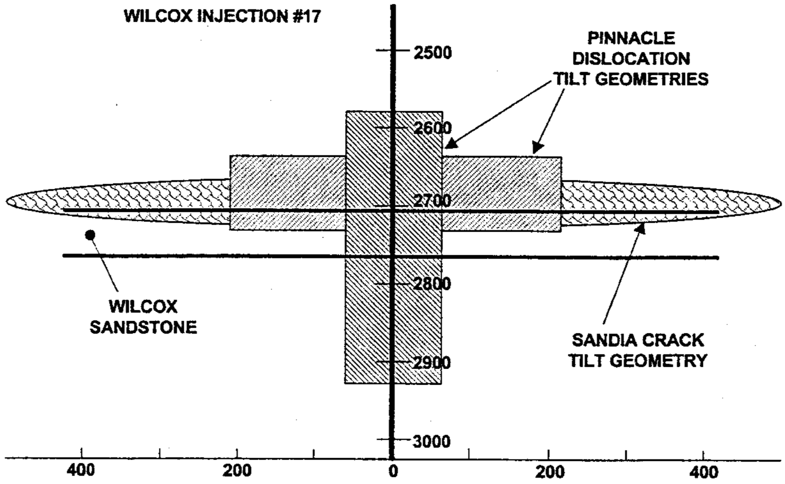

Figure D17. Comparison of Pinnacle dislocation and Sandia crack inversion, Wilcox #17.

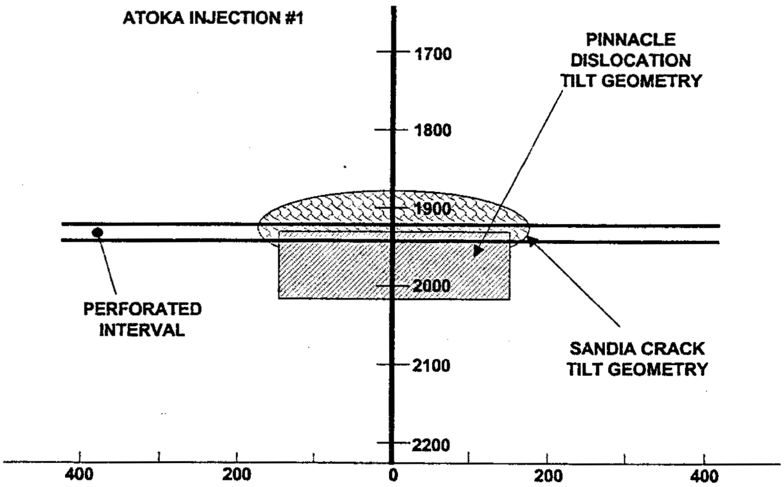

Figure D18. Comparison of Pinnacle dislocation and Sandia crack inversion, Atoka #1.

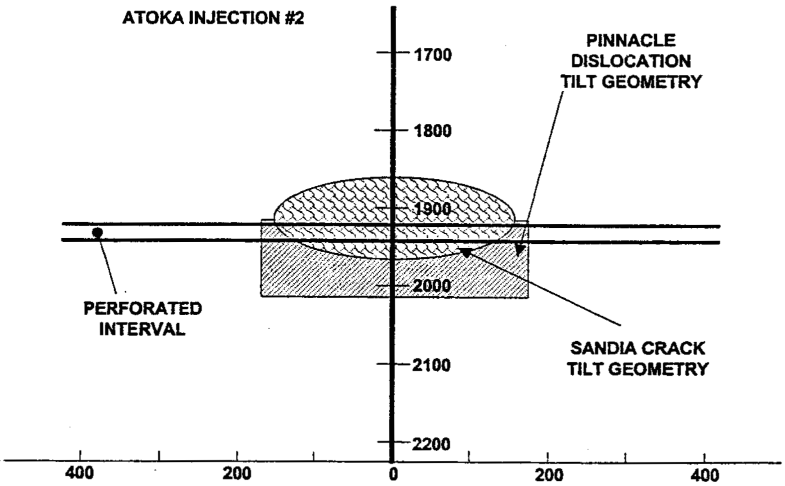

Figure D19. Comparison of Pinnacle dislocation and Sandia crack inversion, Atoka #2.

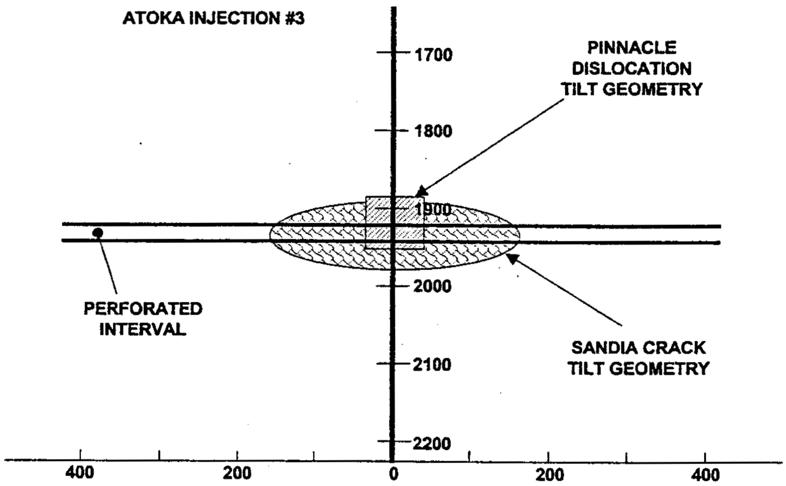

Figure D20. Comparison of Pinnacle dislocation and Sandia crack inversion, Atoka #3.

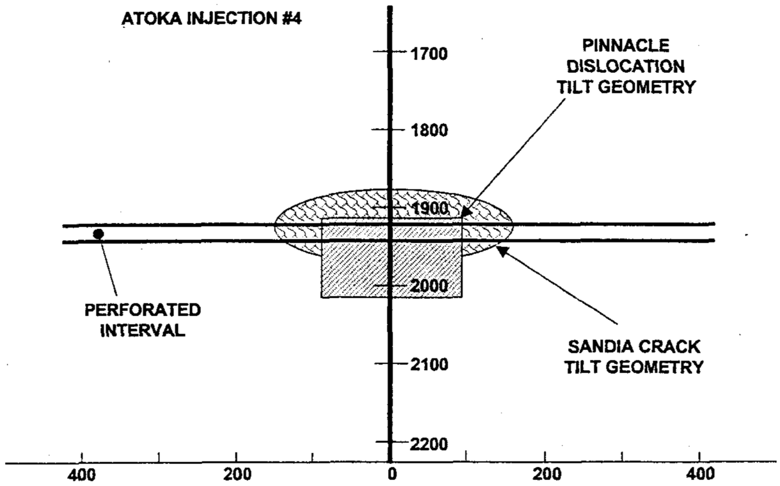

Figure D21. Comparison of Pinnacle dislocation and Sandia crack inversion, Atoka #4.

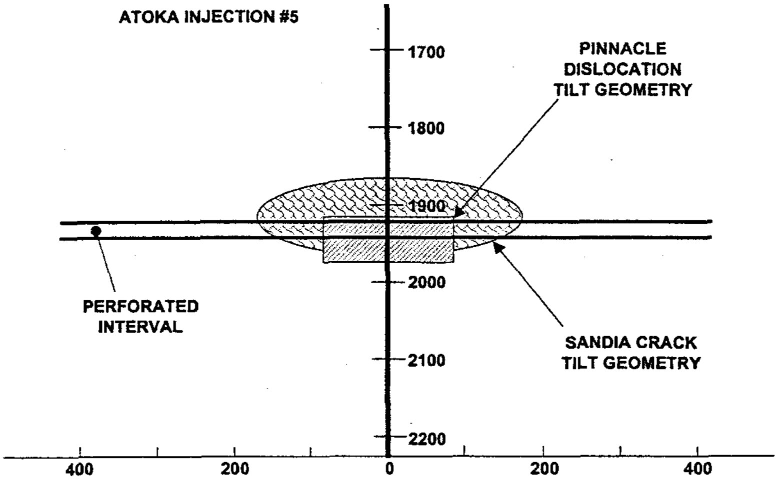

Figure D22. Comparison of Pinnacle dislocation and Sandia crack inversion, Atoka #5.

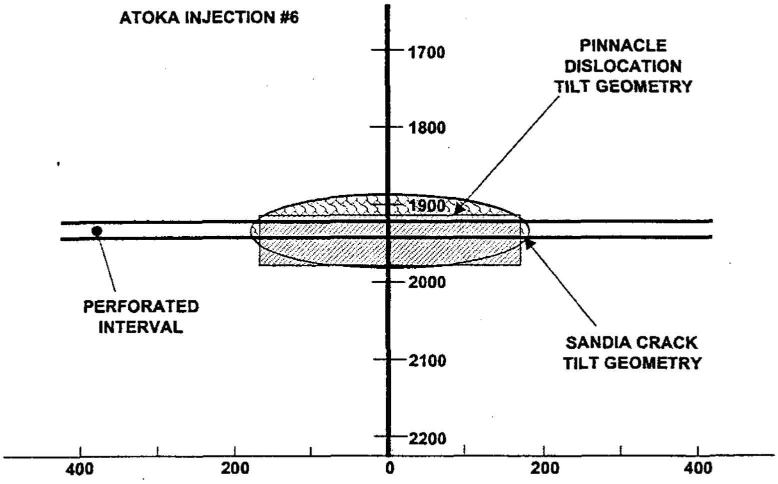

Figure D23. Comparison of Pinnacle dislocation and Sandia crack inversion, Atoka #6.

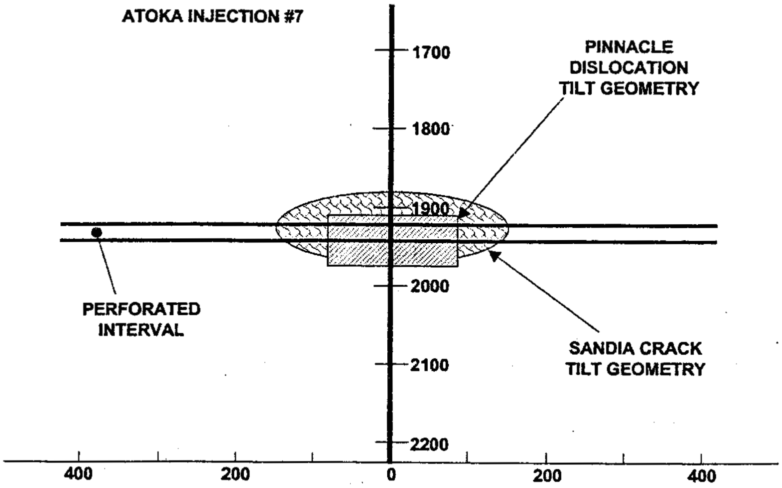

Figure D24. Comparison of Pinnacle dislocation and Sandia crack inversion, Atoka #7.

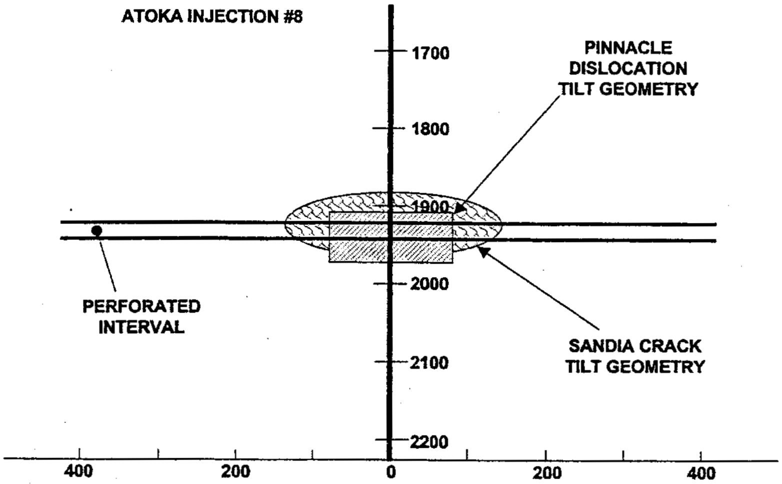

Figure D25. Comparison of Pinnacle dislocation and Sandia crack inversion, Atoka #8.

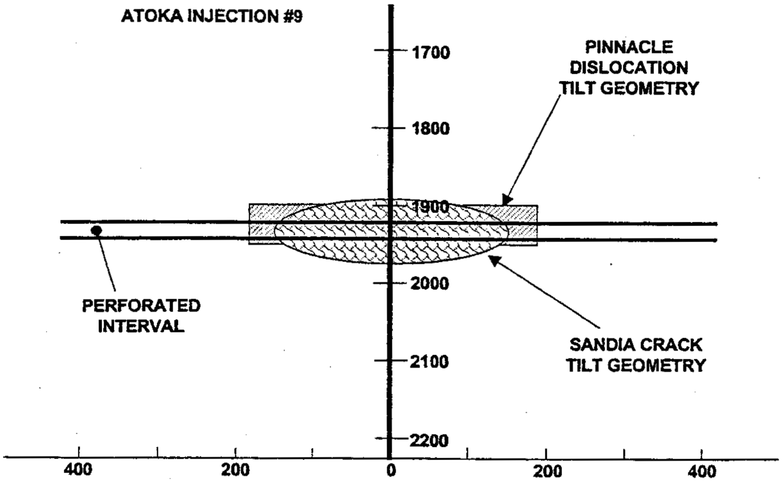

Figure D26. Comparison of Pinnacle dislocation and Sandia crack inversion, Atoka #9.

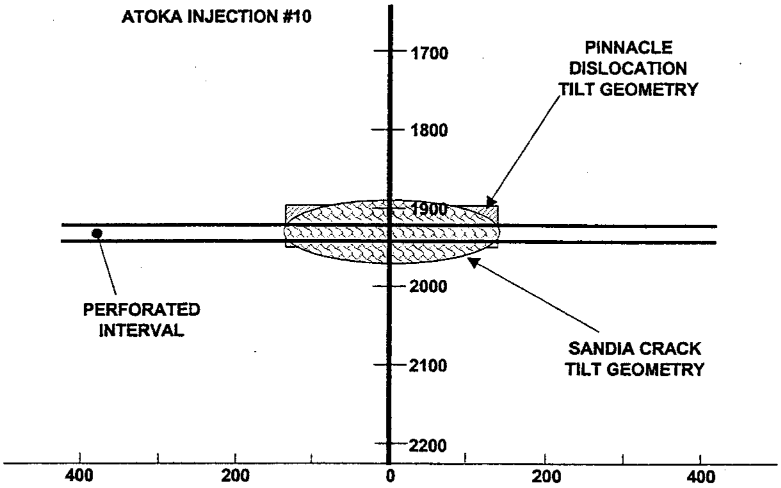

Figure D27. Comparison of Pinnacle dislocation and Sandia crack inversion, Atoka #10.

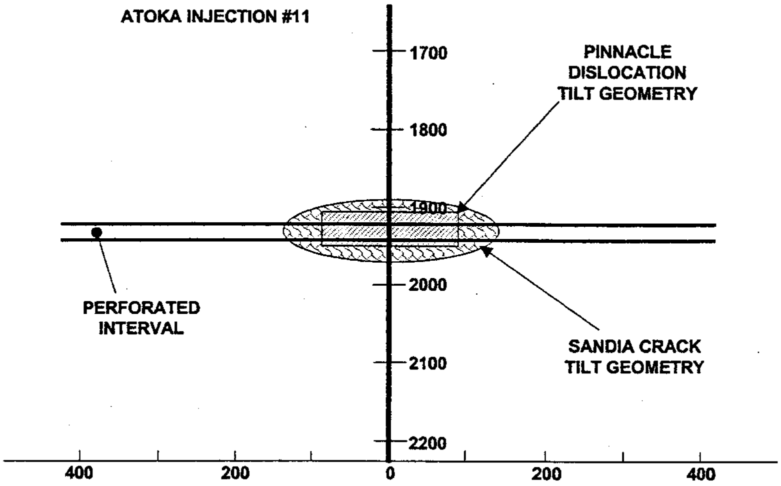

Figure D28. Comparison of Pinnacle dislocation and Sandia crack inversion, Atoka #11.

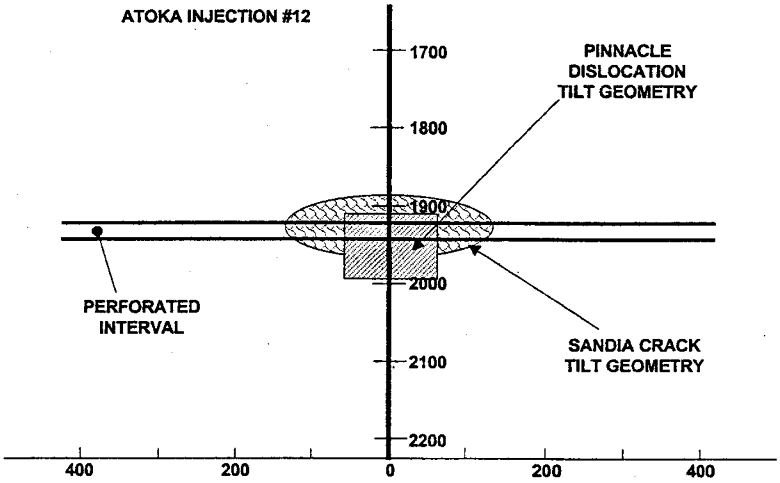

Figure D29. Comparison of Pinnacle dislocation and Sandia crack inversion, Atoka #12.

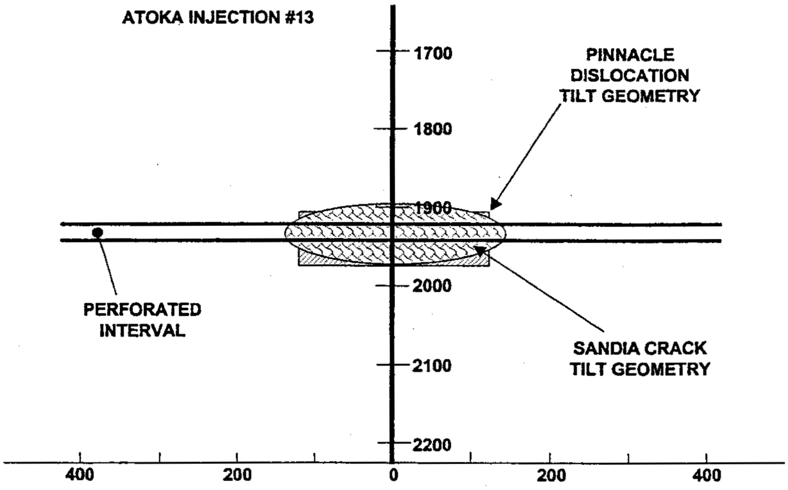

Figure D30. Comparison of Pinnacle dislocation and Sandia crack inversion, Atoka #13.

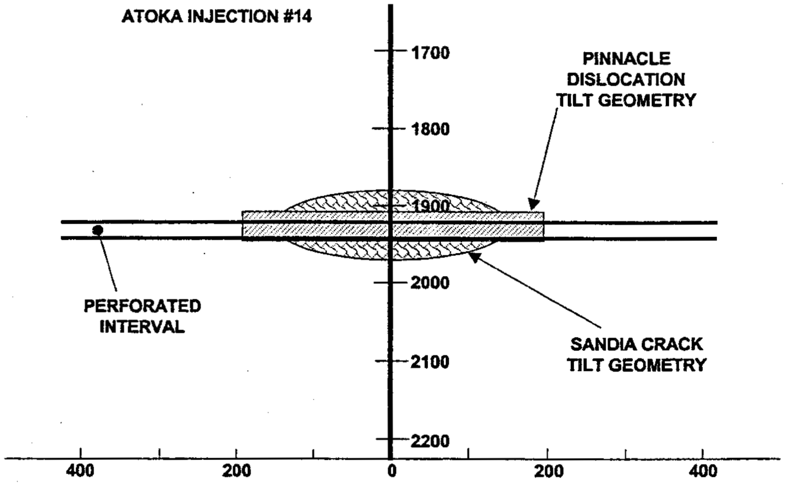

Figure D31. Comparison of Pinnacle dislocation and Sandia crack inversion, Atoka #14.

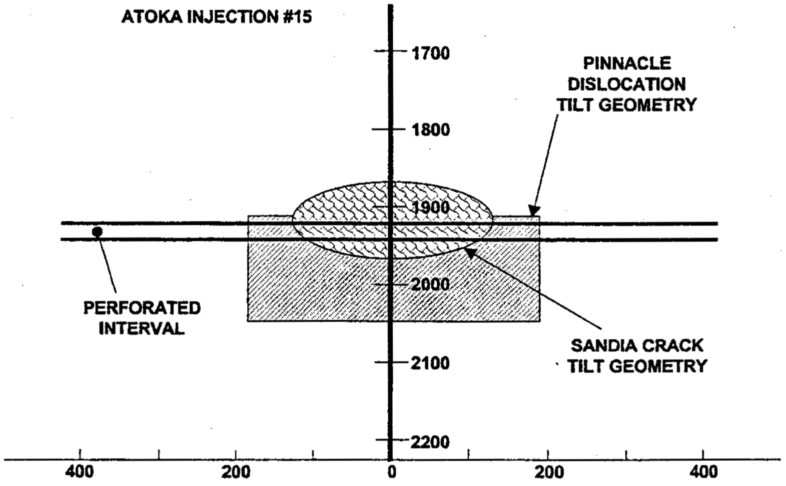

Figure D32. Comparison of Pinnacle dislocation and Sandia crack inversion, Atoka #15.

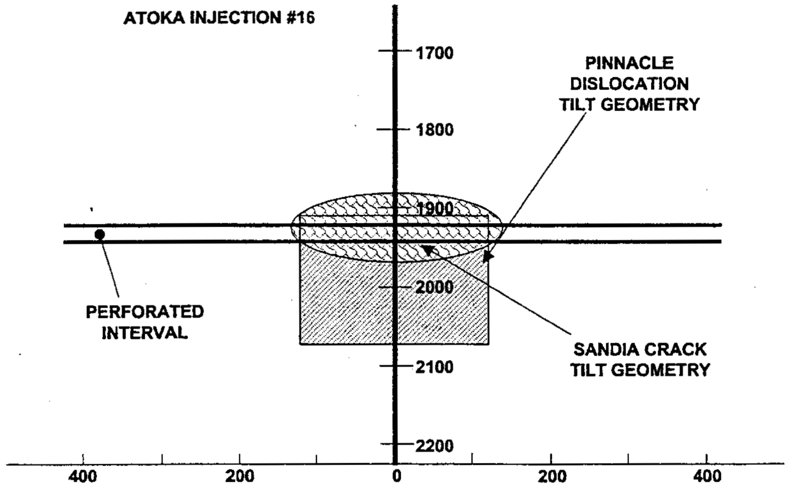

Figure D33. Comparison of Pinnacle dislocation and Sandia crack inversion, Atoka #16.

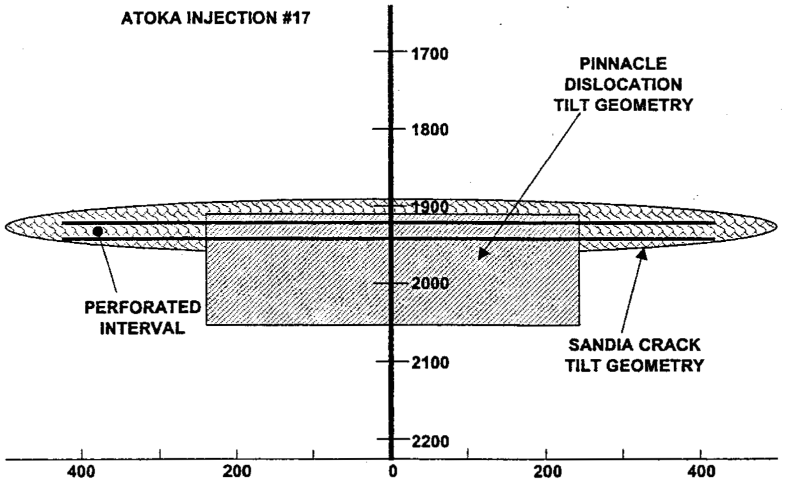

Figure D34. Comparison of Pinnacle dislocation and Sandia crack inversion, Atoka #17.

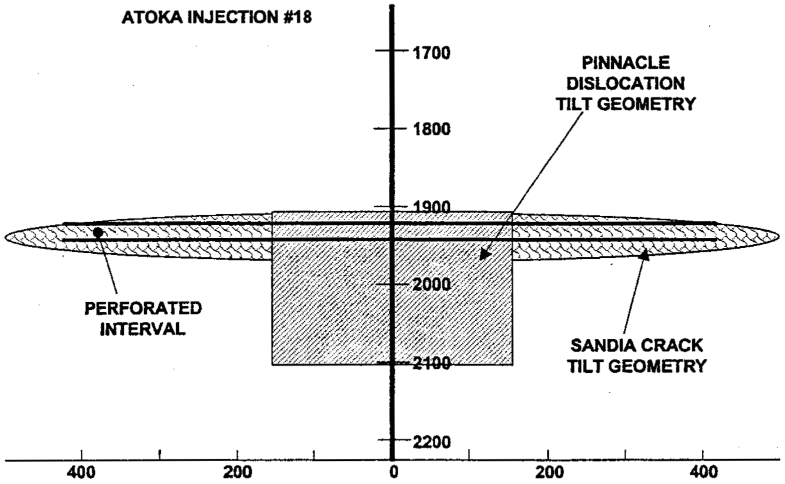

Figure D35. Comparison of Pinnacle dislocation and Sandia crack inversion, Atoka #18.

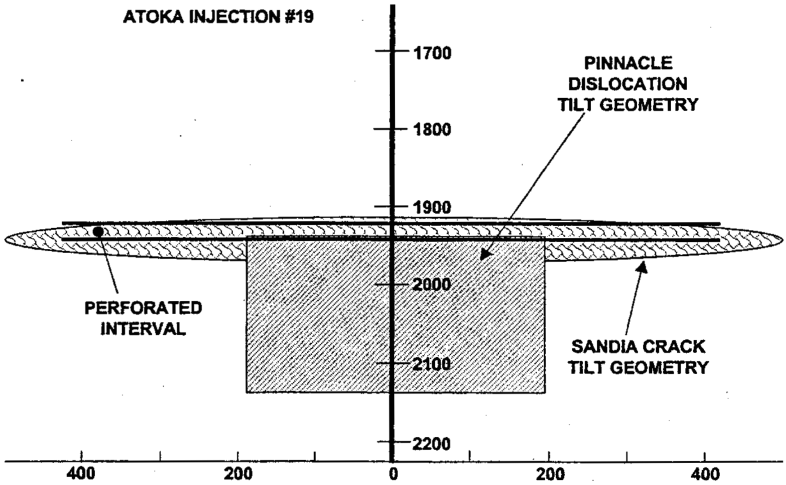

Figure D36. Comparison of Pinnacle dislocation and Sandia crack inversion, Atoka #19.

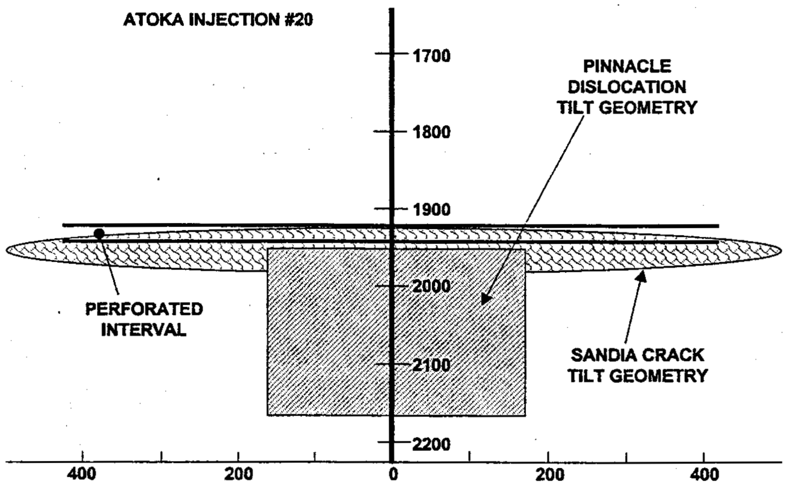

Figure D37. Comparison of Pinnacle dislocation and Sandia crack inversion, Atoka #20.

Appendix D References

1. Griffin, L.G., Wright, C.A., Davis, E.J., Weijers, L. and Moschovidis, Z.A., "Tiltmeter Mapping to Monitor Drill Cuttings Disposal," Proceedings, 37th U.S. Rock Mechanics Symposium, Vail Colorado, pp. 1033-1040, June 6-9, 1999.
2. CD, "Mounds Drill Cuttings Injection Project", S. Wolhart (manager), Gas Research Institute, Chicago, IL, 1999.
3. Okada, Y., "Internal Deformation Due to Shear and Tensile Faults in a Half-Space," *Bulletin of the Seismological Society of America*, **82**, No. 2, pp. 1018-1040, April 1992.

APPENDIX E
TILT EQUATIONS FOR TWO FRACTURES

Although most crack problems with complex geometries are too complicated for analytical solutions, the case of two equal 2D fractures aligned in the same plane has been solved by Willmore.[E1] His solution used a complex potential stress function first deduced in fluid flow problems for two equal flat plates in motion through a fluid at rest. Figure E1 shows the geometry of the problem. The limitation of crack lengths from k to 1 or –k to –1 is not a limitation as the cracks can be scaled to this size.

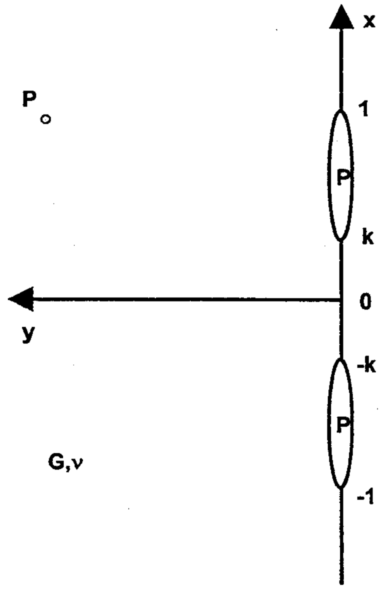

Figure E1. Geometry for Willmore's solution of two pressurized cracks.

Using the standard complex variables approach, the displacement and stresses are given by

$$\begin{aligned}
2Gu &= \mathrm{Re}\left[(2-4v)g(z)+(z-\bar{z})g'(z)\right]\\
2Gv &= \mathrm{Re}\left[-4i(1-v)g(z)+i(z-\bar{z})g'(z)\right]\\
\sigma_{xx} &= \mathrm{Re}\left[2g'(z)+(z-\bar{z})g''(z)\right]\\
\sigma_{yy} &= \mathrm{Re}\left[2g'(z)-(z-\bar{z})g''(z)\right]\\
\tau_{xy} &= \mathrm{Re}\left[i(z-\bar{z})g''(z)\right]
\end{aligned}$$

where z is the complex variable $x+iy$ and $\bar{z}$ is its conjugate. g(z) is the potential function that satisfies the problem.

For this case, Willmore found that the derivative of g(z) is given by

$$g'(z)=\frac{1}{2}P\left[\frac{z^2-\lambda^2}{\sqrt{(z^2-1)(z^2-k^2)}}-1\right]\quad (k<1),$$

where λ^2 = E'/K' with E' and K' being the complete elliptic integrals of the first and second kind for the modulus k' (the complement of k). To find displacements and stresses, the solution is quite tedious because it involves elliptic integrals with complex arguments. However, to find the tilts (which are the gradients of the displacement), only *g'(z)* and g *"(z)* are needed and these can be obtained easily.

The tilt of interest here is $\partial v / \partial x$, which can be found from the displacement as

$$\frac{\partial v}{\partial x} = \frac{1}{2G} \operatorname{Re}\left[-4i(1-\nu)g'(z) - 2yg''(z)\right]$$

which can then be simplified to yield

$$\frac{\partial v}{\partial x} = \frac{1}{G}\left\{2(1-\nu)\operatorname{Im}\left[g'(z)\right] - y\operatorname{Re}\left[g''(z)\right]\right\}$$

The function g"(z) is found by differentiating g'(z) to get

$$g''(z) = \frac{P}{2}\left\{\frac{2z\left(z^2-1\right)\left(z^2-k^2\right) - z^3\left(z^2-1\right) - z^3\left(z^2-k^2\right) + z\lambda^2\left(z^2-1\right) + z\lambda^2\left(z^2-k^2\right)}{\left[\left(z^2-1\right)\left(z^2-k^2\right)\right]^{3/2}}\right\}$$

At this point it is expedient to use the simplifications applied by Sneddon[E2] to Westergaard's stress function for a single crack. Using the notation

$$\begin{aligned} z &= re^{i\theta} \\ z-1 &= r_1 e^{i\theta_1} \\ z+1 &= r_2 e^{i\theta_2} \\ z-k &= r_3 e^{i\theta_{31}} \\ z+k &= r_4 e^{i\theta_{41}} \end{aligned}$$

then the appropriate functions can be deduced. These are

$$\operatorname{Im}\left[g'(z)\right] = \frac{P/2}{\sqrt{r_1 r_2 r_3 r_4}}\left\{r^2 \sin\left[2\theta - \left(\theta_1 + \theta_2 + \theta_3 + \theta_2\right)/2\right] - \lambda^2 \sin\left[-\left(\theta_1 + \theta_2 + \theta_3 + \theta_2\right)/2\right]\right\}$$

and

$$
\begin{aligned}
\operatorname{Re}[g''(z)] = \frac{P/2}{\sqrt{r_1 r_2 r_3 r_4}} \{ & 2r\cos[\theta-(\theta_1+\theta_2+\theta_3+\theta_4)/2] \\
& -\frac{r^3}{r_3 r_4}\cos[3\theta-(\theta_1+\theta_2+3\theta_3+3\theta_4)/2] \\
& -\frac{r^3}{r_1 r_2}\cos[3\theta-(3\theta_1+3\theta_2+\theta_3+\theta_4)/2] \\
& +\frac{r\lambda^2}{r_3 r_4}\cos[\theta-(\theta_1+\theta_2+3\theta_3+3\theta_4)/2] \\
& +\frac{r\lambda^2}{r_1 r_2}\cos[\theta-(3\theta_1+3\theta_2+\theta_3+\theta_4)/2] \}
\end{aligned}
$$

which can then be inserted into the tilt equation to give the final result,

$$
\begin{aligned}
\frac{\partial v}{\partial x} = & \frac{(1-\nu)P}{G\sqrt{r_1 r_2 r_3 r_4}}\{r^2\sin[2\theta-(\theta_1+\theta_2+\theta_3+\theta_4)/2]-\lambda^2\sin[-(\theta_1+\theta_2+\theta_3+\theta_4)/2]\} \\
& -\frac{r\sin(\theta)P}{2G\sqrt{r_1 r_2 r_3 r_4}}\Big\{2r\cos[\theta-(\theta_1+\theta_2+\theta_3+\theta_4)/2]-\frac{r^3}{r_3 r_4}\cos[3\theta-(\theta_1+\theta_2+3\theta_3+3\theta_4)/2] \\
& -\frac{r^3}{r_1 r_2}\cos[3\theta-(3\theta_1+3\theta_2+\theta_3+\theta_4)/2]+\frac{r\lambda^2}{r_3 r_4}\cos[\theta-(\theta_1+\theta_2+3\theta_3+3\theta_4)/2] \\
& +\frac{r\lambda^2}{r_1 r_2}\cos[\theta-(3\theta_1+3\theta_2+\theta_3+\theta_4)/2]\Big\}
\end{aligned}
$$

Appendix E References

Willmore, T.J., “The Distribution of Stress in the Neighbourhood of a Crack”, *Quarterly Journal of Mechanics and Applied Mathematics*,” **II**, Part 1, pp. 53-63, 1949.

Sneddon, I.N., “The Distribution of Stress in the Neighbourhood of a Crack in an Elastic Solid,” *Proceedings of the Royal Society*, Series A, **187**, pp. 229-260, 1946.

APPENDIX F
TILT EQUATIONS FOR POROELASTIC COMPONENT

One simple method to estimate the tilt field induced by pressurization of the reservoir is to use the nucleus of strain approach used by Geertsma[F1] to analyze reservoir subsidence. Following Geertsma's development, the strain at some point in the ground can be found as

$$u_i = \int P(\xi) u_c^*(x,\xi) dV(\xi) \ ,$$

where $P(\xi)$ is the pressure change at some point ξ in the reservoir, u_c^* is the displacement resulting from a unit pressure change at the point ξ, dV is the differential volume of the strain nulcei, and u_i is the total resultant strain..

Geertsma[F1] gives the total displacement vector , but in this case only the horizontal component is of interest. Using the plan view geometry in Figure F1, the monitor well is at a distance d from the fracture. As a result of leakoff, there is a pressurized zone around the fracture of width w.

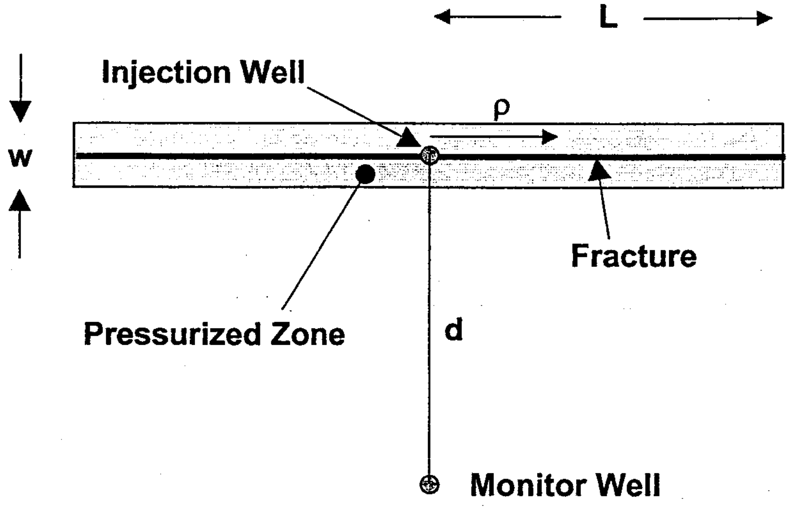

Figure F1. Plan view schematic of fracture pressurized zone.

Using Geertsma's results, the formula for the horizontal component of u_c^* normal to the fracture plane can be given as

$$u_c^* = \frac{c_m}{4\pi}\left[\frac{d}{R_1^3} + \frac{(3-4\nu)d}{R_2^3} - \frac{6z(z+c)d}{R_2^5}\right],$$

with

$$R_1^2 = \rho^2 + d^2 + (z-c)^2$$
$$R_2^2 = \rho^2 + d^2 + (z+c)^2$$

and

$$c_m = \frac{(1-2\nu)\alpha}{2(1-\nu)G} \ ,$$

where α is Biot's parameter and G is the shear modulus. Examining the terms in the displacement equation, it is clear that the last two terms are for the mirror image strain nucleus that yields the traction free surface. For downhole tiltmeters far from the free surface, those two terms are very small and can be ignored if the tiltmeters are deep relative to the fracture depth (i.e, none of the tiltmeters is very close to the surface). If Geertsma's approximation of a thin reservoir is applied and if the width of the pressurized region is assumed small relative to the monitoring distance, then the normal horizontal displacement can be given simply as

$$u_n = \frac{H\,w\Delta P}{4\pi} \int_{-L}^{L} \frac{d \quad d\rho}{\left[\rho^2 + d^2 + (z-c)^2\right]^{3/2}} \,,$$

where ΔP is the injection pressure minus the reservoir pressure, c is the depth to the center of the fracture, z is the depth to tiltmeter location, and ρ is distance from the injection well to a strain nucleus located somewhere on the fracture. The integration is performed across all strain nuclei from $-L$ to L. Performing the integration, the displacement is found to be

$$u_n = \frac{H\,w\Delta P}{2\pi} \left[\frac{d\,L}{\left\{d^2 + (z-c)^2\right\} \sqrt{L^2 + d^2 + (z-c)^2}} \right]$$

and the tilt is given by

$$\frac{\partial u_n}{\partial z} = -\frac{H\,w\Delta P}{2\pi} \left[\frac{2dL(z-c)}{\left\{d^2 + (z-c)^2\right\}^2 \sqrt{L^2 + d^2 + (z-c)^2}} + \frac{dL(z-c)}{\left\{d^2 + (z-c)^2\right\}\left\{L^2 + d^2 + (z-c)^2\right\}^{3/2}} \right].$$

The final question is the determination of an appropriate width of the pressurized zone. Since linear flow out of the fracture into the formation results in a pressure distribution of the form

$$P(x,t) = P_o + \Delta P \,\mathrm{erfc}\left[\mathrm{y} \sqrt{\frac{\varphi\mu c}{\mathrm{kt}}} \right] ,$$

an integration of the pressure disturbance term from zero to ∞ yields a pressure-weighted width function as

$$\overline{w} = \sqrt{\frac{kt}{\pi\varphi\mu c}} \,.$$

This equation yields an appropriate width of the pressurized zone for one side of the fracture, so the actual width is twice this value ($\mathrm{w} = 2\overline{w}$).

It should be stressed that this approach is only an approximation of the poroelastic tilts unless the tiltmeters are far from the fracture and the thickness of the reservoir is small relative to vertical distances to the tiltmeters. Even though the second requirement is not met, these results should provide a reasonable estimate of the poroelastic tilts. Nevertheless, it is not recommended that these equations be used for tilt inversions. Rather, the full integration over the thickness of the zone and the width of the pressurized region should be employed. Furthermore, the tilts parallel to the fracture can also be determined and used in the analysis.

Appendix F References

Geertsma, J., "Problems of Rock Mechanics in Petroleum Production Engineering," Proceedings, 1st Congress of the International Society of Rock Mechanics, Lisbon, **I**, pp 585-594, 1966.

External Distribution

National Petroleum Technology Office
US Dept of Energy
One West Third Street
Tulsa, OK 74103-3519
Attn: Rhonda Lindsay

National Petroleum Technology Office
US Dept of Energy
One West Third Street
Tulsa, OK 74103-3519
Attn: Robert Lemmon

National Energy Technology Lab
P.O. Box 880
Morgantown, WV 26507-0880
Attn: Jim Ammer

National Energy Technology Lab
P.O. Box 880
Morgantown, WV 26507-0880
Attn: Roy Long

National Energy Technology Lab
P.O. Box 880
Morgantown, WV 26507-0880
Attn: Al Yost

Advantek International
Ahmed Abou-Sayed
P.O. Box 16639
Houston, TX 77479

Baroid
Matt Frankl
3120 Southwest Freeway
Suite 300
Houston, TX 77098

Chevron
Keith Hejl
5001 California Avenue
Bakersfield, CA 93302

Chevron
Craig Lewis
2202 Oil Center Court
Houston, TX 77073

Chevron
Peng Ray
2202 Oil Center Court
Houston, TX 77073

Chevron
Jay Avasthi
2202 Oil Center Court
Houston, TX 77073

Chevron
Carole Fleming
2202 Oil Center Court
Houston, TX 77073

Exxon Production Research
Jeff Bailey
3318 Mercer Street
Houston, TX 77027

Exxon Mobil
Steinar Ottesen
P.O. Box 819047
Dallas, TX 75381-9047

Exxon Mobil
Julie Elward-Berry
16945 Northchase
Houston, TX 77060-2108

Exxon Mobil
Charlene Owens
P.O. Box 2189
Houston, TX 77252-2189

Gas Technology Institute (5)
Steve Wolhart
4800 Research Forest Drive
The Woodlands, TX 77381

Halliburton Energy Services
Buddy McDaniel
P.O. Drawer 1431
Duncan, OK 73536-0426

Hughes Christensen
Allen Sinor
9110 Grogan's Mill Road
Houston, TX 77380

PCM Technical, Inc.
Zissis Moschovidis
507 S. Main Street
Suite 507
Tulsa, OK 74103

Pinnacle Technologies
Chris Wright
600 Townsend Street
Suite 160W
San Francisco, CA 94103

Schlumberger
Matt Garber
5 Broadway Executive Park Bldg.
Oklahoma City, OK 73116-8214

Schlumberger
Reid Beecher
525 South Main, #204
Tulsa, OK 74103

Shell E&P Technology
John Dudley
3737 Bellaire Blvd.
Houston, TX 77025

Sperry Sun
Chuck Henkes
9800 W. Reno Avenue
Oklahoma City, OK 73127-2969

Exxon Mobil
Ron Steiger
12322 Gainsborough Drive
Houston, TX 77031

Branagan & Associates
Paul Branagan
6265 Stevenson Way
Las Vegas, NV 89193

Branagan & Associates
Rich Peterson
6265 Stevenson Way
Las Vegas, NV 89193

<u>SNL Distribution</u>

Marianne Walck, 6116, MS-0750
Bruce Engler, 6116, MS-0750
James Uhl, 6116, MS-0750
John Lorenz, 6116, MS-0750
Norman Warpinski, 6116, MS-0750 (25)
Technical Library, 9616, MS-0899 (2)
Central Technical Files, 8940-2, MS-9018
Review & Approval Desk, 9612, MS-0612 For DOE/OSTI